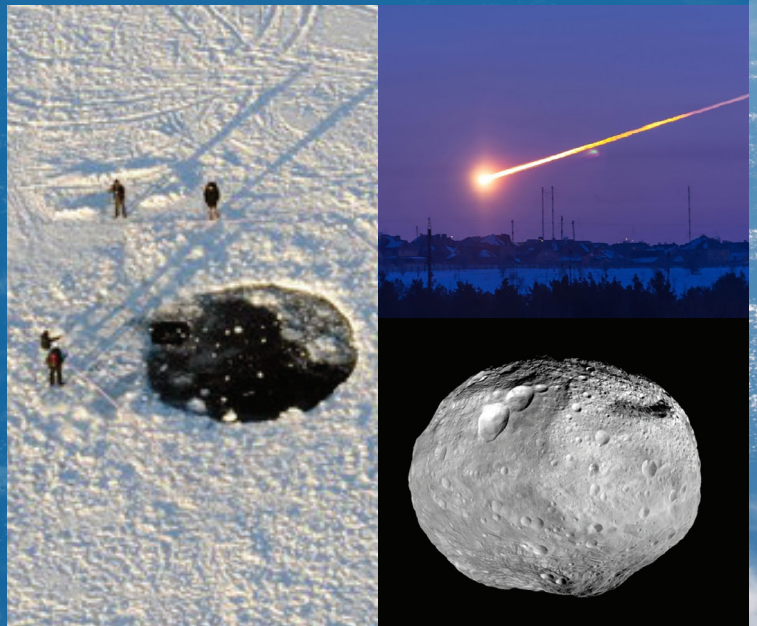


Report of the Near-Earth Object Science Definition Team

Update to Determine the Feasibility of Enhancing the Search and Characterization of NEOs

Prepared at the request of National Aeronautics
and Space Administration, Science Mission
Directorate, Planetary Science Division

SEPTEMBER 2017



National Aeronautics and Space Administration

On the Cover

A. The hole in an ice-covered lake made by the impact of an unnamed asteroid near Chelyabinsk, Russia, on 15 February 2013. The meteor entered Earth's atmosphere with a speed exceeding 19 km/s. Most of the impact energy was released in the atmosphere, but a remnant survived to land in Lake Chebarkul.

Photo credit: Eduard Kalinin. Source: "Earth at Higher Risk of Asteroid Impact, Russian Meteor Reveals," *Space.com*, 6 November 2013; <http://www.space.com/23487-asteroid-threat-earth-russian-meteor-explosion.html>

B. An image of the Chelyabinsk meteor fireball streaking through the atmosphere across the Urals. Source: What's Up with That, "Bigger problems than global warming: NASA discovers 8 new dangerous near-Earth asteroids," 19 January 2015, <https://wattsupwiththat.com/2015/01/19/bigger-problems-than-global-warming-nasa-discovers-8-new-dangerous-near-earth-asteroids/>

C. An image of a typical minor planet as a stand-in for the lack of a precollision picture of the Chelyabinsk asteroid. Here pictured is minor planet Vesta. Photo courtesy of NASA.

A.	B.
	C.

Update to Determine the Feasibility of Enhancing the Search and Characterization of NEOs

Report of the Near-Earth Object Science Definition Team

September 2017

*Prepared at the request of
National Aeronautics and Space Administration,
Science Mission Directorate,
Planetary Science Division*

Signature Page



Grant H. Stokes



Brent W. Barbee



William F. Bottke, Jr.



Marc W. Buie



Steven R. Chesley



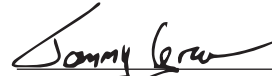
Paul W. Chodas



Jennifer B. Evans



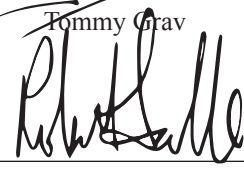
Robert E. Gold



Tommy Grav



Alan W. Harris



Robert Jedicke



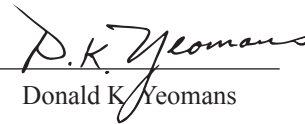
Amy K. Mainzer



Donovan L. Mathias



Timothy B. Spahr



Donald K. Yeomans

EXECUTIVE SUMMARY

Near-Earth Object Science Definition Team Update to Determine the Feasibility of Enhancing Search and Characterization of NEOs

In recent years, there has been an increasing appreciation for the hazards posed by near-Earth objects (NEOs), those asteroids and periodic comets (both active and inactive) whose motions can bring them into the Earth's neighborhood. In August 2002, NASA chartered a Science Definition Team (SDT) to study the feasibility of extending the search for near-Earth objects to smaller limiting diameters. The formation of the 2003 team was motivated by the good progress being made toward achieving the so-called Spaceguard goal of discovering 90% of all NEOs with diameters greater than 1 kilometer by the end of 2008. The 2003 SDT's chartered mission posed the question of what, if anything should be done with respect to the much more numerous smaller, but still potentially dangerous, objects. The team was tasked with providing recommendations to NASA as well as the answers to the following seven specific questions:

1. What are the smallest objects for which the search should be optimized?
2. Should comets be included in any way in the survey?
3. What is technically possible?
4. How would the expanded search be done?
5. What would it cost?
6. How long would the search take?
7. Is there a transition size above which one catalogs all the objects and below which the design is simply to provide warning?

The report of the 2003 SDT (Stokes et al. 2003) was quite influential over the subsequent years as NASA and the community evolved capabilities for asteroid search, and it was the basis for Congressional directions pertaining to the NEO issue.

In the time since the 2003 report was issued, considerable progress has been made cataloging the NEO population, and the technology available for use to search for minor planets has become considerably more advanced. In May 2016, NASA chartered a new SDT to review the same seven questions and to update the answers in light of the new technical capability and the advances in knowledge of population and impact damage modeling. This report documents the output and findings of the 2017 SDT.

Team Membership

The 2017 SDT membership was composed of experts in the fields of asteroid and comet search, including the principal investigators of a major asteroid search effort; experts in orbital dynamics, NEO population estimation, ground-based and space-based astronomical optical systems; and the director of the NASA Center for NEO Studies. Members having familiarity with Department of Defense

space surveillance technology were included. Several of the 2017 members were also members of the original 2003 team.

Analysis Process

The current team approached the task by using a cost/benefit methodology comparable to that used by the 2003 team whereby the following analysis processes were completed:

Population estimation. An estimate of the population of NEOs, including their sizes, albedos, and orbit distributions, was generated by using the best methods in the current literature. We estimate a population of about 934 NEOs larger than 1 kilometer, leading to an impact frequency of about one in a half a million years. The population of NEOs with diameters of 140 meters and larger is estimated to be ~25,000. To the lower limit of an object's atmospheric penetration (about 50 meters in diameter for non-metallic objects), we estimate about half a million NEOs, with an impact frequency of about one in a thousand years.

Impact hazard. The damage and casualties resulting from an impact with members of the hazardous population were estimated. These estimates included ones for direct damage from land impact, as well as ones for the amplification of damage caused by tsunami and global effects. The capture cross section of the Earth was then used to estimate an impact rate and thus a yearly average hazard from NEO impact as a function of their diameter. The sophistication of impact damage assessment has very considerably increased since the 2003 report, and the new analysis is one of the major contributions to the 2017 report.

Search technology. Broad ranges of technology and search systems were evaluated to determine their effectiveness when used to search large areas of the sky for hazardous objects. These systems include ground-based and space-based optical and space-based infrared systems across the currently credible range of optics and detector sizes. Telescope apertures of 2, 4, and 8 meters were considered for ground-based search systems, along with space-based telescopes of 0.5, 1, and 2-meter apertures. Space-based telescopes were assessed in number of orbital locations, including in low-Earth orbit (LEO), in geosynchronous orbit (GEO), in solar orbits at the Lagrange points (L-1 and L-2), and at a point that trails the planet Venus.

Search simulation. A detailed simulation was conducted for each candidate search system, and for combinations of search systems working together, to determine the effectiveness of the various approaches in cataloging members of the hazardous object population. The simulations were accomplished by using a NEO survey simulator, originally developed for the 2003 SDT, which has been updated and revalidated to apply to current systems. Additional simulation tools were used to assess the space-based IR systems included in the 2017 SDT. The simulation process takes into account a broad range of "real-world" effects that affect the productivity of search systems, such as weather, sky brightness, zodiacal background, etc. The use of a substantially common simulation process and tooling enables direct comparisons between the 2003 report and the current report.

Search system cost. The cost of building and operating the search systems described herein was estimated by a cost team employing standard estimation tools. The cost team employed existing and accepted NASA models to develop the costs for space-based systems. They developed the ground-based system cost estimates by analogy with existing systems and updates from the 2003 estimates.

All cost results, stated in FY2017 dollars, were cross-checked by applying inflation to the 2003 cost results for similar systems, where applicable.

Cost/benefit analysis. The cost of constructing and operating potential survey systems was compared with the benefit of reducing the risk of an unanticipated object impact by generating a catalog of potentially hazardous objects (PHOs). PHOs, a subset of NEOs, closely approach Earth's orbit to within 0.05 AU (7.5 million kilometers). PHO impacts capable of causing damage occur infrequently, but the threat is large enough that, when averaged over time, the anticipated yearly average of impact-produced damage is significant. Thus, while developing a catalog of all the PHOs does not actually eliminate the hazard of impact, it does provide a clear benefit by providing awareness of specific potential short-term and long-term threats. The nominal yearly average remaining, or residual, risk in year 2023 associated with PHO impact, assuming an extension of current search systems operations, is estimated to be approximately 180 casualties per year worldwide, plus the attendant property damage and destruction. This level of remaining uncharacterized risk has a dollar value estimated to be ~\$757 million per year. About 5% of the risk is attributed to regional damage from smaller land impacts, >1% to water impacts and the ensuing tsunamis, and 95% to the residual risk of global climatic disruption caused by large impacts. The sophistication of the benefit modeling in this 2017 report has been considerably improved over that used in the 2003 document. Major drivers of those improvements are the following: (1) estimates of the damage caused by each mechanism involved in impacts have been much improved; (2) damage estimates now include the statistical value of injury as well as death; (3) impact rates have been updated based on a more complete knowledge of asteroid population than existed in 2003; (4) the value of property and infrastructure damage has been calibrated by experience gained in natural disasters; and (5) we have made use of improved modeling methods and experience gained by the natural disaster response community since the 2003 document.

PHO Search Goals and Feasibility

The SDT evaluated the capability and performance of a large number of ground-based and space-based sensor systems in the context of the cost/benefit analysis. Basing their findings on this analysis, the team concludes that the next-generation search system can be reasonably constructed to eliminate 90% of the risk posed by unwarned impact with sub-kilometer-diameter PHOs. Such a system would also eliminate essentially all of the global risk remaining after the Spaceguard efforts were completed. The implementation of this recommendation will result in a substantial reduction in uncharacterized risk to a total of fewer than 80 casualties per year plus attendant property damage and destruction. A number of search system approaches identified by the SDT could be employed to reach this goal, all of which have highly favorable cost/benefit characteristics. The final choice of sensors will depend on factors such as the time allotted to accomplish the search and the available investment (see Figures 9-4 and 9-5).

Answers to Questions Stated in SDT Charter

1. What are the smallest objects for which the search should be optimized? The SDT finds that the search system could be constructed to produce a catalog that is 90% complete for PHOs larger than 140 meters, which corresponds to characterizing 90% of the impact risk of sub-global effects. In effect, this characterization also captures 99% of the risk to human populations of an unwarned asteroid impact.

2. *Should comets be included in any way in the survey?* The SDT's analysis indicates that the frequency with which long-period comets (of any size) closely approach the Earth is roughly one-hundredth the frequency with which asteroids closely approach the Earth and that the fraction of the total risk represented by comets is approximately 1%. The relatively small risk fraction, combined with the difficulty of generating a catalog of comets, leads the SDT to the conclusion that, at least for the next generation of NEO surveys, the limited resources available for NEO searches would be better spent on finding and cataloging Earth-threatening near-Earth asteroids and short-period comets. An effective NEO search system would naturally provide an advance warning of at least months for most threatening long-period comets.

3. *What is technically possible?* Current technology offers asteroid detection and cataloging capabilities an order of magnitude better than the capabilities now available in operating systems used for detection and cataloging. NEO search performance is generally not now limited by technology, but rather by resources. This report outlines a variety of search system examples, all of which are possible using current technology. Some of these systems, when operated over a period of 9 to 25 years, would generate a catalog that is 90% complete for NEOs larger than 140 meters (see Figure 9-5).

4. *How would the expanded search be done?* From a cost/benefit point of view, there are a number of attractive options for executing an expanded search that would vastly reduce the risk posed by unwarned PHO impacts. The SDT identified a series of specific space-based, and mixed ground- and space-based systems that could accomplish the next-generation search.

5. *What would it cost?* For a search period from 9 to 25 years, the SDT identified several systems that would characterize, at varying rates, 90% of the sub-global risk for NEO impacts, with costs ranging between \$750 million and \$2 billion in FY2017 dollars. All of these systems have risk-characterization benefits that well exceed the costs of system acquisition and operation.

6. *How long would the search take?* A period of 9 to 25 years is sufficient to generate a catalog 90% complete to 140-meter diameter. The specific period depends on the choice of search technology and the investment allocated.

7. *Is there a transition size above which one catalogs all the objects and below which the design is simply to provide warning?* The SDT concluded that, given sufficient time and resources, a search system could be constructed to completely catalog hazardous objects with sizes down to the limit at which air blasts would be expected for non-metallic objects (about 50 meters in diameter). Below this limit, there is relatively little direct damage caused by the object (excepting the ~5% of metal-rich objects that can penetrate the atmosphere at smaller sizes). Over the 9- to 25-year interval (starting in 2023) during which the next-generation search would be undertaken, the SDT finds that cataloging is the preferred and affordable approach down to approximately the 140-meter-diameter level and that these search systems would inherently provide an impact warning for 60–90% of objects as small as 50 meters.

SDT Specific Findings

The SDT has developed three specific findings for NASA as a result of the analysis effort:

Finding 1. Future goals related to searching for potential Earth-impacting objects are best stated explicitly in terms of the statistical risk characterized and should be firmly based on cost/benefit analyses. This finding recognizes that searching for potential Earth-impacting objects is of interest primarily to eliminate the statistical risk associated with the hazard of unwarned impacts. The “average” rate of destruction from impacts is large enough to be of great concern; however, although a significant impact could occur at any time, the estimated average event rate is quite low. Thus, a search to determine if there are PHOs likely to impact the Earth within the next few hundred years is prudent. Such a search would best be executed in a way that eliminates the maximum amount of statistical risk uncertainty per dollar of investment.

Finding 2. It would be most productive to develop and operate a NEO search program with the goal of discovering and cataloging the potentially hazardous population sufficiently well to eliminate 90% of the uncharacterized risk from sub-kilometer objects (i.e., sub-global impact effects). The above goal is sufficient to reduce the average casualty rate uncertainty from about 180 casualties per year to fewer than 80 per year. Any such search would find the majority of the larger objects remaining undiscovered, thus greatly decreasing the global risk from these larger objects. Over a period of 9 to 25 years, a number of system approaches are capable of meeting this search metric with quite good cost/benefit ratios.

Finding 3. The satisfaction of the 140-meter cataloging objective will require space-based search system(s). Infrared (IR) and visible sensors in the 0.5- to 1.0-meter aperture range are credible and cost/benefit-favorable options that use available technology. The best cost/benefit and lowest-risk systems, of those assessed, are located at L1. The fastest completion of the objective, using the assessed systems, is provided by a large-aperture IR system or a combined visible and IR system located at L1. Search systems located near the Earth (at L1/geosynchronous/low Earth orbit) have the additional advantage of providing a substantial warning benefit while the catalog is being completed.

This page is intentionally blank.

TABLE OF CONTENTS

EXECUTIVE SUMMARY	i
TABLE OF CONTENTS	vii
LIST OF FIGURES	xi
LIST OF TABLES	xvii
1 INTRODUCTION	1
1.1 Background	1
1.2 Science Definition Team Formation and Charter	2
1.3 Team Membership	2
1.4 Study Approach	4
1.5 Updates Since 2003 NEO SDT Report	6
2 POPULATION ESTIMATES	9
2.1 Orbital and Size Distributions	9
2.2 Population Debiasing	11
2.3 Comets	12
2.3.1 Paucity of Small Comets	13
2.3.2 Short-Period Comet Threat	13
2.3.3 Long-Period Comet Threat	13
2.4 Near-Earth Object Absolute Magnitude and Size-Frequency Distributions	15
2.4.1 Progress in Estimating Population and Completion	15
2.4.2 Conversion from Absolute Magnitude to Diameter	18
2.4.3 Diameter Frequency and Albedo Distribution	22
2.5 Impact Frequency, Then and Now	25
Appendix 2-A. Analysis of How Different NEO Orbital Distributions Affect Survey Completeness	28
Appendix 2-B. Understanding How Absolute Magnitude Bins Affect the Differential NEO Population	33
3 IMPACT RISK ASSESSMENT	39
3.1 Probabilistic Impact Risk Model	39
3.1.1 Energy Deposited in the Atmosphere	40
3.1.2 Ground Damage Risks	41

TABLE OF CONTENTS (continued)

3.1.3	Tsunami Modeling	45
3.1.4	Global Effects	47
3.2	Impact Analysis Results	48
3.2.1	Impact Parameter Inputs	48
3.2.2	Local Damage Results	52
3.2.3	Tsunami Damage Results	55
3.2.4	Global Effects Results	56
3.2.5	Combined Risk from All Hazards	58
3.2.6	Potential Risk Uncertainty Reduction Resulting from Surveys	62
	Appendix 3-A. Raw Results of Mapping to the Size Bins Used in the SDT Report	66
4	CANDIDATE TECHNOLOGIES AND SYSTEMS	69
4.1	Ground-Based Systems	70
4.1.1	Current and Recent Ground-Based Systems	70
4.1.2	Expected New Ground-Based Systems	72
4.1.3	Existing Ground-Based Light Sensors (CCDs)	74
4.1.4	Modeled Ground-Based Systems	78
4.1.5	Modeled Ground-Based System Site Characteristics	80
4.1.6	Synthetic Tracking	82
4.2	Space-Based Systems	83
4.2.1	Spacecraft System	83
4.2.2	Orbit	84
4.2.3	Visible and Infrared Sensors	85
4.2.4	Current and Recent Space-Based Systems	86
4.2.5	Modeled Space-Based Systems	87
4.2.6	Future IR Space-Based Systems	90
4.2.7	Future Visible Space-Based Systems	97
5	SEARCH STRATEGY	99
5.1	Search Regions	99
5.2	Infrared Search Strategy—Historical Approach	102
5.3	Cadence and Linking Issues, and Cadence Requirements	102

TABLE OF CONTENTS (continued)

5.4	Synthetic Tracking and Two-Image Cadences	102
5.5	Astrometry	103
5.6	Cataloging versus Warning Strategies	103
5.7	Notes on Survey Optimization	104
5.8	Findings	104
5.9	Difficult-to-Find Objects	104
6	SIMULATION AND PERFORMANCE DESCRIPTION	109
6.1	Population Model for Simulation	109
6.1.1	Population of Impactors for Warning	111
6.2	Simulation Tools	111
6.2.1	FROSST	111
6.2.2	Survey Simulation Tool	116
6.3	Validation of Simulation Tools	117
6.3.1	Validation of FROSST	118
6.3.2	Validation of SST	122
6.4	Establishing a Baseline	122
6.5	Results	126
6.5.1	Cataloging	127
6.5.2	Warning	128
6.5.3	Output Plots and Observations	128
7	SYSTEM COST ESTIMATION	147
7.1	Ground-Based Observatories	148
7.1.1	Ground-Based Telescope Development and Construction	148
7.1.2	Ground-Based Observatory: Instrument Design and Development	150
7.1.3	Ground-Based Observatory Operations and Support	151
7.1.4	Ground-Based Software Development	152
7.1.5	Ground-Based Observatory Cost Roll-up	153
7.2	Space-Based Observatories	154
7.2.1	Spacecraft Bus	155
7.2.2	Space-Based Instruments	158

TABLE OF CONTENTS (continued)

7.2.3	Mission Operations and Support Costs	160
7.2.4	Space-Based Observatory Cost Roll-up	162
7.3	Summary	163
8	COST / BENEFIT CONCLUSIONS	165
8.1	Approach	165
8.1.1	Definition of Benefit	165
8.1.2	Improvements on the Previous Study	166
8.2	Assigning Statistical Values	167
8.2.1	Value of a Statistical Life	167
8.2.2	Property Damage	167
8.2.3	Abbreviated Injury Scale	168
8.2.4	Overpressure Drives Injury and Property Damage	169
8.3	Quantifying Benefit	170
8.4	Benefit Results	170
8.5	Warning	178
8.6	Cost/Benefit Comparison	180
9	SYSTEM COMPARISONS AND SUMMARY OF STUDY RESULTS	183
9.1	Establishing a Realistic Goal	183
9.2	Performance Overview for Systems Designed to Meet the Goal	185
9.2.1	Cataloging and Warning Efficiency	185
9.2.2	Ground-Based Visible Light Systems	186
9.2.3	Space-Based Systems and Combined Ground- and Space-Based Systems	186
9.2.4	Cost/Benefit Ratios	187
9.3	Space-Based IR Systems versus Ground-Based Visible System Performance	187
9.4	Time and Expense Required to Complete the Survey Goal	188
10	RESPONSES TO THE CHARTER QUESTIONS	191
10.1	SDT Specific Findings	192
	APPENDIX 1. 2016 STUDY CHARTER	193
	APPENDIX 2. KEY TO PLOTS (SECTIONS 6, 8, AND 9)	197
	REFERENCES	199
	ACRONYMS AND ABBREVIATIONS	215

LIST OF FIGURES

Figure 1-1.	Study process to develop cost/benefit estimate and findings.	4
Figure 2-1.	Main NEO source regions.	11
Figure 2-2.	Comparison between Granvik et al. (2016) NEO model and Catalina Sky Survey work (7,952 detections of 3,632 NEOs).	12
Figure 2-3.	The lines are model redetection ratio (solid) and completion (dashed) versus asteroid absolute magnitude. The plot circles are the actual redetections of surveys for the past two years. The observed redetections are fit to a 20-year model survey.	16
Figure 2-4.	The differential population estimate of NEOs.	18
Figure 2-5.	Albedo versus diameter for NEOs observed by the Wide-field Infrared Explorer (WISE). Multiple observations are combined.	18
Figure 2-6.	Albedo distribution for NEOs observed by WISE at a constant diameter.	19
Figure 2-7.	Differential size-frequency distribution.	21
Figure 2-8.	Cumulative near-Earth object size-frequency distribution in units of diameter D and absolute magnitude H , with the two over-plotted.	22
Figure 2-9.	The albedo distribution for $D > 100$ m objects generated for our synthetic population.	23
Figure 2-10.	The differential distributions of absolute magnitude (H) as described in Table 2-1 (black line) and as derived from the diameter and albedo based distribution (SDT population, red line) discussed in the text and tabulated in Table 2-2.	24
Figure 2-A-1.	Distributions of orbital elements and Earth encounter velocity comparing the actual observed distribution of discovered large potentially hazardous asteroids (PHAs) with the population model used in the 2003 report and with the newer model distributions of large and small PHAs provided by Bottke.	30
Figure 2-A-2.	The distribution of Earth impact velocities.	32
Figure 2-B-1.	The effect of round-off in population bins.	34
Figure 2-B-2.	The cumulative population of NEOs, with the new bin shown in (a). The cumulative population estimates of Earth-crossing asteroids (ECAs) (b) and potentially hazardous asteroids (PHAs) (c) are shown for the old and new binning.	36
Figure 2-B-3.	The differential population estimate of NEOs.	37
Figure 3-1.	Height-of-burst maps from Glasstone and Dolan (Glasstone 1977) and current Cart3D simulations.	43
Figure 3-2.	The casualty rate for an inundated population is shown as a function of the local flood depth, derived from Koshimura et al. (2013).	46
Figure 3-3.	Curve fits of global effects ranges by impact energy (left) and resulting triangular distribution for a 600-gigaton impact (right).	48

LIST OF FIGURES (continued)

Figure 3-4.	Trajectory input distributions.	49
Figure 3-5.	Albedo distribution (Mainzer et al. 2011e).	50
Figure 3-6.	Asteroid density distributions for the structural types within each compositional type.	51
Figure 3-7.	Density distributions combining all compositional types and structural types for asteroid sizes of 20 m and 200 m or greater.	52
Figure 3-8.	Cumulative expected value curves for average affected populations within different blast overpressure damage zones, based on impact frequencies from the total estimated PHO population.	53
Figure 3-9.	Range of local damage potential as a function of impactor size.	54
Figure 3-10.	Local damage risk contour plot with black contour lines at each order of magnitude and the bold line showing the 10^{-6} probability per year contour.	54
Figure 3-11.	Cumulative expected tsunami damage averages for inundated population and casualties.	55
Figure 3-12.	Range of tsunami damage potential as a function of impactor size.	56
Figure 3-13.	Tsunami damage risk contour plot with black contour lines at each order of magnitude and the bold line showing the 10^{-6} probability per year contour.	56
Figure 3-14.	Range of global damage potential as a function of impactor size.	57
Figure 3-15.	Global damage risk contour plot with black contour lines at each order of magnitude and the bold line showing the 10^{-6} probability per year contour.	57
Figure 3-16.	Total damage risk contour plot with black contour lines at each order of magnitude and the bold line showing the 10^{-6} probability per year contour.	58
Figure 3-17.	Complementary cumulative distribution of the total combined risk from all objects up to 10 km in size.	59
Figure 3-18.	Cumulative expected casualties as a function of impactor size for local (blast and thermal), regional (tsunami), and global risks.	59
Figure 3-19.	Expected casualty estimates presented for the size bins from Table 3-5.	62
Figure 3-20.	Expected casualty estimates for the remaining undiscovered PHO population for the two survey subsets: the projected survey completeness assuming current survey progress until 2023 (left) and the 90% completeness (right).	63
Figure 3-21.	Total expected casualties for the 2023 survey completion (top) and 90% survey completion (bottom) projections.	63
Figure 3-22.	Comparison of risk contour plots for the 2023 and 90% survey completion estimates.	64
Figure 3-23.	Casualty exceedance probability comparisons for the total PHO population and the assumed reduction in risk uncertainty for the 2023 survey projections and at the point at which surveys achieve 90% reduction.	65

LIST OF FIGURES (continued)

Figure 4-1.	Quantum efficiency (QE) of the Semiconductor Technology Associates STA1600 series CCDs as a function of wavelength (from Semiconductor Technology Associates STA1600 data sheet found at http://www.sta-inc.net/sta1600/).	77
Figure 4-2.	Quantum efficiency (QE) of several E2V CCDs as a function of wavelength (from the E2V data sheet available at http://www.e2v.com/resources/account/download-datasheet/1897).	77
Figure 4-3.	The LSST CCD quantum efficiency curves as a function of wavelength as measured by two vendors..	78
Figure 4-4.	In (a) is shown the frequency of the full width at half-maximum of the point-spread function (PSF FWHM) corrected to zenith as a function of local time throughout the night as measured by the Subaru Telescope on Maunakea, Hawaii. The seeing is worse in the first few hours of the night but is relatively stable after about 9:00 p.m. local time. In (b) is the cumulative distribution of the FWHM during almost eight years of observations at the Subaru Telescope on Maunakea.	81
Figure 4-5.	The monthly average clear-sky probability at the Subaru Telescope on Maunakea is shown for the period from May 2000 through May 2011.	82
Figure 4-6.	The scaling of search rate with sensitivity for the IR observatories at L1 for the lowest expected zodiacal background; the filled circle indicates the selected exposure time (and consequent sensitivity).	88
Figure 4-7.	The relationship between sensitivity and sky coverage is a function of exposure time for the three different visible space-based systems listed in Table 4-9.	89
Figure 4-8.	A comparison of the apparent visual magnitudes of PHOs with sizes between 126 and 159 meters at the times of their detections over the course of one year by 50 cm visible and IR telescopes operating at L1 reveals that for the same size aperture, IR systems are more sensitive to NEOs than visible telescopes.	90
Figure 5-1.	Approximate search region for a ground-based optical telescope is highlighted in green for this particular location of Earth.	99
Figure 5-2.	Approximate search region for an infrared survey operating at the Sun-Earth L1 (Lagrange) point is highlighted in red for this particular location of Earth.	101
Figure 5-3.	Approximate search region for telescope operating with an orbit similar to that of Venus is highlighted in green for this particular location of the sensor.	101
Figure 5-4.	Rotating frame depiction of Earth-relative trajectories (the so-called rotating frame) of four example PHA orbits in resonance with Earth.	106
Figure 5-5.	Objects not found by the GEO 2 m survey and not found by the Venus 1 m visible band survey, revealing the resonant objects residing in horizontal strips.	107
Figure 6-1.	Distribution of statistical input population for the simulations: (a) diameter; (b) absolute magnitude H ; (c) albedo; (d) 126 m–159 m bin, distribution in H .	110

LIST OF FIGURES (continued)

Figure 6-2.	Probability of detection curves for forming a tracklet, requiring M out of N frames, as a function of the difference between the apparent magnitude of an object and the limiting magnitude of the sensor field.	115
Figure 6-3.	Distribution of the apparent velocity at time of detection for LINEAR: simulated and actual. A comparison of the 2003 SDT simulation and the modified 2017 SDT simulation.	119
Figure 6-4.	Distribution of the apparent magnitude of output detections for LINEAR: simulated and actual. A comparison of the 2003 SDT simulation and the modified 2017 simulation.	120
Figure 6-5.	Distribution of the absolute magnitude of output detections for LINEAR: simulated and actual. A comparison of the 2003 SDT simulation and the modified 2017 simulation.	121
Figure 6-6.	Establishing a baseline from the uniform statistical model of PHOs. The FROSST simulation estimate for known, cataloged objects is 92%, which is compared to the Harris cumulative completeness model, which is 93%.	124
Figure 6-7.	2023 baseline for remainder of the study. Cumulative completeness in diameter bins. Determined independently with FROSST and with Mainzer et al. (2015) and Grav et al. (2016) (M15G16).	125
Figure 6-8.	Distribution of the statistical input population for the simulations, divided into “known” and “unknown” as of January 2023: (a) diameter; (b) absolute magnitude H ; (c) albedo broken into percent by bin, ranging from 40% known at low albedo to 65% known at high albedo; (d) 126 m–159 m bin, distribution in H .	126
Figure 6-9.	Growth of the catalog (a) over 10 years and (b) over 20 years.	128
Figure 6-10.	Ten-year completeness performance (a), completeness over time at 126 m (b), and warning efficiency (c) for the ground-based systems.	131
Figure 6-11.	Ten-year completeness performance (a), completeness over time at 126 m (b), and warning efficiency (c) for 50 cm space-based systems, across orbit locations and technologies.	134
Figure 6-12.	Ten-year completeness performance (a), completeness over time at 126 m (b), and warning efficiency (c) for 1 m space-based systems, across orbit locations and technologies.	135
Figure 6-13.	Ten-year completeness performance (a), completeness over time at 126 m (b), and warning efficiency (c) for systems located at GEO.	137
Figure 6-14.	Ten-year completeness performance (a), completeness over time at 126 m (b), and warning efficiency (c) for systems located at L1.	138
Figure 6-15.	Ten-year completeness performance (a), completeness over time at 126 m (b), and warning efficiency (c) for 4-meter ground-based visible system networked with space-based visible systems.	141

LIST OF FIGURES (continued)

Figure 6-16.	Ten-year completeness performance (a), completeness over time at 126 m (b), and warning efficiency (c) for 4-meter ground-based visible system networked with space-based IR systems.	142
Figure 6-17.	Ten-year completeness performance (a), completeness over time at 126 m (b), and warning efficiency (c) for networked with space-based IR and space-based visible systems.	144
Figure 6-18.	Ten-year completeness performance (a), completeness over time at 126 m (b), and warning efficiency (c) for all simulated systems. The systems in the legend are listed in order of performance at ~140 meter for cataloging and at 50 meter for warning.	146
Figure 8-1.	Accrued annual benefits of all modeled NEO search systems, expressed as a percentage of the total sub-global PHO impact risk uncertainty eliminated.	173
Figure 8-2.	Accrued annual benefits of all modeled NEO search systems, expressed as sub-global PHO impact risk uncertainty elimination benefit value in millions of FY2017 U.S. dollars per year.	174
Figure 8-3.	Accrued annual benefits of modeled space-based NEO search systems, expressed as a percentage of the total sub-global PHO impact risk uncertainty eliminated.	176
Figure 8-4.	Accrued annual benefits of modeled ground-based NEO search systems, expressed as a percentage of the total sub-global PHO impact risk uncertainty eliminated.	177
Figure 8-5.	Accrued benefits in terms of the percentage of sub-global PHO impact hazard uncertainty elimination value earned relative to the value available to be earned at the start of operations in January 2023.	178
Figure 8-6.	Warning efficiency of modeled systems as a function of PHO diameter.	179
Figure 8-7.	Warning benefit value earned by the modeled systems over time.	180
Figure 8-8.	Total benefit value earned by each modeled system, in millions of dollars, over 10 years of operations.	182
Figure 9-1.	Cumulative expected casualties per year as a function of undiscovered object size.	183
Figure 9-2.	Fraction of impact hazard uncertainty eliminated as a function of size of PHO for which population is discovered to 90% completeness.	184
Figure 9-3.	Simulation of 1000 NEOs, each 1 km in diameter (red dashed line), with albedos given by the distribution of Mainzer et al. (2011e) and Wright et al. (2016).	185
Figure 9-4.	For various ground-based, space-based, and combined search systems, the system cost is plotted versus the percentage of the sub-global risk uncertainty remaining after a 10-year survey.	188
Figure 9-5.	The cost of various space-based and ground-based search systems is plotted against the number of search years required to reduce by 90% the sub-global risk uncertainty from impacts by sub-kilometer sized objects.	189

This page is intentionally blank.

LIST OF TABLES

Table 1-1.	The Science Definition Team membership.	4
Table 2-1.	NEO population, impact frequency, and projected completion.	26
Table 2-2.	Total number of NEOs and PHAs as derived by NEOWISE data.	27
Table 3-1.	Minimum, nominal, and maximum values for triangular distributions of global casualty rates by impact energy, based on Stokes et al. (2003)	47
Table 3-2.	Asteroid size bins, increments between bins, and number of impact scenarios modeled in each bin.	49
Table 3-3.	Relative abundance, base density distribution parameters, and asteroid density limits for hydrous stone, anhydrous stone, and iron compositional types.	50
Table 3-4.	Porosity distribution parameters for coherent, fractured, and rubble pile structural types.	51
Table 3-5.	Average expected casualties from local, tsunami, and global damage by asteroid size.	60
Table 3-A-1.	Average casualties from each damage source for the asteroid sizes modeled in the impact risk assessment simulations.	66
Table 4-1.	Top five NEO surveys, 2003–2014.	70
Table 4-2.	Top five expected new ground-based NEO surveys in 2016–2026.	72
Table 4-3	Typical characteristics of three large-format CCDs currently used or considered for asteroid surveys.	76
Table 4-4	Performance characteristics of existing ground-based telescope system prototypes for Table 4-5	79
Table 4-5.	Performance characteristics of modeled ground-based telescope systems.	79
Table 4-6.	Space-based NEO survey systems modeled in this study.	87
Table 4-7.	Performance characteristics for a 0.5-meter space-based IR telescope in either L1 or Venus-trailing orbit.	91
Table 4-8.	Performance characteristics for a 1.0-meter space-based IR telescope in either L1 or Venus-trailing orbit.	92
Table 4-9.	Required and current best estimate performance for LWIR HgCdTe arrays.	93
Table 4-10.	Performance characteristics for three space-based visible telescopes.	98
Table 6-1.	Signal-to-noise parameters, definitions, and source of values for ground-based and space-based visible systems.	112
Table 6-2.	Simulated space-based systems.	132
Table 7-1.	Estimated telescope construction cost (TCC) for ground-based observatories, by aperture diameter (meters).	150
Table 7-2.	Instrument acquisition costs for ground-based observatories.	151

LIST OF TABLES (continued)

Table 7-3.	Operations and support (O&S) costs for ground-based observatories.	152
Table 7-4.	Software development sizes (reported in source lines of code [SLOCs]) by software module for ground-based observatory options, based on 2003 data.	152
Table 7-5.	Estimated software development costs and schedule durations for ground-based observatory options.	153
Table 7-6.	Estimated life-cycle ground-based observatory options cost (in FY2017 \$M), with unallocated cost reserves.	153
Table 7-7.	Estimated costs of space-based observatory options (visible), with 30% unallocated cost reserves (FY2017 dollars).	157
Table 7-8.	Estimated costs of space-based observatory options (infrared), with 30% unallocated cost reserves (FY2017 dollars).	158
Table 7-9.	System-specific cost model inputs.	159
Table 7-10.	Space-based instrument cost summary.	160
Table 7-11.	Estimated Phase E costs (FY2017 \$M), for space-based observatory options (visible).	162
Table 7-12.	Estimated Phase E costs (FY2017 \$M), for space-based observatory options (IR).	162
Table 7-13.	Estimated life-cycle space-based observatory option costs (FY2017 \$M), with unallocated cost reserves (visible).	162
Table 7-14.	Estimated life-cycle space-based observatory option costs (FY2017 \$M), with unallocated cost reserves (IR).	163
Table 8-1.	AIS values mapped to VSI values as fractions of VSL.	169
Table 8-2.	Overpressure intervals and their effects.	169
Table 8-3.	Accumulated total benefit value, including global effects, for each modeled system.	171
Table 8-4.	Accumulated benefits for all modeled NEO survey systems as percentage of sub-global hazard uncertainty eliminated and millions of dollars per year.	172
Table 8-5.	Benefit/cost ratios for the modeled NEO survey systems.	181

1 INTRODUCTION

1.1 Background

In a 1992 report to NASA (Morrison 1992), a coordinated Spaceguard Survey was recommended to discover, verify, and provide follow-up observations for Earth-crossing asteroids. This survey was expected to discover within 25 years 90% of these objects larger than one kilometer. Three years later, another NASA report (Shoemaker 1995) recommended search surveys that would discover 60% to 70% of short-period, near-Earth objects larger than one kilometer within ten years and obtain 90% completeness within five more years. In 1998, NASA formally embraced the goal of finding and cataloging, by 2008, 90% of all near-Earth objects (NEOs) with diameters of 1 kilometer or larger that could represent an impact risk to Earth (see Stokes et al. 2003, Appendix 1: “1998 Statement before Subcommittee on Space and Aeronautics”). The 1-kilometer-diameter metric was chosen after considerable study indicated that an impact of an object smaller than 1 kilometer could cause significant local or regional damage but would be unlikely to cause a worldwide catastrophe (Morrison 1992). The impact of an object much larger than 1 kilometer in diameter could well result in worldwide damage up to, and potentially including, extinction of the human race. The NASA commitment has resulted in the funding of a number of NEO search efforts that achieved the objective of discovering at least 90% of the 1-kilometer or larger NEOs by 2011 (Mainzer et al. 2011e; Harris and D’Abramo 2015; Granvik et al. 2016).

In 2002, as it became obvious that the goal of finding 90% of the very large NEOs was well along the way to being accomplished, NASA chartered a Science Definition Team (SDT) to study the possibility of discovering objects smaller than 1 kilometer in diameter that would still pose a substantial threat to the Earth’s population in the event of an impact. That SDT report titled “Study to Determine the Feasibility of Extending the Search for Near-Earth Objects to Smaller Limiting Diameters” (hereafter NEO SDT report) was chaired by Dr. Grant H. Stokes from MIT Lincoln Laboratory and recommended the objective of discovering 90% of the potentially hazardous objects (PHOs) larger than 140 meters in diameter (Stokes et al. 2003). This study differentiated between NEOs from a broad class of minor planets, most with zero probability of impacting the Earth, and the smaller subset (~20% of the NEO population) of PHOs that can closely approach the Earth’s orbit and thus represent impact dangers. The term PHO was chosen to reflect the fact that a small fraction of the NEOs and PHOs are active and inactive short-period comets versus objects classified as asteroids. Throughout this report, as in the 2003 NEO SDT report, we will most often refer to NEOs and PHOs, generally meaning the set of near-Earth asteroids and short-period comets and excluding long-period comets. However, the terms near-Earth asteroids (NEAs) and potentially hazardous asteroids (PHAs) will also be used when appropriate. Because the number of asteroids completely dominates the cometary members (more than 16,000 asteroids versus only 106 comets are known to date) of the NEO and PHO groups, the reader can normally assume that the populations of NEOs and NEAs are nearly identical, as are the populations of PHOs and PHAs.

The 2003 NEO SDT report was quite influential as the nation formulated an approach to the NEO impact issue. In 2005, the objectives recommended by the NEO SDT report were captured in a Congressional direction to NASA (George Brown Act). In addition, the NASA Authorization Act of 2005 elevated NEO detection, tracking, and research to one of seven explicitly stated purposes of NASA.

1.2 Science Definition Team Formation and Charter

Given the progress that has been made in search technology and impact-damage estimation, as well as the improved knowledge of the minor planet population provided by an additional ~15 years of search operations since the 2003 NEO SDT report (see Section 1.5), it is natural to ask what action, if any, should be taken to update the objectives or approach to the search for potential impactors. In addition, the February 2013 impact of a ~20-meter-diameter object near Chelyabinsk, Russia, has motivated renewed discussion of the potential to catalog or warn against objects smaller than the 140-meter cataloging objective set by the 2003 SDT. In June 2015, NASA initiated the formation of a Science Definition Team with a charter to develop a current understanding and update of the threat posed by near-Earth objects smaller than one kilometer and to assess methods for providing warnings of potential impacts. The team was instructed to provide findings to NASA and to outline an executable approach to addressing any specific findings. Specifically, the team was instructed to address the following questions:

1. What are the smallest objects for which the search should be optimized?
2. Should comets be included in any way in the survey?
3. What is technically possible?
4. How would the expanded search be done?
5. What would it cost?
6. How long would the search take?
7. Is there a transition size above which one catalogs all the objects, and below which the design is simply to provide warning?

The complete formal charter for the SDT is contained in Appendix 1 of this report.

1.3 Team Membership

The SDT was chaired by Dr. Grant H. Stokes from MIT Lincoln Laboratory. The team members, carefully chosen to represent the breadth and depth of expertise required to address the questions posed in the charter, are listed in Table 1-1, along with their institutions and technical specialties. Many of the team members were also members of the original 2003 SDT that was composed to answer these same questions. This overlap in team membership enabled an efficient reconsideration of the seven questions, following the methodology established by the 2003 SDT, to update the answers, given the changes in population knowledge, impact damage analysis, and search capabilities.

Table 1-1. The Science Definition Team membership.

Name	Institution	Technical Specialty
Dr. Grant H. Stokes	MIT Lincoln Laboratory	Asteroid search, PI for LINEAR, DoD SSA
Brent W. Barbee	NASA Goddard Space Flight Center	Asteroid mission design and planetary defense
Dr. William F. Bottke Jr.	Southwest Research Institute	Asteroid and comet population models
Dr. Marc W. Buie	Southwest Research Institute	Infrared-space survey simulations and astrometry
Dr. Steven R. Chesley	NASA Jet Propulsion Laboratory, CNEOS	Hazard assessments and search strategies
Dr. Paul W. Chodas	NASA Jet Propulsion Laboratory, CNEOS	Asteroid and comet orbit determination and impactor warning times
Jenifer B. Evans	MIT Lincoln Laboratory	Detector systems and survey simulations
Dr. Robert E. Gold	Johns Hopkins University Applied Physics Laboratory	Spacecraft and detector systems
Dr. Tommy Grav	Planetary Science Institute	Survey simulations and NEO populations
Dr. Alan W. Harris	NASA Jet Propulsion Laboratory (retired)	Hazard assessments, NEA population, and search strategies
Dr. Robert Jedicke	University of Hawaii	NEO population and search strategies
Dr. Amy K. Mainzer	NASA Jet Propulsion Laboratory	NEO populations, survey simulations, and infrared surveys
Dr. Donovan L. Mathias	NASA Ames Research Center	Asteroid impact effects and risk assessment
Dr. Timothy B. Spahr	NEO Sciences LLC	Small body astrometry and orbit determination
Dr. Donald K. Yeomans	NASA Jet Propulsion Laboratory (retired)	Comet populations
Ex Officio Members		
Lindley N. Johnson	NASA Headquarters	Planetary Defense Officer
Dr. Kelly E. Fast	NASA Headquarters	Planetary astronomy
Dr. Michael S. Kelley	NASA Headquarters	Asteroid geology and meteorite connections
Team Support		
Jane E. Daneu	MIT Lincoln Laboratory	Administrative assistant
Cheryl Reed	Johns Hopkins University Applied Physics Laboratory	Program management
Dorothy S. Ryan	MIT Lincoln Laboratory	Editor
Dr. Erik Syrstad	Space Dynamics Laboratory	Instrument cost estimates
Lorien F. Wheeler	NASA Ames Research Center (CSRA)	Asteroid energy deposition and risk assessment
Lawrence Wolfarth	Johns Hopkins University Applied Physics Laboratory	Cost analyst

1.4 Study Approach

Providing authoritative answers to the questions posed to the team requires an understanding of the relationships between the costs of implementing a search effort for smaller NEOs and the benefits accrued. Thus, the study process was constructed along the lines of a cost/benefit analysis, as shown in Figure 1-1, which parallels the methodology of the 2003 SDT.

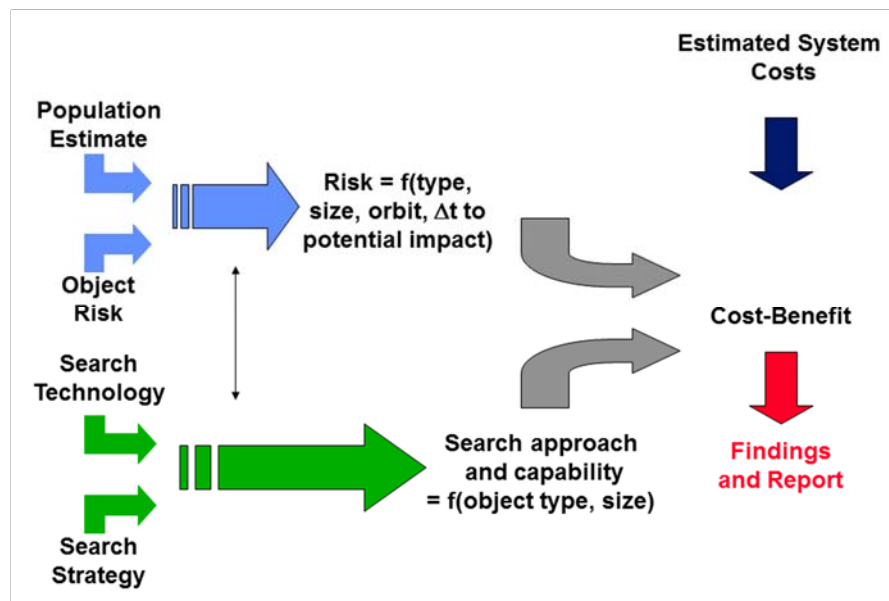


Figure 1-1. Study process to develop cost/benefit estimate and findings.

The six areas that need to be explored to produce the cost/benefit analysis are as follows:

1. Population estimate: The population of asteroids as a function of size, orbital distribution, and albedo must be accurately estimated to approximate the impact rate of asteroids with the Earth as a function of size and orbital parameters and to provide the basis for an estimation of the search capabilities of potential systems.
2. Object risk: The impact damage associated with the impact of an asteroid must be quantified as a function of impactor size. The damage, including effects for both land and water impacts, can be combined with an impact rate to yield an expected damage per year as a function of asteroid size. Assuming that advance warning allows some fraction of the damage and loss of life to be avoided, this assessment represents an estimate or upper bound for the benefit that can be accrued in return for the cost of conducting a search.
3. Search technology: The capabilities of potential search technologies, or combinations of technologies, to execute the search must be assessed as a function of the size, albedo, and orbital parameters of the asteroid population.
4. Search strategy: The method of operating a particular search system must be defined to determine search effectiveness. The capabilities of a search system to find any particular

population of asteroids will depend not only on the inherent capabilities of the system but also on how it is employed with respect to scan pattern, integration time, etc.

5. System costs: The costs of developing and operating the search system(s) must be quantified. The funds required to build and operate the search system form the cost element of the cost/benefit analysis.
6. Search Benefits: The benefits, in terms of casualty avoidance and property loss, must be quantified.

The six inputs discussed above provide the basic information required to

1. Estimate the danger to the Earth from impacts of asteroids as a function of size; and
2. Estimate the performance and cost/benefit of a range of search systems intended to provide notification of impending risk.

An assessment of the productivity for a search system is complex and requires a realistic accounting for real-world effects that degrade its theoretical performance. These effects include the weather, moonlight, air mass, and zodiacal light background. Some of these effects can be determined by the geometry of the observations (e.g., the effect of the Moon and air mass, which are coupled), while others can be estimated only by statistical methods (e.g., the weather). Many historical analyses of asteroid search systems have either ignored these effects, especially when proposing a specific system for funding, or treated them with some form of estimated correction factor. However, the effects of the real-world degradations to a search are intimately related to the details of the search operation and will have a large influence on the search productivity. For the purposes of this study, the performance of a search sensor, or a network of sensors, was estimated by using a detailed simulation process that “displays” the population of asteroids as a function of time and operates the search sensors in the chosen search modes to see what is found. This approach allows the geometry-dependent effects to be modeled specifically for each search area, resulting in a high-fidelity performance estimate. In addition, the simulation includes realistic noise from the background and from a comprehensive list of sources. Both ground-based and space-based sensors are modeled, along with backgrounds and noise sources appropriate to each operating environment. Networks consisting of combinations of various sensor types and in various locations may be modeled together to assess their combined performance.

The inputs to the simulation are

1. The asteroid population, including orbital parameters, diameter, absolute magnitude (H), and albedo for each asteroid;
2. The sensor model(s), including parameters of the sensor(s) such as sensitivity as a function of integration time, step and settle time, site location or ephemeris, and site characteristics;
3. The search pattern(s) for each sensor; and
4. The time ranges over which to simulate.

The output of the simulation is a list of detections as a function of time. From these detections, the performance of the search system and strategy may be compared on a realistic basis with the performance of other configurations.

The benefits provided by a given search system need to be measured relative to the system costs. The costs of a given system are governed by the construction and operational expenses, which can be estimated in a relatively straightforward manner, while the benefit side of the equation is much more challenging for several reasons. Most importantly, the benefits provided by a system cannot be described in strictly financial terms because of both the potential for casualties and the various political and emotional considerations that are relevant to the problem of asteroid impact. Furthermore, the benefit depends directly upon estimates of the hazard posed by NEOs, and these estimates are plagued by large uncertainties.

The direct benefit of a search program comes from two sources, cataloging and warning. Cataloging refers to the idea that the statistical impact risk is only posed by the still undiscovered component of the NEO population. Therefore, by discovering and cataloging NEOs and by verifying that none will impact within the next century, we reduce the potential risk to life and property on Earth. If an object is actually discovered on a threatening trajectory, there will presumably be many years, even decades, in which to execute a plan to deflect or disrupt the impactor. Hence, the cataloging approach enables the complete mitigation of future impacts, saving both population and infrastructure.

The term *warning* describes a situation in which an impactor is first detected and recognized some days to months before the event. This warning period would afford civil authorities an opportunity to take actions that would mitigate the impact effects, but there would be insufficient time to avert the impact. In such a scenario, the warning benefit is largely composed of casualties avoided through the evacuation of affected areas. Major infrastructure would not typically be saved, but, time permitting, some portion of the physical infrastructure might be removed to a safe distance.

Additionally, the SDT recognizes a number of benefits of searching for minor planets, which, since they are not directly related to potential impact, are not quantified in the report. Some examples of these benefits are

1. Understanding the NEO and main-belt populations is of fundamental importance to Solar System science;
2. Developing a more complete NEO catalog will allow the identification of suitable targets for robotic and human exploration;
3. Resource-bearing NEOs may be identified for future utilization.

1.5 Updates Since 2003 NEO SDT Report

The 2017 SDT followed the methodology of the 2003 SDT and made a number of improvements that have led to a more robust understanding of the asteroid impact threat to Earth and of the methods to characterize that threat. Listed below are the areas of major change and the report sections in which the material is addressed:

1. There is a better understanding of the NEO population, based on 15 years of additional discoveries and the advance of source and evolution modeling (Section 2).
2. The realism of the impact damage assessment has been improved, especially for small objects and tsunami-related damage (Section 3).

3. Search technology has improved, especially in the maturity of space-based infrared (IR) capabilities, and the assessment of search system performance under realistic conditions has also improved (Sections 4 and 6).
4. Realistically estimated connections between NEO populations characterized in absolute magnitude (H) and in diameter (D), as well as search system performance in H and in D , have been developed. These developments allow comparisons between the performances of IR and visible surveys (Sections 2, 4, and 6).
5. The survey simulation process has been updated to include space-based IR systems (Section 6).
6. The conservatism of the formal NASA costing process has increased (Section 7).
7. The benefits estimation process has been updated to reflect the current statistical value of a human life and the statistical value of injury, and property damage short of destruction has been included. More realistic warning valuation has been used to reflect Federal Emergency Management Agency (FEMA) evacuation planning and execution criteria and timelines (Section 8).

This page is intentionally blank.

2 POPULATION ESTIMATES

This section discusses methods by which the population of synthetic near-Earth objects (NEOs) used in the study simulations was created. NEOs are defined as asteroids and comets that have perihelion distances $q \leq 1.3$ AU and aphelion distances $Q \geq 0.983$ AU. The main subgroups within the NEO population are the Apollos ($a \geq 1.0$ AU; $q \leq 1.0167$ AU) and Atens ($a < 1.0$ AU; $Q \geq 0.983$ AU), which are on Earth-crossing orbits, and the Amors (1.0167 AU $< q \leq 1.3$ AU), which are on nearly-Earth-crossing orbits exterior to Earth. Amors may evolve into Earth crossers over potentially short timescales. Objects located just inside Earth's orbit, called Atiras (0.718 AU $< Q < 0.983$ AU), represent another NEO group, though their population is small enough that we do not consider them here. NEOs that are potentially hazardous to life or can produce substantial property damage range in size from roughly 10 meters in diameter (D) all the way to several tens of kilometers (i.e., the two largest NEOs, both Amors, are (1036) Ganymed, with $D \sim 32$ km, and (433) Eros, with dimensions of $34.4 \times 11.2 \times 11.2$ km).

2.1 Orbital and Size Distributions

The orbital distribution of our synthetic NEOs is derived from the model results of Granvik et al. (2016). Granvik et al. can be considered an updated and more detailed version of the NEO population described by Bottke et al. (2002) that was used in the 2003 Science Definition Team (SDT) report titled "Study to Determine the Feasibility of Extending the Search for Near-Earth Objects to Smaller Limiting Diameters" (hereafter NEO SDT report) (Stokes et al. 2003). Here we briefly describe the methods used by Granvik et al. (2016), some of their model improvements over Bottke et al. (2002), and the way they arrived at their results.

Over the last two decades, scientists have recognized that the majority of the NEO population are made up of fragments produced by cratering or disruption events in the main asteroid belt that have reached planet-crossing orbits by a combination of Yarkovsky thermal drift forces and resonances (Bottke et al. 2015; Vokrouhlický et al. 2015). The Yarkovsky effect describes a small but significant force that affects the orbital motion of asteroids smaller than 30 to 40 kilometers in diameter. It is caused by sunlight; when these small bodies heat up in the Sun, they eventually reradiate the energy away as heat, in turn creating a tiny thrust. This recoil acceleration is much weaker than solar and planetary gravitational forces, but it can produce substantial orbital changes over timescales ranging from millions to billions of years. Within the main asteroid belt, these orbital changes mean that small asteroids slowly drift inward toward or outward away from the Sun, provided they have retrograde or prograde spin vectors, respectively. This drift allows some asteroids to migrate into planetary resonances, i.e., special regions where planetary gravitational perturbations can increase an asteroid's orbital eccentricity enough to reach planet-crossing orbits (see Stokes et al. 2003 for additional discussion). In other cases, asteroids may simply drift directly onto Mars-crossing orbits without reaching any resonance, with the combination of Mars perturbations and resonance activity eventually delivering them onto NEO orbits.

Models show this slow steady process kept the NEO population in a quasi-steady state over billions of years, with variations of a factor of perhaps 2–3 or so (Bottke et al. 2015). Intriguingly, studies of lunar and terrestrial crater ages suggest the impact flux over the last ~ 300 million years (Myr) from

kilometer-sized asteroids may be a factor of 2–3 higher than over the previous ~700 Myr (e.g., Mazrouei et al. 2017). If this estimate is true, the reason for this putative increase over relatively recent times would be the disruption of particular asteroids in the main belt well positioned to produce NEOs (e.g., Bottke et al. 2007; Nesvorný et al. 2009).

Taking advantage of this new knowledge about how main belt asteroids reach planet-crossing orbits, Granvik et al. (2016) created a new NEO model population by dynamically tracking populations of objects that are likely to become NEOs: (i) synthetic asteroids that escape the main belt and (ii) synthetic Jupiter-family comets that escape transneptunian populations like the Kuiper belt and scattered disk. We describe each in turn.

In considering NEOs coming from the main asteroid belt, Granvik et al. (2016) defined a reference main-belt population that would provide starting conditions for their model NEOs. To this end, they identified 78,355 objects with absolute magnitude H brighter than the current completeness limit of telescopic surveys in the inner, central, and outer main belts (i.e., for those bodies interior to the 3:1 mean motion resonance with Jupiter located at semimajor axis $a = 2.5$ AU, the H limit was 15.9, while for those exterior to this zone, the H limit was 14.4). The high-inclination Hungaria and Phocaea populations were also included in this set of objects, though their numbers were small enough that some bodies were “cloned” to increase statistics. This addition resulted in a starting asteroid population of 92,449. It was assumed that the orbits of these bodies were reasonably representative of smaller main-belt objects below the completeness limit in each main belt zone.

While more extensive modeling details are provided in Granvik et al. (2016), we provide some reference model values here. The test main-belt asteroids in our model were assigned Yarkovsky drift rates commensurate with their chosen size and their physical/spin vector properties. For kilometer-size asteroids, parameter choices included characteristic bulk densities of 2 g/cm^3 , surface thermal inertia values of $200 \text{ J/m}^2\text{/s}^{1/2}\text{/K}$, and rotation periods of a few to a few tens of hours. Asteroid obliquities were chosen to be 0 or 180 degrees, which in turn yields maximized Yarkovsky drift rates outward or inward, respectively. Taken together, these values yielded Yarkovsky drift rates of $da/dt = \pm 2 \times 10^{-4} \text{ AU/Myr}$ for a km-sized asteroid located at $a = 2.5$ AU. Faster rates were found for smaller asteroids input into this model (see Granvik et al. 2016).

These bodies were then followed within the numerical integrator SWIFT (Levison and Duncan 1994) until they reached a perihelion value of 1.3 AU or 100 Myr had elapsed, whichever came first. The runs included gravitational perturbations from the Sun and the planets Mercury to Neptune. Overall, 70,708 test asteroids achieved the $q = 1.3$ AU threshold; the rest were not used. At this point, the timestep was lowered and the remaining bodies were followed until they hit the Sun, a planet, or were ejected out of the inner solar system by a close encounter with Jupiter.

Jupiter-family comets (JFCs) also produce some NEOs. These bodies are defined as “ecliptic” comets given their fairly low inclinations and Tisserand parameters between 2 and 3 (see Stokes et al. 2003 for definitions). Drawing from recent numerical simulations of this population, Granvik et al. (2016) included a numerical representation of the JFC population as well. As discussed below, as well as in Bottke et al. (2002) and Stokes et al. (2003), the other comet populations were not included because they are not expected to provide substantial contributions to the NEO impactor population.

After an analysis of all of the integration results, Granvik et al. identified six primary main belt source regions that can supply NEOs: two high-inclination asteroid groups (i.e., the Hungarias and Phocaeas) and four primary escape routes (i.e., the ν_6 secular resonance and the 3:1, 5:2 and 2:1 mean-motion resonances with Jupiter) (Figure 2-1). The inclusion of JFCs, which come from the outer solar system, yield a seventh source.

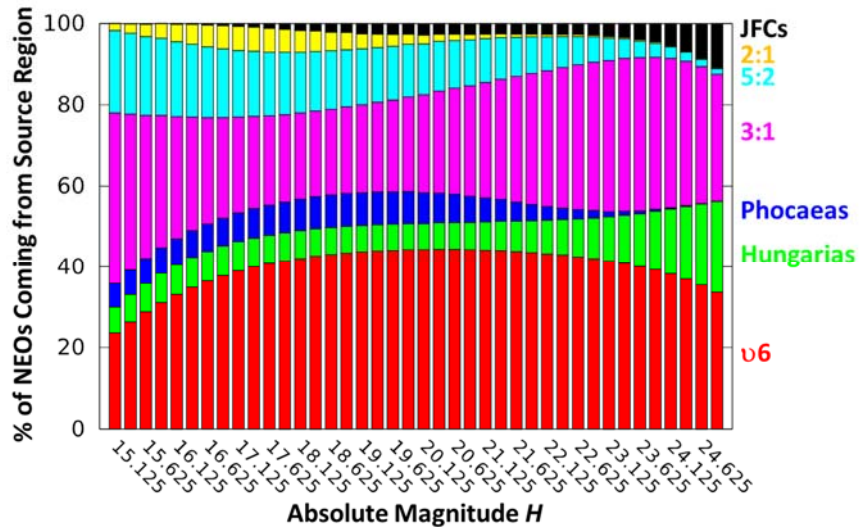


Figure 2-1. Main NEO source regions: two asteroid groups (Hungaria and Phocaea), 4 main belt escape routes (ν_6 secular resonance; 3:1, 5:2, and 2:1 mean-motion resonances with Jupiter), and the Jupiter family comets (JFCs).

The orbital pathways followed by asteroids from a given source traversing NEO space was characterized by computing how much time the bodies spent within a series of semimajor axis, eccentricity, and inclination (a, e, i) bins. The resultant residence time probability distribution, defined by the variable $R_s(a, e, i)$, where the s subscript is the label for the source, describes the nature of the steady state orbital distributions of NEOs coming from a source. Each R_s function was then multiplied by a source specific absolute magnitude H distribution, $N_s(H)$, whose properties were defined in Granvik et al. (2016). Finally, these functions were added together with weighting functions such that the sum was 1. The result was a NEO model of the form $N(a, e, i, H)$. If all seven of the R_s and $N_s(H)$ functions were 100% accurate and were added together in the right proportion to one another, $N(a, e, i, H)$ would represent a complete debiased orbital and absolute-magnitude distribution of the NEO population.

2.2 Population Debiasing

To calibrate the variables and thereby determine which sources provide most NEOs, the model had to be compared in some way with known NEOs. The problem is that known NEOs are biased by observational selection effects that favor the discovery of bodies that spend long periods of time in a survey's search volume above the detection threshold. This led Granvik et al. (2016) to compute the observational selection effects associated with Catalina Sky Survey (CSS), which had a large and

readily available NEO database. This resultant function was called $B(a, e, i, H)$. By multiplying $N(a, e, i, H)$ by $B(a, e, i, H)$, a new function was created that could be fit to thousands of CSS detections of NEOs (Figure 2-2). The best fit yielded their estimate of the NEO orbital and absolute magnitude distributions.

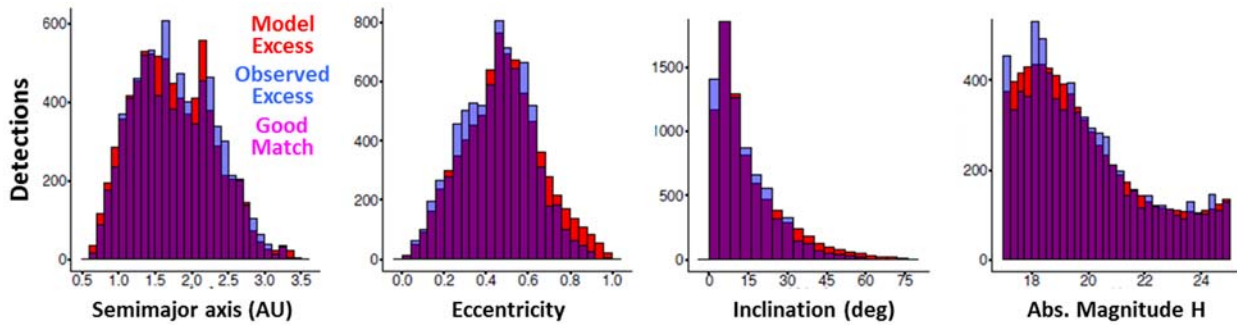


Figure 2-2. Comparison between Granvik et al. (2016) NEO model and Catalina Sky Survey work (7,952 detections of 3,632 NEOs). Red and blue histograms show model and observation detection mismatches, while purple histograms show where the model matches data. This model provides excellent fits for NEOs with diameters $\sim 0.1 < D < \text{few km}$.

For their best-fit model (Figure 2-2), Granvik et al. found there were $(7.32 \pm 1.33) \times 10^5$ NEOs with $17 < H < 25$ and $1,008 \pm 45$ with $H < 17.75$. These values were in reasonable agreement with recent independent estimates of the NEO population (i.e., 981 ± 19 for the population of NEOs with diameter $D > 1$ km by Mainzer et al. (2011e); see also Harris and D’Abramo 2015 and Tricarico 2017). The Granvik et al. model reproduced the relative fractions of Amor, Apollo, and Aten asteroids with $17 \leq H < 17.5$; the observed fractions are 47%, 50%, and 3%, whereas the model predicts $43 \pm 5\%$, $53 \pm 5\%$ and $3.5 \pm 0.6\%$, respectively. The contribution of each source region is shown in Figure 2-1. Most NEOs come from the inner and central main belts; few come from the outer main belt or Jupiter-family comets.

For this report, we use the orbital distribution found in Granvik et al. (2016) but do not use their absolute magnitude distribution. We instead adopt the absolute magnitude and size distributions discussed below.

2.3 Comets

This section reviews the relative importance of long-period comets to the Earth’s impact flux. Analysis included in Stokes et al. (2003) estimated that the threat from long-period comets (LPCs) is only about 1% the threat from NEOs. A recent update of this analysis, given below, confirms this conclusion. Consider the following:

- The number of LPC close Earth approaches per unit time is far less than that for NEOs.
- The higher orbital inclinations for LPCs render them less likely to strike the Earth, compared to the population of NEOs whose inclinations are more closely aligned with the ecliptic.

- The relatively higher Earth encounter velocities of LPCs diminish the Earth's capture cross section relative to NEOs.
- The impact velocities (~ 55 km/s) and impact energies of LPC strikes upon the Earth are somewhat higher on average than the impact velocities (~ 23 km/s) of similarly sized NEOs, but the bulk densities of LPCs (~ 0.6 g/cm³) are less than those of most NEOs (~ 2.6 g/cm³). This means the average mass of an LPC will be $\sim 20\%$ that of a similarly sized asteroid. Combining these two considerations, the impact energy of a LPC impact would be $\sim 30\%$ more than a similarly sized NEO.

Here we briefly discuss some other considerations concerning comets.

2.3.1 Paucity of Small Comets

A number of investigations have concluded that comets with relatively small nuclei are underrepresented in the comet population. Sekanina and Yeomans (1984) found that over the previous 300-year interval, when telescopes and accurate orbit determinations were available, the rate of cometary close Earth approaches remained constant. If there were a significant population of small LPCs, the improvement in telescopes and search techniques would have resulted in an increasing discovery rate. Zahnle et al (2003) studied the crater sizes on Jupiter's moons and concluded there is a pronounced paucity of small ($D < 1$ km) cometary impactors. Samarasinha (2007) studied the nuclear rotation and activity of comets and concluded that there is a real paucity of sub-kilometer comets when compared with the number one would expect on the basis of the size distribution of the known Kuiper belt objects. Fernandez et al. (2013) used the Spitzer Space Telescope's mid-infrared (IR) observations of 89 Jupiter-family comets at large heliocentric distances (4–5 AU) to study the comets' thermal properties and sizes before concluding that the cumulative cometary size distribution lacks many sub-kilometer objects.

2.3.2 Short-Period Comet Threat

Short-period comets (SPCs), defined as those comets with periods of < 200 years, include both the JFCs and the Halley-type comet populations. They have been shown to represent less than 3% of the threat posed by NEOs (Stokes et al. 2013). During the 1900 to mid-2016 interval, close Earth approaches (< 0.1 AU) by 12 different known SPCs occurred. Hence, the relative impact threat level compared to the NEOs ($H < 18$) is $15/649 = 2.3\%$. The closest approach was to within 4.7 lunar distances (0.0121 AU) by comet 1999 J6 SOHO on June 12, 1999, only one month after its discovery by the Solar and Heliospheric Observatory (SOHO) spacecraft in the daytime sky. According to an analysis by M. Knight (personal communication), this comet has a diameter of at least 100 meters. However, SPCs are not in the same threat category as LPCs. Unlike the LPCs, most SPCs are more akin to the NEO population in that they have a great probability of being discovered well in advance of a threatening Earth encounter providing an opportunity for deflection or disruption mitigation activities.

2.3.3 Long-Period Comet Threat

Using the close Earth approach table generator in the NASA Jet Propulsion Laboratory's CNEOS website (<https://cneos.jpl.nasa.gov>), a table of NEO close Earth approaches was generated for the interval between 1900 and mid-2016. In an effort to compare LPCs and NEAs of similar size ranges, the NEOs were limited to those with an absolute magnitude (H) of less than 18 (i.e., diameters ≥ 0.9 km). There

were a total of 649 close Earth approaches less than 0.1 AU (39 lunar distances or 39 LD). Over the same interval, only two such Earth approaches by LPCs occurred—both in 1983. C/1983 H1 Iras-Araki-Alcock passed within 0.031 AU (12 LD) on May 11, 1983, and C/1983 J1 Sugano-Saigusa-Fujikawa passed within 0.063 AU (25 LD) a month later on June 12, 1983. The threat for LPCs, relative to similarly sized NEOs, is then $2/649$ or 0.3%. If NEOs of smaller sizes ($H < 26$) are included in the comparison, the relative threat drops to $2/14718 = 0.01\%$.

LPCs are only a concern at the largest size ranges within the NEO population. LPCs are rarely discovered beyond the orbit of Jupiter, and it takes but nine months for a LPC to travel the distance between the orbit of Jupiter and that of Earth. In addition, the imprecision of astrometric angle data, at large geocentric distances, does not allow the orbit estimate to improve rapidly, and the outgassing of a comet introduces poorly modeled outgassing accelerations upon its motion. Hence, it would take some time beyond discovery before an Earth impact could be confirmed, and there would then be only a few months of warning to implement civil defense efforts.

In an effort to estimate typical warning times for LPCs, Chodas (1996) ran two simulations to estimate the likely warning time for an actual Earth-impacting LPC. They were based on the real comets C/1996 B2 (Hyakutake) and C/1995 O1 (Hale-Bopp). Both had their orbits altered to impact Earth before perihelion for testing purposes.

To discuss his method, it is first useful to know that when a comet or asteroid is discovered, its orbital properties are only modestly well defined. As more observations of the discovered object are made, its orbit becomes more precise, thereby allowing astronomers to predict its future trajectory with increased accuracy. A reasonable analogy is trying to predict by eye whether a car seen near the horizon is going to run into you. The longer you observe the car, the more one can assess the car's trajectory and velocity. In some cases, one can immediately tell that the car cannot strike you. For a car bearing down on you, however, the difference between a hit and a near miss is difficult to determine until the car is dangerously close. As the car approaches, you would likely become more and more nervous, as this anxiety is your brain's way of telling you the probability of an impact is steadily increasing.

Essentially, this approaching-car scenario is the problem astronomers face with hazardous asteroid and comets. To quantify their "worry," Chodas (1996) created test bodies consistent with the known orbit of the body, with orbital uncertainties included, and propagated their trajectories into the future. Those bodies that end up hitting the Earth yielded a probability of impact for that time (i.e., if 50 out of 1000 test bodies strike Earth, the probability of impact is 5%). If the object is destined to hit the Earth, future observations will eventually allow these calculations to reach high probabilities of impact.

We can now return to Hyakutake and Hale Bopp. The smaller and less active comet Hyakutake was discovered at a radial distance of less than 2.5 AU, only two months before its close approach with Earth. If we assume the comet was on a trajectory that would allow it to hit Earth, but that its orbit was refined in concordance with the real observations of Hyakutake, we can calculate how the impact probability increased with time. Here Chodas (1996) found that an impact probability threshold of 5% was not reached until the comet was 50 days from impact. The impact probability did not reach 50% until the final 20 days, largely because of the uncertainty in the effect of the comet's non-gravitational forces caused by outgassing. Twenty days is not much time.

The larger comet Hale-Bopp was discovered about 18 months before perihelion, and it passed close to Earth's orbit about 24 days after that time. The warning time for the 5% impact probability threshold was achieved one year away in this scenario, but, again, the probability did not reach 50% until the final three months. As with the previous case, uncertainties in the non-gravitational accelerations kept the 50% impact probability warning time very short, despite the early discovery and an aggressive simulated observation campaign.

A similar situation occurred with the extremely close encounter of comet C/2013 A1 with Mars (Siding Spring). When estimating the position uncertainty of the comet during its Mars close approach, Farnocchia et al (2014) considered a range of possible magnitudes of the two non-gravitational parameters based on a statistical analysis of the parameters for the LPC population as a whole. C/Siding Spring was more active than C/Hyakutake and was discovered at a range of 7 AU, two years before the Mars encounter. Had that comet been headed for an Earth impact, the warning time for a threshold of 5% impact probability would likely have been roughly a year, and the probability would not likely not have reached 50% until the final few months.

In both of the latter cases, little time would be left for mitigation of an Earth-impacting LPC (deflection or disruption). Extraordinary efforts, perhaps including large IR space-based observatories near the orbit of Jupiter, may be required to discover and track LPCs at larger heliocentric distances. Even these efforts, however, may not appreciably increase the warning times for LPCs.

2.4 Near-Earth Object Absolute Magnitude and Size-Frequency Distributions

Estimation of the NEO absolute magnitude distribution, size-frequency distribution, and the current survey completion are one and the same question because the total population at any given size is just the number discovered divided by the estimated completion in the given size range. Substantial progress has been made since the NEO SDT report (Stokes et al. 2003) in both the methods of estimating survey completion and in the numbers discovered as a function of size. Specific advances that we will address in this section include a new orbit distribution model (as outlined in the preceding sections), improvements in the simulation of surveys and estimation of completion using redetection rates of already known NEOs, and the recent NEO Wide-field Infrared Survey Explorer (NEOWISE) survey in the thermal IR that has allowed us to better quantify the relation between optical absolute magnitude H and diameter D (Mainzer et al. 2011a, 2011e, 2012; Wright et al. 2010). A discussion of how orbital distributions affect our synthetic survey is found in Appendix 2-A.

At the end of this section, we present new estimates of populations for NEOs, Earth-crossing asteroids (ECAs, essentially Apollos and Atens), and potentially hazardous asteroids (PHAs) (minimum orbit intersection distance <0.05 AU, without any distinction on size) in units of absolute magnitude H and diameter D .

2.4.1 Progress in Estimating Population and Completion

Here we discuss methods of how to derive the NEO absolute magnitude distribution from the observed population. At the time of the 2003 NEO SDT report, we noted a recent paper by D'Abramo et al. (2001) describing a method of estimating survey completion that was based on the ratio of redetections of already known objects of a given size to the total number of detections (discoveries plus redetections). In that paper, team member A.W. Harris equated the redetection ratio with

completion, a premise that would be the case if detections were random and all equally probable. This premise, of course, is not the case; objects in some orbits are intrinsically easier to detect than in other orbits.

In a more recent paper by Harris and D’Abramo (2015), a more advanced redetection method was used to estimate the difference between redetection ratio and completion. Using a survey simulation designed to match cadence and sky coverage for existing surveys, and inputting a synthetic NEO population (see previous section and Appendix 2-A), they refined estimates of the NEO population. In the simulated surveys, the number of detections in a given time interval were tracked, which in turn allowed them to make comparisons between how many detections were made of known NEOs versus how many were made of first-time discoveries. Unlike a real survey, however, it is possible to compare results to the input NEO population. This method not only yields the redetection ratio but also the fraction of the population that has been discovered as the survey proceeds.

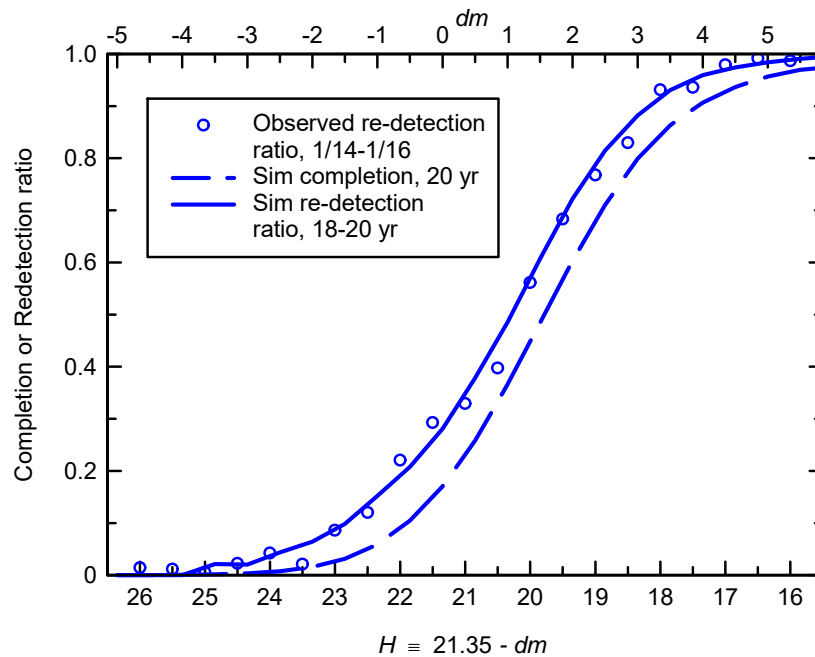


Figure 2-3. The lines are model redetection ratio (solid) and completion (dashed) versus asteroid absolute magnitude. The plot circles are the actual redetections of surveys for the past two years. The observed redetections are fit to a 20-year model survey. See text for details.

Figure 2-3 shows results from a typical simulation. Here H values were not assigned to individual objects, but instead the calculations were completed in units of $dm = V_{lim} - H$, where V_{lim} is the limiting magnitude of the survey. For a fixed value of H , one can think of completion versus dm as a measure of survey performance versus V_{lim} ; or for a fixed survey V_{lim} , completion (or redetection ratio) versus dm is a measure of performance of a given survey over a range of H magnitude. Note the NEO orbital distribution is assumed to be homologous here, which we argue is a reasonable approximation (Appendix 2-A).

Studies using this method indicate that the redetection ratio is a robust measure of NEO population completion in surveys and is nearly independent of the survey details. The ratio of the number of known objects detected to the total number detected in any size range should be fairly constant; all that changes is the total number of each, with deeper and wider surveys scoring more of each but in about the same proportion.

Team member Harris has studied individual surveys, including CSS, Lincoln Near-Earth Asteroid Research (LINEAR), Panoramic Survey Telescope and Rapid Response System (Pan-STARRS), and Spacewatch, and has found the redetection ratio to be stable between different surveys. The most important factor is that the surveys must be blind, that is, plowing the sky without regard to whether objects are known, or have the intent to redetect earlier discoveries. This approximation cannot be fully accurate, with some telescopes used to go after targets of opportunity from time to time, but it holds true to reasonable accuracy.

Given that real surveys have redetection statistics that follow closely the model redetection curves like those in Figure 2-3, one can adjust the horizontal scales between the model dm and the actual redetection ratios for a real survey versus H so they match up. This approach allows one to take the completion curve (lower dashed line) as representing survey completion versus H from the lower scale. Once the current survey completion level has been “calibrated” as above, estimating the total population can be derived by dividing the number of objects currently known in each size bin by the estimated completion at that H magnitude.

This method allows us to assess the current situation regarding completeness for NEOs, though the redetection ratio method is restricted to a rather narrow range of absolute magnitude (Figure 2-3). For large NEOs with $H < 17.75$, there are almost no new objects being discovered. For small NEOs with $H > 24$, there are almost no redetections of previously known objects. Harris and D’Abramo (2015) show (in their Equation 5 and Figure 3) that the expected completion at small sizes is proportional to $10^{-0.8H}$. With this extension of the completion function, it is possible to estimate the NEO population at all sizes.

The next step in the analysis is to compute the estimated differential population in each absolute magnitude bin. An example plot for NEOs, where we have used a new binning method as discussed in Appendix 2-B, is presented in Figure 2-4. The revised estimate of $N (H < 17.75) = 934$. New estimates of the populations of NEOs, Earth-crossing asteroids (ECAs, essentially Apollos and Atens), and potentially hazardous asteroids (PHAs) (minimum orbit intersection distance < 0.05 AU, without any distinction on size), are presented below.

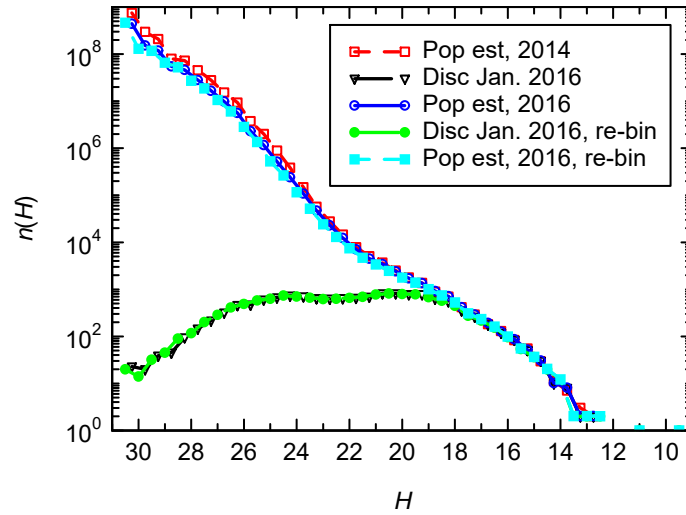


Figure 2-4. The differential population estimate of NEOs.

2.4.2 Conversion from Absolute Magnitude to Diameter

A key goal of NEO studies is to relate actual diameters of NEOs to their absolute magnitudes, which is the actual quantity measured by an optical survey. This progress is attributable mainly to the NEOWISE thermal IR survey, which measures diameters more directly (Mainzer et al. 2011a; Mainzer et al. 2014; Wright et al. 2010). By combining those measurements with optical H magnitudes, one can derive albedos, and from enough such diameters and albedos, one can determine the albedo distribution of NEOs.

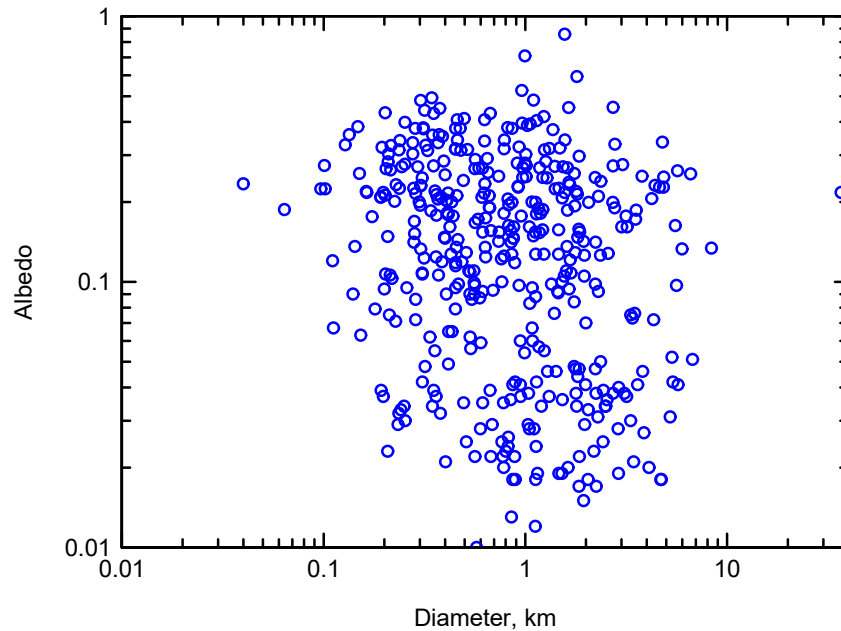


Figure 2-5. Albedo versus diameter for NEOs observed by the Wide-field Infrared Explorer (WISE). Multiple observations of the same object are combined.

Figure 2-5 is a plot of albedo versus diameter of 415 NEOs observed by the WISE satellite (Mainzer et al. 2011e; Mainzer et al. 2012). Clusters of high- and low-albedo objects are clearly seen, with few in between. Little, if any, apparent trend to the albedo distribution can be seen over the two-decade range of sizes observed. Thus, in our analysis that follows, we assume that the albedo distribution is constant with respect to diameter. This approximation would suggest the conversion between diameter and absolute magnitude is straightforward for NEOs. Curiously, there are a number of subtle issues that need to be considered to do this work correctly.

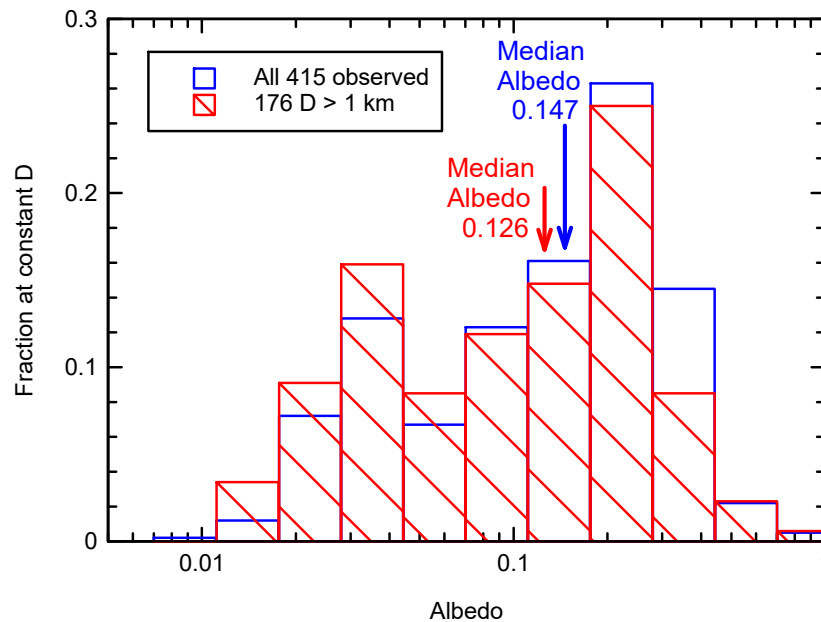


Figure 2-6. Albedo distribution for NEOs observed by WISE at a constant diameter.

In Figure 2-6, we present histograms of two distributions, binned in the same way as we employ for the size-frequency distribution calculations to follow. In those analyses, we adopt bin widths of 0.5 magnitudes of H ; such magnitudes correspond to a factor of 1.585 in albedo at constant diameter or a factor of 1.259 in diameter at constant albedo. The distribution plotted in blue is for all NEOs observed by WISE (as plotted in Figure 2-5) and has a median albedo of 0.147. Plotted in red is the distribution of only those NEOs with $D > 1.0$ km (Mainzer et al. 2011e). That distribution has a median albedo of 0.126 and appears rather similar.

Using these data, one can compute inversions between H and D distributions for NEOs using both albedo distributions, assuming a constant distribution of albedos over all sizes. The problem, however, is that an albedo distribution that is constant over diameter is not constant with respect to H magnitude. Since the NEO size-frequency distribution has more smaller (fainter) asteroids than larger (brighter) asteroids, the albedo distribution at constant H magnitude is distorted in favor of more higher-albedo (thus smaller) asteroids and fewer lower-albedo (thus larger) asteroids.

The degree of distortion of the distribution depends on the slope of the size-frequency distribution over a selected range of H . This conversion can be complicated, but, in general, the average albedo at a given H magnitude is considerably higher than the average albedo with respect to diameter. If we had a size-frequency distribution in units of D , and a constant distribution of albedos at constant D over the entire range of D , that D distribution could be analytically transformed to a size-frequency distribution in units of H . Unfortunately, the inverse transformation, from H to D , cannot be done exactly because the transfer function (albedo distribution at constant H) is itself not constant but is a function of H , or rather the local slope of the size-frequency distribution.

After some experimentation and trial and error, we arrived at the following algorithmic approach. For each size bin in the H distribution (Figure 2-4), we decomposed the composition of the bin into the appropriate size (D) bins by taking the D albedo distribution (Figure 2-5) but then multiplying the fractions in each albedo bin by the ratio of the population in the target bin (H implied by the albedo being considered) to the population in the H bin being distributed into the D bins. The approximation here is that we are using the D albedo distribution, distorted by the H size-frequency distribution, to redistribute the H bins into D bins, which is only an approximation of the real H albedo distribution. Because of the variations in slopes, total numbers were not conserved by this transformation, so the initial results had to be scaled to conserve total numbers.

The reverse transformation, from D back to H , is analytic and exact, so we next back-transformed the putative distribution to verify that it returned the original size-frequency distribution in H units. Some variation, in the few percent range, probably could be reduced with an iterative procedure, but we did not bother. A second check was to verify that the derived size-frequency distribution in D units did indeed result in the constant input albedo distribution with respect to D over the entire size range.

The resulting differential size-frequency distribution is shown in Figure 2-7, using the albedo distribution for NEOs of $D > 1$ km (red in Figure 2-7) and showing both the H distribution and the D distribution, shifted to best overlay one on the other in the range of $17 < H < 18$. It is apparent from this plot that the general character of the size-frequency distribution is similar in either D or H units, and one can assume an object of $H = 17.75$ is the same as $D = 1$ km. This conversion corresponds to an effective albedo of 0.14.

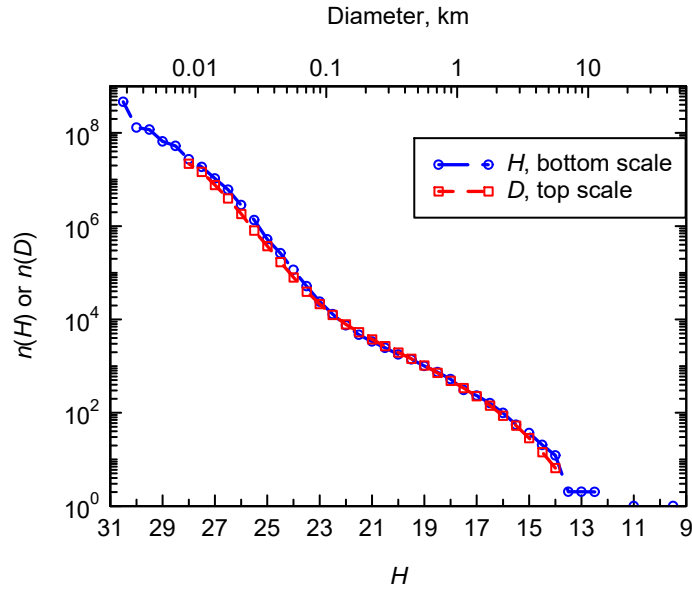


Figure 2-7. Differential size-frequency distribution.

Lastly, we can accumulate the running sum population $N (>D)$ to produce the usual integral size-frequency plot seen many times, but this time with real, computed numbers in diameter units (Figure 2-8). The estimate of $N (D > 1 \text{ km})$ using the albedo distribution for all NEOs is 817, but when we run the same inversion using the albedo distribution for only NEOs of $D > 1 \text{ km}$ (red in Figure 2-8, median albedo of 0.126), we obtain $N (D > 1 \text{ km}) = 902$. This population turns out to be very close to our estimate of $N (H < 17.75) = 934$.

Mainzer et al. (2011e) estimate the population $N (D > 1 \text{ km}) = 981$. Thus, it appears that our $N (H < 17.75) = 934$ estimate splits the difference between the NEOWISE estimate directly from diameter and our transformed-from- H estimate for the number $D > 1 \text{ km}$. We then adopt the proxy of $H = 17.75$ equivalent to $D = 1 \text{ km}$, implying a mean albedo of 0.14 and a population $N (H < 17.75) = N (D > 1 \text{ km}) = 934$. In the risk analysis that follows, we will adopt that size-frequency distribution, pinned to the equivalence of $H = 17.75$ and $D = 1 \text{ km}$.

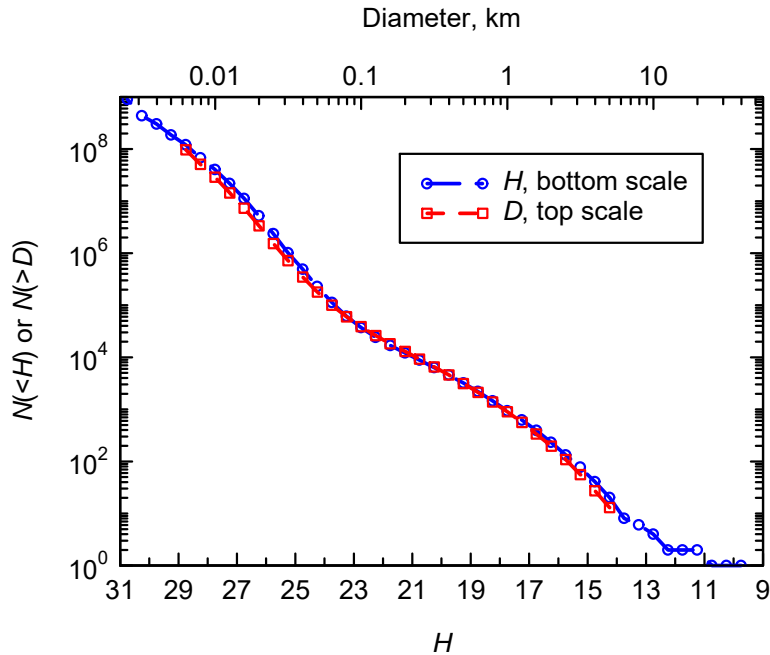


Figure 2-8. Cumulative near-Earth object size-frequency distribution in units of diameter D and absolute magnitude H , with the two over-plotted.

We note two final items:

1. We have aligned the H -to- D overlays in Figures 2-7 and 2-8 to match in the range of H around 17–18, where completion is so high that we know the absolute numbers quite closely. In the smaller size range, the H and D curves deviate by as much as a factor of 1.5, but uncertainty in exact numbers is even greater.
2. Even in the large size range, the very slight difference in albedo distribution between all NEOs and only those of $D > 1$ km changes the estimated number $N (>D)$ by more than 10%. Thus, one should be cautious of small error bars one often sees in estimates of $N (D > 1 \text{ km})$. The number almost certainly falls in the range from 900 to 1000 but may not be known much better than that. Nevertheless, the fraction that has been discovered is close to 93%–94%, which implies the number not yet discovered is close to 55–60.

2.4.3 Diameter Frequency and Albedo Distribution

It is also useful to examine the size distribution of NEOs derived directly from infrared surveys like NEOWISE. Using the albedo data in Figure 2-5, Mainzer et al. (2011e) and Wright et al. (2016) computed an albedo distribution for NEOs as shown in Figure 2-9. We refer the reader to these two papers for model details.

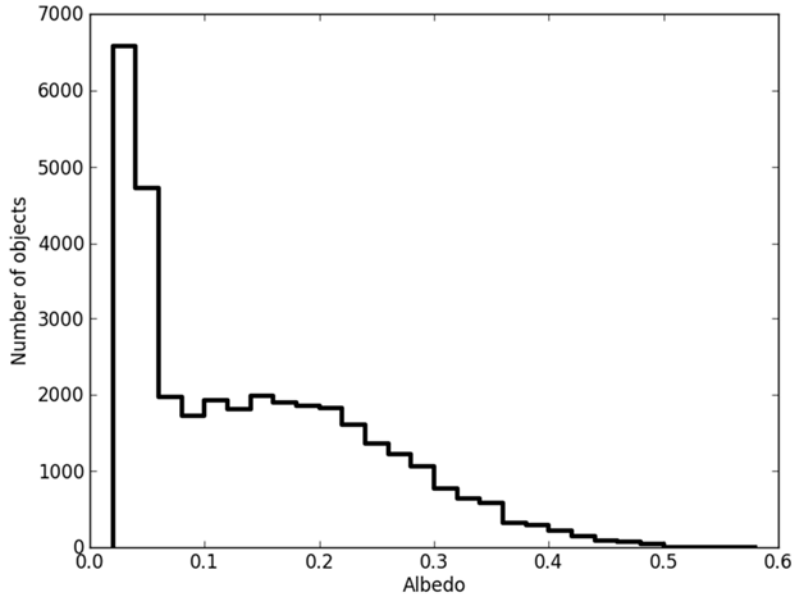


Figure 2-9. The albedo distribution for $D > 100$ m objects generated for our synthetic population. This function was derived from the NEOWISE data set shown in Figure 2-5, with methods discussed in Mainzer et al. (2011e) and further explained in Wright et al. (2016). The albedo distribution is constant across diameter space.

Mainzer et al. (2011e) also used these data to derive a diameter frequency distribution for the NEO population that was best represented by a broken power law with a slope of 1.32 ± 0.14 for the population $D < 1.5$ km. It yields $20,500 \pm 3000$ objects with $D > 100$ m. The NEOWISE sample included only four NEOs with $D < 100$ meters and did not try to derive the slope of the size frequency for that size range.

Mainzer et al. (2012) re-analyzed the NEOWISE data and looked at NEO sub-populations between $0.1 < D < 1$ km, where the power law slopes vary from 1.40 ± 0.18 for the Amors to 1.63 ± 0.30 for the Atens. The slope for the PHAs was found to be fairly steep at 1.50 ± 0.20 for objects between 100 meters and 1 kilometer. By combining the diameter-frequency distribution and the albedo distribution of the NEOWISE results, one can derive an H distribution that is shallower than those derived on the basis of the optical observations as described above, but still consistent at 1 sigma (with 24,393 objects brighter than $H > 22.25$ in Table 2-2 from the optical surveys and 19,761 objects in the NEOWISE model).

To derive a synthetic model that can be used for all of our simulated systems (described in Section 4), one has to generate both diameter and albedos for all the synthetic objects so that we can compute fluxes for detections in both the optical and thermal regime. It is the absolute magnitude distribution derived from the optical surveys, however, that have the largest sample size and cover the range of values in which this study is interested (~ 10 m to ~ 10 km).

As discussed above, there are disadvantages in inverting the absolute magnitude distribution to a diameter-frequency distribution using a derived albedo distribution. The procedure can be

complicated and may be inexact. Here, as an alternative, the synthetic population was generated by a trial-and-error process in which a triple-sloped diameter-frequency power law was used with a variety of slopes and break points to find a population that has a constant albedo distribution as discussed in Figure 2-5 and mimics the behavior of the H distribution derived above (see Table 2-1). It was found that the following size-frequency distribution satisfied this criteria: a cumulative slope of -2.75 for diameters $D > 1.5$ km, a cumulative slope of -1.6 for $70 \text{ m} < D < 1.5$ km, and a slope of -3.2 for $D > 70$ m.

Figure 2-10 shows the comparison of the optically derived model from Table 2-1 with the synthetic population generated from the size and albedo distributions discussed above. The total number of NEOs and PHAs, along with the edges of the diameter bins are given in Table 2-2. Note that the synthetic population tails off at the faintest absolute magnitudes because it is limited to objects with $D > 10$ m while the optical survey model includes objects smaller than this.

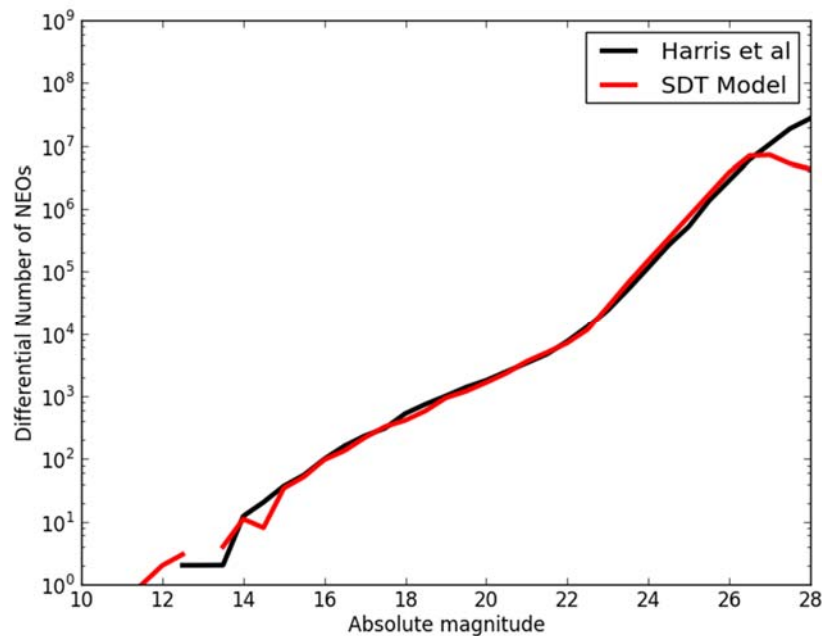


Figure 2-10. The differential distributions of absolute magnitude (H) as described in Table 2-1 (black line) and as derived from the diameter and albedo based distribution (SDT population, red line) discussed in the text and tabulated in Table 2-2. Note that the SDT population is limited to objects with $D > 10$ m. When these values are converted to H , the new population yields few $H > 27$ objects, which in turn explains why the red and black curves are different in this H range.

The resulting model has 955 objects with $D > 1$ km, and this number is consistent with the estimates provided above, increasing to $\sim 25,000$ objects 140 meters and larger. This value is larger than the number of objects estimated by Mainzer et al. (2011e). The fact that we model the diameter range from $70 \text{ m} < D < 1.5$ km as a single slope is the main cause of this difference, which can be seen as a

slight overpopulation of objects between $19 < H < 22$. It is apparent that a higher-fidelity diameter-frequency distribution is needed, but the limited data available on diameters and albedos at the 100-meter range leads one to believe that these differences reflect the uncertainties that exist in the current size frequency distribution estimates.

2.5 Impact Frequency, Then and Now

In the previous sections, we presented our current estimates of the population of NEOs, in binned differential form and in integral form (total number larger than a given size). To evaluate the risk posed by asteroid impacts, we need numerical values of population versus size, and an estimate of the per-object impact frequency. The latter is obtained by computing the Opik impact frequency for each orbit in the distribution of synthetic orbits used in our simulations, and then averaging over the number in the sample (in our case, 100,000) to estimate the mean impact frequency per object in the distribution.

We find that frequency, $f(1)$, to be $1.66 \times 10^{-9} \text{ yr}^{-1}$. Thus, a single “average” NEO would impact the Earth once in 600 million years. A population of 1000 NEOs (the approximate number of $D > 1 \text{ km}$) should result in one impact in 600,000 years. A population of 600 million objects should have an impact frequency of one a year. This rate corresponds to the number of NEOs down to a diameter of ~ 3 meters; thus, we expect an impact (bolide) of an object that size or larger about once per year, an estimate that corresponds fairly closely with actual bolide frequency.

It should be noted, though, that it is impact frequency that is a constant for a given population of defined orbit distribution. Thus, if one looks at a subset population of only those bodies that actually can impact, for example the PHA population, then one must increase the estimated impact frequency in the same proportion as the decreased number in the subpopulation. Thus, in counting only PHAs, at 20% of the total population, the impact frequency per PHA becomes five times greater, or $8.3 \times 10^{-9} \text{ yr}^{-1}$.

In Table 2-1, we present the numerical tabulation of impact frequencies versus size of objects to be used in the analysis that follows in the next chapter. We present two frequencies, the frequency of impacts from the entire population and the frequency from the fraction of the population in a given size range that currently remain undiscovered. The rationale is that since the NEOs that have been discovered are known not to be on impact trajectories within the next 50 or 100 years, they do not contribute to the short-term impact risk. Only those that remain undiscovered pose a possible short-term risk.

The first column of the table, labeled D_1 – D_2 , lists the diameter range of a given size bin (row of the table), in kilometers. The next column, $\langle D \rangle$, is the geometric mean diameter, i.e., the “center” of the bin range. Following that is the range of absolute magnitude H of the bin, and following that, the mean H (since H is a logarithmic scale already, $\langle H \rangle$ is just the arithmetic mean value). It should be further noted that since the fundamental independent variable used in determining the size-frequency distribution is H magnitude rather than diameter, the H magnitude columns are fundamental, and the diameter columns are derived/inferred as described in this section. The next column, $\langle E \rangle$ MT is the impact energy, in megaton equivalent TNT. To compute this energy, we take the mean impact velocity to be 18 km/s (see Appendix 2-A) and assume a mean density of the object to be 2.5 gm/cm^3 . The conversion to MT is $1 \text{ MT} = 4.185 \times 10^{15} \text{ joule}$. The next column, $N(>D_1)$, is mainly for reference,

listing the cumulative population of objects larger than D_1 , or actually of $H < H_1$. The next column, $n(D_1-D_2)$, is the differential number in each size bin. Following that is the impact frequency, $f(n)$, for the entire population in that size bin, just the product of $n(D_1-D_2)$ times 1.66×10^{-9} . The next column, $(1-C)$ is the estimated fraction of the total population of that size that remains undiscovered. The next column, $(1-C)n$ is the estimated number of yet undiscovered objects in that size range. One can note from this column that the largest size for which we estimate even a single remaining undiscovered NEO is around $H = 15.0$, or about 3.5 kilometers in diameter. Above that, the numbers can be thought of as the probability that even one NEO remains undiscovered. Finally, the last column is the estimated impact frequency from the fraction of remaining undiscovered NEOs of that size range

Table 2-1. NEO population, impact frequency, and projected completion.

D_1-D_2	$\langle D \rangle$	H_2-H_1	$\langle H \rangle$	$\langle E \rangle$ MT	$N(>D_1)$	$N(D_1-D_2)$	$f(n)yr^{-1}$	$(1-C)$	$(1-C)n$	$F(1-C)$
.0200-.0251	.0224	25.75-26.25	26.0	4.523-01	5.22e6	2.85e6	4.73e-3	1.000	2.85e6	4.73e-3
.0251-.0316	.0282	25.25-25.75	25.5	9.02e-01	2.37e6	1.35e6	2.24e-3	1.000	1.35e6	2.24e-3
.0316-.0398	.0355	24.75-25.25	25.0	1.80e+00	1.02e6	5.26e5	8.73e-4	.999	5.25e5	8.72e-4
.0398-.0501	.0447	24.25-24.75	24.5	3.59e+00	4.93e5	2.63e5	4.37e-4	.997	2.62e5	4.35e-4
.0501-.0631	.0562	23.75-24.25	24.0	7.16e+00	2.30e5	1.16e5	1.93e-4	.994	1.15e5	1.91e-4
.0631-.0794	.0708	23.25-23.75	23.5	1.43e+01	1.14e5	5.20e4	8.63e-5	.987	5.13e4	8.52e-5
.0784-.1000	.0891	22.75-23.25	23.0	2.85e+01	6.15e4	2.42e4	4.02e-5	.974	2.36e4	3.91e-5
.100-.126	.112	22.25-22.75	22.5	5.69e+01	3.74e4	1.30e4	2.16e-5	.951	1.24e4	2.05e-5
.126-.158	.141	21.75-22.25	22.0	1.14e+02	2.44e4	7.49e3	1.24e-5	.912	6.83e3	1.13e-5
.158-.200	.178	21.25-21.75	21.5	2.26e+02	1.69e4	4.68e3	7.77e-6	.853	3.99e3	6.62e-6
.200-.251	.224	20.75-21.25	21.0	4.52e+02	1.22e4	3.38e3	5.61e-6	.772	2.61e3	4.33e-6
.251-.316	.282	20.25-20.75	20.5	9.02e+02	8.84e3	2.46e3	4.08e-6	.670	1.65e3	2.74e-6
.316-.398	.355	19.75-20.25	20.0	1.80e+03	6.38E3	1.78E3	2.95E-6	.555	988.	1.64e-6
.398-.501	.447	19.25-19.75	19.5	3.58e+03	4.60e3	1.38e3	2.30e-6	.435	605.	1.00e-6
.501-.631	.562	18.75-19.25	19.0	7.16e+03	3.21e3	1.01e3	1.68e-6	.324	327.	5.43e-7
.632-.794	.708	18.25-18.75	18.5	1.43e+04	2.21e3	744.	1.24e-6	.228	170.	2.82e-7
.794-1.00	.891	17.71-18.25	18.0	2.85e+04	1.46e3	528.	8.76e-7	.157	82.9	1.37e-7
1.00-1.26	1.12	17.25-17.75	17.5	5.69e+04	934.	308.	5.11e-7	.107	33.0	5.47e-8
1.26-1.58	1.41	16.75-17.25	17.0	1.14e+05	626.	233.	3.87e-7	.0725	16.9	2.80e-8
1.58-2.00	1.78	16.26-16.75	16.5	2.26e+05	393.	161.	2.67e-7	.0493	7.94	1.32e-8
2.00-2.51	2.24	15.75-16.25	16.0	4.52e+05	232.	99.4	1.65e-7	.0345	3.43	5.69e-9
2.51-3.16	2.82	15.25-15.75	15.5	9.02e+05	133.	55.5	9.1e-8	.0263	1.46	2.42e-9
3.16-3.98	3.55	14.75-15.25	15.0	1.80e+06	77.5	36.8	6.11e-8	.0221	.081	1.35e-9
3.98-5.01	4.47	14.25-14.75	14.5	3.59e+06	40.7	20.4	3.39e-8	.0202	0.41	6.8e-10
5.01-6.31	5.62	13.75-14.25	14.0	7.16e+06	20.3	12.2	2.03e-8	.017	.021	3.4e-10
6.31-7.94	7.08	13.25-13.75	13.5	1.43e+07	8.07	2.03	3.37e-9	.014	0.03	4.7e-11
7.94-10.0	8.91	12.75-13.25	13.0	2.85e+07	6.04	2.02	3.35e-9	.010	0.02	3.4e-11
$f(n) = n^*f(1) = n^*1.66e-9 yr^{-1}$										

Table 2-2. Total number of NEOs and PHAs as derived by NEOWISE data.

Lower D Boundary	Upper D Boundary	Number of NEOs	Number of PHAs
10.011	12.603	2	0
7.952	10.011	2	0
6.316	7.952	4	1
5.017	6.316	8	2
3.985	5.017	13	3
3.166	3.985	24	5
2.515	3.166	44	9
1.997	2.515	75	15
1.587	1.997	136	27
1.260	1.587	244	49
1.001	1.260	403	81
0.795	1.001	444	89
0.632	0.795	601	120
0.502	0.632	852	170
0.399	0.502	1,222	244
0.317	0.399	1,767	353
0.251	0.317	2,489	498
0.200	0.251	3,561	712
0.159	0.200	5,128	1,026
0.126	0.159	7,357	1,471
0.100	0.126	10,313	2,063
0.080	0.100	14,450	2,890
0.063	0.080	37,539	7,508
0.050	0.063	107,553	21,511
0.040	0.050	240,196	48,039
0.032	0.040	539,653	107,931
0.025	0.032	1,203,233	240,647
0.020	0.025	2,718,367	543,673
0.016	0.020	6,093,278	1,218,656
0.013	0.016	13,386,264	2,677,253
0.010	0.013	14,915,756	2,983,151

Appendix 2-A. Analysis of How Different NEO Orbital Distributions Affect Survey Completeness

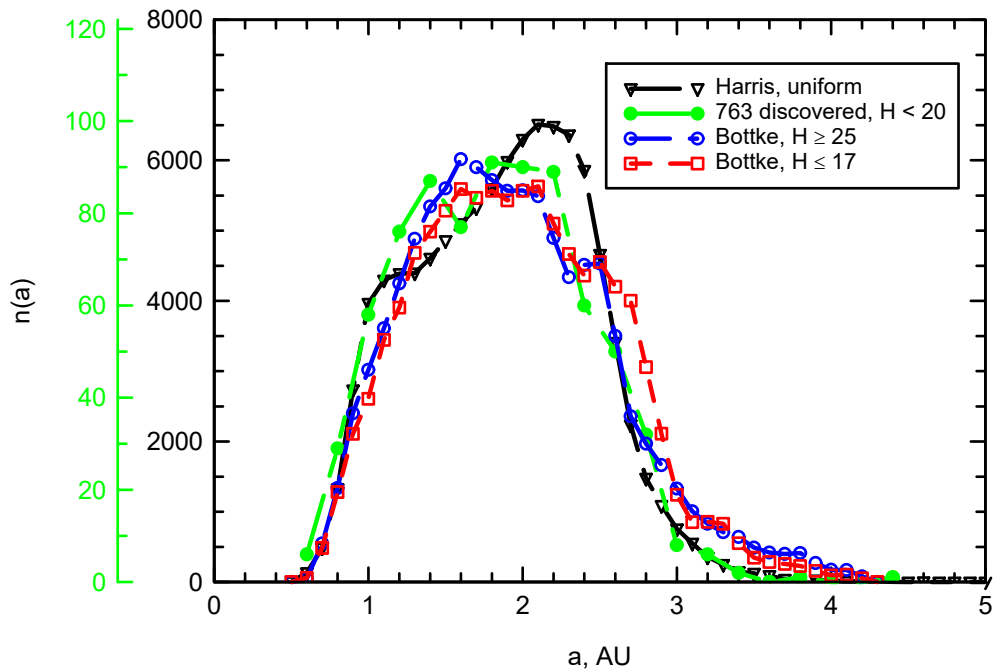
In this appendix, we discuss how the use of different orbital distributions for the NEO and PHA populations could potentially affect our synthetic survey results. The methods and analysis performed here were developed and applied by team member A. Harris.

In the 2003 NEO SDT report (Stokes et al. 2003), the NEO and PHA orbital distributions that were applied to the survey simulator were taken from the NEO model of Bottke et al. (2002). Several recent publications, however, have revisited the orbital distribution of NEOs expected from various source regions located beyond the Earth's orbit (Greenstreet et al. 2012; Granvik et al. 2016). In this report, as discussed earlier in this section, we used the Granvik et al. (2016) NEO orbital distribution. Note that this newer orbital distribution is in reasonable agreement with that of the known large NEOs, which are now complete enough (>90%) that their orbit distributions can have very little bias from discovery selection effects. We further note that the different orbit distributions show only modest variation at smaller sizes compared to larger ones ($H \sim 25$ versus $H \sim 17$).

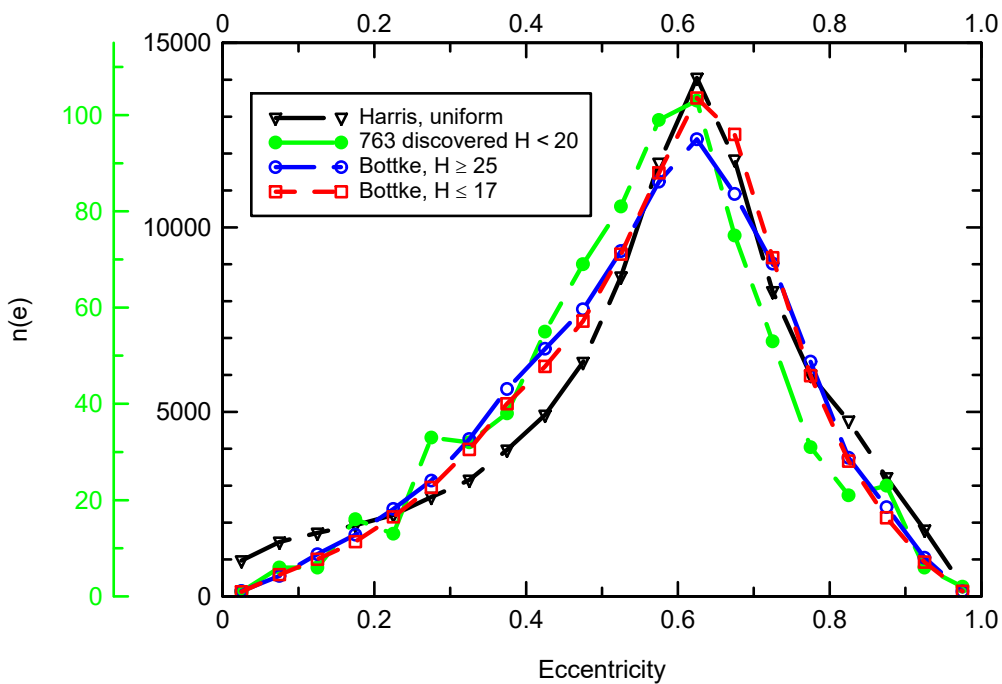
The following orbital distributions of PHAs are compared to one another as a series of histograms in semimajor axis a , eccentricity e , inclination i , and Earth encounter velocity. (Figure 2-A-1):

- The population used in Stokes et al. (2003) (labeled "Harris")
- The population from Granvik et al. (2016) (labeled "Bottke" after team member Bottke, who was on the Granvik et al. 2016 paper)
- 763 known PHAs with $H < 20$

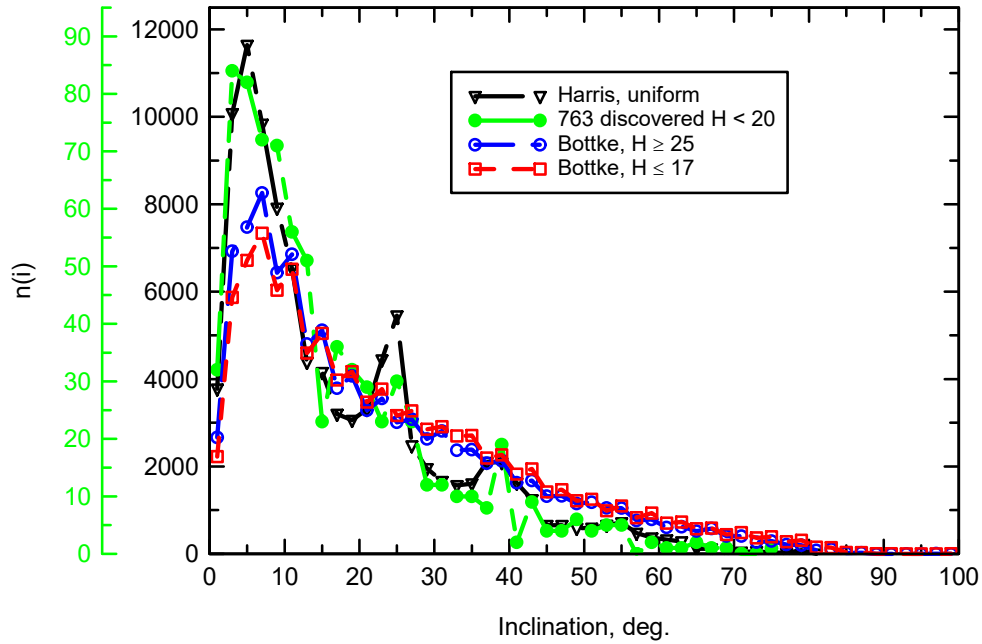
They show few differences. In particular, the orbital distribution of small bodies labeled Bottke ($H > 25$) yield approximately the same results as the much brighter bodies labeled Bottke ($H < 17$). This overall similarity implies that for survey purposes, it is a reasonable approximation to use the same orbital distribution for both small and large bodies.



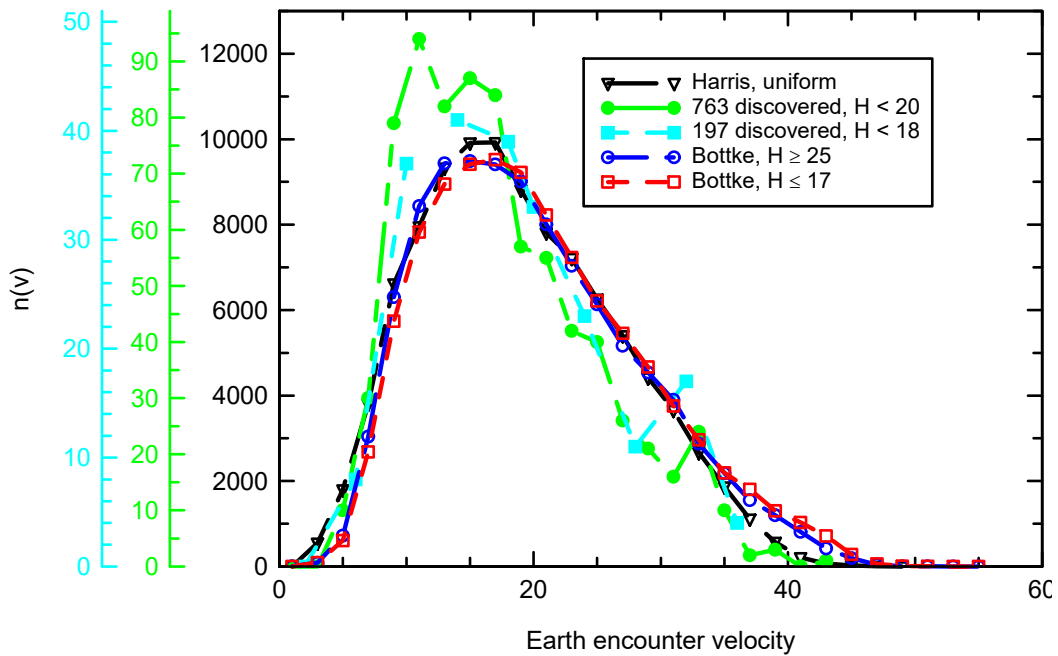
(a)



(b)



(c)



(d)

Figure 2-A-1. Distributions of orbital elements and Earth encounter velocity comparing the actual observed distribution of discovered large potentially hazardous asteroids (PHAs) with the population model used in the 2003 report and with the newer model distributions of large and small PHAs provided by Bottke. Distributions are for semimajor axis (a), eccentricity (b), inclination (c), and Earth encounter velocity (d).

An important point to mention is the distribution of Earth encounter velocity (v_{enc} , or sometimes v_{∞}). In Figure 2-A-1d, it appears that the models differ from the discovered population, but when we restrict the discovered population to only the very large ($H < 18$) objects, most of the excess goes away. It is possible that much of the discrepancy is a residual selection effect (slower moving objects are easier for surveys to detect), so we have reasonable confidence that our model distribution is accurate. Note the especially good agreement in v_{enc} between the Bottke model and the earlier Harris model.

Lastly, note that the distribution of Earth encounter velocities is not the same as that expected of the population of objects actually hitting the Earth. There could be many reasons for this lack of agreement: imprecision in the methods used to compute impact velocities, the model and observed populations are different in some manner, etc. It is also possible that slower-moving NEOs have a much higher probability of impacting, in part because of the gravitational focusing of the Earth, such that the effective collision cross section of the Earth increases as v_{enc}^{-2} for velocities slower than the surface escape velocity of the Earth, v_{esc} (11.2 km/sec). We examine this idea briefly below.

One of the fundamental quantities that can be computed for each of the orbits in a synthetic element set is the Öpik impact probability, essentially the probability per year of an object in an (a,e,i) orbit colliding with the Earth (with gravitational focusing included). If we weight the Earth-encounter velocities by the relative impact probability, we can obtain the distribution of velocities expected of the actual impacting flux. For our study, this parameter is important, especially when it is adjusted for the actual impact velocity, $v_{\text{imp}}^2 = v_{\text{enc}}^2 + v_{\text{esc}}^2$.

In Figure 2-A-2, we present the differential and integral distributions of v_{imp} , weighted by the relative impact probabilities, for the Granvik et al. (2016) orbit element distributions. Note that the impact velocity distribution peaks at the very low value of ~ 14 km/s, and the median impact velocity (where the integral curve reaches 50%) is only a bit over 17 km/s. Also plotted is the observed impact velocity distribution of 1-meter bolides provided by Brown et al. (2016). The observed distribution is in fairly close agreement, if anything a bit slower still.

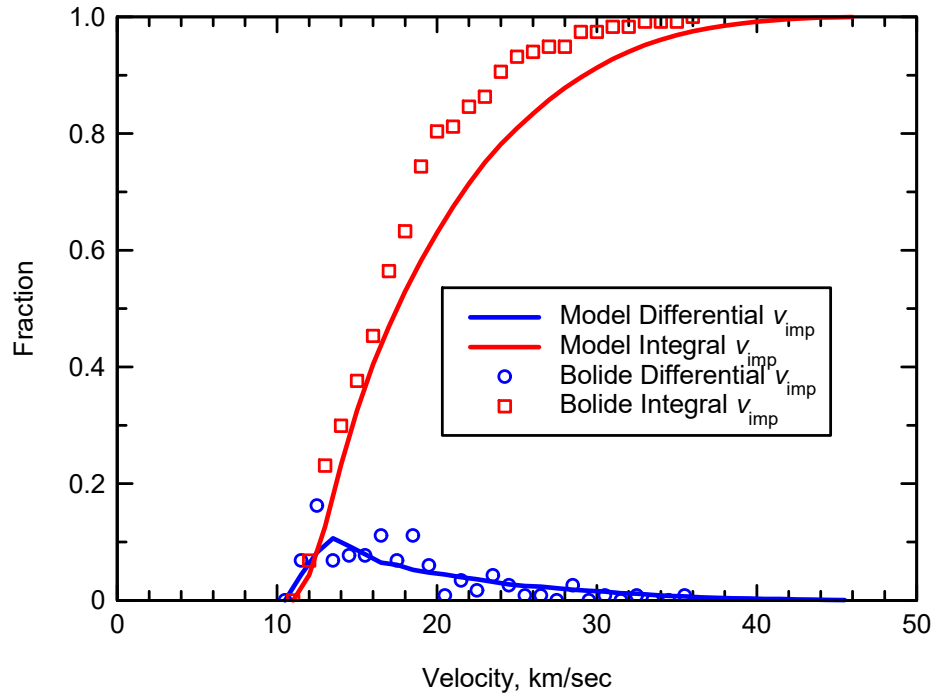


Figure 2-A-2. The distribution of Earth impact velocities. The model distributions have been weighted by the Opik impact probabilities. Bolide data are provided by P. Brown.

Appendix 2-B. Understanding How Absolute Magnitude Bins Affect the Differential NEO Population

For many years, team member A. Harris has been binning the discovered population of NEOs by half magnitudes to characterize the current population and estimate total population. Specifically, in Harris and D’Abramo (2015), Harris chose bins by even half magnitudes and took the bin boundaries from $>H$ to $\leq H + 0.5$, for example $17.50 < H \leq 18.0$. The issue is that because the Minor Planet Center lists H magnitudes rounded to 0.1, the real boundaries of our bins are shifted by 0.05, in the example given $17.55 < H < 18.05$. The distinction between “less than” and “less than or equal to” goes away at a 0.05 magnitude threshold because there are no values there; they are all either 18.0 (83 objects in the tabulation we used) or 18.1 (105 objects), and there were no values in between.

The difference caused by this subtle bin shift was brought to light recently in a manuscript by Tricarico (2017). In that paper, he claimed a population of large NEOs ($H < 17.75$, considered equivalent to $D > 1$ km) of 900 ± 10 , compared to the Harris and D’Abramo estimate of 990 ± 20 . Upon examining the paper, we found that the difference was due entirely to Tricarico’s having made the opposite bin boundary assumptions to what we had. He took his bins to be even full magnitudes, but chose the “equal to” side on the lower rather than upper boundary. Thus, because of the same rounding problem, his bin $17.0 \leq H < 18.0$ actually corresponds to limits of $16.95 < H < 17.95$, a 0.05 magnitude shift in the opposite direction from ours. This shift of only 0.1 magnitude between his bins and ours is small compared to some of the other uncertainties, but recall that there are between 80 and 100 objects among the discovered population in a 0.1 magnitude interval in the key size range around 17.75, thus exactly explaining the difference between Tricarico’s estimate and ours.

Figure 2-B-1 illustrates the problem resulting from round-off with numbers of discovered NEOs as tabulated by the Minor Planet Center. Tricarico’s selection of the “equal to” boundary leads to underrepresenting the population in the bin, while the assumption made by Harris and D’Abramo (2015) results in over-representing the population. The problem goes away if one selects bin boundaries at 0.05 magnitude because the round-offs to 0.1 magnitude result in implicit boundaries at 0.05 magnitude.

Once this problem was recognized, a correction was applied to re-bin the discovery and redetection statistics with half-magnitude bins with boundaries between 0.25 and 0.75. A fringe benefit of this re-binning was that the assumed $D = 1.0$ km boundary fell on the bin boundary at $H = 17.75$, so no interpolation would be needed to extract that number.

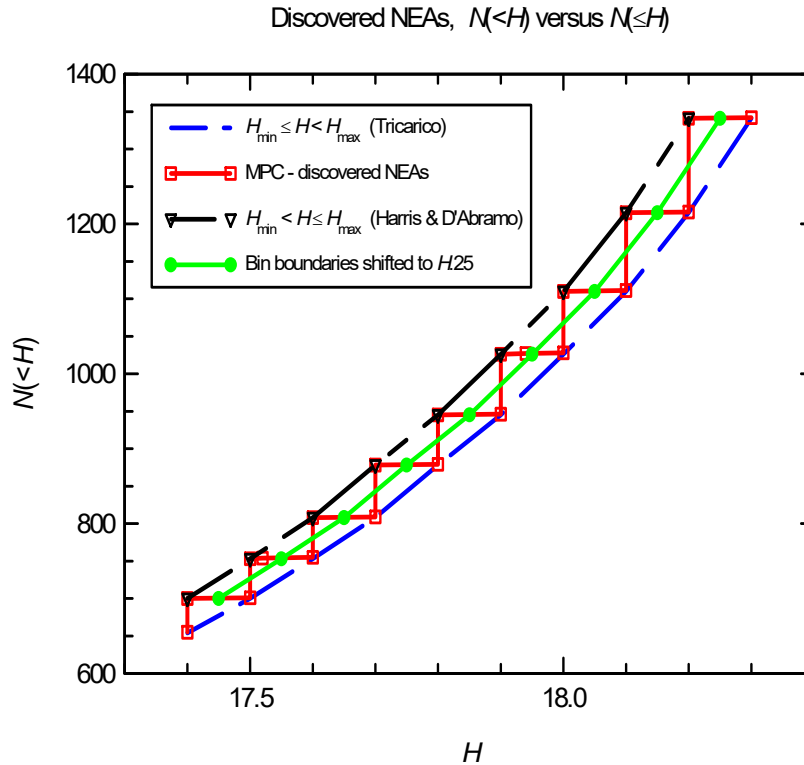
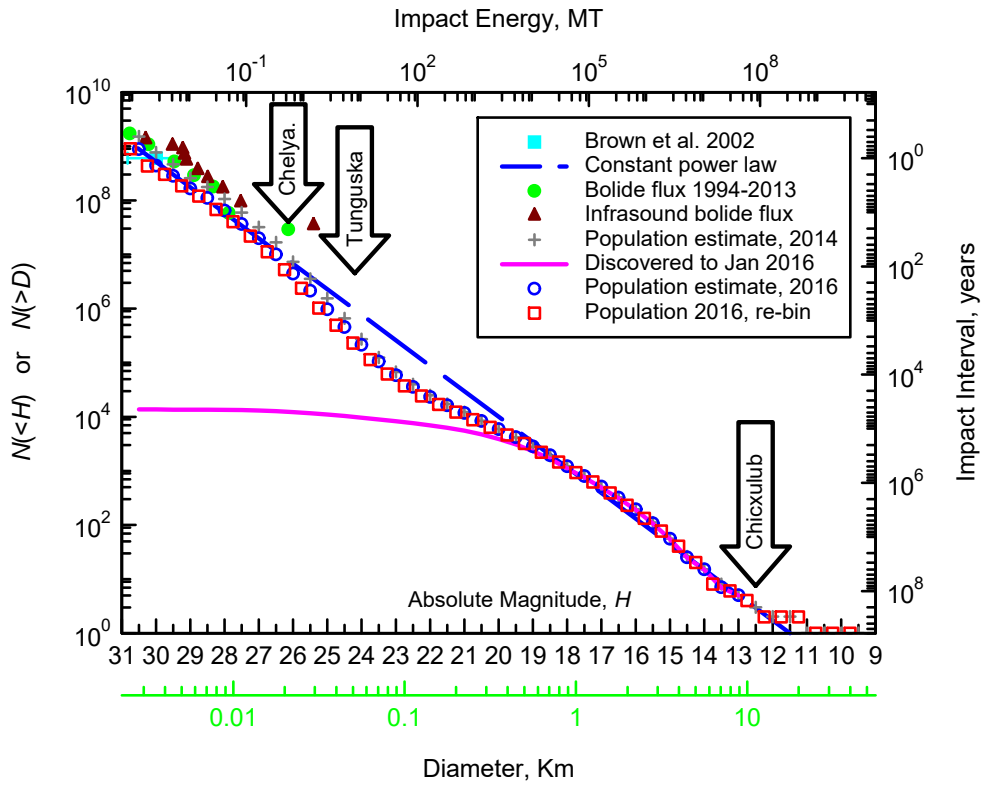


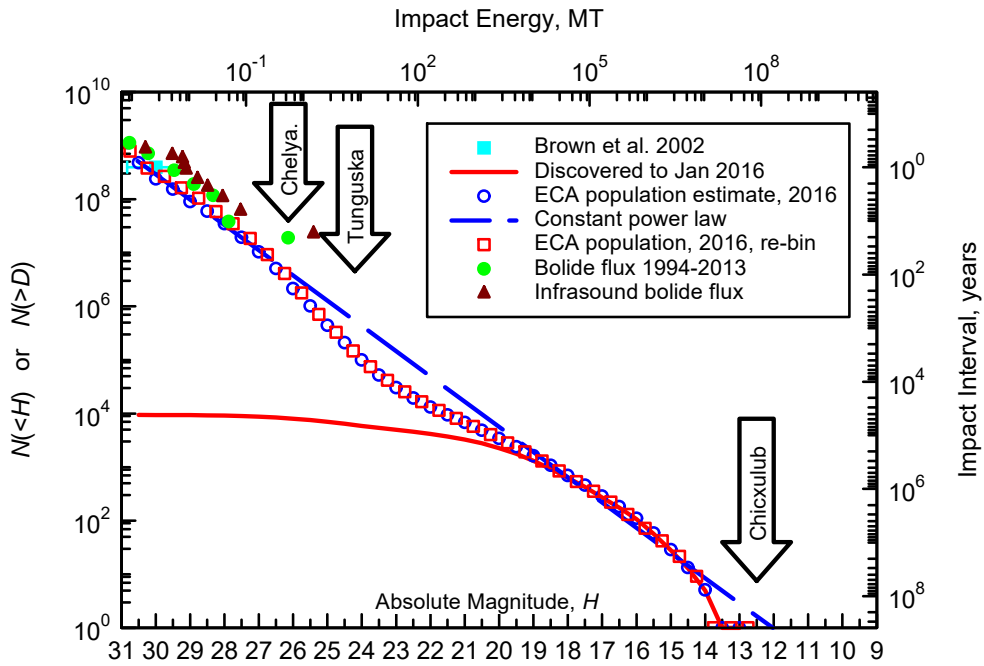
Figure 2-B-1. The effect of round-off in population bins.

In this plot, we see the change from the previous binning to the new binning is very small, in fact generally less than the difference in population estimates from year to year (2014 versus 2016). Nevertheless, in the range of frequent interest at $H = 17.75$, the difference is significant. Similar estimates were made for the population of Earth-crossing asteroids (ECAs, essentially Apollos and Atens, excluding Amors) and potentially hazardous asteroids (PHAs with minimum orbit intersection distance < 0.05 AU, but without a lower size limit). Next, we compute the running sum population to obtain estimates of the number $N(<H)$ larger than (brighter than, actually) a given value of H . We present these results in Figures 2-B-2a and 2-B-2b. The revised estimate of $N(H < 17.75) = 934$, down from 990 with the previous binning, is due solely to the round-off effect in the previous binning; the same discovery statistics were being analyzed. Another substantial difference is the completion implied in the re-binned estimate. With the number of 878 discovered NEOs of $H < 17.75$ used in the analysis, a population estimate of 990 implied 112 remaining undiscovered, for a completion of 89%. The new population estimate of 934 implies only 56 remaining undiscovered, for a completion of 94%.

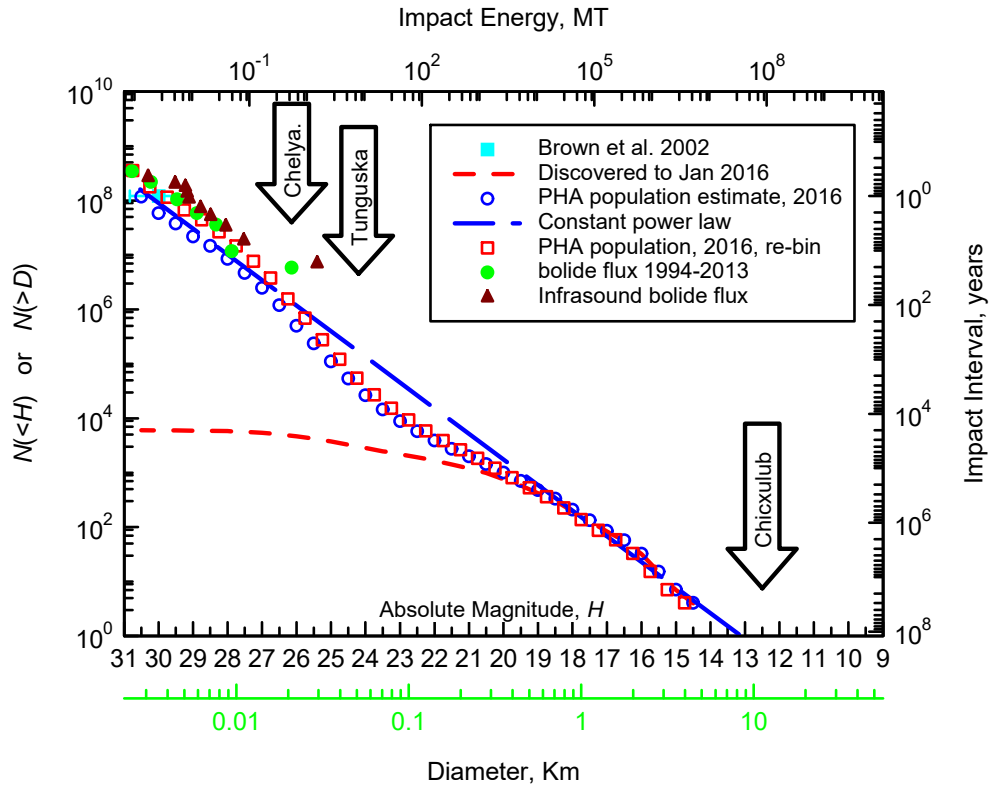
Using these results, we can examine how different binning schemes affect the differential population in each size bin. An example plot for NEOs is presented in Figure 2-B-3. Here we can see the change from the previous binning to the new binning is very small, in fact generally less than the difference in population estimates from year to year (cf. 2014 versus 2016). Nevertheless, in the range of frequent interest at $H = 17.75$, the difference is significant. Similar estimates were made for the population of Earth-crossing asteroids (ECAs, essentially Apollos and Atens, excluding Amors) and potentially hazardous asteroids (PHAs with minimum orbit intersection distance < 0.05 AU, but without a lower size limit).



(a)



(b)



(c)

Figure 2-B-2. The cumulative population of NEOs, with the new bin is shown in (a). The cumulative population estimates of Earth-crossing asteroids (ECAs) (b) and potentially hazardous asteroids (PHAs) (c) are shown for the old and new binning. Note that the impact interval scale on the right remains about the same for ECAs as for NEOs, in spite of the lower population. This is because non-ECAs (Amors) add nothing to the impact frequency. The scale for PHAs is a bit artificial because the timescale between impacts is generally longer than the time a given object spends as a PHA.

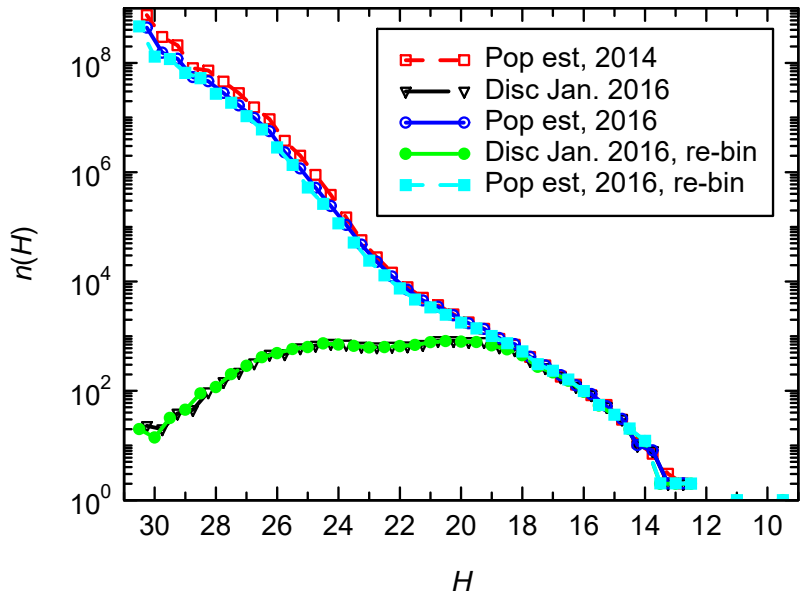


Figure 2-B-3. The differential population estimate of NEOs.

One last item to examine with the new population estimates is the completion at the very large sizes. As noted, the number of new discoveries goes rapidly to zero in the largest size range, so the redetection ratio goes to 1.0 and provides no meaningful estimate of the population remaining to be discovered. For example, the largest objects discovered between 2015-2017 fall in the $16.75 < H < 17.25$ bin, and only five fall in the $17.25 < H < 17.75$ bin.

An examination of the last decade of discoveries, however, reveals a quite dramatic trend in the rate of discoveries in these larger bins. It is even possible to take some account of the ever-improving surveys by normalizing the rates of discovery in the largest bins by the rate of discovery each year in a smaller size range, where completion is still low and one can expect the annual variations are a measure of survey success for the year. Taking the $20.75 < H < 21.25$ size range as a measure of annual survey power and normalizing the discovery rates for each of the size bins from $17.75 < H < 18.25$ on down to larger (lower H) sizes, we can see that the normalized discovery rate has dropped by about a factor of three over the decade, more or less uniformly in the larger size bins.

Two conclusions can be drawn from this observation. First, the e-folding time for final completion seems to be nearly a decade so, for example, to reduce the estimated number of NEOs of $H < 17.75$ from the current 56 down to unity will take about 40 years at the current level of survey. A second, perhaps more provocative conclusion is that the completion trend, factor-of-three per decade, seems to be fairly constant over all the size bins from 18.0 on down until there are no discoveries at all. This finding suggests that the depth of survey is not very important for such large objects; one just needs to wait until the last few objects chance to wander into a discoverable range.

A typical example could be an object with semimajor axis within 0.01 AU of the Earth's orbit. If such an object were hiding behind the Sun, it would be on the order of 30 years before it would drift out into a discoverable zone, at which time it would almost immediately be discovered by any of the

operating surveys. The only way to hasten such a discovery would be a space-based survey in heliocentric orbit. Nevertheless, even though the statistical fraction of the total population that remains undiscovered stands at around 98% to 99% when integrated up to the very largest NEOs, because of the steeply decreasing numbers of large bodies, the estimated number remaining undiscovered falls off very sharply. Indeed, the largest remaining undiscovered NEO can be estimated to be in the $H \sim 15$ size range, or about 3 kilometers in diameter. There are only 40 such objects of $H < 15.0$, and our estimated population to that size is 40.67 so, although that number represents 98% completion as noted, it still amounts to the largest bin in which we expect possibly one more object to be found. Estimates in the still larger bins amount to the fractional probability that even one remains undiscovered.

3 IMPACT RISK ASSESSMENT

Our understanding of the consequences of an asteroid impacting Earth has matured significantly since the 2003 Science Definition Team report, “Study to Determine the Feasibility of Extending the Search for Near-Earth Objects to Smaller Limiting Diameters” (hereafter referred to as the 2003 NEO SDT report), was published. This section provides a current assessment of the risk that asteroid impacts pose to Earth’s population. Physical models of the impact hazard, i.e., the damage-causing *potential* of impacts, are combined with the likelihood of such strikes described in the previous section. The assessment is described in the subsequent sections, but is still based on the approach of the 2003 NEO SDT report (Stokes et al. 2003).

The following are significant changes in the current analysis since the 2003 NEO SDT report:

- A Monte Carlo risk model is used to assess risk on a scenario-by-scenario basis.
- Scenario parameters, including the trajectory and impactor characteristics, are sampled from uncertainty distributions for each scenario.
- Assessment of each scenario uses a new fragment-cloud model for the simulation of the atmospheric entry trajectory and breakup.
- Blast overpressure damage is considered for a range of overpressure levels and is based on simulations for large impact energies.
- Thermal radiation is also considered as an impact effect that can cause ground damage.
- The tsunami model has been updated to incorporate local topography and distributed world population, and is assessed for each ocean impact scenario.
- The presentation of results incorporates both average/expected values and distributions of the range of possible outcomes.

3.1 Probabilistic Impact Risk Model

The impact risk is assessed by using a Monte Carlo simulation framework, following the approach of Mathias et al. (2017). Each assessment analyzes millions of hypothetical impact scenarios constructed by sampling input parameters from uncertainty distributions to create the pre-impact object characteristics, initial trajectory, and impact location. An integration of the atmospheric entry trajectory is performed for each scenario, including the effects of thermal ablation and fragmentation. The entry simulation produces an energy deposition curve that characterizes the rate at which the object’s kinetic energy is converted into other energy forms, such as light, heat, or pressure waves. The ground damages resulting from blast overpressure, thermal radiation, and tsunami inundation are all considered on the basis of the energy deposition curve. Gridded population distributions (CIESIN et al. 2005) are used to determine the number of people within the local blast or thermal damage areas and/or the regional tsunami inundation areas around the sampled impact location. For

large impacts, global casualties from climatic effects are also estimated. The impact model tracks the results for each scenario and generates a statistical result summary.

The steps of the impact risk modeling process are as follows:

1. Sets of impact scenarios are generated for each size bin by sampling uncertainty distributions for each asteroid and impact parameter.
2. Atmospheric entry and breakup are modeled for each scenario to compute the energy deposited in the atmosphere and to determine the airburst altitude and remaining energy striking the surface.
3. Local blast overpressure and thermal radiation damage areas are computed on the basis of the impact energy and airburst altitude.
4. The local population within the largest of the blast or thermal damage areas is computed at the impact coordinates sampled for the scenario.
5. Casualties resulting from global effects from large impacts are computed on the basis of the total kinetic energy and a sampled severity distribution.
6. Tsunami inundation modeled for ocean impacts is based on the amount of kinetic energy striking the surface after entry or airburst.
7. The affected population or casualty results from the different damage sources are combined with expected impact frequencies for each size bin to generate aggregate annual risk probabilities.

3.1.1 Energy Deposited in the Atmosphere

Entry flight modeling for each scenario begins at 100 kilometers above the surface of the Earth. The single-body flight equations are integrated, following the fragment-cloud model (FCM) of Wheeler et al. (2017), extending the work of Register et al. (2017), to produce a height, velocity, and mass record as the body encounters the atmosphere. Fragmentation onset is assumed when the local stagnation pressure exceeds the sampled aerodynamic strength of the body. In FCM, a percentage of the parent body mass is released as a dust or debris cloud, and the remaining mass is split into a specified number of discrete fragments. On the basis of FCM sensitivity studies reported by Wheeler et al. (2017), 50% of the parent body mass is split into two even fragments, and the other 50% is put into a debris cloud. FCM cases modeled with moderate cloud mass and two even fragments produce energy deposition profiles representative of catastrophic bursts, where the energy deposition peak provides a reasonable range of burst altitudes within the flare.

The emerging fragments are each given an increased aerodynamic strength (σ_f) that is based on the parent strength (σ_0), parent mass (m_0), child mass (m_f), and a Weibull scaling parameter (α) (Weibull 1951):

$$\sigma_f = \sigma_0 (m_0/m_f)^\alpha$$

Each fragment is subsequently treated as an independent body, and its trajectory is integrated using the equations of motion until its aerodynamic strength is again exceeded by the stagnation pressure, causing another break event and again splitting into two fragments and a debris cloud. Each debris

cloud is assumed to initiate as a strengthless, aggregate mass with the density of the parent object. Following the approach originally presented by Hills and Goda (1993), the cloud flies within a common bow shock but spreads laterally during flight because of the aerodynamic pressures experienced. This expanded frontal area increases the drag and ablation rate, and is the primary mechanism for airburst energy deposition in the model. The fragmentation and flight integration continues until all components have ablated or reached the ground. Energy deposition is tracked as a function of altitude and used as the basis for evaluating the corresponding ground damage.

3.1.2 Ground Damage Risks

Ground damage risks are the physical manifestations of the asteroid kinetic energy that pose a threat to population and infrastructure. Local risks considered in this assessment include blast overpressure and thermal radiation damage. While impact cratering events pose hazards of their own, ground impacts are treated as airbursts at ground level in the current model because damage from blast waves extends to farther than the crater areas. Regional risks include tsunamis and earthquakes generated by asteroid impacts. As in the 2003 NEO SDT report, impact-triggered earthquakes are not included because their risk has been assessed as negligible. Global effects result when the impact energy is so great that climatic changes occur. The following section describes the models of blast overpressure, thermal radiation, asteroid-generated tsunamis, and global effects used in this assessment.

3.1.2.1 Blast Damage

Blast damage results from the pressure wave associated with aerodynamic breakup of the asteroid, normally corresponding to the flare of emitted light observed during meteor bursts. True representation of this process takes into consideration the motion of the mass and the finite duration of energy release (Boslough and Crawford 2008; Aftosmis et al. 2016a). Modeling the blast propagation from the entire entry breakup process requires computational effort beyond what can be incorporated into the kind of fast-turnaround framework needed for statistical studies, so a point-source airburst proxy is used. Aftosmis et al. (2016a) have compared the differences between blasts propagated from static and moving sources, and the differences are not considered significant relative to other uncertainties for an ensemble risk assessment. Traditionally, nuclear test data (Glasstone and Dolan 1977) are used to produce curve fits of the ground-damage footprint from a given airburst energy and height, as was done in Hills and Goda (1993). The ground footprint is defined as the area inside which the overpressure is 4 psi or greater. For the current assessment, this convention will be followed when referring to resulting casualties, but additional overpressure footprints will be computed for survey cost/benefit assessment, as described in Section 8.

Representing the burst as a point-source proxy generally relies on a height-of-burst map, which provides the maximum distance from ground zero at which a given overpressure limit is exceeded, requiring only blast energy and burst altitude as inputs. Hills and Goda (1993) initially used the full entry kinetic energy of the asteroid as the blast energy, and this protocol was adopted for the risk assessment in the 2003 NEO SDT report (Stokes et al. 2003). However, Hills and Goda (1998) later suggested a fraction of the kinetic energy would convert to overpressure, and Toon et al. (1997) suggest 50% as an appropriate amount. While the argument that not all of the energy converts to pressure is valid, Boslough and Crawford (2008) have shown that the motion of the asteroid during the airburst contributes momentum, not just energy, to the atmosphere, and the result is that the corresponding ground footprints appear as if they came from sources larger than a static burst would

imply. Aftosmis et al. (2016b) also showed larger blast damage areas for moving sources, both for steep entries with low burst altitudes and also for oblique entries with higher burst altitudes. To maintain the damage-causing potential associated with the moving sources, 100% of the kinetic energy is used to initiate the static burst analogs in this assessment. Comparisons between point-source estimates and full energy deposition curves from FCM show good agreement (Aftosmis et al. 2016a, 2016b). For the purpose of comparing the point-source and energy deposition curve estimates, the airburst altitude for a realistic entry is defined as the altitude of peak energy deposition from the FCM assessment.

The need to produce footprints at multiple overpressure levels precludes the use of the curve fit from Hills and Goda (1998), which provides a 4-psi area only. Instead, height-of-burst maps from Glasstone and Dolan (1977) are used in conjunction with results of high-fidelity blast propagation simulations to provide damage areas for 1-, 2-, 4-, and 10-psi thresholds. The nuclear-based height-of-burst maps from Glasstone and Dolan (1977) provide good estimates for smaller burst energies, and these are used at burst energies at 5 megaton (Mt) and below. For energies of 100 Mt or higher, however, the blast footprints cannot be accurately energy-scaled by using a single parameter. At large energies, the thermal buoyancy causes the hot blast region to elongate upward, and the resulting shockwave structure on the ground is different from that for a smaller blast. Particularly, the Mach stem/reflection occurs at a different distance and changes the scaled decay of the pressure with distance. To produce more faithful overpressure curves at larger energies, three-dimensional (3D) simulations of 250 Mt bursts were performed at a broad range of altitudes (Aftosmis et al. 2016a) using the Cart3D code (Aftosmis et al. 1998). The resulting overpressure curves were then energy scaled to a yield of 1 kiloton (kt). For a given airburst, the equivalent 1 kt distance is found for the desired overpressure level. This distance is then rescaled to fit the actual airburst energy. For energies below 5 Mt, the standard Glasstone and Dolan (1977) curves are used; for energies greater than 250 Mt, the Aftosmis simulation results are used; and for energies between 5 Mt and 250 Mt, the results are interpolated between the Glasstone and Dolan (1977) and Aftosmis simulation results. Recent comparisons have shown very good agreement between the 250 Mt blast overpressures predicted by Cart3D and hydrocode simulations with the xRage, CTH, and ALE3D hydrocodes (Aftosmis et al. 2016b).

Figure 3-1 shows the height-of-burst maps from the two sources for peak overpressures of 1, 2, 4, and 10 psi on the ground. The Glasstone and Dolan (1977) map shows the peak overpressures on the ground as a function of height of burst and distance from ground zero for a 1 kt nuclear explosion in ideal terrain, surface, and meteorological conditions. The curves demonstrate the Mach reflection region, where the incident and reflected wavefronts merge, taking place at lower altitudes with increasing overpressure. As the energy yield increases for a given burst height, the Mach reflection starts nearer to ground zero, and the overpressure above the ground becomes larger. This effect can be seen in the larger, lower peak of the simulation height-of-burst curves in Figure 3-1.

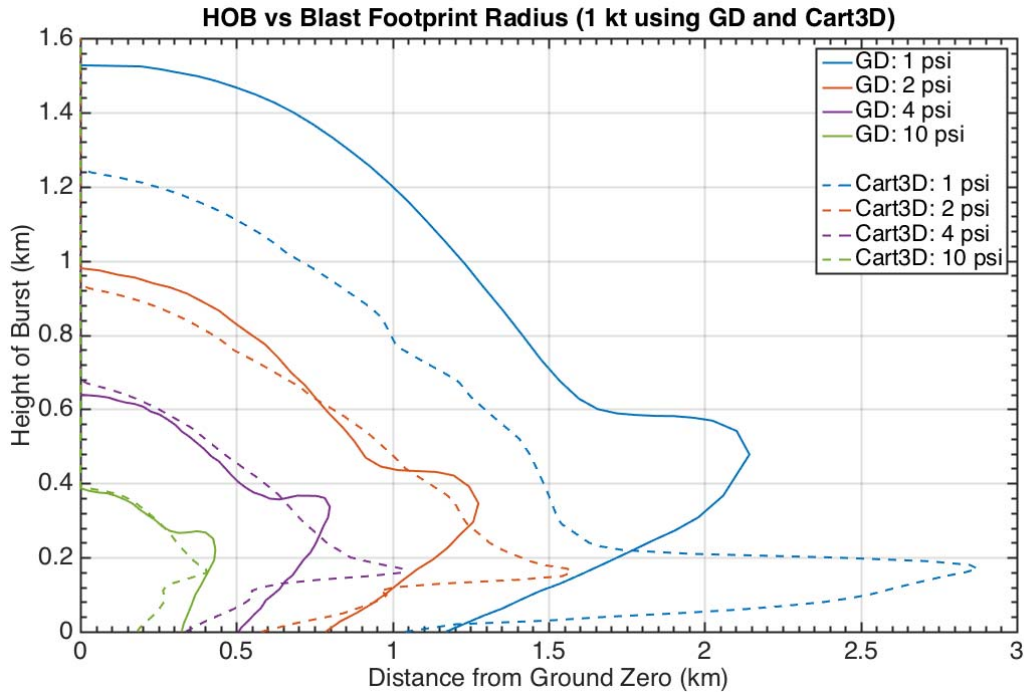


Figure 3-1. Height-of-burst maps from Glasstone and Dolan (GD) (1977) and current Cart3D simulations. The current simulations were performed for 250 Mt with the energy scaled to 1 kt. When the larger blasts are simulated, the hot gases rise because of buoyancy and change the ground overpressure footprint. At higher altitudes, the simulated ground damage is much less, in a relative energy sense, but at low burst altitudes the Mach reflection is highly pronounced and produces significantly more damage.

In order to compare the characteristics of the Glasstone and Dolan (1977) peak overpressure maps to those produced by Cart3D, it is necessary to use scaling laws. Scaling laws are based on the theoretical principle that a given pressure will occur at a distance from the burst that is proportional to the cube root of the energy yield:

$$\frac{D}{D_1} = \left(\frac{W}{W_1}\right)^{\frac{1}{3}}$$

Distance D_1 and energy W_1 correspond to the values of distance from reference explosion of W_1 kt energy at a given overpressure. D represents the distance for that same overpressure, given the explosion energy W .

However, full-scale tests have demonstrated that these relationships hold only up to the megaton range (Glasstone and Dolan 1977). Hence, we use both of these height-of-burst maps to determine the peak overpressures on the ground by weighing the damage given by both models with the proximity to energies for which each model corresponds. For example, airbursts with energy yields closer to 250 Mt result in blast footprints similar to the Cart3D while airbursts closer to 5 Mt result in blast footprints closer to the Glasstone and Dolan radii. Interpolation between the two data sets is performed as

$$D = D_{GD} \times \left(\frac{W_h - W}{W_h - W_l} \right) + D_{Cart3D} \times \left(\frac{W - W_l}{W_h - W_l} \right)$$

where distance D is the damage footprint at a given overpressure using the 1 kt scaled damage given by Glasstone and Dolan (1977) D_{GD} and Cart3D D_{Cart3D} . W represents the airburst energy, and it is weighted by comparing proximity to the high and low energy bounds, $W_h = 250$ Mt and $W_l = 5$ Mt. After the damage is calculated for the scaled 1 kt burst, D_1 above, scaling laws are necessary to appropriately determine the damage expected on the ground for that energy yield.

3.1.2.2 Thermal Radiation

While light is readily emitted during atmospheric entry, the thermal radiation considered here is that released during an explosive airburst flare or ground impact, i.e., radiation energy capable of causing burns or starting fires. Modeling of the damage potential is based on the approach of Collins et al. (2005). As presented by Collins et al., a distance can be computed at which a specific damage threshold is reached. For example, the distance at which third-degree burns occur, incorporating the threshold scaling values from Glasstone and Dolan (1977), is given by

$$r = \sqrt{\eta E / (2\pi \Phi_{i(1Mt)} E_{Mt}^{\frac{1}{6}})}$$

where η is the luminous efficiency, or fraction of energy transmitted as heat, E is the total impact energy in joules, E_{Mt} is the impact energy in megatons, and $\Phi_{i(1Mt)} = 4.2 \times 10^5$ J/m² is the thermal exposure threshold scaling factor for third-degree burns. This formulation assumes that the heat is distributed over a hemispherical surface, as in the case of a crater-forming impact. For an airburst at altitude, the area over which the energy is distributed becomes a sphere and the energy per unit area decreases accordingly. However, for large airbursts, or bursts at low altitudes, the true radiation area is between a sphere and hemisphere. In Collins et al. (2005), r represents the ground distance corresponding to the damage threshold. For the general case, r represents the radial distance from the burst and must be converted to a ground distance, R_{ground} , based on the altitude, h :

$$R_{ground} = \sqrt{r^2 - h^2}$$

Because thermal radiation only contributes to the ensemble risk for large objects, which also tend to deposit energy low or at the ground, the hemispherical area assumption is used as the bounding case. Also, the uncertainty associated with the surface area, less than a factor of two, is much less than that of the luminous efficiency that varies between 10^{-4} and 10^{-2} (Collins et al. 2005).

The risk model compares the thermal damage radius to that from the 4 psi blast overpressure and uses the larger of the two for the affected population calculation.

3.1.3 Tsunami Modeling

Scenarios that impact in ocean regions are examined for airburst and thermal radiation damage as described above. However, ocean impacts are also capable of producing tsunami-like waves that can result in coastal damage. The current model utilizes the energy deposition curves from FCM to initialize an analytic tsunami inundation model, based on the approaches of Chesley and Ward (2006) and Ward and Asphaug (2000), as reported by Mathias et al. (2016). Findings presented at the 2016 NASA- and NOAA-sponsored Second International Workshop on Asteroid Threat Assessment: Asteroid-generated Tsunami (AGT) and Associated Risk Assessment (Morrison and Venkatapathy 2017), indicate that airburst energy deposited above the surface of the water couples very weakly to water-wave generation, and that only about 1% of the surface impact energy converts to the water wave (Boslough 2016; Robertson 2016; and Wheeler et al. 2016). Therefore, only the energy remaining at the water surface is used in this analysis, and a 1.5% energy conversion is assumed to bound the assumption, given the associated uncertainty. This scaled surface impact energy fraction is used to form the initial transient water cavity as in Chesley and Ward (2006). Since the analysis is tied to the Monte Carlo impact scenarios, the crater depth is limited to the ocean depth at the impact location (Amante and Eakins 2009).

Wave propagation also follows the 2006 Chesley and Ward model, assuming a flat ocean bottom, so the wave amplitude decays inversely with the propagation distance. Run-up is also computed by using the approach and assumptions in Chesley and Ward (2006), which computes deep-water wave decay at a given distance and then adds a shoaling amplification factor to obtain wave run-up height at the shore. The model performs a check of all coastal cells (cells within 10 kilometers of the shore) from the NOAA bathymetry file, within 6000 kilometers of the impact point. The check consists of a comparison between the run-up height at the given distance, assuming open ocean propagation to that point, and the local topography. If the run-up height exceeds the coastal elevation, the location is flagged for a secondary check. Once all of the coastal cells have been screened, a secondary check is performed to determine if any land obstructions exist between the impact point and the cell in question. If land exists between the points and its elevation exceeds the run-up height, the cell is assumed safe from flooding. Essentially, this assumption is a line-of-sight approximation that prevents flooding across large land masses. The population within cells that remain “flooded” after the secondary screening is considered affected. To determine the casualty rate within inundated areas, the difference between the run-up height and the local elevation above sea level is used to compute a flood depth. Flood depth is related to a percentage of casualties using the fragility curves from Koshimura et al. (2013), as shown in Figure 3-2.

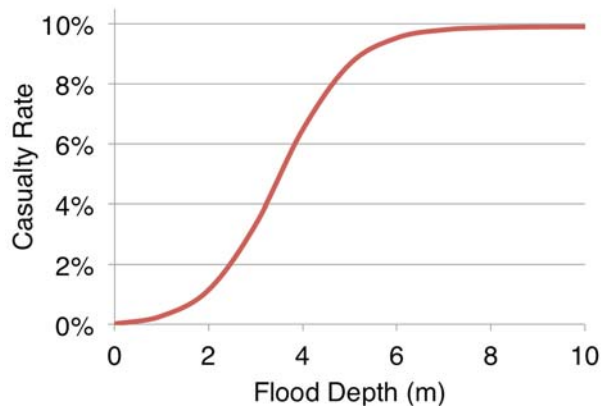


Figure 3-2. The casualty rate for an inundated population is shown as a function of the local flood depth, derived from Koshimura et al. (2013).

This approach represents the need to link each specific, sampled impact scenario to tsunami consequences with a model that runs quickly enough to assess a large number of scenarios. For this reason, a number of simplifying assumptions were required and are explicitly identified:

- Airburst coupling to tsunami wave is neglected: Studies have shown that the airburst wave energy is largely reflected by the ocean surface. The energy transmitted to the ocean is very inefficient at producing a gravity wave capable of traveling long distances. There are other potential coupling mechanisms (Boslough 2016), but the likelihood is believed very low for the general case.
- Flat-bottom ocean is assumed: This assumption is required for performing a closed-form propagation solution. Treatment of the true bathymetry requires location-specific numerical solution of governing equations, well beyond the scope of an engineering model suitable for ensemble risk assessment, given current computational assets. While the flat-bottom assumption is a gross simplification of the problem, it provides a pessimistically bounding assumption (more predicted damage than would occur) since true changes in bathymetry are likely to decrease the propagation efficiency (Van Dorn et al. 1968).
- Inundation is assumed based on open-ocean propagation and run-up: When large waves encounter the shore, the coastal topography serves to inhibit flooding. However, once flooding occurs, the damage is more linked to run-in than to run-up. The current model has no inherent run-in limit and neglects potential protective factors, such as harbors or continental shelves.
- Line-of-sight wave propagation is assumed: This assumption is required, within the context of the current model, so that waves do not artificially propagate through large land masses or into low-lying regions that are near, but not on, the coast. As a result, the potential for waves to wrap around small peninsulas or islands is neglected. However, the pessimistic inundation distances produced by neglecting bathymetry interference, harbor protection, or other run-in limiting factors are believed to more than compensate for any populations missed by neglecting potential wrap-around effects.

These assumptions all can have a significant effect on the wave propagation and inundation. However, the current model overpredicts the damage compared to higher-fidelity simulations

(Berger 2016; Wheeler et al. 2016) and as a result is still considered an upper bound on the asteroid-generated tsunami risk.

3.1.4 Global Effects

For large-scale impacts, the model includes estimates of the percentage of the world population that would be casualties as a result of global climatic effects from substantial impact ejecta in the atmosphere. The casualty percentage estimates are based on values given in the 2003 NEO SDT report (Stokes et al. 2003), adapted into a triangular distribution of minimum, maximum, and nominal casualty percentages as a function of impact energy, as listed in Table 3-1. For each impact case, curve fits of the minimum, nominal, and maximum values are interpolated on the basis of the impact energy and a random number sampling to determine the severity within the potential range for that energy. Figure 3-3 shows the curve fits of the minimum/nominal/maximum percentages in Table 3-1 and a sample of the resulting triangular distribution that would be sampled for an impact of 600 gigatons.

Table 3-1. Minimum, nominal, and maximum values for triangular distributions of global casualty rates by impact energy, based on Stokes et al. (2003).

Impact Energy (megatons)	Casualty Percentage		
	Minimum	Nominal	Maximum
4.E+04	0	0	0
8.E+04	0	0	10
2.E+05	0	0	20
3.E+05	0	10	30
6.E+05	0	20	40
1.E+06	10	30	50
2.E+06	20	40	60
5.E+06	30	50	70
1.E+07	40	60	80
2.E+07	50	70	90
4.E+07	60	80	100
8.E+07	70	90	100

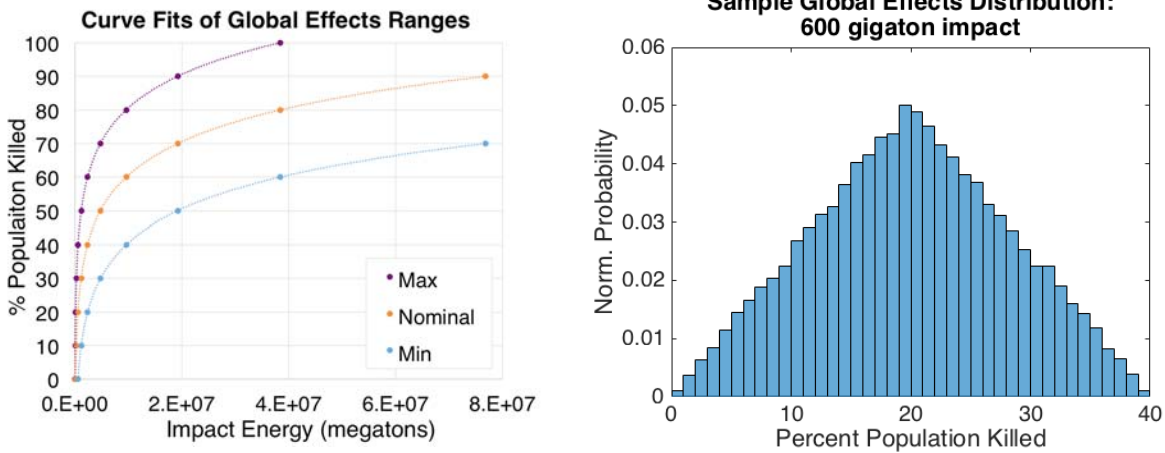


Figure 3-3. Curve fits of global effects ranges by impact energy (left) and resulting triangular distribution for a 600-gigaton impact (right).

For cases that trigger global effects, the global casualties are compared with the local/regional affected population, and the greater value is taken as the overall population damage count for that case.

3.2 Impact Analysis Results

The modeling approach described in the preceding section is applied to assess the integrated asteroid impact risk, given the current state of knowledge about physical characteristics and estimates of impact frequencies. Enough scenarios were simulated such that the average risk for each size bin converged to the value that would be obtained using an average, uniform world population density. The distributions of asteroid properties and impact parameters used to generate the probabilistic impact scenarios are presented below, followed by the damage and risk results for local ground damage, regional tsunami damage, and global effects. Quantitative risk results are produced by combining the damage results from each modeled scenario with the expected impact frequencies for a given size range. These aggregate risk results are presented using both average values and full output distributions. Lastly, the risks attributed to each damage source are combined and compared, and the potential risk reduction resulting from survey discoveries is considered.

3.2.1 Impact Parameter Inputs

An assessment of a set of nearly 60 million impact scenarios used 56 fixed-size bins (Table 3-2). Although asteroids can vary significantly in shape, the asteroid sizes for each bin represent an equivalent spherical diameter for a range of mass and density combinations. Bin sizes were chosen to cover the range of objects that pose measurable risk to humanity and that are reasonably detectable with emerging survey technology. Scenario counts for each bin were selected to provide adequate convergence (Mathias et al. 2017). Each scenario was assigned a random impact location, uniformly distributed over the Earth. Entry angles were also randomly selected between 0 and 90 degrees, with 45 degrees being the most likely entry angle. Impactor velocities were derived from the orbital model described in Section 2. Histograms of velocity and entry angle are shown in Figure 3-4.

Table 3-2. Asteroid size bins, increments between bins, and number of impact scenarios modeled in each bin.

Size Range (equivalent diameter)	Bin Diameter Increment	Scenarios per Bin
20–30 m	10 m	1M
40–70 m	10 m	5M
80–100 m	10 m	2M
110–300 m	10 m	1M
350–500 m	50 m	1M
600—1900 m	100 m	500K
2,000–10,000 m	1,000 m	50K

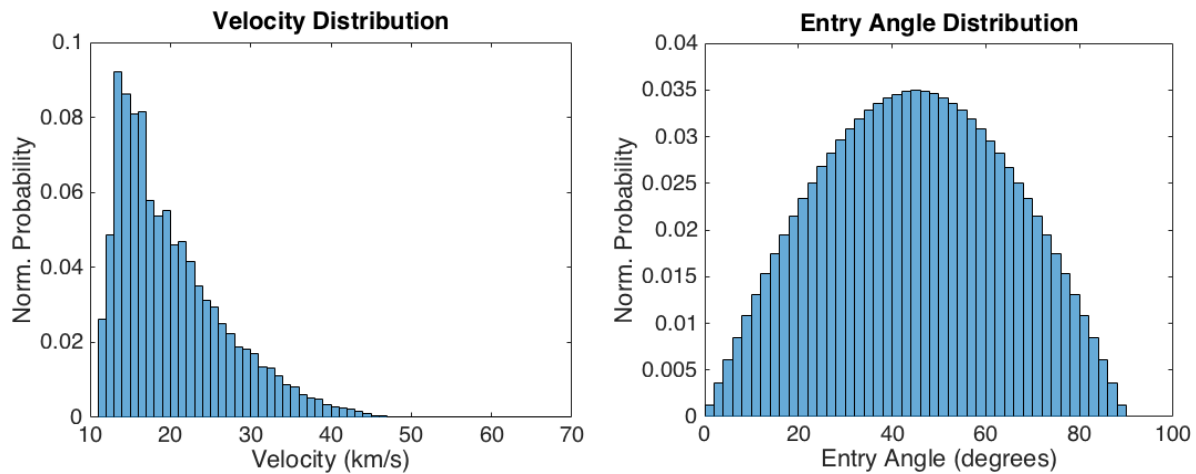


Figure 3-4. Trajectory input distributions.

All of the risk assessment was performed on the basis of the defined bin sizes, so no translation between size and H magnitude was required. However, the objects were randomly assigned an albedo sampled from the NEO Wide-field Infrared Survey Explorer (NEOWISE) distribution (Mainzer et al. 2011e). The resulting histogram of object albedo is shown in Figure 3-5. Albedo was used to correlate the objects with a composition type. Five percent were assumed to be irons, and the remaining 95% were classified by their albedo; albedo values of 0.1 and lower were assumed hydrous stones, and those with albedo values above 0.1 were anhydrous stones. This classification approach resulted in 5% irons, 35% hydrous stones, and 60% anhydrous stones.

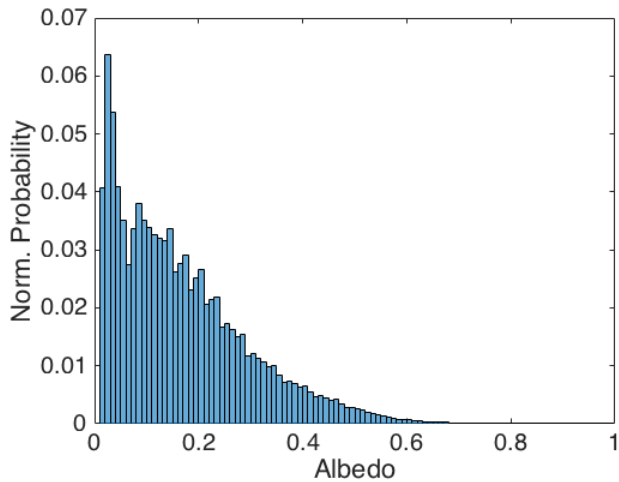


Figure 3-5. Albedo distribution (Mainzer et al. 2011e).

Each type was associated with a base density distribution, defined by using a truncated normal distribution. To obtain overall asteroid densities, the base densities were combined with porosity distributions for three different structural types: coherent, fractured, or rubble pile. All irons were assumed to be coherent, but the relative abundance of the structural types varied depending on size for the two stone compositional types; 15% of the stones were assumed to be fractured across all sizes, while the fraction of coherent objects decreased from 80% to 5% and the fraction of rubble piles conversely increased from 5% to 80% as size increased from 20 to 200 meters. Between 20 and 200 meters, the percentages were linearly interpolated based on size, and objects larger than 200 meters all maintained the same percentages. The final asteroid densities were determined by modifying the sampled base density value by a sampled porosity value corresponding to the assumed structure.

Table 3-3 gives the base density distribution parameters along with the asteroid density limits and relative abundances for each compositional type. Table 3-4 gives the porosity distributions associated with each structural type. Figure 3-6 shows the density distributions that result from applying the structural porosities within each compositional type, and Figure 3-7 shows the size-based variation of the total density distribution obtained by combining the relative abundances of all compositional and structural types.

Table 3-3. Relative abundance, base density distribution parameters, and asteroid density limits for hydrous stone, anhydrous stone, and iron compositional types.

Compositional Type	Abundance	Base Density Mean (g/cc)	Base Density Std. Dev. (g/cc)	Asteroid Density Limits (g/cc)
Hydrous stone	35%	1.9	0.58	1.1–2.5
Anhydrous stone	60%	2.9	0.54	1.4–3.2
Iron	5%	7.0	0.6	1.8–7.5

Table 3-4. Porosity distribution parameters for coherent, fractured, and rubble pile structural types.

Structural Type	Abundance within Compositional Type	Mean	Std. Dev.	Min	Max
Coherent irons	100%	5%	2%	0%	10%
Coherent stones	80–5% (20–200+ m)	5%	2%	0%	50%
Fractured stones	15%	22%	5%	0%	50%
Rubble stones	5–80% (20–200+ m)	40%	5%	0%	50%

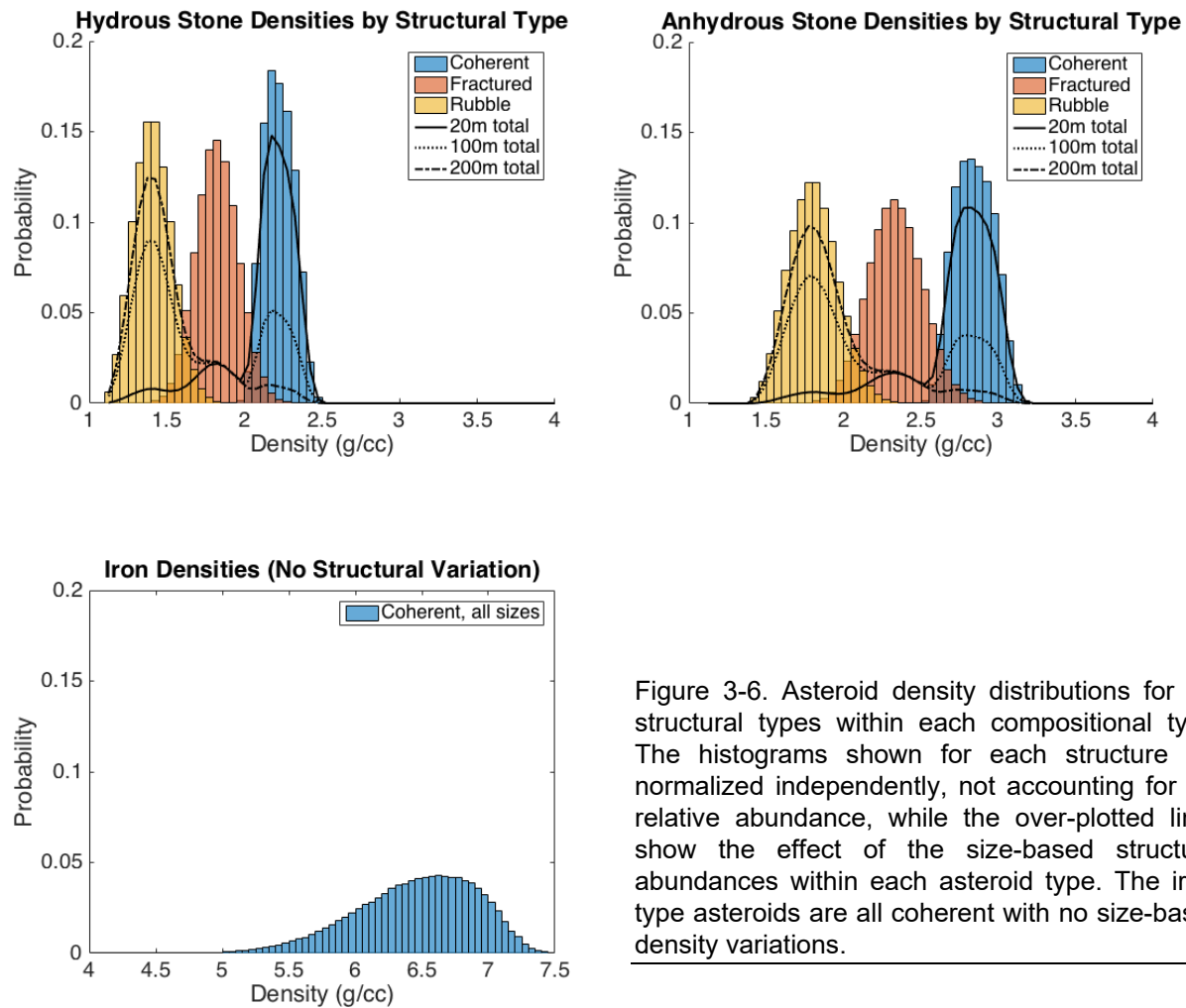


Figure 3-6. Asteroid density distributions for the structural types within each compositional type. The histograms shown for each structure are normalized independently, not accounting for the relative abundance, while the over-plotted lines show the effect of the size-based structural abundances within each asteroid type. The iron-type asteroids are all coherent with no size-based density variations.

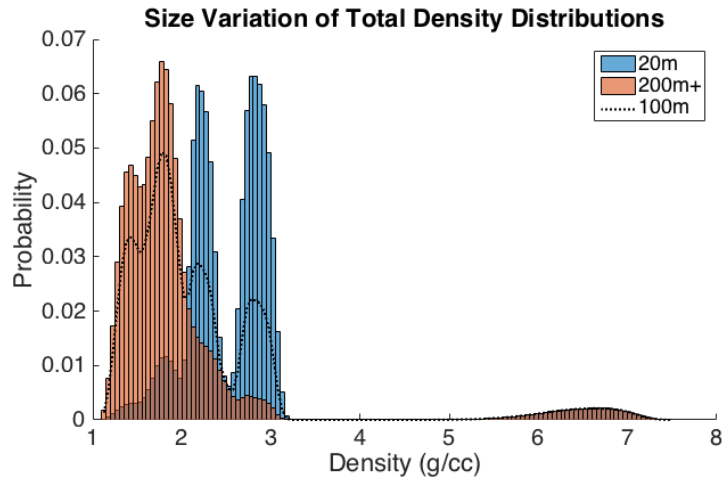


Figure 3-7. Density distributions combining all compositional types and structural types for asteroid sizes of 20 m and 200 m or greater. Objects between 20 m and 200 m have intermediate distributions, as shown by the dashed line for 100 m objects.

Strength modeling inputs consist of two parts—an initial breakup, or aerodynamic, strength and an exponent controlling the gain in strength with decreasing fragment size. Stone asteroids were assumed to all possess a logarithmically distributed initial aerodynamic strength between 0.1 and 2.0 MPa (Popova et al. 2011). Strength gain exponents were 0.1 for hydrous and 0.2 for anhydrous stones. It was assumed that iron asteroids were of high strength and would never fragment during entry.

3.2.2 Local Damage Results

Local damage is determined by assessing blast overpressure and thermal radiation levels. For local blast damage, affected populations are counted within areas exposed to overpressure ranges of 1–2 psi, 2–4 psi, 4–10 psi, and 10+ psi. Figure 3-8 contains the expected value of affected population, as a function of impactor size for each overpressure range. The results are shown as cumulative by size, representing the average damage from asteroids up to the given size threshold or smaller, weighted by the annual impact probability corresponding to each size range. The 4-psi threshold is used to compute casualties and graduated overpressure results are used as the local damage metric for the cost/benefit monetization presented in Section 8.

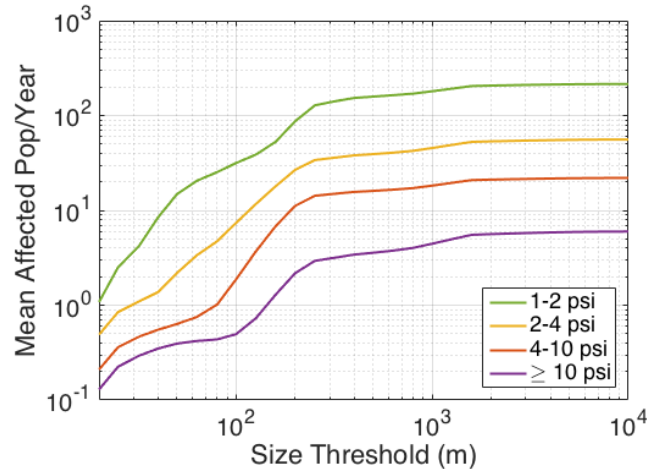


Figure 3-8. Cumulative expected value curves for average affected populations within different blast overpressure damage zones, based on impact frequencies from the total estimated PHO population. The results are cumulative by size, giving the mean casualties per year expected from objects of each given size threshold or smaller.

Alternately, the local casualties are determined for each scenario by comparing the 4-psi blast overpressure and third-degree-burn thermal radiation areas, and using the population within the larger area as the casualty estimate for each impact case. Figure 3-9 shows the minimum, mean, and maximum local casualty simulation results as a function of object size. Because most impacts occur over uninhabited regions and/or deposit their energy high in the atmosphere, the majority of cases result in little-to-no local casualties. As a result, the mean local impact risk is dominated by a small number of high-consequence events. This is reflected in Figure 3-9 as the mean impact values tend to be close to the minimum values. The variations in the maximum curve are a consequence of the Monte Carlo sampling of the inputs for each scenario. These maximum values are the maximums obtained from the simulated scenarios, not the absolute worst-case scenario possible, and should be treated as a reasonable upper bound. Averaging the results eliminates the fluctuations in the mean curve, and the minimum curve is bounded by zero, thus also eliminating fluctuations.

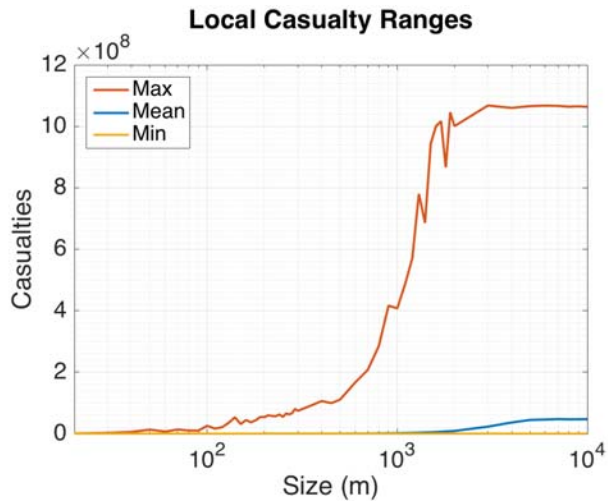


Figure 3-9. Range of local damage potential as a function of impactor size. The curves show the minimum, mean, and maximum local casualty estimates from blast overpressure or thermal radiation for each size bin.

A more complete picture of the local impact risk (blast and thermal) is shown in Figure 3-10. The horizontal axis represents the number of affected population and the vertical axis the size of the impactor. The field is colored by the probability per year that the number of people on the horizontal axis, or greater, will be affected by an object of the given size or smaller. Solid black lines show the probability contours at each order of magnitude from $1:10^3$ to $1:10^8$, with the bold line showing the $1:10^6$ contour.

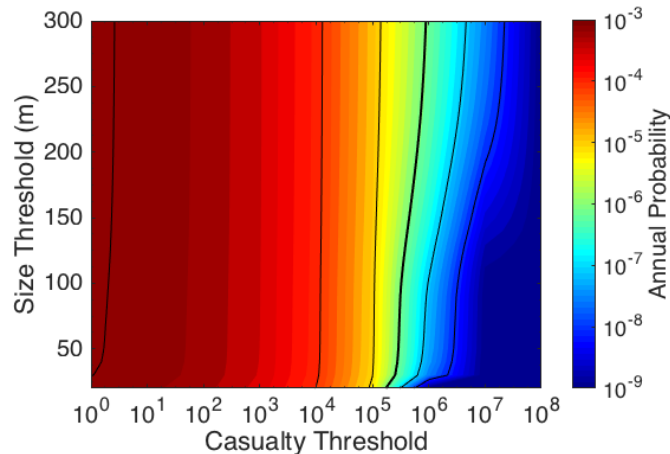


Figure 3-10. Local damage risk contour plot with black contour lines at each order of magnitude and the bold line showing the 10^{-6} probability per year contour.

Comparing Figure 3-8 with Figure 3-10 highlights the difference between an average expected value and the range of possible outcomes for a low-likelihood, high-consequence event, such as an asteroid impact. In such cases, the expected values are meaningful over a very long time and many impact epochs. The contour plots provide a probabilistic estimate on how likely the ranges of possible outcomes are.

3.2.3 Tsunami Damage Results

Every impact scenario is checked for local damage, but many impacts occur over the ocean away from populated areas. The risk of such events is represented with the asteroid-generated tsunami model described previously. Figure 3-11 shows a plot of the cumulative average population inundated and average casualties resulting from an impact-generated tsunami. On average, tsunami risk is lower than local damage risk, totaling approximately 3 people per year in expected casualties and approximately 40 people per year in inundated affected population. For reference, the blast-damage affected population (assuming 1–2 psi threshold) and expected casualties (assuming 4–10 psi) are nearly an order of magnitude higher. At the small size ranges, most of the objects airburst rather than impact the surface, and such bursts were shown to cause blast damage, as presented in Section 3.2.2. However, the airburst coupling to the water appears to be very inefficient and does not, in general, lead to significant waves. On the large end of the size range, where objects are likely to impact the ground with significant energy, global effects dominate the loss, as will be shown in the next section.

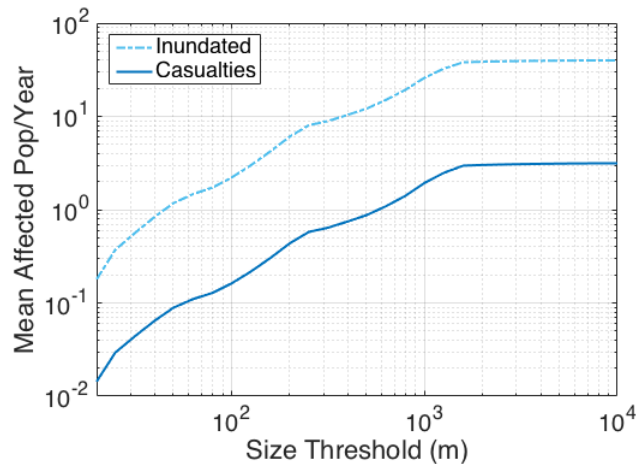


Figure 3-11. Cumulative expected tsunami damage averages for inundated population and casualties. The results are cumulative by size, giving the mean casualties per year expected from objects of each given size threshold or smaller.

The average tsunami casualty estimates should not be interpreted to mean that asteroid-generated tsunamis do not pose a risk; they certainly do, but they contribute little to the average ensemble risk relative to the other damage sources. Figure 3-12 shows the minimum, mean, and maximum casualty estimates as a function of object size. Although most ocean impact cases do not produce damaging tsunami waves, in the worst cases losses can exceed one million people, according to the current model. Figure 3-13 shows the damage exceedance risk contour plot for tsunami-only damage.

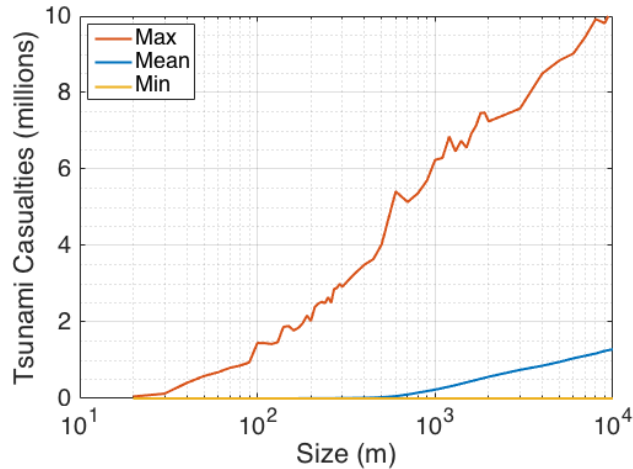


Figure 3-12. Range of tsunami damage potential as a function of impactor size. The curves show the minimum, mean, and maximum casualty estimates from the tsunami model for each size bin.

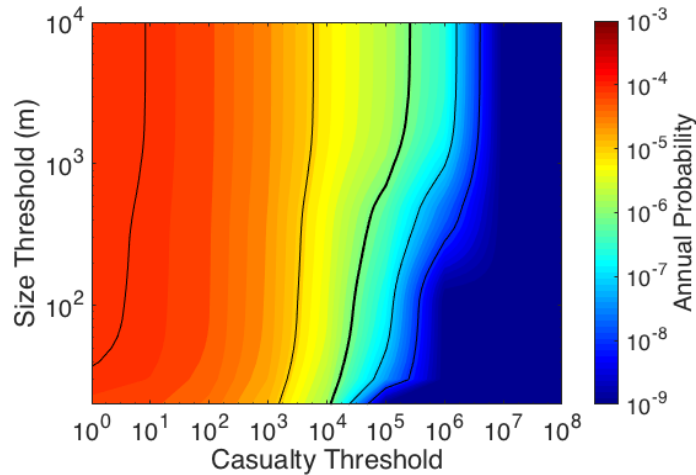


Figure 3-13. Tsunami damage risk contour plot with black contour lines at each order of magnitude and the bold line showing the 10⁻⁶ probability per year contour.

3.2.4 Global Effects Results

Impacts with energies greater than 40 gigatons have the potential to trigger the global effects model, which samples global casualty percentages as described in Section 3.1.4. With the current velocity and density distributions, the smallest asteroid size to cause any global effects was 280 meters, though only for the edge case with the highest possible velocity and density. More notable global effects begin to ramp up for sizes over 600 meters, with 50% of 1000-meter asteroids, and 100% of asteroids over 1600 meters causing global effects.

Figure 3-14 shows the range of global effects casualties for impacts within each size bin. Sizes larger than 4000 meters are capable of affecting the entire Earth's population, while sizes up to 3000 meters maintain the potential to cause no global effects. Although the potential damage for these large impacts is very high, the expected impact frequency is also very low. The high-consequence but low-probability nature of global effects is shown in Figure 3-15. This plot illustrates how global effects phase in relatively steeply with size and have large associated consequences across most of the applicable range. The plot scales are kept constant across Figures 3-10, 3-13, and 3-15 to highlight the relatively infrequent occurrence of such impacts.

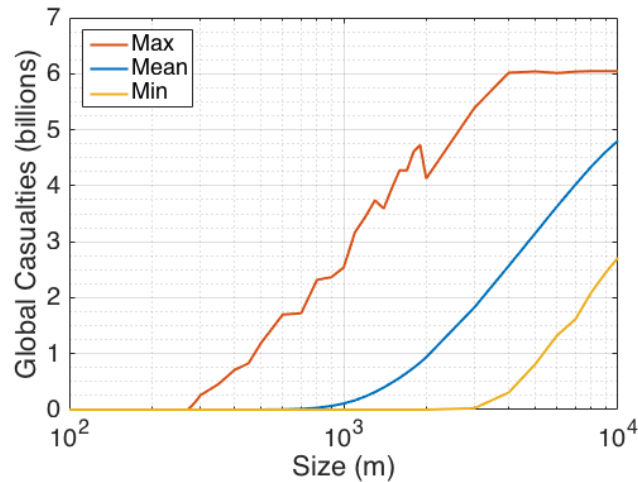


Figure 3-14. Range of global damage potential as a function of impactor size. The curves show the minimum, mean, and maximum casualty estimates from the global effects model for each size bin.

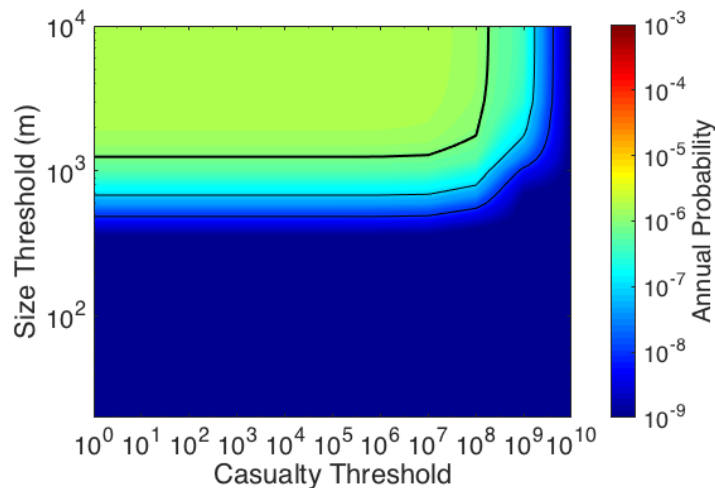


Figure 3-15. Global damage risk contour plot with black contour lines at each order of magnitude and the bold line showing the 10⁻⁶ probability per year contour. Color scales are held constant with previous plots for comparison.

3.2.5 Combined Risk from All Hazards

Figure 3-16 shows the total risk contour plot for the combined damage from all hazards. For each individual impact scenario modeled, the total casualty value is taken as the casualties from the greatest of each hazard source (local blast/thermal, tsunami, or global effects). The total casualty values are not the sum of each hazard source, as that would introduce likely double-counting of casualties within an area. Figure 3-17 shows the complementary cumulative distribution of the total combined risk from all objects up to 10 kilometers in size. This curve represents the total probability per year of an object up to 10 kilometers in size striking earth and causing at least the given casualty thresholds or greater. The plot is equivalent to a horizontal cross section of the probabilities at the largest size threshold in the Figure 3-16 contour plot. Figure 3-18 shows the cumulative, average expected casualties per year from each hazard source, along with the total combined expected casualties. On average, local damage affects more population than tsunami across the entire size range, and global effects begin to affect more population at sizes above 700 meters. Global effects begin to drive the risk at lower sizes than reported in the 2003 NEO SDT report (Stokes et al. 2003) because the range of densities and velocities included in this assessment introduces a small percentage of high-energy objects as compared to the mean impactor parameters used in the 2003 study. This finding is not surprising because the expected values are dominated by a small number of highly catastrophic events. By sizes of 1000 meters, the globally affected population exceeds the local and regionally affected population by an order of magnitude. If objects up to 10,000 meters in size are considered, the expected value of affected population is approximately 2500 per year when the entire potentially hazardous object (PHO) population is considered.

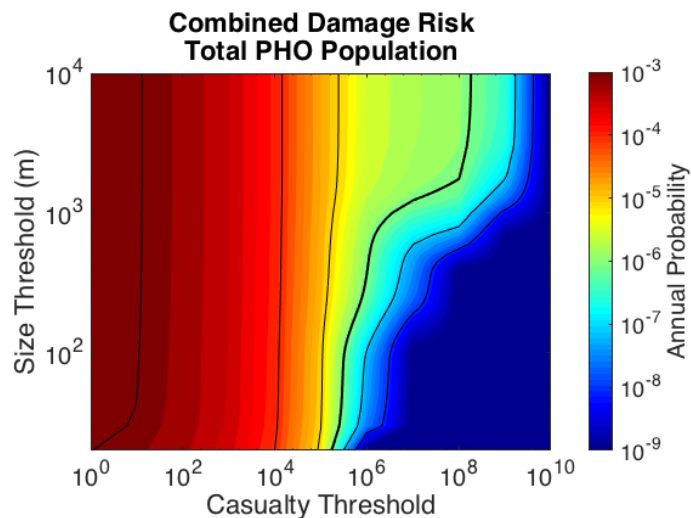


Figure 3-16. Total damage risk contour plot with black contour lines at each order of magnitude and the bold line showing the 10^{-6} probability per year contour. The total damage represents the casualties from the greatest hazard for each individual impact scenario.

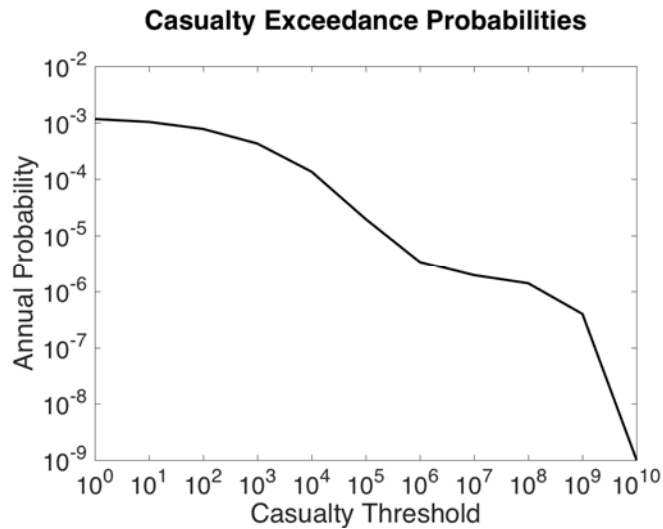


Figure 3-17. Complementary cumulative distribution of the total combined risk from all objects up to 10 km in size. The curve represents the annual probability of an impact causing at least the given casualty threshold on the horizontal axis.

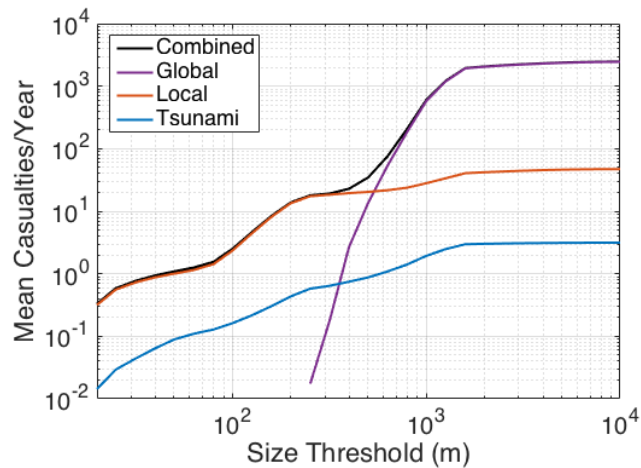


Figure 3-18. Cumulative expected casualties as a function of impactor size for local (blast and thermal), regional (tsunami), and global risks. The combined values represent the greatest of the three damage sources for each impact case. The results are cumulative by size, giving the mean casualties per year expected from objects of each given size threshold or smaller. By sizes of 1000 m, global effects exceed other damage sources by approximately 10 times.

Table 3-5 gives the average expected casualties per year from each type of risk, broken into the *H*-magnitude-based size bins used in the PHO population estimates presented in Section 2, “Population Estimates,” and the risks discussed in Section 8, “Cost/Benefit Conclusions.” The tabulated values give the expected casualties from PHO impacts for each individual size bin, rather than the cumulative values shown in Figure 3-18. To map the simulation cases from Table 3-2 to the bins in Table 3-5, the full set of scenarios was used to create a cumulative casualty distribution as a function of impactor size. The change in the cumulative distribution across each bin in Table 3-5 was used to calculate an average impact consequence for the bin (not the same as the consequence corresponding to the bin-center sized objects). The total number of PHOs in each bin was used to create the impact frequency for the bin and was multiplied with the average impact consequence to yield the values in Table 3-5.

Table 3-5. Average expected casualties from local, tsunami, and global damage by asteroid size. Note: These values are the average casualties per year expected from potentially hazardous object (PHO) impacts within the size range of each individual bin.

<i>H</i>-Magnitude (Bin Center)	Min Size (m)	Max Size (m)	Local Casualties (average per year)	Tsunami Casualties (average per year)	Global Casualties (average per year)
26	20	25	3.17E-01	1.43E-02	0.00E+00
25.5	25	32	2.40E-01	1.50E-02	0.00E+00
25	32	40	1.78E-01	1.56E-02	0.00E+00
24.5	40	50	1.41E-01	1.95E-02	0.00E+00
24	50	63	1.25E-01	2.44E-02	0.00E+00
23.5	63	80	1.42E-01	2.08E-02	0.00E+00
23	80	100	2.83E-01	1.89E-02	0.00E+00
22.5	100	126	9.17E-01	3.32E-02	0.00E+00
22	126	159	2.07E+00	5.50E-02	0.00E+00
21.5	159	200	3.71E+00	8.63E-02	0.00E+00
21	200	252	5.30E+00	1.31E-01	0.00E+00
20.5	252	317	3.94E+00	1.44E-01	1.75E-02
20	317	399	9.83E-01	6.27E-02	1.59E-01
19.5	399	502	1.13E+00	1.05E-01	2.48E+00
19	502	632	9.03E-01	1.29E-01	1.11E+01
18.5	632	796	1.30E+00	2.14E-01	4.01E+01
18	796	1000	2.08E+00	3.17E-01	1.31E+02
17.5	1000	1259	4.24E+00	5.25E-01	3.93E+02
17	1259	1589	5.65E+00	5.47E-01	6.14E+02
16.5	1589	2000	6.85E+00	4.86E-01	7.33E+02
16	2000	2518	1.47E+00	4.82E-02	1.18E+02
15.5	2518	3170	1.25E+00	3.69E-02	9.63E+01
15	3170	3991	1.19E+00	2.80E-02	8.40E+01
14.5	3991	5018	9.90E-01	2.12E-02	7.00E+01

H-Magnitude (Bin Center)	Min Size (m)	Max Size (m)	Local Casualties (average per year)	Tsunami Casualties (average per year)	Global Casualties (average per year)
14	5018	6321	7.99E-01	1.84E-02	6.45E+01
13.5	6321	7955	5.08E-01	1.25E-02	4.57E+01
13	7955	10000	3.19E-01	8.57E-03	3.19E+01
Total			47	3	2435

Figure 3-19 shows the total annual expected casualties for the size bins in Table 3-5, with the differential results for each individual bin on the left and the cumulative expected casualty curve on the right. The solid points show the mean values, and the vertical bars illustrate the associated 1-sigma variation. The bars that extend to the bottom of the plots show where the no-casualty outcome falls within one standard deviation from the mean. The local peaks in the differential curve help illustrate the relative risk posed by impactors across the size range modeled. Individual impacts of 20-meter objects, for example, do not contribute to tsunami or global effect risks and at worst create very localized damage. In fact, the majority of 20-meter objects deposit their energy high enough in the atmosphere that no ground damage occurs, and only the small percentage of irons contribute measurably to the risk. While the damage is localized, impactors of this size are relatively frequent compared to the larger impactors. The risk decreases as the objects get larger, up to around 50–60 meters, because the impact frequency decreases with size faster than the local damage region increases. At around 50–60 meters, the more common stony objects begin to penetrate deeply enough into the atmosphere to cause ground damage when they airburst. At around 150–200 meters, the decreasing impact frequency outpaces the increase in ground damage, so the bin-wise risk falls off until the onset of global effects. The same trend is seen above approximately 2 kilometers, where global effects have the potential to affect large fractions of world population, limiting the upper end of the damage potential, but the impact probability becomes low. The peaks in the differential plot correspond to the steep-sloped regions of the cumulative plot. Relative variation in casualties decreases with impactor size because the impact location is the largest contributor to the uncertainty. As damage areas increase with object size, the specific impact locations become less important. This correlation is highlighted by the sharp decrease in uncertainty with the onset of global effects; in these cases, the impact consequences are assumed independent of the local population distribution.

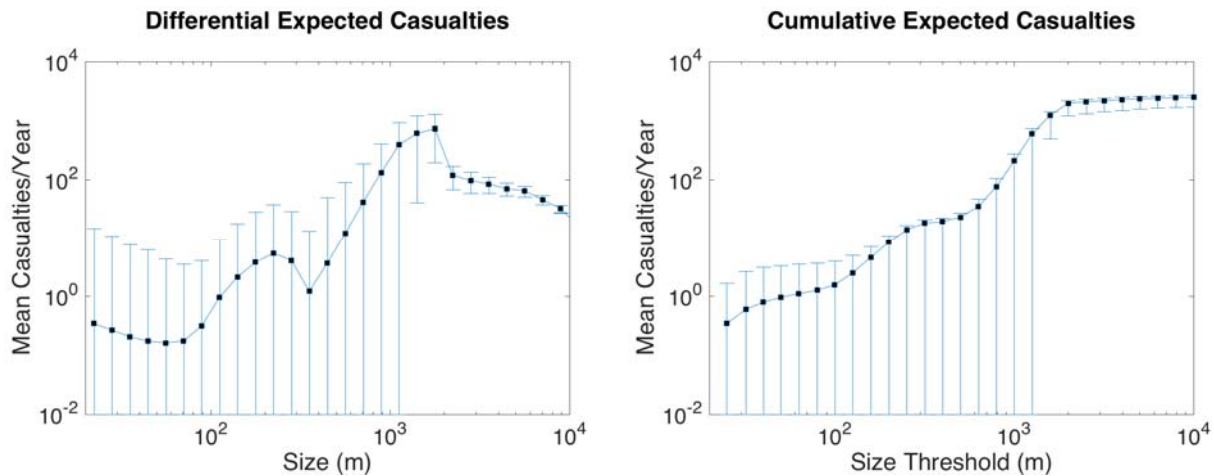


Figure 3-19. Expected casualty estimates presented for the size bins from Table 3-5. The left plot shows the differential results for each individual size bin, and the right plot shows the cumulative results for sizes up to the size threshold. The solid points represent the mean total expected casualty values, and the vertical bars show the one standard deviation uncertainty range.

3.2.6 Potential Risk Uncertainty Reduction Resulting from Surveys

The results so far have been based on the entire estimated PHO population. Two subsets of the population are considered for comparison. The first considers objects remaining undiscovered as of January 2023—the point at which alternate search options are assumed to become viable—assuming current survey discovery rates. The second subset consists of the PHOs that remain undiscovered at the point where surveys reduce the sub-global risk uncertainty by 90%. The implicit assumption is that the objects discovered by the surveys contribute negligible risk. A complete discussion of the survey systems, strategies, and results is presented in the subsequent sections of the report.

Figure 3-20 shows the mean expected casualty curves by hazard source for the projected 2023 and 90% survey completion sets. Figure 3-21 contains the combined expected casualty results with standard deviations for both survey completion sets. The general trends are similar to the total PHO results for the small to mid-sized impactors, but the low number of undiscovered objects at the larger sizes reduces the risk significantly. The total combined risk drops by more than an order of magnitude for the assumed 2023 undiscovered population, and the 90% survey completion decreases the risk by another 60%. The high percentage of large objects detected also reduces the uncertainty associated with the risk, but there is little effect at the smaller sizes where most objects remain undetected.

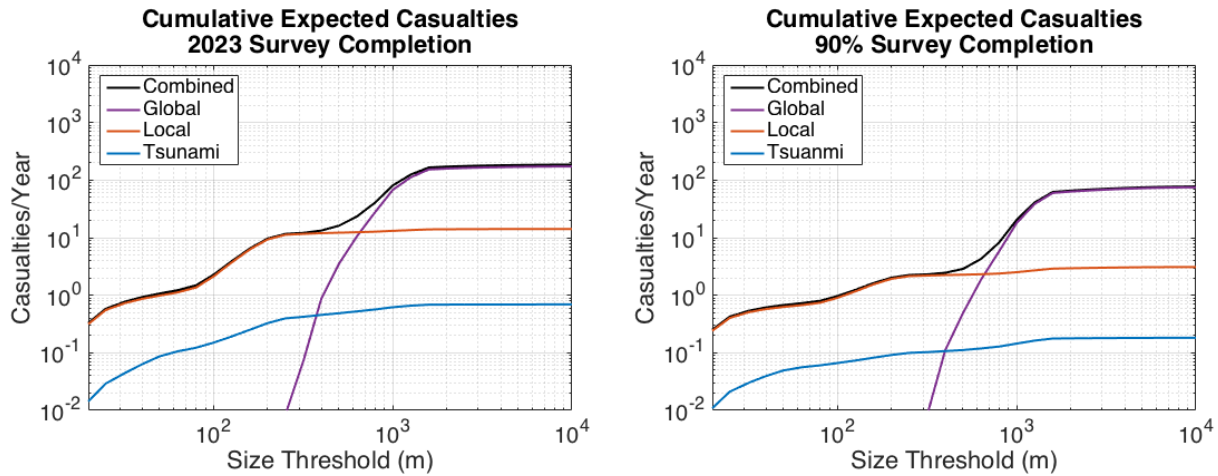


Figure 3-20. Expected casualty estimates for the remaining undiscovered PHO population for the two survey subsets: the projected survey completeness assuming current survey progress until 2023 (left) and the 90% completeness (right).

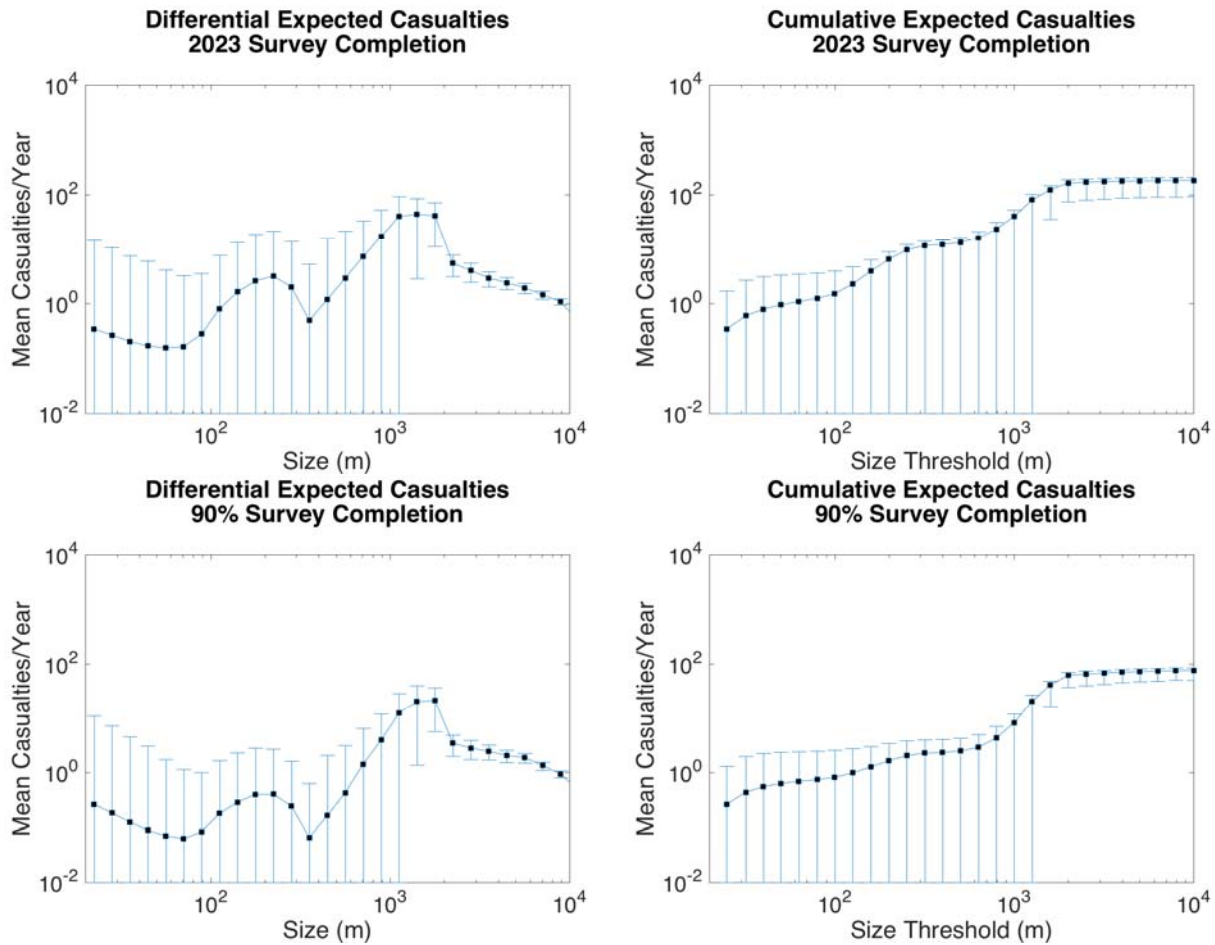


Figure 3-21. Total expected casualties for the 2023 survey completion (top) and 90% survey completion (bottom) projections. The left plots show the differential results for each individual size bin, and the right plots show the cumulative results for sizes up to the size threshold. The solid points represent the mean total expected casualty values and the vertical bars show the $1-\sigma$ standard deviation uncertainty range.

Figure 3-22 shows a comparison of the risk contours for the 2023 and 90% survey completion results. As before, the solid black lines show the probability contours at each order of magnitude, with the bold line showing the 1:10⁶ probability contour. Though the average expected casualties dropped by a factor of ~10 when discounting objects assumed to be discovered by 2023, when a more severe outcome is considered, the damage level at a 1:10⁶ probability decreases by more than a factor of 100.

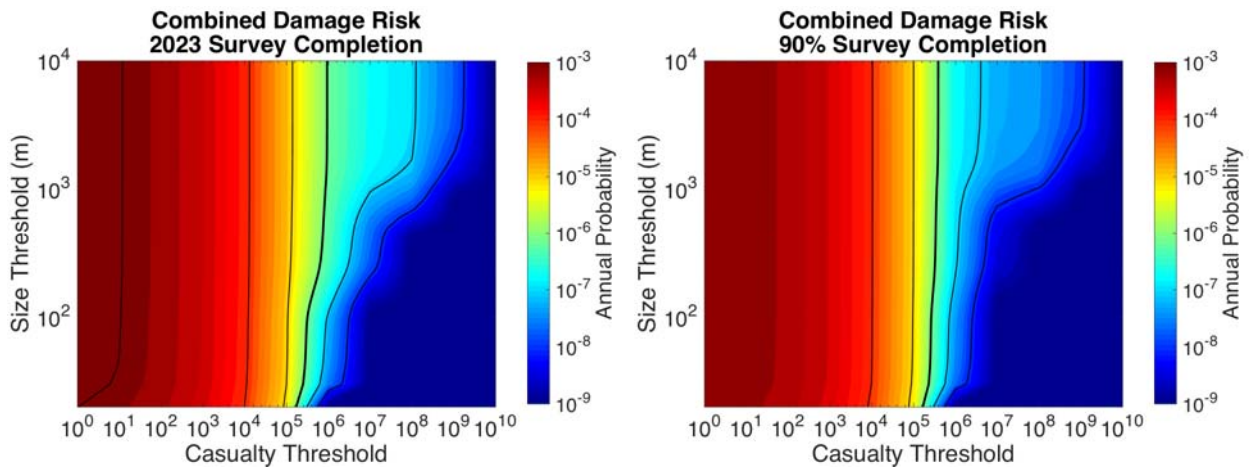


Figure 3-22. Comparison of risk contour plots for the 2023 and 90% survey completion estimates. Black contour lines are shown at each order of magnitude, with the bold line showing the 10⁻⁶ probability contour.

Figure 3-23 compares the complementary cumulative distributions of the combined risk from all objects up to 10 kilometers in size for the total PHO population as well as the 2023 and 90% survey subsets. These curves highlight the survey benefit clearly in terms of reducing the uncertainty associated with high-consequence events—a benefit not fully conveyed by comparing long-term averages. All three curves show approximately the same likelihood per year of an impact resulting in 10,000 casualties or more. However, when considering events with 1 million or more casualties, the differences span two orders of magnitude. The average casualty values do provide a meaningful way to compare the cost/benefit relationships of survey options, but additional survey benefits lie in the even larger reduction of the highest consequence events.

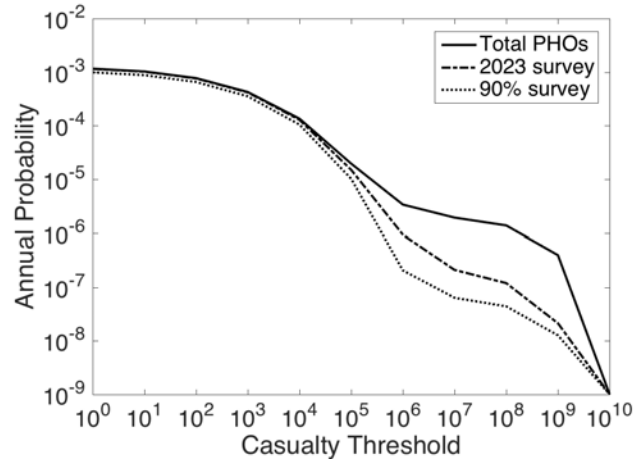


Figure 3-23. Casualty exceedance probability comparisons for the total PHO population and the assumed reduction in risk uncertainty for the 2023 survey projections and at the point at which surveys achieve 90% reduction.

Appendix 3-A. Raw Results of Mapping to the Size Bins Used in the SDT Report.

The impact risk results in Section 3 are presented using a set of size bins established for consistency within the current report and enable straightforward comparison with the 2003 SDT Report. As shown in Table 3-2, the impact risk simulations were performed by using a set of fixed-sized impactors chosen to resolve the risk estimates. Section 3.2.5 explains how the raw results were mapped to the size bins used in the report. However, the mapping process requires assumptions that affect the results. While these mapping assumptions do not alter the report’s findings, the raw results are presented in Table 3-A-1 to allow readers access to the underlying results.

Table 3-A-1. Average casualties from each damage source for the asteroid sizes modeled in the impact risk assessment simulations. Note: The total casualties represent the casualties from the worst hazard from each impact case (not the sum of all hazards).

Diameter (m)	Mean Local Casualties	Mean Tsunami Casualties	Mean Global Casualties	Mean Total Casualties
20	6.96E+01	1.11E+00	0.00E+00	7.08E+01
30	1.40E+02	6.35E+00	0.00E+00	1.47E+02
40	2.49E+02	2.17E+01	0.00E+00	2.71E+02
50	3.54E+02	4.89E+01	0.00E+00	4.03E+02
60	4.70E+02	9.12E+01	0.00E+00	5.62E+02
70	7.75E+02	1.52E+02	0.00E+00	9.27E+02
80	1.74E+03	2.26E+02	0.00E+00	1.96E+03
90	3.92E+03	3.34E+02	0.00E+00	4.25E+03
100	7.88E+03	4.54E+02	0.00E+00	8.33E+03
110	1.38E+04	5.97E+02	0.00E+00	1.44E+04
120	2.14E+04	7.70E+02	0.00E+00	2.22E+04
130	3.05E+04	9.50E+02	0.00E+00	3.14E+04
140	4.24E+04	1.17E+03	0.00E+00	4.36E+04
150	5.42E+04	1.45E+03	0.00E+00	5.57E+04
160	6.73E+04	1.67E+03	0.00E+00	6.90E+04
170	8.15E+04	1.96E+03	0.00E+00	8.35E+04
180	9.84E+04	2.32E+03	0.00E+00	1.01E+05
190	1.16E+05	2.71E+03	0.00E+00	1.18E+05
200	1.33E+05	2.99E+03	0.00E+00	1.36E+05
210	1.51E+05	3.37E+03	0.00E+00	1.55E+05
220	1.66E+05	3.76E+03	0.00E+00	1.70E+05
230	1.78E+05	4.20E+03	0.00E+00	1.82E+05
240	1.80E+05	4.57E+03	0.00E+00	1.85E+05

Diameter (m)	Mean Local Casualties	Mean Tsunami Casualties	Mean Global Casualties	Mean Total Casualties
250	1.84E+05	5.13E+03	0.00E+00	1.89E+05
260	1.87E+05	5.64E+03	0.00E+00	1.92E+05
270	1.83E+05	5.95E+03	0.00E+00	1.89E+05
280	1.83E+05	6.25E+03	1.13E+02	1.90E+05
290	1.85E+05	6.71E+03	4.92E+02	1.92E+05
300	1.88E+05	7.73E+03	1.48E+03	1.97E+05
350	1.94E+05	1.06E+04	6.32E+03	2.11E+05
400	2.11E+05	1.47E+04	5.10E+04	2.75E+05
450	2.46E+05	2.06E+04	2.73E+05	5.34E+05
500	2.96E+05	2.97E+04	8.71E+05	1.18E+06
600	4.41E+05	5.92E+04	3.79E+06	4.23E+06
700	6.45E+05	1.03E+05	1.28E+07	1.34E+07
800	9.04E+05	1.50E+05	3.28E+07	3.35E+07
900	1.21E+06	1.92E+05	6.56E+07	6.63E+07
1000	1.58E+06	2.31E+05	1.10E+08	1.11E+08
1100	2.00E+06	2.71E+05	1.67E+08	1.68E+08
1200	2.54E+06	3.10E+05	2.36E+08	2.36E+08
1300	3.05E+06	3.47E+05	3.13E+08	3.14E+08
1400	3.72E+06	3.85E+05	3.97E+08	3.97E+08
1500	4.40E+06	4.20E+05	4.83E+08	4.83E+08
1600	5.16E+06	4.54E+05	5.69E+08	5.69E+08
1700	6.00E+06	4.83E+05	6.58E+08	6.59E+08
1800	6.92E+06	5.15E+05	7.50E+08	7.50E+08
1900	7.98E+06	5.38E+05	8.40E+08	8.40E+08
2000	8.87E+06	5.67E+05	9.36E+08	9.36E+08
3000	2.28E+07	7.48E+05	1.83E+09	1.83E+09
4000	3.63E+07	8.55E+05	2.57E+09	2.57E+09
5000	4.47E+07	9.55E+05	3.15E+09	3.15E+09
6000	4.58E+07	1.05E+06	3.63E+09	3.63E+09
7000	4.72E+07	1.12E+06	4.02E+09	4.02E+09
8000	4.66E+07	1.17E+06	4.34E+09	4.34E+09
9000	4.68E+07	1.24E+06	4.60E+09	4.60E+09
10000	4.72E+07	1.29E+06	4.80E+09	4.80E+09

This page is intentionally blank.

4 CANDIDATE TECHNOLOGIES AND SYSTEMS

To estimate the performance achievable by a near-Earth object (NEO) survey system based on current technology, the Science Definition Team (SDT) chose to implement a detailed survey simulation. The simulation, described in detail in Section 6, takes as input the estimates of the NEO population of interest (i.e., size, orbital parameters, albedo, etc.) and “observes” this population over a years-long simulation time with a variety of search systems. A critical input to this simulation is the set of characteristics of the search systems. This section describes the methodology behind the selection of potential systems and estimates each system’s performance.

The primary objectives of the systems are (1) the detection of previously unknown potentially hazardous objects (PHOs) and (2) the acquisition of a sufficient number of accurate astrometric measurements of each PHO to enable timely PHO orbit estimation and eventual cataloging of the PHOs. Key goals of PHO cataloging are to ascertain whether the PHOs have significant probabilities of future Earth impact and to do this far in advance of the potential Earth impact date(s). The SDT also assesses the abilities of the systems to provide warning of previously uncataloged PHOs that are on an impact trajectory but not detected until their final solar orbit before Earth impact. Warning performance is assessed separately from cataloging performance.

The systems and technologies chosen for evaluation include the following:

1. Ground-based, visible-band search telescopes. Existing versions of such systems have provided the vast majority of discoveries and observations to date.
2. Space-based visible-band search telescopes, which have potential advantages with respect to search duty cycle and timely access to a larger portion of the sky ($\sim 3\pi$ solid angle) than is achievable from the ground. In addition, the seeing and background noise are favorable because of the lack of an atmosphere. These advantages, however, typically come at the expense of higher costs associated with fabricating, launching, and operating space systems.
3. Space-based infrared (IR) search telescopes. These systems have the advantages associated with space-based visible-band systems, as well as additional detection sensitivity advantages. Furthermore, the background clutter (i.e., stars) is much less in the far IR band, yielding advantages in the PHO detection process. However, the advantages of observing in the IR are accompanied by the increased system complexity associated with cooling the telescope and focal plane. Moreover, the maturity of IR focal plane array technology lags behind that of visible focal planes. Infrared detection (for cataloging or warning purposes) from ground-based systems is not considered feasible because of the interference of the atmosphere (the high background at thermal IR wavelengths limits the sensitivity).

Other technologies, especially active methods such as radars or lidars, were considered by the SDT to be unsuitable because of the relatively small search volume these methods can achieve compared to the volume achievable by passive optical search techniques.

To map the cost/benefit potential of each system and technology, the SDT defined realizable search systems that span the current range of capabilities. These are described herein.

4.1 Ground-Based Systems

4.1.1 Current and Recent Ground-Based Systems

Ground-based, visual-light survey telescopes have continued to improve since the publication of the Near-Earth Object Science Definition Team’s 2003 “Study to Determine the Feasibility of Extending the Search for Near-Earth Objects to Smaller Limiting Diameters” (hereafter NEO SDT report)¹. In this subsection, we highlight the top five NEO discovery surveys (Table 4-1) in terms of the number of NEOs “discovered”² since 2003 (Jedicke et al. 2015) and briefly discuss the winning technologies or subsystems that contributed to their success.

Table 4-1. Top five NEO surveys, 2003–2014.

Note: These five surveys contributed about 85% of all NEO discoveries from 2003 through 2014 and are presented in order of decreasing number of discoveries.

Survey	Location	Operations	Aperture
Catalina Sky Survey (CSS)	Arizona	2005–present	1.5 m
Catalina Sky Survey (CSS)	Arizona	1998–present	0.68 m
LINEAR	New Mexico	1997–2010	1.0 m
Pan-STARRS 1 (PS1)	Hawaii	2010–present	1.8 m
Spacewatch	Arizona	1985–present	0.9 m

4.1.1.1 Catalina Sky Survey (CSS, observatory codes G96 and 703)

Survey characteristics: Two-telescope complementarity, dedicated NEO surveying, standardized software, regular incremental improvements.

The two Catalina Sky Survey (CSS) telescopes (Larson et al. 1998), working in tandem for the past two decades, top the NEO discovery list for the time period since the last NEO SDT report (Jedicke et al. 2015). Their success can be credited primarily to their singular focus on NEO discovery and their dedicated, long-term, experienced crew and management. Implementing the same software and hardware wherever possible at all CSS sites simplified operations (a third site in Australia was decommissioned because the strength of the Australian currency made it more expensive to fund the system with U.S. dollars). The utilization of common software and hardware allows the CSS operations crews to assist each other and operate any of the system’s telescopes. The combination of the 1.5-meter aperture, moderate field-of-view (FOV) G96 site, and the 0.68-meter-diameter, 8.2-

¹ Up-to-date detailed statistics on NEO survey performance (current and historical) are available at <https://cneos.jpl.nasa.gov/stats/> (last accessed on 5 April 2017).

² A discovery is defined as an object observed over >1 night by more than one observatory code. Not all objects that are discovered have orbits known well enough to allow for targeted recovery in subsequent apparitions.

square-degree FOV 703 site Schmidt telescope allowed the CSS team to search most of the night sky each lunation and include a deeper ecliptic search.

4.1.1.2 *Lincoln Near-Earth Asteroid Research (LINEAR, observatory code 704)*

Survey characteristics: Fast pointing and settling telescope, fast full-frame readout charge-coupled devices (CCDs), moderate FOV.

The LINEAR system (Stokes et al. 2000) had access to a U.S. Department of Defense satellite tracking telescope with rapid point and settle time, and fast full-frame readout of their large-format (at the time) CCDs. The survey was in routine operations for about 15 years, from March 1998 through May 2013, and was the dominant NEO discovery system every year from 1997 through 2004. By the time LINEAR ceased operations, its technological superiority over other systems enabled it to achieve the status of the top asteroid discovery telescope and the third most prolific NEO discovery telescope of all time. LINEAR discovered more than a third of all the 1-kilometer-diameter or larger NEOs. The LINEAR team is now focusing on operations of the 3.5-meter-diameter Space Surveillance Telescope (SST) (see Section 4.1.2).

4.1.1.3 *Panoramic Survey Telescope and Rapid Response System 1 (PS1, observatory code F51)*

Survey characteristics: Large aperture, large FOV, excellent location, gigapixel camera, fast readout.

The Panoramic Survey Telescope and Rapid Response System 1 (Pan-STARRS-1 or PS1) has been the top NEO discovery telescope in the world for a few years because of its recent near-dedication to the NEO surveying effort (Kaiser et al. 2002; Denneau et al. 2013). It is also currently the largest-aperture NEO survey telescope and the largest camera in the world with a focal plane containing about 1.4 billion pixels. Furthermore, the camera can be read out in about 12 seconds, and the telescope sits at one of the world's premier astronomical sites atop Haleakala on the island of Maui, Hawaii. The PS1 camera is composed of 60 orthogonal transfer array (OTA) CCDs that have the capability of performing real-time shifting of the pixel charges *during* an exposure in what is effectively a first-order tip-tilt adaptive optics (AO) correction without the need for AO hardware and control systems. Despite its promise for improving a system's point-spread function at the focal plane, the OTA technology was never successfully implemented in PS1 operations and should not be considered a viable technology without significant investment (the PS1 system simply operated the CCDs without implementing the OTA capability). The PS1 was supposed to be the first of four telescopes in the Pan-STARRS system, for which a sophisticated end-to-end asteroid detection, simulation, and science system was developed (Denneau et al. 2013).

4.1.1.4 *Spacewatch (observatory code 691)*

Survey characteristics: Very high survey time efficiency, automated detection of asteroids.

The Spacewatch team pioneered the use of CCDs and time-delay integration (TDI, also known as drift scanning) for asteroid surveying (Rabinowitz 1991). The TDI technique was critical at a time when CCD readout times could be very long relative to the exposure times, with typical on-sky efficiency of 50% (i.e., only half the observing time was used for on-sky imaging because the other half of the time was required to read out the camera). The TDI technique enabled Spacewatch to achieve ~90% on-sky efficiency, thereby effectively doubling the sky coverage relative to what could have been achieved with traditional expose-then-read techniques. Spacewatch also introduced the use of automated detection of asteroids with software. Spacewatch held the top spot in the NEO discovery

rate for four years, from 1993 through 1996, and in 2005 transitioned from making NEO discoveries to conducting follow-up observations.

4.1.2 Expected New Ground-Based Systems

Several new ground-based survey systems have recently started operations, and a couple more are expected within a decade (Table 4-2). In this subsection, we summarize some of the expected strengths of each system.

Table 4-2. Top five expected new ground-based NEO surveys in 2016–2026. Surveys are listed in time order of first actual or expected NEO discovery.

Survey	Location	Expected Date of Survey Operations	Aperture
Space Surveillance Telescope (SST)	New Mexico/ Australia	2015/2018	3.5 m
Asteroid Terrestrial Last Alert System (ATLAS)	Hawaii	2017	2 × 0.5 m
Pan-STARRS 2 (PS2)	Hawaii	2017	1.8 m
Large Synoptic Survey Telescope (LSST)	Chile	2021	8.4 m (6.4 m effective)
Fly-Eye	Southern Europe (TBD) ³	2018 or 2019 ³	1.1 m

4.1.2.1 Space Surveillance Telescope (observatory code G45)

Survey characteristics: Curved CCDs, large focal plane, fast readout, fast pointing and settling, large nightly area coverage.

The Space Surveillance Telescope (SST) (Monet et al. 2013) is the next-generation version of the LINEAR survey. The SST reported more asteroid observations to the Minor Planet Center (MPC) in 2015 than any other survey reported, although the SST’s NEO discovery rate is only about a few percent of the total number of NEOs discovered in the past few years. Operational and technical details are difficult or impossible to obtain because the system is funded and operated by the Defense Advanced Research Projects Agency (DARPA), but the $f/1.0$ optics on a 3.5-meter-diameter telescope provide an ≈ 6 -square-degree FOV and the camera has a 0.9 arcsec pixel scale. The fast optical system generates a high-curvature focal plane for which curved CCDs were custom-made for each position in the camera, i.e., the shape of the CCD is curved to follow the shape of the focal plane. This technology is uncommon and is likely beyond the funding capabilities of non-defense-funded surveys. Furthermore, modern optical design is probably capable of designing flat, or reduced-curvature, focal planes suitable for traditional flat CCDs. Finally, the telescope is designed for fast point-and-settle times, and the camera can be read out very fast to provide high survey-time efficiency. The SST will operate for a few months into 2017 and then be shut down for transport to Australia where it will be recommissioned in late 2018. It is expected that the system will continue

³ Personal communication, Dr. Detlef Koschny (ESA).

its asteroid mission after recommissioning in Australia, but this mode of operation will require U.S. Air Force approval.

4.1.2.2 Asteroid Terrestrial Last Alert System (ATLAS, observatory code T05)

Survey characteristics: Large FOV, large format CCDs, large-area coverage every night, self-follow-up.

The Asteroid Terrestrial Last Alert System (ATLAS) (Tonry 2011) consists of small but fast cameras on two telescopes that image a large fraction of the sky five times in a single night. The system is reporting a prolific number of asteroid detections and NEO discoveries to the MPC and is currently discovering a few percent of the annual number of new NEOs. The system is designed to provide self-follow-up for all NEOs that are brighter than the system's limiting magnitude, which the ATLAS team eventually expects to be $V \sim 20$ magnitude. The two telescopes are housed in independent observatories on Mauna Loa and Haleakala, Hawaii, with a separation of about 150 kilometers. The spatially separated observatories were initially thought to be useful for the parallactic information provided for orbit determination, but additional studies have shown that the separation is not necessary (Vereš et al. 2014).

4.1.2.3 Pan-STARRS 2 (PS2) (observatory code F52)

Survey characteristics: Large FOV, large-format CCDs, large-area sky coverage every night, self-follow-up.

PS2 is essentially a copy of the PS1 telescope described earlier. The two observatories are physically located within a few dozen meters of each other at Haleakala Observatories on Maui, Hawaii. PS2 operations have been delayed by problems with multiple subsystems, but the project management is hopeful that NEO surveying will begin in earnest in fall 2017. The camera currently has OTA CCDs like those in PS1, but the project hopes to obtain funding to pave both telescopes' focal planes with large, high-quality, monolithic CCDs.

4.1.2.4 Large Synoptic Survey Telescope (LSST, observatory code TBD)

Survey characteristics: Large aperture, large FOV, large camera, fast readout, high processing power, large-area night sky coverage every four to five nights.

Capabilities for the Large Synoptic Survey Telescope (LSST) are being actively modeled, and candidate survey strategies that balance the LSST's varied scientific goals are under development (Izevic et al. 2008). The system has the potential to be a prolific NEO discovery engine. The 2003 NEO SDT report (Stokes et al. 2003) suggested that such a system could singlehandedly reach about 60% completion for PHOs in a 10-year survey and provide warning for 60% to 70% of all sizeable Earth impactors (e.g., Stokes et al. 2003, Figure 6-8). The large-aperture system with the effective light-gathering power of an unobstructed 6.4-meter mirror, combined with fast optics for a wide FOV, will allow the system to image the entire sky to $V \approx 24.5$ every four or five nights. Part of the innovative system design is the detailed attention to software development and plans for massive computing power, in available CPU and in RAM, to allow essentially all the processing to take place without having to access disk space.

4.1.2.5 NEO Survey Telescope (NEOSTEL, or Fly-Eye) (observatory code TBD)

Survey characteristics: ≈ 45 deg² FOV, 100% fill-factor optical design.

The European Space Agency's (ESA) NEO Survey Telescope (NEOSTEL), also known as Fly-Eye, is designed to identify space debris and NEOs (Cibin et al. 2012). The 1.1-meter aperture telescope will have a FOV of ≈ 45 square degrees and, therefore, requires less than 900 exposures to image the entire sky (or the night sky multiple times). Furthermore, the system design plans for a 100% fill factor such that there are no uninstrumented areas on the focal plane. The camera achieves this design with a special optical system that splits the image into 16 subimages, each of which has its own dedicated, seamless focal plane consisting of a single E2V CCD (Table 4-3).⁴ ESA expects the installation of the telescope at the observatory site in Sicily (not yet finalized) to take place by the end of 2018. They hope to build a second identical system in Chile at a European Southern Observatory site, but funding for the second telescope has not been committed.

4.1.3 Existing Ground-Based Light Sensors

The physical size and performance of ground-based light sensors has continued to improve. In this section, we provide a brief overview of some of the sensors currently or soon to be in use in astronomical survey telescopes. All the light sensors introduced below and considered for implementation in the ground-based survey simulations are CCDs because the CCD industry is mature and these CCDs represent the forefront of the technology that will likely be operational during the time period of the simulations. In the future, two competing light-sensing devices,⁵ the sCMOS and electron-multiplying CCDs (EMCCDs), may be cheaper or more sensitive than CCDs, but these devices are not yet mature enough for consideration in this study. Although CCDs are a proven technology, there are still concerns about the challenges of producing the large-format, small-pixel CCDs required for wide-field astronomical imaging. The market driving the production of ever-improving CCD quality and smaller pixels is the digital camera and cellphone consumer market, not the astronomical market.

4.1.3.1 E2V CCD290-99 (85 Mpix)

"The sensor has an image area having 9216×9232 pixels with registers at both top and bottom, each with eight outputs for short readout times. The pixel size is $10 \mu\text{m}$ square. The image area has two separately connected sections to allow full-frame or split full-frame readout modes. Depending on the mode, the readout can be through 8 or 16 of the output circuits... The output amplifier is designed to give very low noise at readout rates of up to 3 MHz.... The package provides a compact footprint with guaranteed flatness at cryogenic temperatures.... The sides may be close butted if needed. Specifications are tested and guaranteed at 173K (-100°C)."⁶

Fourteen of these E2V CCD290-99 devices are installed at the focal plane of JPCam, the wide-field camera built for the Javalambre Physics of the Accelerating Universe Astrophysical Survey (J-PAS), but the camera and telescope have not yet seen first light. The J-PAS team reports that they are currently operating two separate telescopes using single CCD290-99 e2V detectors and both cameras

⁴ Personal communication, Dr. Detlef Koschny (ESA), 2016.

⁵ <https://www.teledynedalsa.com/imaging/knowledge-center/appnotes/ccd-vs-cmos/> provides a good overview of the costs and benefits associated with CCD, CMOS, and EMCCD devices.

⁶ From <http://www.e2v.com/resources/account/download-datasheet/1897>.

are working as expected.⁷ These devices are also the CCD choice for the planned upgraded focal planes for both the PS1 and PS2 asteroid survey systems.

4.1.3.2 STA1600LN (111 Mpix)

“The STA1600LN is a 10560 × 10560 image element solid-state charge-coupled device (CCD) full-frame sensor. This CCD is intended for use in high-resolution scientific, space based, industrial, and commercial electro-optical systems. The STA1600LN is organized in two halves each containing an array of 10560 horizontal by 5280 vertical photosites. The pixel spacing is 9 μm × 9 μm.... This imager is available in a full-frame transfer configuration... [that] allows readout through two... quadrants. The STA1600LN is offered as a backside-illuminated version for increased sensitivity and [ultraviolet] UV response in the same package configuration.”⁸

Single science-grade CCDs are currently being used in the CSS G96 and 703 cameras and in the two ATLAS cameras;⁹ both projects report excellent performance.

4.1.3.3 LSST CCDs 4k × 4k (16 Mpix)

The LSST camera will incorporate 189 science-grade CCDs from two different vendors. The sheer number of devices required for the LSST camera and the rigorous requirements for their performance characteristics suggest that these devices, or very similar ones, will be available for other astronomical surveys.

⁷ Personal communication (Antonio Marín-Franch).

⁸ <http://www.sta-inc.net/sta1600/>.

⁹ <http://fallingstar.com/specifications.php>.

Table 4-3. Typical characteristics of three large-format CCDs currently used or considered for asteroid surveys.

Imager	E2V CCD290-99 ₆	STA1600 ⁷	LSST CCD ⁹
Example camera	JPCam ¹⁰	CSS G96 & ATLAS	LSST
Pixel width (microns)	10 × 10	9 × 9	10 × 10
Number of pixels (total)	85 Mpix	111 Mpix	16 Mpix
Number of pixels (V × H)	9232 × 9216	10,560 × 10,560	4,907 × 4,000
Active area dimension (mm × mm)	92.2 × 92.4	95.04 × 95.04	49.07 × 40.00
Active area (cm ²)	85.38	90.33	19.63
Package dimensions (mm × mm)	98.5 × 93.7	≈97 × ≈97 ¹¹	40.45 × 41.03
Fill factor when butted	92%	79% ¹¹	91% ¹²
Quantum efficiency (@ 550 nm)	88% (see Figure 4-1)	92% (see Figure 4-2)	86% (see Figure 4-3)
Dark current (e ⁻ /pixel/hr @ -100°C)	2	3	720 ¹³
Read noise (e ⁻)	4 @ 0.5 MHz	5 @ 1MHz	8.8 @ 0.6 kHz
Readout time (s) @ 1 MHz	5.3 @ 1 MHz	6.9 @ 1 MHz	2 ¹⁴ @ 0.6 MHz

¹⁰ <http://www.j-pas.org/news/show/58>.

¹¹ Image area is 95.04 mm × 95.04 mm and standard package is 164.34 mm × 117.09 mm. There is a “variant” that provides “less than 12 mm of space between active pixel regions.” Assuming 12 mm in both directions yields 79% fill factor.

¹² Personal communication, Lynne Jones (LSST), 2016. More information in <https://github.com/rhiannonlynne/notebooks/blob/master/FillFactor.ipynb>.

¹³ Dark current is not a driving factor in LSST camera design because of the LSST’s short exposure times of 15 seconds. At the time of this writing, LSST has not specified its operating temperature.

¹⁴ <http://lsst.org/scientists/keynumbers>.

Typical QE at -100°C

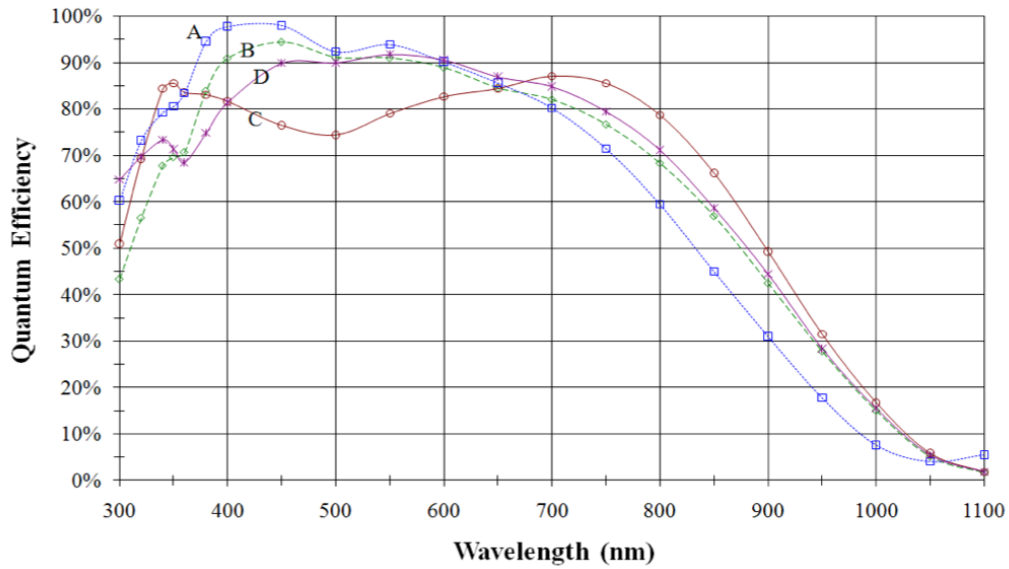


Figure 4-1. Quantum efficiency (QE) of the Semiconductor Technology Associates STA1600 series CCDs as a function of wavelength (from Semiconductor Technology Associates STA1600 data sheet found at <http://www.sta-inc.net/sta1600/>). This report and Table 4-3 assume the use of the science-grade version of the STA CCD represented by QE curve B.

Typical QE at -100°C. Deep depletion silicon

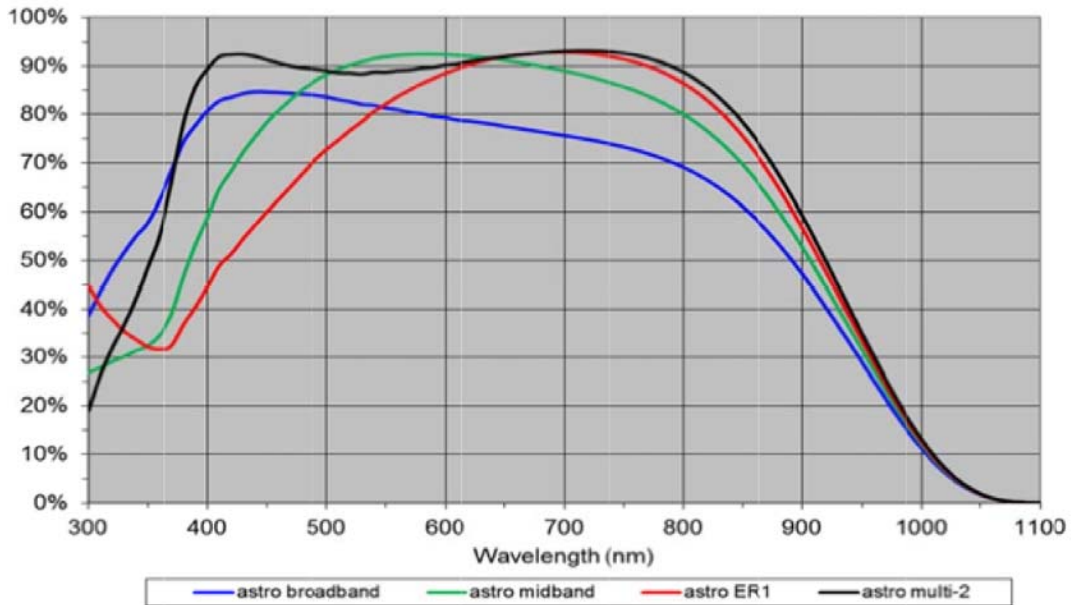


Figure 4-2. Quantum efficiency (QE) of several E2V CCDs as a function of wavelength (from the E2V data sheet available at <http://www.e2v.com/resources/account/download-datasheet/1897>). This report and Table 4-3 assume the use of the astro multi-2 version of the E2V CCD that is designed for a wide range of astronomical applications.

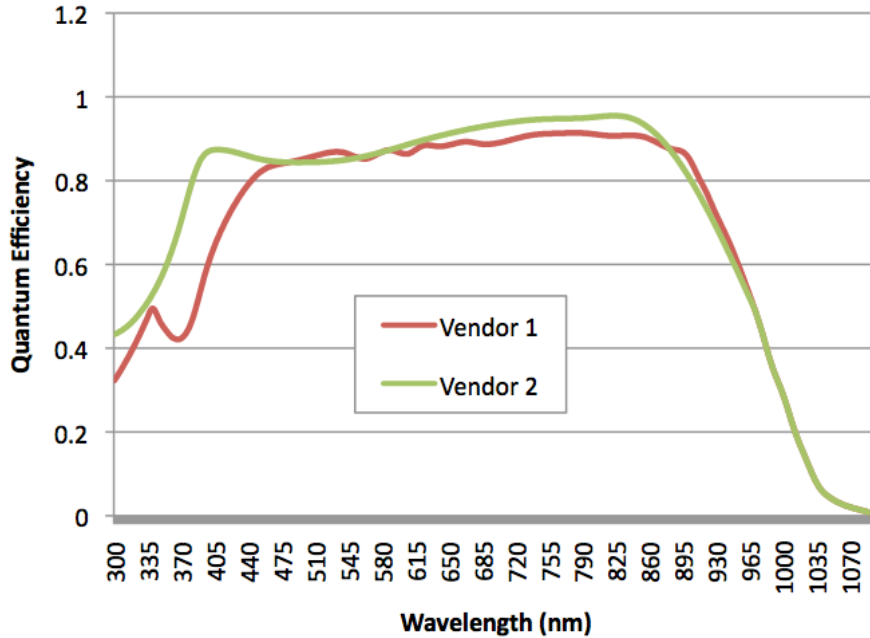


Figure 4-3. The LSST CCD quantum efficiency curves as a function of wavelength as measured by two vendors. Data for this figure come from https://github.com/lsst-pst/syseng_throughputs/tree/master/components/camera/detector.

4.1.4 Modeled Ground-Based Systems

The ground-based systems modeled in this report, as summarized in Table 4-5, represent technologies that are realistically achievable within the next decade and are motivated by existing systems or advanced designs for expected systems. We understand that these systems carry the risk of not anticipating a new technology that could revolutionize ground-based surveying and do not take advantage of advanced telescope designs. For instance, it is likely that advanced optical designs and mirror-figuring capability could enable off-axis fast telescope systems (Moretto et al. 2012) that could obviate the central obscuration caused by the secondary mirror, thereby improving the system’s limiting magnitude, reducing image artifacts such as diffraction spikes, and increasing the NEO discovery rate. Similarly, the hardware and software techniques developed over the past few decades to detect and catalog large NEOs may not translate directly to the discovery of smaller but still dangerous NEOs that move quickly across the telescope’s focal plane and leave “trails” rather than point sources or “stubs.” Efficient trail detection (Waszczak et al. 2017) or the technology of “synthetic tracking” (see Section 4.1.6; Heinze et al. 2015; Shao et al. 2014) could improve detection performance for small, trailed NEOs.

We anchored the smallest-aperture ground-based survey system (G2) at roughly the aperture of the currently largest-aperture operating survey (1.8 meters) and include two additional systems with roughly 4× (G4) and 16× (G8) the light-collecting area. The G2 system allows a direct comparison with the actual performance of the PS1 survey for calibration purposes. Each of the performance characteristics in Table 4-5 was motivated by the prototype system’s (Table 4-4) actual or expected

performance, with allowance (based in part on the experiences learned from each of the prototypes) for enhanced mechanical and optical design in the next decade.

For each of the modeled ground based systems, we simulate the performance of a camera with a mosaic focal plane fully paved with CCDs of the type specified in Table 4-5, with the stated fill-factor.

Table 4-4. Performance characteristics of existing ground-based telescope system prototypes for Table 4-5 (Morgan et al., 2006; Onaka et al. 2012; Magnier et al. 2013; https://www.noao.edu/meetings/decam/media/DECam_Technical_specifications.pdf; Soares-Santos 2016).

System	Pan-STARRS 1	Blanco/DECam	LSST (design specs)
Primary aperture	1.8 m	4 m	8.4 m
Effective aperture	1.4 m	3.6 m	6.4 m
f#	4.4	2.7	1.2
FOV	≈7 deg ²	≈3 deg ²	≈9.6 deg ²
FOV diameter (mm)	419 mm	391 mm	641 mm
Secondary obscuration	25% (38% w/ baffling)	20%	37%
Retargeting time (time to move one FOV diameter, stop, settle, track)	13 s (dominated by readout time)	17 s (readout)	5 s
CCD	CCID58 (Lincoln Laboratory)	(Dalsa & LBNL)	(LSST custom)
Mosaic fill-factor	≈80%	85%	90%

Table 4-5. Performance characteristics of modeled ground-based telescope systems.

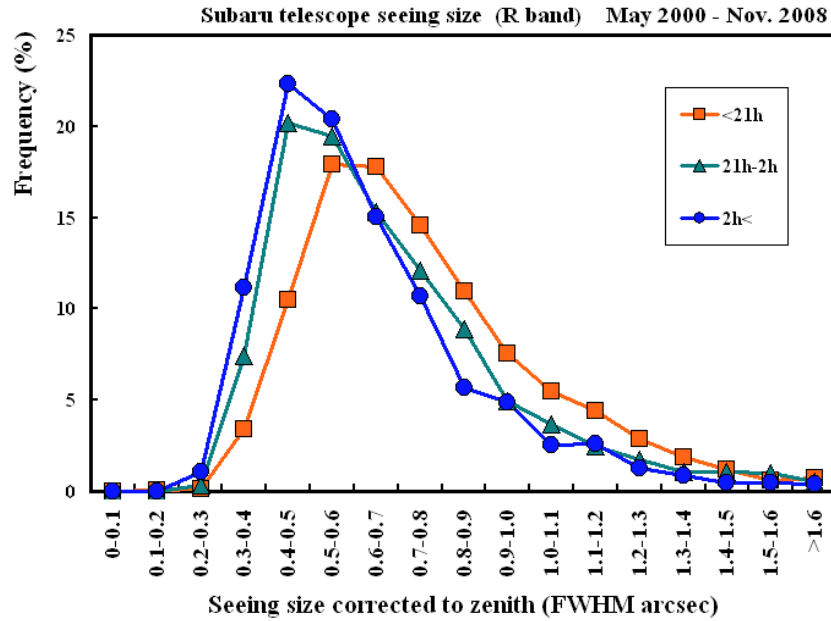
System	G2	G4	G8
Primary aperture	2 m	4 m	8 m
f#	4	2	1
FOV	9 deg ²		
FOV diameter	473 mm		
Secondary obscuration	25%	32.5%	40%
Effective aperture	1.73 m	3.29 m	6.20 m
Retargeting time (time to read CCD, move one FOV diameter, stop, settle, track)	5 s		
CCD	E2V CCD290-99		
Mosaic fill-factor	92%		

4.1.5 Modeled Ground-Based System Site Characteristics

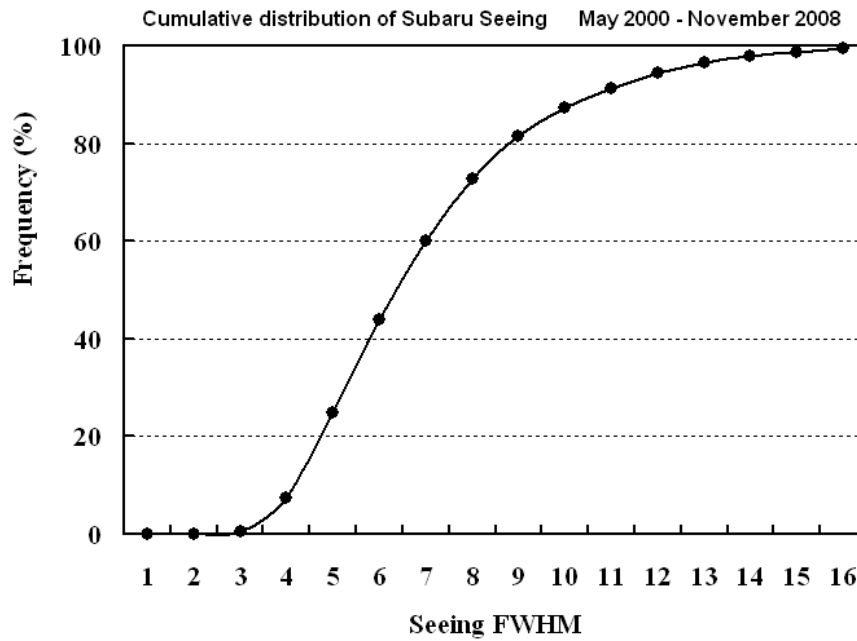
The modeled ground-based survey systems are assumed to be located at observing sites with excellent seeing conditions because it makes sense to locate an advanced NEO survey system at a superior site. With the exception of Dome C in Antarctica (Lawrence et al. 2004), the best astronomical sites in the world, in terms of the stellar point-spread function, clear sky probability, and low humidity, are located in Hawaii and Chile. The Subaru Telescope¹⁵ is one of the most advanced monolithic mirror telescopes in the world and, therefore, represents what could be achieved with modern telescope system design at an excellent site. The National Astronomical Observatory of Japan, which operates the Subaru Telescope, has characterized its seeing and clear sky probabilities¹⁶ as illustrated in Figures 4-4 and 4-5. The values in these two figures are used as the standard site characteristics for each of the modeled systems in Section 4.1.4.

¹⁵ <http://subarutelescope.org/Introduction/>

¹⁶ <http://subarutelescope.org/Observing/Telescope/ImageQuality/Seeing/>



(a)



(b)

Figure 4-4. In (a) is shown the frequency of the full width at half-maximum of the point-spread function (PSF FWHM) corrected to zenith as a function of local time throughout the night as measured by the Subaru Telescope on Maunakea, Hawaii. The seeing is worse in the first few hours of the night but is relatively stable after about 9:00 p.m. local time. In (b) is the cumulative distribution of the FWHM during almost eight years of observations at the Subaru Telescope on Maunakea.

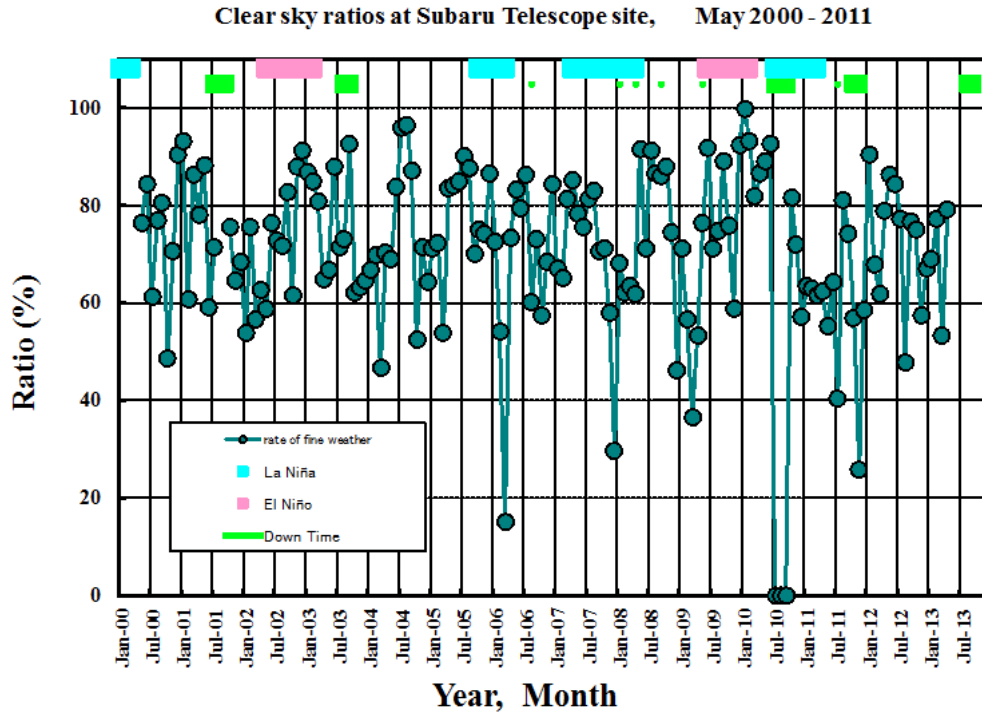


Figure 4-5. The monthly average clear-sky probability at the Subaru Telescope on Maunakea is shown for the period from May 2000 through May 2011.

Figure is from the Subaru Telescope website at <http://www.naoj.org/Observing/Telescope/ImageQuality/Seeing/>.

4.1.6 Synthetic Tracking

The conventional synthetic tracking (CST) technique (Holman et al. 2004; Kavelaars et al. 2004) takes many images of the same field of sky and shifts them on many different possible NEO trajectories to search for point sources in the stacked and medianed frames. This technique has been successfully employed to identify fainter moving sources than could normally be identified with the same telescope for relatively slow-moving outer solar system objects and main-belt minor planets, but it has yet to be demonstrated for the discovery of an NEO. The CST technique allows small telescopes to reach fainter limiting magnitudes (similar to the track-and-stack technique for observing known NEOs), but observing in this fashion dramatically reduces the system’s sky coverage because it requires the telescope to observe the same field for long time periods. That issue may be addressed, in some cases, by using shorter exposures to reduce the limiting magnitude to what is desired for follow-up observations.

LINEAR experimented with what is referred to herein as synthetic tracking, although the LINEAR implementation was described as a velocity matched filter (VMF).¹⁷ While the VMF technique yielded

¹⁷ In the VMF, detections are not made in each frame before looking along the track; instead, one looks along the track, adds up the pixels at each posited location, and then applies a detection threshold to the sum. The VMF is a variant of a 3D matched filter, which goes far back in the literature.

an approximately half-magnitude improvement in single-object detection sensitivity (about half the theoretical improvement), the false-alarm rate was too high for submitting NEO candidates to the MPC's NEO Confirmation Page, despite extensive efforts to reduce the false-alarm rate. However, the experimental VMF detections were still submitted to the MPC, where they were utilized in a limited fashion by correlating them to known objects for purposes of improving estimates of the objects' orbits. Other attempts to utilize the technique were also hampered by high false-alarm rates (Gural et al. 2005).

The introduction of modern large-frame, high-speed, low-noise complementary metal-oxide semiconductor (CMOS) detectors, such as the Zyla 5.5 sCMOS,¹⁸ has created interest in the possibility of digital synthetic tracking (DST) (Shao et al. 2014; Heinze et al. 2015), an approach not feasible with conventional CCDs. Very low-noise sCMOS detectors, such as the aforementioned Zyla detector, can operate at many tens of frames per second to acquire an image equivalent to a single long exposure with conventional CCDs, but without the long readout time and with the benefit of acquiring every single frame in the sequence. Thousands of these frames could then be processed with modern graphics processing units (GPUs), as with CST, to identify objects that move rapidly across the field of view. In principle, a network of small telescopes employing DST might be able to achieve similar survey speed and depth to a single larger telescope. It is advantageous to be able to identify trailed detections, and DST is likely superior to conventional imaging techniques for identification of trailed objects. This likely superiority would make DST a good choice for detecting small, nearby, fast-moving objects. While DST is likely preferable for very small objects (e.g., perhaps tens of meters in diameter), it is unnecessary for large (e.g., ~1-kilometer diameter) objects. However, the object diameter at which DST becomes preferable is currently not known.

Because neither CST nor DST have yet been employed to discover NEOs, the technology is not yet sufficiently mature for the trade studies that would be required to assess whether multiple smaller telescopes employing DST would be preferable to a traditional larger telescope. Additional technical issues with the practical application of DST must also be addressed, such as how to produce accurate, precise astrometry from the shifted and stacked frames in which the NEO would be detected. Therefore, this study did not consider synthetic tracking for NEO surveying.

4.2 Space-Based Systems

The number of space-based systems considered by the SDT include visible and IR instruments in free-flying spacecraft. Observatories in low-Earth orbits (LEO), geostationary orbits (GEO), Sun-Earth L1 and L2 Lagrange point halo orbits, and Venus-like orbits were modeled. The SDT also studied a small IR telescope co-hosted on board a geostationary satellite.

4.2.1 Spacecraft System

The spacecraft bus used to support either a visible or IR instrument must carry components and expendables suitable for supporting a multiyear survey mission. The instrument designs for either the 0.5-meter or 1-meter apertures use a three-axis stabilized spacecraft bus to slew between field centers. A one-time ejectable dust cover, similar to that used on either the Spitzer or Kepler missions,

¹⁸ Currently, the largest commercially available option, see <http://www.andor.com/scientific-cameras/neo-and-zyla-scmos-cameras/zyla-55-scmos>.

is used to protect the telescope before and during launch. A hydrazine propulsion system is assumed to be necessary to achieve and maintain either L1, L2, or Venus-like orbits. A fixed Ka-band telecommunications subsystem can support up to ~150 Mbps downlinks from L1 or L2 by using NASA's Deep Space Network without significantly impinging on survey time.

Some form of lossy data compression is required for missions in Venus-trailing orbits, leading to an as-yet-unquantified loss of sensitivity (see below). The other effect of downlinking only regions of interest is that the remainders of the images are no longer available to be searched for precovery detections at a later time. Precovery can significantly extend observational arcs.

The geostationary instrument is assumed to be co-hosted on board a large telecommunications satellite (see Section 4.2.6.6).

4.2.2 Orbit

For either visible or IR systems, the choice of orbit significantly influences space telescope mission architecture considerations, including data rate, field of regard, and thermal environment.

Orbits that take the flight system far from Earth (e.g., Venus-trailing) must use lossy data compression techniques that are less well understood and tested than are techniques that can downlink full individual images. A system's performance is a sensitive function of its ability to extract faint sources with high reliability and completeness. All current NEO surveys operate on full-frame images (e.g., Catalina, Pan-STARRS, and NEO Wide-field Survey Explorer [NEOWISE]) and do not perform lossy compression on them prior to source extraction. A Venus-trailing orbit decreases the data rate by a factor ranging from 4900 to 29,000 depending on the relative positions of Earth and Venus as compared to a spacecraft in near-Earth space. The technology to implement calibration and source-extraction routines in flight software using the limited processing and memory resources available on board a spacecraft has not been demonstrated and at present remains at a theoretical level in the astronomical community.

It is possible to select only regions of interest around individual sources to reduce the data volume that must be downlinked, similar to what the Kepler mission has done (Jenkins et al. 2010). However, Kepler targets stationary objects (stars) as opposed to moving objects whose positions are not known a priori. The impact of performing source identification and extraction with the limited resources of a spacecraft processor and memory boards, instead of the resources of a modern ground-based computer cluster, has not yet been quantified. For example, optimal source extraction is performed on WISE images by considering all exposures collected at each part of the sky (typically ~10 on the ecliptic and rising to hundreds at the ecliptic poles) and at all available wavelengths (Cutri et al. 2012; WISE Explanatory Supplement Section IV.4.b). Using an analog of a flight processor and memory card to extract sources from raw image data, one could evaluate the effects of windowing on source completeness and reliability as a function of source brightness by making a comparison to published source lists. However, this analysis is not yet available in the literature.

For the purposes of this study, we assumed that data compression for observatories in Venus-like orbits had no impact on performance compared to observatories in L1 orbits; sensitivity was assumed to be identical for same-sized telescope apertures. A laser communications system was assumed for the Venus-like orbiting missions to deliver identical data rates to a Ka-band system used

at L1; the only impact of adding the laser communications package was assumed to be the impact to cost. The low Technology Readiness Level of onboard moving-object source-extraction routines was accounted for solely in the costing of observatories in Venus-like orbits.

Viewing constraints from the Sun, Moon, and Earth must be considered and incorporated into the survey plan and fault protection systems (Tables 4-7, 4-8, and 4-9). All systems must be carefully optimized to guard against stray light.

The heat load from Earth is significant for IR systems in LEO or GEO orbits. For example, when the WISE mission's solid hydrogen coolant was exhausted in 2010, the telescope and focal planes equilibrated to ~ 75 K (see Section 4.2.3). Lower temperatures cannot be achieved readily through purely passive means in LEO or GEO orbits but could in principle be reached using cryocoolers. The L1 or L2 Sun-Earth Lagrange point environments reduce the heat load from Earth significantly for IR imagers compared to Earth orbits. Moreover, the heat load at either L1 or L2 is half that of a Venus-trailing orbit. While it is possible to achieve the required temperatures for an IR telescope passively from L1 or L2 orbit, an IR telescope in Venus-trailing orbit requires the use of cryocoolers (Section 4.2.6.5).

4.2.3 Visible and Infrared Sensors

There are a number of advantages in employing a space-based visible system over an IR system. The visible CCDs and optical elements do not need to be cooled to the same low temperatures as the elements of IR systems (although temperatures must still be well-controlled to maintain image quality). Moreover, as described in Section 4.1.3, a wider selection of visible detectors is available for consideration compared to the selection of available IR focal planes. We assume that it is possible to build visible systems with FOVs larger than those of IR systems because CCDs with larger formats than those of IR focal planes are now more readily available.

Astronomers observe asteroids at thermal IR wavelengths for the following reasons: (1) asteroids emit hundreds of times more photons at thermal IR wavelengths than at optical wavelengths; (2) with thermal IR measurements of sufficient quality and adequate sampling of an object's light curve and thermal emission peak, effective spherical diameter can be constrained to within ± 10 – 20% (Mainzer et al. 2011b, c; Usui et al. 2014); (3) thermal IR sensors have been shown to be approximately equally sensitive to low and high albedo objects, including the approximately one-third of NEOs that are dark (Stuart and Binzel 2004; Mainzer et al. 2011e, 2012; Wright et al. 2016), reducing a source of bias in population estimates (Grav et al. 2011; Mainzer et al. 2011c); (4) visible albedos can be computed when IR measurements are combined with visible light fluxes; albedo is correlated with taxonomic type, composition, and density (Tholen 1984; Bus and Binzel 2002; DeMeo et al. 2009; Mainzer et al. 2011d; Thomas et al. 2011). Diameter and density are essential for determining impact energy. An instrument that is cooled so that its sensitivity is limited by the natural zodiacal light is equivalent to thousands of 8-meter ground-based IR telescopes because of the reduction in thermal background from the atmosphere and the telescope.

All space-based sensors benefit from the lack of atmospheric distortion and weather. However, the aperture required for an optical telescope to reach the equivalent sensitivity of a 0.5-meter IR telescope is larger than 0.5 meter because the asteroids are less intrinsically bright. A 0.5-meter thermal IR telescope integrating for 150 seconds can reach the equivalent of $V \sim 24$ magnitude at the

apparition of discovery (Figure 4-8). By contrast, visible systems can have larger fields of view (Figures 4-6 and 4-7).

Space-based IR telescopes have been used extensively to discover and characterize small bodies (see Mainzer et al. 2015 for a summary). Advances in IR detector technology have resulted in significant improvements in sensitivity and spatial resolution over previous generations of IR space telescopes, such as the Infrared Astronomical Satellite (IRAS) (Neugebauer et al. 1984; Tedesco et al. 2002a), the Midcourse Space Experiment (MSX) (Mill et al. 1994; Price et al. 2001a; Tedesco et al. 2002b), and the Infrared Space Observatory (ISO) (Kessler et al. 1996). Infrared sensors have advanced from the 62-pixel hand-assembled focal plane employed by IRAS to monolithically fabricated 1024^2 arrays. Consequently, the number of NEOs discovered at thermal IR wavelengths has gone from a handful of NEOs discovered by IRAS to ~235 discovered by the NEOWISE effort of the WISE mission.

4.2.4 Current and Recent Space-Based Systems

At present, NEO surveys using visible light are performed with ground-based facilities (Section 4.1). The Hubble Space Telescope has been used to survey for and discover objects in more distant orbits, such as Kuiper Belt objects (KBOs). However, its small field of view makes it poorly suited to searching for NEOs because they are spread over a much wider swath of sky than are KBOs.

Since the 2003 NEO SDT report, a number of space-based IR telescopes have been successfully launched, including the Spitzer Space Telescope, AKARI, WISE, the Herschel Space Observatory, and the telescope on the Planck spacecraft. The Spitzer, AKARI, WISE, and Herschel telescopes were cryogenically cooled during their prime mission phases, and all but Herschel continued to operate in a passively cooled mode following depletion of their cryogenes. The Spitzer and Herschel missions performed targeted observations of previously known objects; neither mission has been widely used for asteroid discovery (Trilling et al. 2010; Müller et al. 2014a, b). AKARI carried out an all-sky survey and performed targeted spectroscopic and imaging observations (Murakami et al. 2007). After the liquid cryogen boiled off, only near-IR observations in a targeted mode were carried out. AKARI did not discover new asteroids; the all-sky observing cadence did not support the multiple observations needed to discover new moving objects (Usui et al. 2011, 2013, 2014).

Launched on December 14, 2009, into a 525-kilometer Earth orbit, WISE surveyed the entire sky at 3.4, 4.6, 12, and 22 μm by using a 40-centimeter telescope (Wright et al. 2010). The survey's scientific objectives were to find the cool stars and luminous galaxies. Modifications to the WISE science data processing pipeline allowed for the discovery of moving objects in real time (Mainzer et al. 2011a). The baseline mission was completed in July 2010, and the solid hydrogen cryogen used to cool the 12 μm and 22 μm detectors was fully exhausted on September 30, 2010. The mission continued in a post-cryogenic phase, with the goal of observing NEOs until February 1, 2011, with the passively cooled 3.4 μm and 4.6 μm channels. After this, it was placed into hibernation for 32 months. During the prime mission, >158,000 asteroids were detected, including ~34,000 new discoveries. The spacecraft was reactivated in 2013, renamed NEOWISE, and retasked to discover and characterize the NEO population by using the 3.4 μm and 4.6 μm channels, which are passively cooled to ~74 K. Survey operations resumed on December 21, 2013, and are expected to continue until late 2017. During the course of this reactivation mission, the spacecraft has observed ~19,000 minor planets, including ~500 NEOs, a rate of ~0.7 to 0.8 NEOs per day (Mainzer et al. 2014, 2016; Nugent et al. 2015, 2016).

4.2.5 Modeled Space-Based Systems

The space-based systems listed in Table 4-6 are modeled in this study. Infrared systems are described in Section 4.2.6, and visible systems are discussed in Section 4.2.7. These selected systems are intended to be representative of a variety of possible implementation options. The fundamental technological aspects of these systems and their components are described in the sections that follow. Figures 4-6 and 4-7 illustrate the scaling of search rate (i.e., the ability to cover area on the sky) with sensitivity for the IR and visible systems, respectively. Figure 4-8 shows the difference in sensitivity to NEOs between visible and IR systems.

Table 4-6. Space-based NEO survey systems modeled in this study.

	Orbital Location	Aperture (m)	Band
1	LEO	0.5	Visible
2	GEO	0.5	Visible
3	LEO	1.0	Visible
4	GEO	1.0	Visible
5	LEO	2.0	Visible
6	SEL1	0.5	Visible
7	Venus-trailing	0.5	Visible
8	SEL1	1.0	Visible
9	Venus-trailing	1.0	Visible
10	SEL1	0.5	IR
11	Venus-trailing	0.5	IR
12	SEL1	1.0	IR
13	Venus-trailing	1.0	IR
14	GEO (co-hosted)	0.2	IR
15	GEO	2.0	Visible
16	SEL2	0.5	Visible
17	SEL2	1.0	Visible

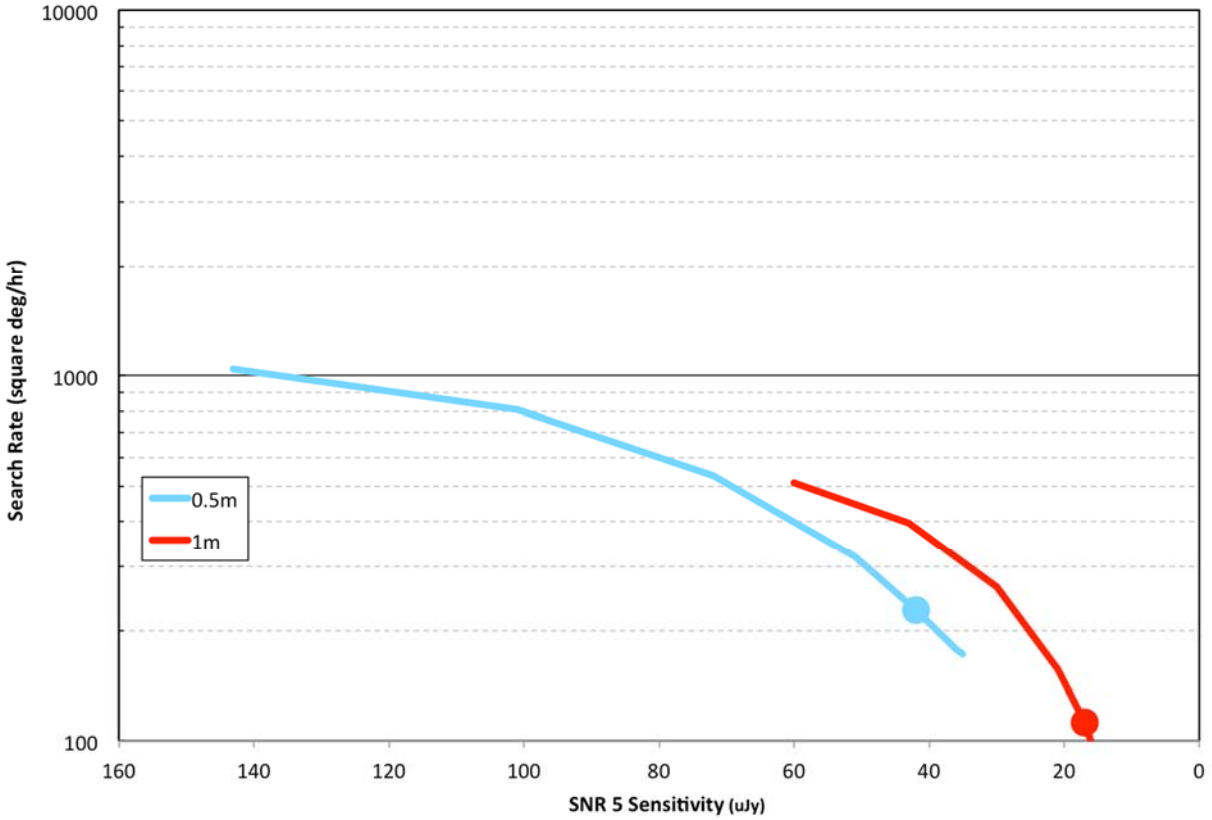


Figure 4-6. The scaling of search rate with sensitivity for the IR observatories at L1 for the lowest expected zodiacal background; the filled circle indicates the selected exposure time (and consequent sensitivity). Exposure time is ultimately limited by the point at which trailing losses become appreciable for a substantial fraction of objects.

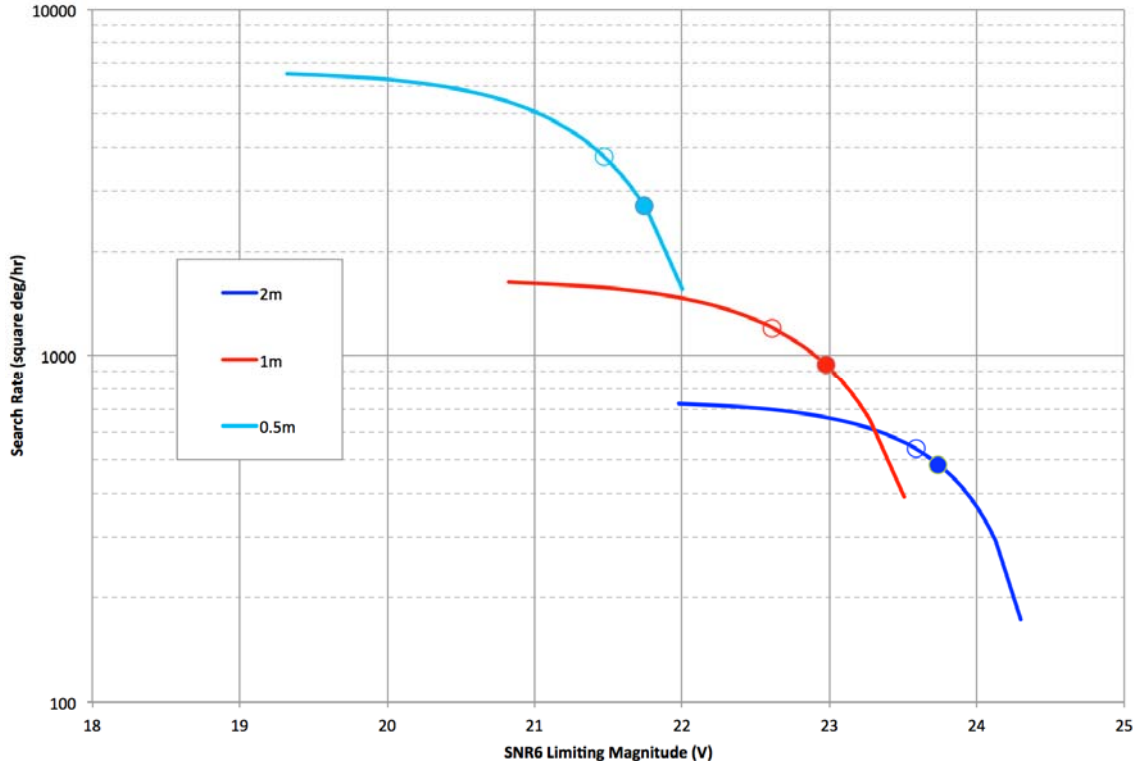


Figure 4-7. The relationship between sensitivity and sky coverage is a function of exposure time for the three different visible space-based systems listed in Table 4-9. Integration time matched to 1 deg/day object motion for either pixel size (filled circles) or for seeing (open circles).

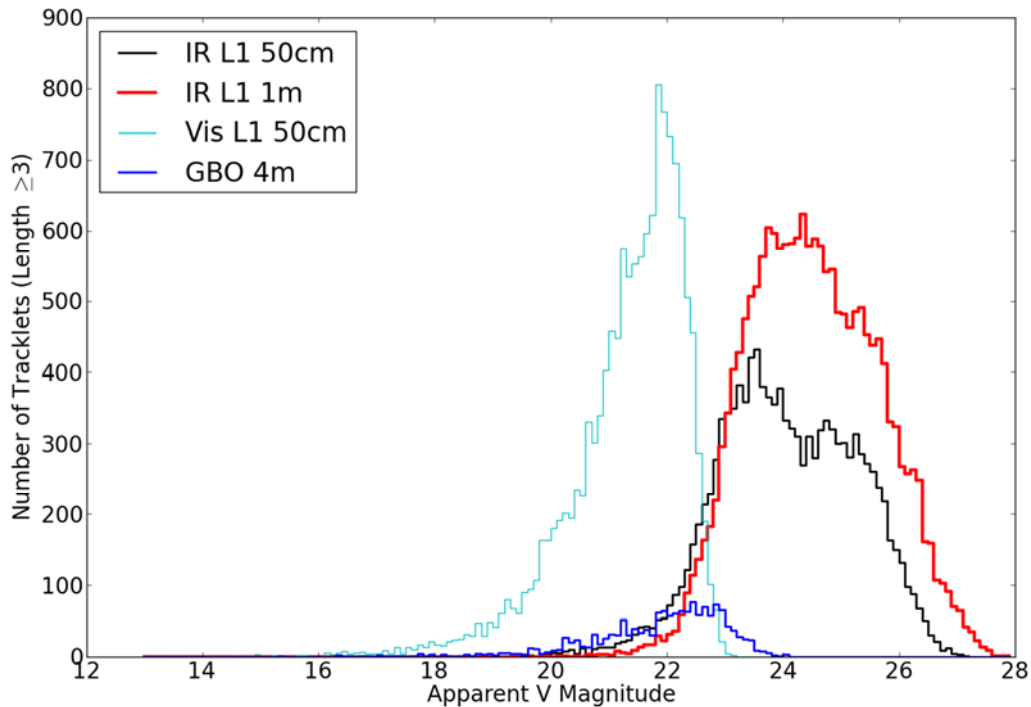


Figure 4-8. A comparison of the apparent visual magnitudes of PHOs with sizes between 126 and 159 meters at the times of their detections over the course of one year by 50 cm visible and IR telescopes operating at L1 reveals that for the same size aperture, IR systems are more sensitive to NEOs than visible telescopes. The apparent magnitudes of a 4-meter ground-based observatory (GBO) are shown for comparison.

4.2.6 Future IR Space-Based Systems

In this report, we consider 0.5-meter and 1-meter aperture thermal IR space telescopes in Sun-Earth L1 Lagrange point halo orbits and Venus-trailing orbits. Tables 4-7 and 4-8 summarize the assumed characteristics of the IR telescopes. It is assumed that all of these systems employ detector arrays with the performance given in Table 4-9. Both Venus-trailing and Sun-Earth L1-orbiting telescopes are assumed to have identical performance in terms of sensitivity, data rate, temperatures, slew rate, etc., despite differences noted in the technical implementations as described below. We also consider a 20-centimeter IR telescope mounted on a geostationary platform (Table 4-6). This payload is assumed to be co-hosted on board a large telecommunications satellite that can accommodate a maximum volume of less than or equal to 1 m^3 and a mass of less than $\sim 160 \text{ kg}$ (Section 4.2.6.6).

4.2.6.1 Space-Based IR System Design Methodology

Using a space-based IR dedicated for NEO discovery is not a new idea; Price & Egan (2001), Cellino et al. (2000, 2004), Tedesco et al. (2000c), and Cellino (2004) studied the possibility of using a cryogenically cooled IR telescope in various orbits to discover NEOs. The 2003 NEO SDT report opted not to consider space-based IR systems because of the immaturity at that time of the detector and cooling system technologies. However, given recent advances, we now describe the design considerations for space-based IR telescopes.

Space-based IR telescopes require cooling both to reach the required operational temperature for the detectors and to achieve low background performance. The exact temperature required depends on the details of the optical system design as well as on the type of detector used. However, some general principles can be derived from basic physics. At thermally dominated wavelengths ($\sim 10 \mu\text{m}$), the main source of natural background is thermal emission from zodiacal dust, the remnant cloud surrounding our solar system that was left after the formation of the solar system. The density of zodiacal dust increases as $1/R$, where R is the radial distance to the Sun; the flux of the dust increases as $1/R^2$ (Leinert et al. 1998; Wright 1998). To be background limited, the detector and the optics must be sufficiently cold to contribute less signal than the zodiacal dust. For a camera operating out to $\sim 9\text{--}10 \mu\text{m}$, the telescope must be cooled to $< \sim 60 \text{ K}$ to be natural background limited over most of the field of regard.

Table 4-7. Performance characteristics for a 0.5-meter space-based IR telescope in either L1 or Venus-trailing orbit.

Note: Since point-source sensitivity varies with ecliptic latitude, longitude, and heliocentric distance, the point-source sensitivity is specified near the midpoint of the viewing zones for each survey, or ($0^\circ, 90^\circ$) for L1 and GEO, and ($0^\circ, 180^\circ$) at 0.7 AU heliocentric distance for the Venus-trailing survey.

Parameter	L1	Venus-trailing	Co-hosted GEO
Aperture (m)	0.5	0.5	0.2
Bandpass (μm)	6–10	6–10	6–10
Field of view ($^\circ$), including gaps	1.7×7.13	1.7×7.13	7×3.5
Viewing zones (solar elongation; $^\circ$)	$\pm(45\text{--}115)$	180 ± 75	>70
Viewing zones (ecliptic latitude; $^\circ$)	± 40	± 40	± 42
Number of pixels	16 million	16 million	8 million
Plate scale (arcsec/pixel)	3	3	6
Fill factor (%)	95	95	95
Slew time (s)	30	30	30
Dwell time (s)	~ 150	~ 150	~ 150
Image FWHM (arcsec)	4	4	7.5
Minimum background current (e-/sec)	~ 1000	~ 1000	~ 600
Point-source sensitivity (μJy , SNR = 5)	65	65	~ 750

Table 4-8. Performance characteristics for a 1.0-meter space-based IR telescope in either L1 or Venus-trailing orbit.

Note: Since point-source sensitivity varies with ecliptic latitude, longitude, and heliocentric distance, the point-source sensitivity is specified near the midpoint of the viewing zones for each survey, or (0°, 90°) for L1, and (0°, 180°) at 0.7 AU heliocentric distance for the Venus-trailing survey.

Parameter	L1	Venus-trailing
Aperture (m)	1.0	1.0
Bandpass (μm)	6–10	6–10
Field of view (°)	1.7 x 3.5	1.7 x 3.5
Viewing zones (solar elongation, °)	±(45–120)	180 ± 75
Viewing zones (ecliptic latitude, °)	±20	±20
Number of pixels	32 million	32 million
Plate scale (arcsec/pixel)	1.5	1.5
Fill factor (%)	95	95
Slew time (s)	80–120	80–120
Dwell time (s)	~150	~150
Image FWHM (arcsec)	2	2
Minimum background current (e-/s)	~1000	~1000
Point-source sensitivity (μJy, SNR = 5)	21	21

4.2.6.2 Detectors

Several types of detector architectures have been employed for ground- and space-based telescopes. Dark current varies with detector material, temperature, and cutoff wavelength (λ_{co}).

- *Indium antimonide (InSb)*: 256² InSb arrays were used for the 3.6 μm and 4.5 μm channels on the Spitzer Space Telescope’s Infrared Array Camera (Fazio et al. 2004); the arrays operated at ~15 K during Spitzer’s prime mission and at ~29 K during the Spitzer Warm Mission after the depletion of Spitzer’s liquid helium coolant (Storrie-Lombardi and Dodd 2012). However, InSb detectors cut off at ~5 μm, which is shortward of the 10 μm thermal emission peak for a ~300 K NEO.
- *Mercury cadmium telluride (HgCdTe)*: HgCdTe arrays can operate over the range ~0.4 μm to longward of 10 μm. Wavelengths between 1 μm and 3 μm are referred to as short-wavelength IR, or SWIR; wavelengths between 3 μm and 5 μm are defined as midwave IR, or MWIR; wavelengths longer than 5 μm are referred to as long-wavelength IR, or LWIR. They operate based on thermal excitation, so the temperature required to achieve low dark currents depends on the cutoff wavelength. At $\lambda_{co} = 5 \mu\text{m}$, dark current for >90% of pixels is ~0.01 e-/s at ~50 K and ~0.3 e-/s at ~75 K (Rauscher et al. 2011). For $\lambda_{co} = 10 \mu\text{m}$, dark current for >90% of pixels is <200 e-/s at 40 K (McMurtry et al. 2013; 2016; Dorn et al. 2016).

Megapixel HgCdTe arrays have been flown on a number of scientific and strategic space missions, with cutoff wavelengths λ_{co} ranging from ~1.7 μm to 5.4 μm. Missions that have employed SWIR HgCdTe arrays in 1024² formats include the Orbiting Carbon Observatory 2 ($\lambda_{co} = 1.7 \mu\text{m}$; Pollock et al. 2010) and the Wide-Field Camera 3 ($\lambda_c = 1.7 \mu\text{m}$; Baggett et al. 2008). The WISE mission used 1024²

MWIR HgCdTe arrays for its 3.4 μm and 4.6 μm channels (Wright et al. 2010; Mainzer et al. 2008). Arrays that are 2048² MWIR ones are also space-qualified for use in the Near-Infrared Camera and Near-Infrared Spectrometer instruments (both with $\lambda_{\text{co}} = 5.4 \mu\text{m}$; Greene et al. 2010) for the James Webb Space Telescope, and have flown on the Commercially Hosted Infrared Payload (CHIRP) mission (Levi et al. 2010; Ewart and Lowell 2011).

Longwave IR HgCdTe arrays suitable for astronomical backgrounds have not yet flown in space. However, LWIR HgCdTe array performance for low noise applications has advanced significantly in the last 10 years. The root cause of high dark current pixels is defects in the material (Bailey et al. 1998). In 2003, operability was measured to be 50–70% in 512² format LWIR arrays (Bacon et al. 2005; Bacon et al. 2010). Improvements in the material growth and hybridization processes have resulted in a substantial reduction in the density of electrically active defects over the past 15 years. NASA technology development funds were awarded to NASA’s Jet Propulsion Laboratory (JPL) and the University of Rochester (UR) in 2011 to mature LWIR detector technology. Subsequently, a team consisting of JPL, UR, and Teledyne Imaging Systems (TIS) produced a series of 1024² LWIR arrays with >90% operable pixels (McMurtry et al. 2013). Cutoff wavelengths ranged between 10.3 μm and 10.7 μm . The devices were bonded to a TIS HAWAII 1RG (H1RG) multiplexer (see below). Subsequent work has shown the devices to be robust against charged particles (Girard et al. 2014; Dorn et al. 2016; McMurtry et al. 2016). The performance of the arrays is summarized in Table 4-9.

Table 4-9. Required and current best estimate performance for LWIR HgCdTe arrays.

Parameter	Requirement	Current Best Estimate
Array format	1024 × 1024	2048 × 2048
Pixel size (μm)	18	18
Cutoff wavelength (μm)	10.0	10.7
Operating temperature (K)	40	35-40
Dark current (e-/s)	200	1
Read noise (correlated double sample; e-)	30	22
Well depth (e-)	>44,000	65,000
Quantum efficiency (%)	>55	65
Operability	>90	95

The 1K × 1K format arrays fabricated by the NEOCam team in 2011 have been demonstrated to have dark currents well below the required 200 e-/s, with >90% of pixels having dark currents ≤ 1 e-/s (McMurtry et al. 2013). Quantum efficiency (QE) has been demonstrated to be >60% before the antireflection coatings were applied; this is comparable to the QE measured on MWIR and SWIR devices. Similarly, read noise is consistent with the level measured for SWIR and MWIR devices. In 2015, the project fabricated 2K × 2K arrays, and they have been demonstrated to perform at the same level as the 1K × 1K arrays (McMurtry et al. 2016).

- *Silicon-arsenic (Si:As)*: Si:As detectors are silicon arrays that are doped with arsenic atoms through ion implantation. Unlike InSb and HgCdTe arrays, space-suitable arrays rely on impurity band conduction (IBC), meaning that charge is carried through impurities introduced by the

implantation of the arsenic atoms. Because these arrays rely on IBC, they must be cooled to ~7–8 K to reduce thermal generation of charge carriers so that IBC dominates. Si:As arrays are responsive to light from ~5–28 μm . A 256^2 array was used in the Spitzer Multiband Imaging Photometer instrument (Rieke et al. 2004), and a $1\text{K} \times 1\text{K}$ version was employed for the 12 μm and 22 μm channels for WISE (Wright et al. 2010; Mainzer et al. 2008). A $1\text{K} \times 1\text{K}$ version has been space qualified for the Mid-Infrared Instrument for the James Webb Space Telescope (Ressler et al. 2015).

4.2.6.3 Readout Circuits

A source-follower astronomy readout (such as the HAWAII family of devices manufactured by Teledyne) is the preferred choice for HgCdTe arrays, as opposed to capacitive transimpedance amplifier (CTIA) or direct injection readouts. While these latter readouts are extensively used for tactical and Earth-observing applications, CTIA and direct injection readouts expend too much power and are generally too noisy for low-background astronomy applications. The source-follower input of the HAWAII readouts requires that reverse bias be placed across the detector to store adequate charge.

Historically, the low-noise, low-power source-follower input circuit typically used for astronomy applications has prevented the use of LWIR HgCdTe detectors because of their susceptibility to defect-assisted tunneling currents under reverse bias (Bacon et al. 2005). However, significant reduction in material defects achieved by Teledyne in the last 15 years has allowed LWIR HgCdTe focal plane arrays to be produced with high well depth, low dark current, and low read noise.

Teledyne's HxRG ($x = 1, 2, \text{ and } 4$) family of readouts is fabricated in a 0.25 μm CMOS process that provides radiation tolerance suitable for use in Earth-orbiting or interplanetary environments. The HxRG arrays share a common architecture that is optimized for low-light-level astronomy applications and that addresses the following requirements: (1) lowest readout noise, (2) ability to track and compensate for effects of noise on bias voltages, (3) low-power operation, (4) no amplifier glow, and (5) multiside buttability for making large mosaic focal plane arrays.

The H2RG readout has been selected for use in the James Webb Space Telescope (JWST) and has been qualified to Technology Readiness Level (TRL) >6; this readout has been hybridized to the $2\text{K} \times 2\text{K}$ LWIR detector material by the NEOCam team.

4.2.6.4 Telescope

For a 0.5-meter aperture, a three-mirror anastigmat (TMA) design can produce a low-distortion, wide-field imager. The TMA has no central obscuration and can be implemented in an all-aluminum design so that the telescope shrinks uniformly as it cools. An FOV of ~12 square degrees results from using a plate scale of 3 arcsec per pixel with a mosaic of 16 megapixels. For a larger 1-meter aperture, we assumed that doubling the aperture size using a similar TMA implementation produces a FOV of ~6 square degrees, assuming a mosaic of 32 megapixels with 1.5 arcsec per pixel plate scale.

4.2.6.5 Cooling Systems

Infrared telescopes require operating temperatures of ~35–40 K for their detectors and ~<60 K for their optics. Several cooling options are available that have been demonstrated on other missions; these options include passive cooling and active methods such as cryostats or cryocoolers.

- *Passive Cooling:* Passive cooling relies on using the nearly ideal thermal environment of space to reach operating temperatures. In Sun-Earth L1 orbit, the flight system has an uninterrupted view of cold space with an effective temperature of ~ 5 K, with a small heat load from Earth. Passively cooled designs radiatively and conductively isolate detectors and optics from the Sun and the warm spacecraft bus. Radiators dissipate heat. The design uses thermal shields, high-emissivity paint, multilayered insulation, and low-conductivity struts to maintain operating temperatures over the range of orientations that result from the mission's observing and downlink modes.

The principles of passive cooling have been demonstrated on previous missions and were proposed in the 1980s and early 1990s for the EDISON/POIROT mission concept (Lee et al. 1990; Thronson et al. 1992; Hawarden et al. 1995). After its superfluid helium was depleted in 2008, the Spitzer Space Telescope's coldest focal planes warmed from the original operating temperature of 1.4 K. Now, the Spitzer Warm Mission is operating with its 3.6 μm and 4.5 μm focal planes at ~ 29 K (Storrie-Lombardi and Dodd 2010). Similarly, after the WISE mission's solid hydrogen cryogen was depleted, the telescope warmed to 74 K. Now renamed NEOWISE, it is currently operating at ~ 74 K at 3.4 μm and 4.6 μm (Mainzer et al. 2014).

The thermal environment is a sensitive function of the orbit. For example, NEOWISE cannot equilibrate below ~ 74 K because of the heat load from the Earth in its 525-kilometer orbit. The heat load from the Sun for observatories in heliocentric orbits interior to Earth increases as the inverse square of the heliocentric distance; therefore, a mission in Venus-trailing orbit has a heat load that is double that of a spacecraft at L1 or L2. A background-limited IR telescope operating at $\sim <60$ K has not yet been demonstrated for spacecraft interior to Earth's orbit. At this distance from the Sun, passive cooling is not an option; instead, cryocoolers would be required to achieve operating temperatures. In L1 orbit, either passive cooling or a cryocooler implementation is possible. For purposes of this study, we assumed that either passive cooling or cryocoolers would achieve the required temperatures; the only impact of using the cryocooler is to system cost.

- *Cryocoolers:* Cryocoolers can in principle simplify ground testing, but this benefit must be weighed against their cost, mass, power, and risk of failure, plus possible complications from vibrations. At present, a cryocooler exists that could in principle achieve the required temperatures for the estimated heat load; however, approximately one to two years of work are needed to bring a suitable vibration isolation system to TRL 6. The cryocooler consumes 250 W of additional heat that must be rejected.
- *Cryogenics:* A liquid helium cryostat can readily achieve temperatures of ~ 4 K; filling the cryostat with superfluid helium allows for even lower temperatures (e.g., the Spitzer Space Telescope during its fully cryogenic prime mission, which operated at 1.4 K; Werner et al. 2010; Finley et al. 2006). The IRAS, ISO, Herschel, and AKARI missions also used cryostats for cooling. Spitzer's cryostat lasted for 5.5 years, the longest cryogenic lifetime for an astronomy mission.

4.2.6.6 Co-hosted IR Instrument

An IR instrument co-hosted on a GEO platform can also be considered for surveying for PHOs. In this case, the telescope would be hosted on the nadir deck of a large communications or government satellite and would point in its velocity or anti-velocity direction, conducting its survey on or near the equatorial plane. Within a 24-hour period, the FOV will drift 15 degrees every hour, setting a fundamental limit on the dwell time for each pointing. Viewing constraints will have a significant

impact on a geostationary co-hosted instrument. To maximize the number of NEOs detected, it is desirable to observe as close to the ecliptic plane as possible; however, this proximity to the ecliptic plane results in the Sun passing within 23 degrees of the FOV once a day, and twice a year the Sun will pass through the center of the FOV.

As with a free-flying spacecraft, an IR telescope on a GEO platform must still be cooled to $\sim <60$ K, and its detectors must be cooled to $\sim 35\text{--}40$ K to operate at $6\text{--}10$ μm . The close proximity of the Sun to the telescope boresight therefore requires the use of an actuator-driven cover that can open and close as needed to keep the Sun out. The specifications on the baffles and lid, as well as the tolerance to scattered light and heating, set the lower limit on the solar elongation and thus the fraction of the 24-hour orbit that is usable for observing NEOs. As a baseline, we assume that the instrument would be baffled in such a way as to support observations as close as 70 degrees from the Sun on either the morning or evening sides.

In addition to a cover mechanism, a two-axis pointing mirror is needed to stabilize the image and flip between neighboring FOVs in the direction of increasing/decreasing equatorial longitude. We assume that the time it takes to slew the pointing mirror between positions is $<10\%$ of the on-sky time. The mirror would only be required to articulate a small amount in the second (equatorial latitude) axis. The steering mirror must be at least as large as the instrument's primary mirror and must be cooled to the same temperature as the rest of the optical system.

To maintain its temperatures, the instrument would need to employ cryocoolers, such as a pulse tube cryocooler. The pulse tube cold head has no moving parts to cause wear; the compressor uses flexure springs to hold and maintain close noncontacting alignment for the moving motors and pistons. The instrument's aperture would double as a deployable radiator; however, flexible loop heat pipes have only been flown in missions requiring a limited number of deployments and have not been used as a repetitive mechanism. More work needs to be done to verify fatigue life in such a joint.

With a commercially hosted payload, the customer does not pay for the spacecraft, launch, or operations but only for hosting costs (Andraschko et al. 2011; Hosted Payload Guidebook 2010), which include a hosting fee, payload integration, and spacecraft services (e.g., transponder leasing for sensor data downlink) that would not occur in the absence of the hosted payload. This hosting business model was demonstrated with the U.S. Air Force's CHIRP program (Simonds et al. 2010; Schueler 2012).

While the hosted payload must conform to the available volume on the host spacecraft, it is also beneficial to the hosted payload customer to minimize hosted mass because the spacecraft's commercial operator's hosting price rises with increased hosted mass. This is not due to increased launch cost of adding hosted mass to the spacecraft, but is due to reduced spacecraft on-orbit "maneuverable life" caused by reduced fuel to compensate for hosted payload mass. Fuel tanks are filled to take the spacecraft to maximum launch mass. A hosted payload requires cutting a kilogram of fuel for every kilogram of hosted mass to stay within maximum satellite launch mass, thus reducing end-of-fuel-life revenue.

Co-hosted GEO payloads are provided power and uplink/downlink interfaces to the instrument electronics from the host spacecraft. Data rates up to ~ 100 Mbps have been demonstrated.

4.2.7 Future Visible Space-Based Systems

We have considered three different space-based visible telescopes in this study. These observatories are assumed to use CCD technology identical to that of the ground-based visible telescopes described in Table 4-5 and spacecraft bus designs similar to those of the IR space telescopes. Table 4-10 summarizes the assumed parameters of the three visible space telescopes, which range in aperture from 0.5 meters to 2 meters. The three telescopes were each taken to be in low-Earth, GEO, L1, L2, and Venus-like orbits, with instantaneous fields of regard given in Table 4-9.

All systems were assumed to use the E2V CCD, which contains $9.2\text{K} \times 9.2\text{K}$ pixels with a 10-micron pitch. The focal planes are tiled with a 2×1 mosaic for a total of 170 million pixels. With a 42-second exposure cycle (12-second exposures plus 30 seconds for slewing between adjacent fields), the data volume that must be downlinked each day is ~ 2 Tbits after Rice compression. If data transmission times are limited to ~ 1 hour/day, this limit necessitates a data rate of ~ 700 Mbits/s. For Earth-orbiting systems, this data rate is achievable with standard technology. However, for systems in L1/L2 or Venus-like orbits, a laser communications system and some form of onboard data processing to reduce the data volume are needed.

Table 4-10. Performance characteristics for three space-based visible telescopes.

Parameter	Telescope 1	Telescope 2	Telescope 3
Aperture (m)	0.5	1	2
Bandpass (μm)	0.4–1.0	0.4–1.0	0.4–1.0
Field of view ($^{\circ}$), including gaps	10.6 \times 5.3	5.3 \times 2.6	3.5 \times 1.8
Viewing zones (solar elongation; $^{\circ}$)	180 \pm 135	180 \pm 135	180 \pm 135
Viewing zones (ecliptic latitude; $^{\circ}$)	\pm 80	\pm 80	\pm 80
Number of pixels	170 million	170 million	170 million
Plate scale (arcsec/pixel)	2	1	0.69
Fill factor (%)	99	99	99
Slew time (s)	30	30	30
Dwell time (s)	24	12	12
Image FWHM (arcsec)	1	0.5	0.5
Point-source sensitivity (mag, SNR = 5)	21.7	22.8	23.8

Space-based visible telescopes benefit from the lack of atmospheric distortion to the image. While the “seeing” of a ground-based telescope typically dominates its image quality, a space telescope does not suffer from this effect. Instead, the image quality of a space telescope is determined by a combination of the optical system’s diffraction limit (a best-case scenario), any optical aberrations, and the spacecraft’s pointing stability during the integration interval. The latter is likely to dominate image quality for a search system with a fast step-and-settle time. The attitude control system for the space-based visible telescopes was assumed to complete slews between integration intervals in the same time as IR telescopes with the same aperture diameter.

5 SEARCH STRATEGY

This section presents a relatively minor update to the search strategies covered in the Science Definition Team (SDT) 2003 report titled “Study to Determine the Feasibility of Extending the Search for Near-Earth Objects to Smaller Limiting Diameters.” While infrared observing technology has improved substantially and been successfully demonstrated via the Wide-field Infrared Survey Explorer (WISE) mission, the optical survey search strategy story is much the same now as it was in 2003. For either infrared or visual wavelength bandpasses, covering large areas (thousands of square degrees of sky per night) to faint magnitudes or infrared sensitivities is essential to completing the inventory of small near-Earth objects (NEOs) and providing warning of imminent impactors.

5.1 Search Regions

Historically, ground-based optical surveys have searched the opposition region of the sky for NEOs (Figure 5-1). This is a matter of simple efficiency: asteroids are at their brightest when they are in proximity to the Earth and are observed at full phases. Additionally, this area of sky is easy to observe because it is highest in the sky at midnight and can be observed for several hours each night. In addition to being easy to observe, NEOs discriminate well from the background population of main-belt asteroids at opposition, and nightly parallax can help improve orbit determinations. Since the 2003 NEO SDT report, a number of improvements have been made to methods used to discriminate NEOs from main-belt objects, furthering the effectiveness of the opposition search strategy. The Minor Planet Center’s (MPC) Digest 2 program (Keys 2006; McNaught 1999) has been used at the MPC to assist in discriminating NEOS from main-belt asteroids (MBAs) and in selecting objects for placement on the NEO Confirmation web page.

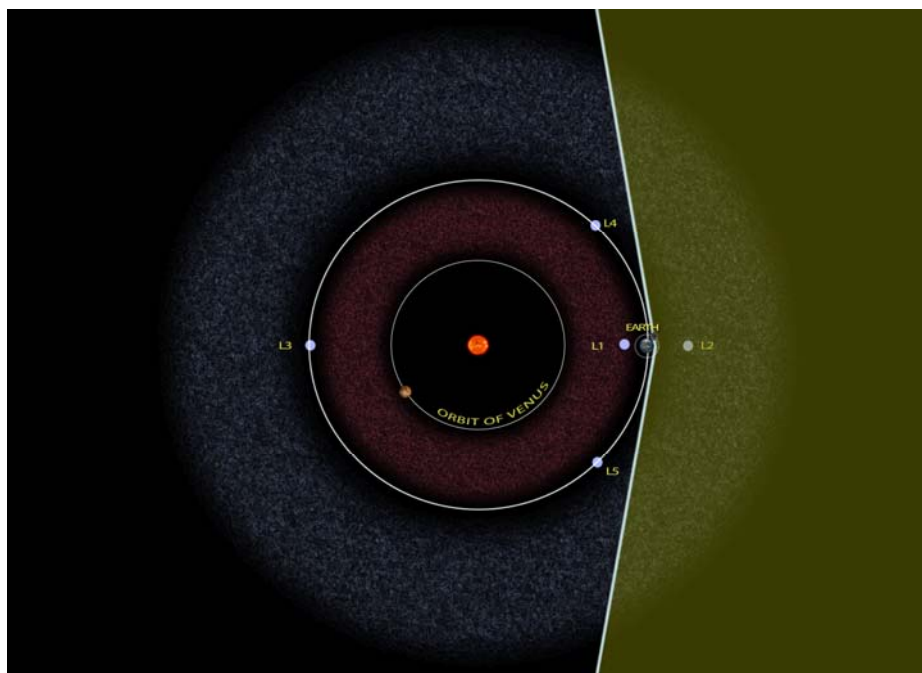


Figure 5-1. Approximate search region for a ground-based optical telescope is highlighted in green for this particular location of Earth.

All optical systems modeled in this report are capable of covering very large areas of sky (more than 10,000 square degrees) each month with multiple visits sufficient for linkages and orbit determination. Because of the volume of sky and faint limits, generally >23rd magnitude, all of these systems are designed for self-follow-up of all discoveries. The systems will not be able to rely on meter-class telescopes to confirm NEOs, as is currently done.

Space-based observatories can easily survey areas of sky that are larger than those surveyed by ground-based systems. In addition, the longer duty cycle and better observing conditions of space-based systems can substantially improve survey performance. Moreover, surveying from space can be done in the infrared as well as visual wavelengths.

Infrared telescopes at the Earth-Sun L1 Lagrange point can best survey the sky from ~45 degrees to 120 degrees solar elongation (Figure 5-2). When telescopes are placed in a heliocentric orbit interior to the Earth, the optimal regions shift more to the anti-Sun direction, e.g., 80–180 degrees solar elongation. Both infrared options provide varying degrees of complementary sky coverage to a ground-based optical survey.

By combining infrared and optical efforts, one can complete a survey faster by targeting different objects or provide more detailed physical observations by obtaining both optical and infrared brightness measurements. The infrared brightness is much less dependent on phase angle, thus making small solar elongation regions even more profitable to survey in the infrared. Natural exclusion zones from L1 are the region around the Sun and the opposition region containing the Earth, as well as smaller restriction zones associated with the Moon. The point is that near-Sun regions of the sky are much more difficult to observe optically from the Earth, and it is precisely the most efficient area in which a thermally operating system can be used for NEO discovery. Optimizing a near-Venus-orbit observation must contend with higher background than an L1 survey caused by zodiacal dust but is not affected by the Earth or Moon (Figure 5-3).

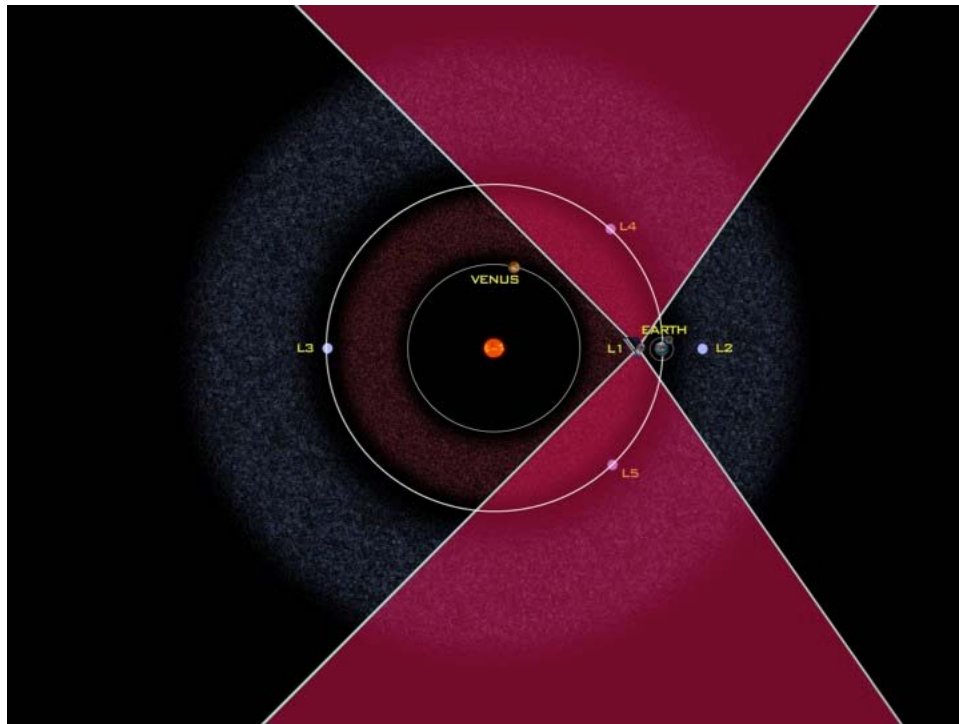


Figure 5-2. Approximate search region for an infrared survey operating at the Sun-Earth L1 (Lagrange) point is highlighted in red for this particular location of Earth.

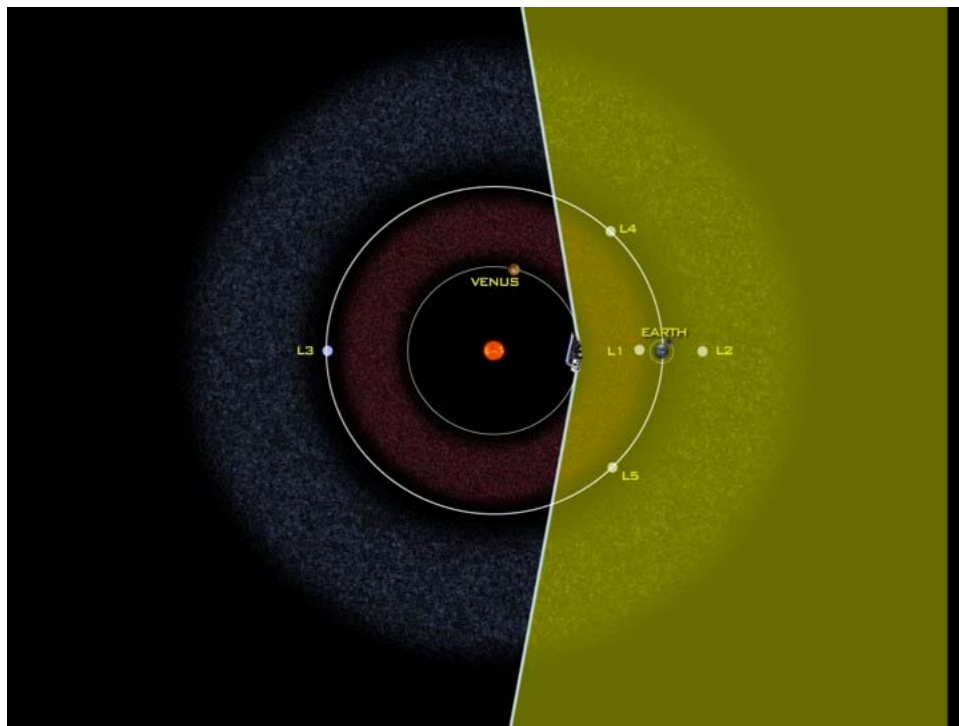


Figure 5-3. Approximate search region for telescope operating with an orbit similar to that of Venus is highlighted in green for this particular location of the sensor.

5.2 Infrared Search Strategy—Historical Approach

While the history of search strategy used in ground-based optical surveys is now decades old, we have but one example of an infrared telescope routinely performing NEO discoveries. The WISE mission (Wright et al. 2010) conducted an all-sky survey at four infrared bands using a single cryo-cooled detector. The WISE survey pattern was a simple scanning technique that covered the sky in a 7-arcminute-wide patch from ecliptic pole to ecliptic pole. This strategy was designed for astrophysics survey goals. WISE was simply designed to cover the entire observable fixed sky over approximately six months in the four infrared bands. While WISE turned out to be quite efficient at discovering NEOs (Mainzer et al. 2011e), nearly all discoveries required follow-up from other ground-based observing stations because the telescope was unable to perform targeted follow-up.

5.3 Cadence and Linking Issues, and Cadence Requirements

The observational cadences applied to all systems modeled in this report are identical and intentionally conservative. Each field is observed four times per night, with a baseline of ~1 to 2 hours from first to last image. In this baseline scenario, each image is assumed to be the result of a single read from a detector with its full share of random noise (e.g., readout noise) and quasi-random noise (e.g., cosmic-ray strikes). Other strategies that include robust stacking of multiple readouts are not considered here and would require their own detailed analysis. The assembled four positions pertaining to a single object are called a tracklet. The same fields are subsequently revisited at least two more times over the next ~21 days. Linking together the individual tracklets (at least three) of data with this periodicity to form a track, and computing the resulting orbits, is currently considered routine operation at the MPC. Orbits determined from tracks of this length can be easily identified with future tracks observed with a similar cadence. The computation of the impact hazard from tracks of this length is also routine, and with the expected astrometric improvement from new star catalogs, we can expect this computation to be more accurate than current ones. For the purposes of this report, an object is deemed to be cataloged if it is observed on a minimum of three separate tracklets joined to form a track with an interval of about one day between the tracks. If the interval between the first and third tracklet is greater than 25 days, the object will not be considered to be cataloged because of the difficulty of linking tracklets over this long of an interval. However, it should be noted that if pairs of tracklets can be joined together over intervals of ~20 days, these tracklets can often be used for rudimentary hazard calculations and short-term ephemeris predictions even in the absence of the critical third tracklet.

5.4 Synthetic Tracking and Two-Image Cadences

The SDT has chosen not to address the synthetic tracking technique for NEO discovery (cf. Shao et al. 2014; see extended discussion in Section 4) in this section because this method is not yet effectively demonstrated for the discovery of large numbers of NEOs. Likewise, observational cadences using less than three images have yet to be demonstrated on a large scale for NEO discovery; if successful, such cadences would allow coverage of larger areas of sky than are discussed here. It should be noted that the combination of large areas of sky (~10,000 square degrees per month with multiple visits sufficient for orbit determination) to the faintest limiting magnitudes is required to speed the search for NEOs much smaller than 1 kilometer in diameter. Simply increasing sky coverage at the expense of sensitivity will not provide a meaningful increase in the discovery rate.

5.5 Astrometry

Astrometric catalogs now are far superior to those used in the early 2000s. The current state of the art is the Gaia catalog (Lindegren et al. 2016), which contains more than a billion stars measured with astrometric accuracy of <0.01 arcseconds. Astrometric catalogs of this accuracy and images that fully sample the average point spread function will allow extremely precise astrometry and will place new demands on the precision of timing when an exposure is taken. Secondly, the ability to measure precise positions of faint objects at low signal-to-noise ratios will contribute to substantial astrometric error. What we do know, however, is that there will be effectively no contribution from star catalog error to minor planet measurement error. With such precise measurements possible, future linking techniques and orbit determinations will be much more precise and accurate than in the past.

5.6 Cataloging versus Warning Strategies

The default cadence selected in this report was chosen conservatively to ensure ease of operation and compatibility with existing linking and orbit determination approaches. Existing methods to compute impact hazards on both short and long arcs (via NASA's Sentry or Scout monitoring systems, or the methods at NEODys2 [Near Earth Objects Dynamic Site]) work extremely well with the minimum cadence requirements set in this report. Orbits with ~ 21 -day arcs are more than sufficient for predicting potential impacts with the Earth decades in the future, especially with the high quality of the astrometry expected with these systems.

In this report, we define warning as the time from recognition of an impact threat to the actual impact. For large objects that can be detected at great distances from Earth, simply cataloging them will generally provide decades of warning. If an object has a nonzero impact probability far in the future, the object can be selected for additional astrometric measurements, or radar measurements, when it comes within range in order to confirm or rule out an impact. However, if the warning time is measured in only days to months, it is paramount to determine the probability of impact as soon as possible if only to allow an area sufficient time to be evacuated. Recent advances in orbit determination and computation of impact probabilities have allowed much better recognition of future impacts, even with arcs of only about an hour, with the Scout impact-monitoring system. Since impacting objects can appear virtually any place in the sky on their final approach, wide-field systems such as described in this report are essential to provide adequate warning. It must be stressed, however, that $\sim 50\%$ of all impactors will come from the sunward hemisphere and will thus be largely invisible to ground-based systems during final approach of those impactors. To provide the longest warning possible, sensitivity and sky coverage are critical to finding the objects before they are on final approach. Systems at Earth Lagrange points or from Venus-like orbits may provide more warning than Earth-based systems will provide, although many small impactors will not be visible at even a tenth of an astronomical unit from the Earth. In general, warning and cataloging systems are compatible with similar observing strategies and are thus complementary. Large systems with faint limiting magnitudes or sensitivities may allow discovery of impactors before their final orbit and thus provide much longer warnings times.

5.7 Notes on Survey Optimization

It should be noted that the optimization of search strategies, such as was performed in the 2003 NEO SDT report for ground-based telescopes, has not been undertaken for the simulations performed in this report. While many of the systems presented here are capable of complete coverage of the field of regard on multiple visits per month, the largest aperture infrared systems have fields of view sufficiently small and exposure times sufficiently long that they cannot cover large areas of sky (>10,000 square degrees) with enough visits to meet the cataloging requirement defined in Section 5.3. As such, integral completeness numbers could be higher if appropriate telescope-specific search strategies were undertaken. We expect optimization could influence completeness numbers on the 10- and 20-year baseline survey efforts by <10% at most.

5.8 Findings

All systems simulated in this report are capable of covering large areas of sky to faint limiting magnitudes or infrared sensitivities. Optical surveys perform best when surveying large areas of sky at opposition, and near-Earth space-based infrared surveys cover complementary areas of sky at small solar elongations while heliocentric space-based surveys cover a completely different search volume. A combination of ground-based visible and space-based infrared assets provides excellent sky coverage and large discovery rates when both systems perform optimally. Each system will observe similar areas over multiple times each month to perform self-follow-up of their discoveries. Observing at high faint limits and infrared sensitivities and covering large areas of sky allow the longest warning times for imminent impactors. Search regions for warning and cataloging are similar, and warning is best accomplished by using a combination of assets. Advances in astrometric catalogs, linking techniques, and recognition of NEOs against the background of main-belt asteroids will enable future surveys to operate more efficiently and accurately than did surveys of the past.

5.9 Difficult-to-Find Objects

For every survey, real or simulated, there is a residual population of objects not discovered or cataloged by that survey. If an object is to be discovered, it must be in the search area and bright enough to detect, and it must remain so for a time period long enough to allow for cataloging, say a few weeks at a minimum. Conversely, the objects that are not cataloged either do not enter the search area for long enough, or while in the search area, they are not bright enough for long enough.

For small objects, just being in the search region is typically insufficient for discovery because they must also be relatively close to the observatory in order to be bright enough to detect. However, even for objects with large diameters, typically a few percent remain undiscovered after a 10-year survey, whether ground-based or space-based, primarily because these objects never enter the search region. They are bright enough that if they did enter the search region, they would be readily detected. These cases represent hard-to-find objects that are on peculiar orbits, a sort of blind spot for an observatory. Of course, while these objects remain undetectable in their orbits, they are also not an immediate impact hazard to Earth; however, objects of this nature are susceptible to short warning impacts, or no warning at all, particularly if they are coming from the direction of the Sun and we rely only on ground-based surveys.

These hard-to-detect orbits come from three primary categories:

1. *High-eccentricity, long-period orbits.* Objects in this category of orbit are only bright enough to detect when at or near perihelion, and yet they reach perihelion only a few times in a 10-year survey. For example, objects with an orbital period over five years (semimajor axis ~ 2.9 AU) reach perihelion no more than twice in 10 years. For a semimajor axis larger than ~ 4.7 AU, the orbital period exceeds 10 years, and there is at most a single perihelion passage in a decade-long survey. Thus, to detect such an object, the observatory must be situated at the right orbital longitude at the right time to ensure that the body will enter the search region when it brightens around perihelion. For some fraction of the objects in this category, those fortuitous observing circumstances do not occur, and so there is no discovery opportunity.
2. *Long-synodic period orbits.* These objects orbit the Sun with nearly the same orbital period as that of the survey telescope. For a ground-based survey, for example, any asteroids that have a one-year period will stay at roughly the same orbital longitude relative to the Earth since they revolve at the same rate on average. If the asteroid has orbital eccentricity, there will be some oscillation about the mean, but the key point is that if that asteroid is on the far side of the Sun from Earth, then it will remain unobservable for as long as its period matches that of Earth. The same is true for space-based observatories in Earth orbit or at an Earth-Sun Lagrange point, such as L1. Of course, if the orbital period of the asteroid is slightly greater or less than one year, then it will slowly advance or fall back toward the longitude of Earth. However, if the orbital period is within ~ 10 days of one year, then the synodic period—the time it takes for the asteroid to “lap” the Earth—is at least 40 years, which means that the relative longitude can change by no more than 90 degrees in 10 years. Thus, if the geometry is unfavorable, such an object could remain obscured by the Sun for the full duration of a decade-long survey. Similarly, a survey telescope orbiting with the same orbital period as Venus (225 days) would not be able to detect asteroids with that orbital period if the asteroid were on the far side of the Sun at the start of the survey. If the asteroid has an orbital period within about five days of the Venus period, then the synodic period relative to Venus is again more than 40 years, and such an asteroid can evade detection during a 10-year survey.
3. *Resonant orbits.* Objects with an orbital period that is in exact ratio with that of Earth represent a generalization of the long-synodic period orbits, which are in the 1:1 resonance. Objects that are in a resonance can only repeat the same Earth-relative trajectory, and if that happens to avoid a survey's search region, then the object will not be discoverable. Figure 5-4 depicts the Earth-relative trajectories of some example resonant orbits and shows that such cases never enter the typical opposition search region. Some resonances actually exhibit a dynamical “shepherding” that causes objects to remain near the resonance despite other perturbations, but most objects are slowly drifting relative to the resonant trajectory so that eventually they do drift into the search region; however, this may not happen until well after the 10-year survey has concluded.

For ground-based observatories located at mid-latitudes, the blind spot becomes more literal and less figurative. If the survey site is situated, say, in the northern mid-latitudes, much of the southern skies are not searchable at all. This issue can accentuate the difficulty in detecting certain objects, which may be only rarely detectable because of high eccentricity or a resonance, since these objects may only brighten enough for detection when they are too far south for a northern observatory, or vice versa.

Because survey systems in a Venus-trailing orbit revolve about the Sun with a different period from that of Earth, there is a remarkable synergy between such surveys, which can readily find objects in an Earth resonance, and surveys that stay on or near Earth, which can readily discover objects in the Venus resonances. Therefore, the combined efforts of a Venus-trailing and, for example, a ground-based survey will serve to effectively eliminate the resonance “blind spots” that each observatory has when operating individually. Such a survey network will rapidly raise the completeness at large sizes to ~100%, whereas the individual surveys tend to stall at ~97% completeness at the largest sizes. Figure 5-5 depicts the objects not found in simulations by an Earth-based survey and those not found by a Venus-trailing survey. The resonant “striping” in semimajor axis is clearly visible for either approach acting alone. But these stripes are substantially removed by the joint effort of both surveys, with the exception of the objects near semimajor axis of 2.1 AU, which happen to be close to the 3:1 Earth resonance and the 5:1 Venus resonance. Some fraction of the high-eccentricity, long-period orbits at upper right are not found by either survey.

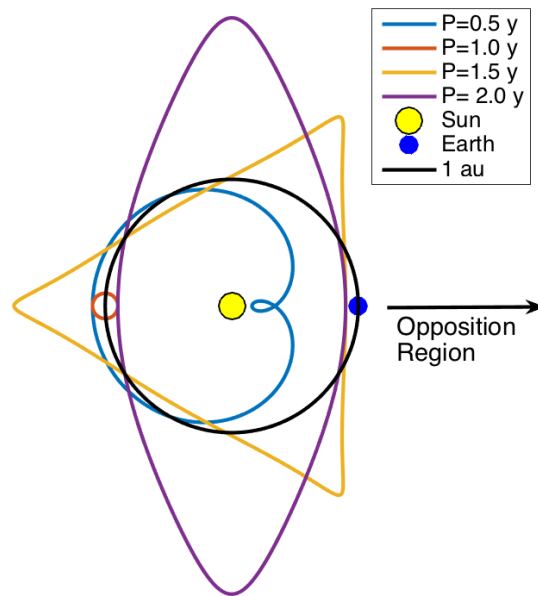


Figure 5-4. Rotating frame depiction of Earth-relative trajectories (the so-called rotating frame) of four example PHA orbits in resonance with Earth. The Earth is always fixed at the right of the Sun in this depiction, and the asteroids circulate on the depicted paths with respect to the Earth. In all four of these examples, the asteroid always remains more than 90 degrees from the opposition region.

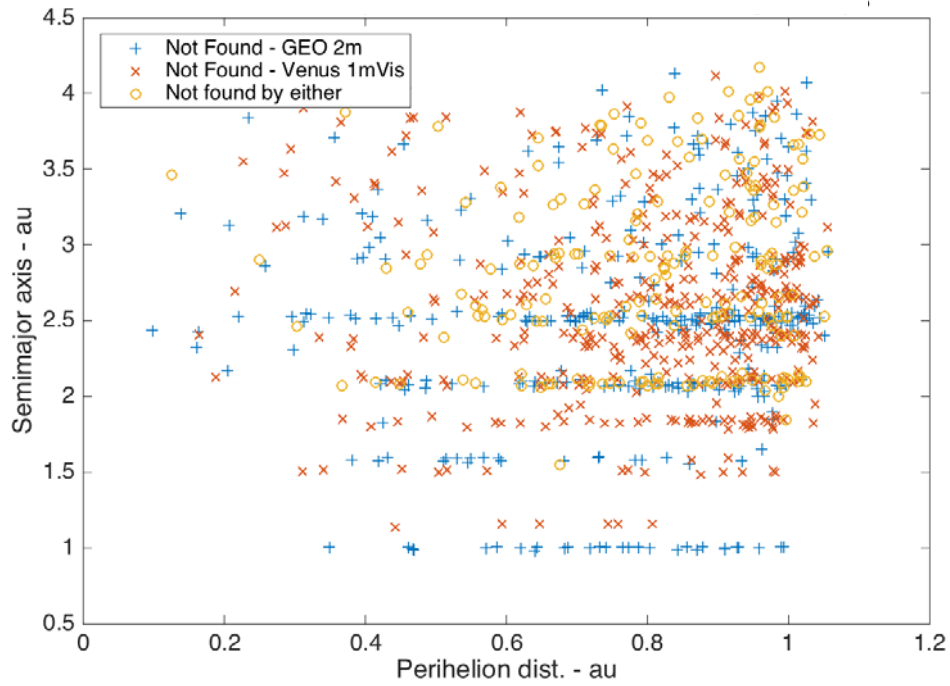


Figure 5-5. Objects not found by the GEO 2 m survey and not found by the Venus 1 m visible band survey, revealing the resonant objects residing in horizontal strips. The combined catalog from the two surveys substantially removes the resonant hiding places, except for objects at semimajor axis ~2.1 AU, which are approximately in resonance with both Earth (3:1) and Venus (5:1).

This page is intentionally blank.

6 SIMULATION AND PERFORMANCE DESCRIPTION

Previous sections in this report have discussed population estimates, the impact risk associated with the population, candidate technologies to search for the population, and strategies for searching for and cataloging the population. This section begins to tie these parts together. It is an overview of the performance capabilities of the candidate technologies and the ability of each candidate system to reduce the risk uncertainty of the estimated population, using the recommended search strategies and cataloging requirements.

This evaluation is done with simulation, as was done for the 2003 Science Definition Team (SDT) report, “Study to Determine the Feasibility of Extending the Search for Near-Earth Objects to Smaller Limiting Diameters” (hereafter referred to as the 2003 NEO SDT report)

The approach used, and discussed in more detail below, includes the following:

- Defining the population used for the simulation
- Developing the simulation tools
 - FROSST for ground-based and space-based visible
 - Survey Simulation Tool (SST) for space-based infrared (IR)
- Validating the simulation tools
- Estimating a 2023 baseline population
- Summarizing results and observations

6.1 Population Model for Simulation

Determining the appropriate input population for the simulations is key to generating useful output. While many asteroid survey studies have focused on near-Earth objects (NEOs), it was determined that this study should only focus on NEOs that have a chance of impacting the Earth, i.e., objects with minimum orbit intersection distance (MOID) <0.05 AU, also called potentially hazardous objects (PHOs). Note that for the purposes of this report, all objects with MOID <0.05 are considered, regardless of the size and magnitude.

This study is focused on the risk of asteroid impacts and the ability to reduce the risk uncertainty. The greatest risk is carried by large objects even though they are fewer in number. Small objects, which number in the millions, carry significantly less risk but not zero risk. If a traditional PHO population model is used, the detection, or non-detection, of a single large object could significantly change the risk-reduction benefit of a single system. We face the issue of statistics of small numbers.

To avoid the statistics of small numbers problem, and simultaneously reduce the CPU processing required for the millions of small objects, a statistical representation of the PHO population was developed for the survey simulations. Ten thousand objects were put in each of 31 different bins. The bins are defined in diameter space and correspond to the H and diameter parameters in Table 2-1

and repeated in Table 3-5, plus three additional bins extending the population down to 10 meters. The orbital elements were provided by Granvik et al. (2016), and the H -diameter-albedo distributions were chosen to match Mainzer et al. (2011e, 2012). Using a statistical model allows for determining the percent completeness for each bin, in which each simulated detection represents 0.01% of the population. This method allows for the low statistical probability that there remain undiscovered large PHOs that carry significant risk.

The distribution of the statistical population input to the simulation is shown in Figure 6-1. The population is uniform in diameter (Figure 6-1a) and is relatively uniform in H , but includes tails caused by high and low albedo objects. Figure 6-1d is the distribution in H of a single diameter bin, corresponding to 126–159 meters. The distribution in this bin ranges from $20.25 \leq H \leq 24.24$, with a median of $H = 22.1$. For comparison, the $H = 22$ bin is frequently mapped to 140-meter objects when assuming an albedo of 0.14.

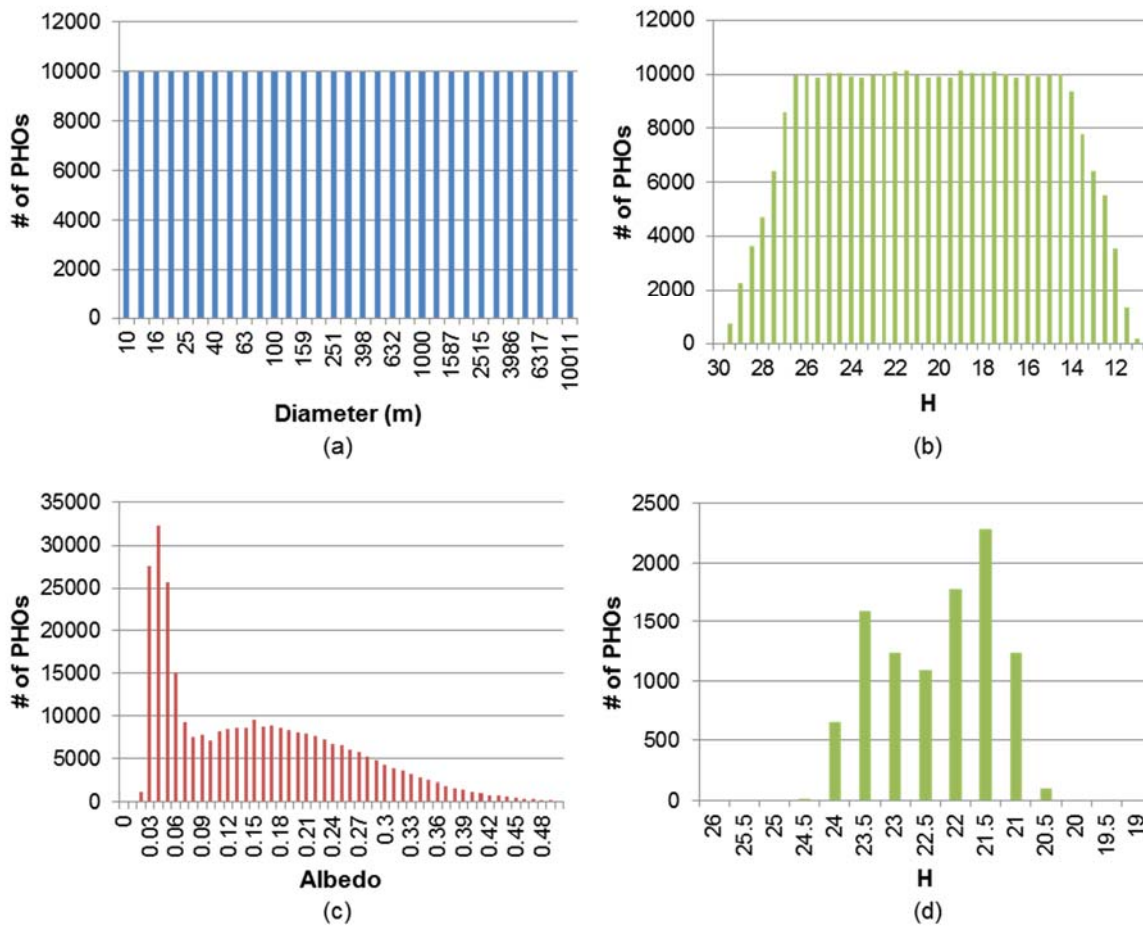


Figure 6-1. Distribution of statistical input population for the simulations: (a) diameter; (b) absolute magnitude H ; (c) albedo; (d) 126 m–159 m bin, distribution in H .

6.1.1 Population of Impactors for Warning

Any model representing the actual PHO population does not have enough potential impactors in it to accurately assess the capability of a system to warn against impactors. To reasonably assess a system's warning efficiency, a population of 990 impactor orbital elements was compiled by Steven Chesley for the 2003 NEO SDT report and reused for this study. All of the simulated impactors in this population had impact dates spread across a one-year period. To assess the warning efficiency of the systems, the orbital elements for these objects were combined with 990 unique H -diameter-albedo parameters for each diameter bin discussed above. The input population for the impactor study is the same 990 orbital elements, repeated 31 times, but with varying brightness and sizes, bin to bin.

6.2 Simulation Tools

System performance analysis for ground-based and space-based systems, as well as networked systems, requires robust, flexible simulation tools that assure parity between simulations. Two different simulation tools were used for this study. The Fast Resident Object Surveillance System (FROSST) was used for the 2003 NEO SDT report and used again for this study for the ground-based and space-based visible systems. With the addition of the space-based IR systems, a second simulation capability, the Survey Simulation Tool (SST; Mainzer et al. 2015, Grav et al. 2016) was added.

6.2.1 FROSST

FROSST began as a space surveillance tool for satellites and space debris. It was modified for the 2003 NEO SDT report to include asteroid search and detection. It takes as an input the catalog of either satellites and space debris or a catalog of asteroids, and a network of sensors, and then generates an output list of detections. Input sensor types include ground-based optical, ground-based radar, space-based visible, and space-based radar. FROSST is written in C++ and can accept new sensors and new sensor models, and it is easily adapted for enhanced detection models.

The underlying algorithm in FROSST is the signal-to-noise ratio (SNR) equation:

$$SNR = \frac{\text{Mean Target Signal}}{\text{RSS'd Noise}} = \frac{A_{\text{eff}} q_e \tau_{\text{optics}} \tau_{\text{path}} k_f N_0 10^{(-0.4V_m)} T_{\text{int}}}{\sqrt{\sigma_0^2 + \sigma_{DC}^2 + \sigma_B^2 + (\eta_{DC} \bar{S}_B)^2 + (\eta_{q_e}^2 + \eta_{\text{clutter}}^2) \bar{S}_B^2 + \sigma_T^2 + \text{other}^2}} \quad (6-1)$$

where $\bar{S}_B = A_{\text{eff}} \Omega_{ij} q_e \tau_{\text{optics}} \tau_{\text{path}} N_0 10^{(-0.4V_B)} T_{\text{int}}$.

Table 6-1. Signal-to-noise parameters, definitions, and source of values for ground-based and space-based visible systems.

Term	Definition	Ground-Based Visible	Space-Based Visible
A_{eff}	Effective aperture	Optical design	
Ω	Solid angle per pixel	Optical design & focal plane definition	
q_e	Quantum efficiency	Focal plane definition.	
τ_{optics}	Optical transmittance	Optical design	
τ_{path}	Path transmittance	Atmosphere.	n/a
k_f	Straddle factor	Optical PSF. Seeing. Trailing loss.	Optical PSF. Trailing loss.
N_0	Solar constant in-band radiance	5.79×10^{10}	
T_{int}	Integration time (seconds)	Varies night to night	Constant
V_B	Background magnitude	Lunar sky brightness.	Zodiacal light
V_m	Target apparent magnitude	f (solar phase angle, distance)	
σ_0	Read noise	Focal plane definition.	
σ_{DC}	Noise of dark current (Poisson)	Poisson. $\sqrt{S_{DC}}$	
σ_B	Noise of background (Poisson)	Poisson. $\sqrt{S_B}$	
σ_T	Noise of target signal (Poisson)	Poisson. $\sqrt{S_T}$	
η_{DC}, η_{qe}	Fixed pattern noise	Focal plane dependent	
\bar{S}_{DC}	Mean dark current	Focal plane dependent. f (temperature, T_{int})	
\bar{S}_B	Mean background signal	See equation	

The majority of the terms are determined by the choice of technologies, including optical design and focal plane, as discussed in Section 4 and enumerated in Tables 4-3 and 4-5. The remaining terms are integration time, path transmittance, seeing, sky background, and apparent magnitude of the objects.

- Integration time is determined by the search strategy. It varies night to night for ground-based systems because of the varying sunrise and sunset over the year. Integration time is a constant for space-based systems, chosen to optimize search rate and sensitivity.
- Path transmittance is computed for each step of the simulation for ground-based systems, accounting for the varying field elevation and additional losses away from zenith.
- Seeing is computed once per night for the ground-based systems. It is implemented as a random draw from a chi-square distribution, which matches the Subaru seeing history, as shown in Figure 4-4.
- Sky background for ground-based systems is set to a visual magnitude of 21.7 then is degraded as appropriate by the lunar illumination. It is a function of the search pattern pointing, proximity of the field to the Moon, the phase of the Moon, and multiple sensor parameters. Typical losses caused by lunar illumination are <1.5 visual magnitudes, but can be 3–5 visual magnitudes when the search pattern brings the pointing within a few degrees of the full Moon.
- Sky background for space-based systems is driven by the zodiacal light, or the gegenschein. Roach and Gordon (1973) tabulated the sky background as a function of ecliptic longitude and latitude, and the background is implemented as a look-up table used for each pointing.
- Both ground-based and space-based systems suffer additional sky background losses if the pointing field is near the galactic plane. The galactic plane loss is implemented as a look-up table developed from the observing experience of the Lincoln Near-Earth Asteroid Research (LINEAR) program.
- Apparent magnitude of the object is determined from the solar phase equation, which encompasses the location of the object with respect to the Sun and the observer.

Additional FROSST input parameters that are not reflected in the SNR equation pertain to operations. Both ground-based and space-based systems have a step-and-settle time, which is the time between frames and drives the search rate, and a readout time for the focal plane. There are also operational constraints, such as keep-out zones for the Sun, Moon, and Earth for space-based systems, and minimum elevation angles and astronomical twilight and daybreak constraints for ground-based systems.

The most important input parameter not reflected in the SNR equation is the search strategy. The space-based visible systems have a high enough search rate that there is no problem supporting the cataloging cadence of three tracklets in 25 nights discussed in Section 5. There was no incentive to optimize the search pattern for these systems. The space-based IR systems have a slightly limited search rate driven by long integration times. A simple attempt to optimize the search pattern was made. The ground-based systems are significantly limited in search capacity because of the limited viewing hours each day and weather outages. Therefore, the search strategy for the ground-based systems needed more optimization. The 2003 NEO SDT report included a detailed and thorough optimization section. For this study, the optimal strategy from 2003 was considered the starting point, and small variations around that point were explored. For example, there is a tradespace between nights between revisits and total sky coverage, and a tradespace between integration time

and total sky coverage. For this study, a seven-night revisit was implemented, and an integration time of 15–25 seconds was used, varying with the available hours to observe, with an average near 20 seconds. The same search strategy was used for all the ground-based systems.

The basic processing loop for FROSST is described below:

- For each sensor in the network, determine pointing.
- Propagate all objects to the time of interest.
- Determine which objects fall in the field of view.
- Compute the apparent magnitude of each object.
- Degrade the apparent magnitude for object motion, e.g., trailing loss.
- Compute sensor sensitivity.
- Degrade sensitivity for air mass, extinction, Moon brightness, sky background, etc.
- Compare the apparent magnitude and sensor sensitivity.
- Apply a probability of detection to each object to determine detection.
- Output detections.

The FROSST simulation has a few stochastic aspects. As noted above, the seeing is determined nightly by a random draw from a chi-square distribution, chosen to mimic the Subaru seeing history shown in Figure 4-4. There is a random “weather” term which varies by season, with the odds of observing on any given night based on observing history from the Subaru Telescope, Gemini Observatory, and European Southern Observatory (ESO) (Gemini 2012; ESO 2012; Miyashita 2004).

The probability of detection is a random draw based on *M*-out-of-*N* probability of detection theory. Intuitively, the higher the SNR for a target, the more likely the target will be detected. The lower the SNR, the less likely the target will be detected. This relationship is defined in detection theory as (Meyzonnette 2007)

$$SNR_{\text{Min}} = g(P_d) - g(P_{fa}) \quad (6-2)$$

P_d = Probability of Detection

P_{fa} = Probability of False Alarm

For a Gaussian signature, this becomes

$$SNR_{\text{Min}} \approx \sqrt{2}erf^{-1}(2P_d - 1) + \sqrt{2}erf^{-1}(1 - 2P_{fa}) \quad (6-3)$$

The apparent magnitude of a target that gives an SNR = 5 response can be determined from Equation 6-1 by solving for V_m , where V_m is the sensor sensitivity for that field, or the limiting magnitude of that field. If the actual apparent magnitude of the target is brighter than the limiting magnitude, then the SNR would increase accordingly, and the likelihood of detection increases. Assuming a constant false-alarm rate of 10^{-4} , Equation 6-3 defines that likelihood; it defines how the probability of detection changes with SNR. Together, Equations 6-1 and 6-3 define how the probability of detection

for a single frame changes with the difference between the apparent magnitude of a target and limiting magnitude of the sensor field. However, this probability of detection is for just a single frame. Detection algorithms typically require M -out-of- N detections to form a tracklet, so an additional level of binomial detection theory gets added (DeGroot 1975). Note, this is the step where the fill-factor (F_f) of the sensor can be accounted for:

$$P_{trk} = \binom{N}{M} (P_d F_f)^M (1 - P_d F_f)^{N-M} \quad (6-4)$$

Figure 6-2 shows how FROSST integrates these multiple equations to determine the probability a tracklet was formed for a given object. The x -axis is the difference between the apparent magnitude of the target and the limiting magnitude of the sensor. If the apparent magnitude is less than the limiting magnitude, the probability of detection goes to zero. If the apparent magnitude becomes much brighter than the limiting magnitude of the sensor, the probability of detection reaches a maximum, where the maximum is defined by the fill factor. This effect is best seen in the 3-out-of-3 detection curve. The fill factor for the 4×4 array of charge-coupled devices (CCDs) in the focal plane assemblies simulated in the ground-based systems is 93%. Regardless of how bright a target is, there is a 7% chance it will fall in a gap for any given frame of data. If 3-out-of-3 detections are required, then any single frame in which the target falls in the gap results in a non-detection. Therefore, the maximum probability of detection is $(0.93)^3 = 0.804$, as is seen in Figure 6-2. By comparison, allowing 3-out-of-4 detections drives the maximum probability of detection to 97%. For this study, 3-out-of-4 detections were allowed for all ground-based and space-based systems, and the search strategies and search rates reflect the four revisits per frame.

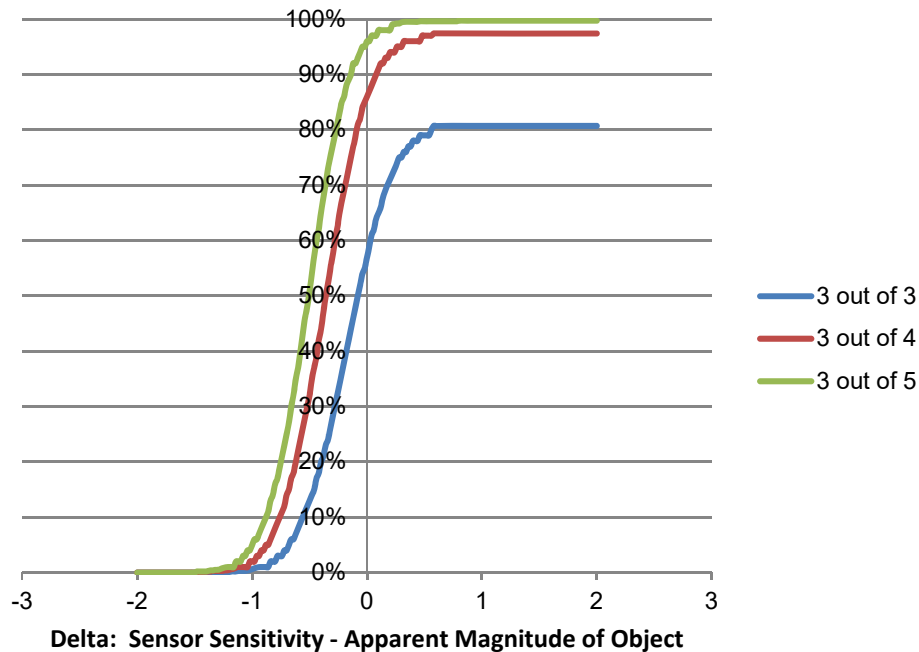


Figure 6-2. Probability of detection curves for forming a tracklet, requiring M out of N frames, as a function of the difference between the apparent magnitude of an object and the limiting magnitude of the sensor field.

6.2.2 Survey Simulation Tool

The Survey Simulation Tool (SST) is used to evaluate the performance of IR space telescopes as described in Mainzer et al. (2015) and ground-based telescopes in Grav et al. (2016) and summarized here. The SST was originally developed to study populations of asteroids and comets observed and detected by the Wide-field Infrared Survey Explorer (WISE) and NEOWISE spacecraft (e.g., Mainzer et al. 2011e; Grav et al. 2011, 2012; Bauer et al. 2017). The SST uses as input (1) observatory parameters, (2) the survey cadence, and (3) a model of the small body population, described in Section 6.1. The outputs of the SST are the fraction of objects in each population that are detected by each IR observatory. The SST allows detailed evaluation of properties of the expected dataset by outputting fluxes, positions, and times for each object in the population model on a frame-by-frame basis for the entire survey. The SST is written in Python and has been run using the Jet Propulsion Laboratory's (JPL) high-performance computing facilities.

The SST takes inputs from the observatory's sensitivity model. The observatory model represents the properties of the flight system, including an instrument model that incorporates its bandpasses, radiometric sensitivity, image quality, field of view, detector gaps, and field of regard (FOR). More detailed description of the instruments for the IR observatories can be found in Section 4.

The sensitivity model of the observatory uses as its metric noise equivalent spectral irradiance (NESI), in units of micro-Jansky (μJy). The detection threshold is set at five times the NESI, which is equivalent to $\text{SNR} = 5$, or $\text{NESI}_5 = 0.5 \times \text{NESI} = 5 \times (N/R)$, where R is the instrument responsivity ($\text{e-}/\mu\text{Jy}$) and N is the total noise (e-). The instrument responsivity is $R = S/E_v = A Q \tau t_{\text{int}} \Delta\nu/h\nu$ where S is the detected signal (in e-), E_v is the aperture spectral irradiance from the asteroid (in $\text{W}/\text{m}^2/\text{Hz}$), A is the telescope area, Q is the detector quantum efficiency, τ is the instrument transmission, t_{int} is the integration time, $\Delta\nu$ is the filter bandwidth, and ν is the band center frequency. For our actual intensity estimates of N and R , these band center formulae are replaced by numerical integrations across the passband.

All IR system simulations account for the contribution of background and noise from zodiacal light. The zodiacal light background can be larger than the flux from the source at the detection limit. The noise is given by $N = \sqrt{N_p \{I_{\text{zodi}} + I_{\text{therm}} + I_{\text{DC}} + I_{\text{stray}}\} t_{\text{int}} + R N^2}$ where N_p is the image quality in noise pixels (see below), I_{zodi} is the instrument response to zodiacal emission, I_{therm} is the response to the instrument self-emission, I_{DC} is the dark current, I_{stray} is the contribution from stray light, and R_N is the total read noise in e- .

Zodiacal emission is given by the three-dimensional zodiacal dust model of Wright (1998) and Leinert et al. (1998). The observatory model also represents the flight system's orbit (including the uncertainty in its position and time at each exposure), the pointing system's performance, and overhead estimates such as slew times, downlink, momentum unloading, and safe modes. Current best-estimate values are based on experimental measurements of key instrument subsystem properties, including the detectors; test results are described in Section 4 and McMurtry et al. (2013, 2016) and Dorn et al. (2016).

For a complete assessment of sensitivity impacts that are due to image quality, we use the formalism of noise pixels (Wright 1985) convolve pointing error and pixelization effects with the optical point-spread function (PSF) and are the equivalent number of pixels contributing noise for

optimal point source detection. Noise pixels have been used to define image quality for space telescopes, including WISE (Sampath et al. 2010; Schwalm et al. 2005), Spitzer (Hoffmann et al. 2003; Gerhz and Romana 2003) and Hubble (Hartig et al. 2003). Sensitivity is proportional to the square root of image quality in units of noise pixels.

The SST takes as an input a frame-by-frame list of all pointings for the entire survey. The survey cadence takes into account Moon avoidance, Earth and Sun avoidance zones, downlinks, momentum management, slew times, and other overheads, including an allowance for safe mode. As described in Section 6.1 above, the IR surveys were assumed to employ the same cataloging cadence of three tracklets in 25 nights discussed in Section 5.

With the observatory model, survey plan, and asteroid population model in hand, the next step was to use the SST to analyze which objects would be detectable by each IR observatory on a frame-by-frame basis. The SST was used to perform the following analyses on the model population objects:

1. Propagate state vectors for each object using the SWIFT symplectic integrator code (Levison and Duncan 1994; Wisdom and Holman 1991) for the 20-year surveys.
2. Using the observatory orbit and object state vectors, compute which objects fall within the IR observatory field of view (FOV) for each survey frame.
3. For each object that falls within an FOV, compute the IR and visible light fluxes.
4. Assess whether each object appears above the $\text{SNR} = 5$ cutoff for the IR channel by using the radiometric sensitivity model of the observatory, which varies as a function of ecliptic latitude and longitude.
5. Assess whether each detection would fall into gaps between the focal plane arrays.
6. For detected objects, evaluate if rates of motion and total time span for all detections fall within the required range to form a tracklet as described in Section 5.
7. Link tracklets into tracks (which are sets of tracklets for the same object) according to survey design rules (cf. Mainzer et al. 2015), and output the number of objects for which tracklets and tracks are formed.

The SST outputs all detections, including observatory and object state vectors, object coordinates, times, phase angles, on-sky velocity, and IR and visible fluxes.

6.3 Validation of Simulation Tools

The validation of all simulation tools is necessary before using the tools to draw important conclusions about system performance and, therefore, conclusions on system benefits. Because there are two different tools in use, both tools need to be independently validated. Additionally, there should be an effort to do a cross-validation between the tools to assure a level of parity. While some simulation tools are more conservative than others in estimating system performance, it is important that both tools used for this study are of a similar nature.

6.3.1 Validation of FROSST

The FROSST simulation was developed to study proposed space surveillance networks. The simulation has been widely used and proven to be robust and reliable for that purpose. Before proceeding with using the FROSST simulation for asteroid detection, a thorough effort was made to validate the software for the 2003 NEO SDT report. The validation is well documented in that study. The underlying methodology was to simulate the two LINEAR telescopes over a period of stable activity and compare the FROSST output detections to the actual LINEAR experience. The 2003 effort focused on proper modeling of system noises and losses, such as sky brightness caused by the Moon, weather outages, automation of the search strategy, etc. All enhancements introduced for 2003 have been retained for this study.

Modifications made to the FROSST simulation tool for this study were limited to three areas: an improved SNR sensitivity model that is represented by the SNR equations in Section 6.2.1; an improved probability of detection algorithm, also described in Section 6.2.1, that replaced the heuristic LINEAR experience; and an improved seeing model that is based on historical Subaru data (Miyashita 2004).

Given the thoroughness of the validation effort in 2003 and the limited enhancements to the simulation, the validation effort for this study consisted primarily of comparing the 2003 NEO SDT report's FROSST simulation results, the 2017 NEO SDT study's modified FROSST simulation results, and the baseline truth of the LINEAR system detection data.

While LINEAR's observing experience was used to enhance FROSST via statistics, at no time were actual LINEAR detection algorithms, search fields, or operational parameters specific to LINEAR used in FROSST. The FROSST inputs were kept generic so that the inputs could be extrapolated to the candidate systems in the study. The time period for which the comparison was made is a 16-month period from late 2001 to early 2003, during which there were no significant variations in the LINEAR hardware, post-processing, or operations plan. While it may seem tempting or logical to move the time period of the study to something more contemporary, the 2003 results are only available for the 2001–2003 time period.

The performance measure for the simulation is the detection of NEOs. Two different NEO input populations were used for revalidation. One population was the actual known NEO population as of January 2003, as downloaded from the Minor Planet Center. The second population was a simulated NEO population generated by W. Bottke for the 2003 study.

Figure 6-3 shows velocity distribution of NEOs detected by LINEAR, and the velocity distributions of the FROSST predicted detections for both of the input populations. The peaks, shapes, and sizes of all curves agree nicely.

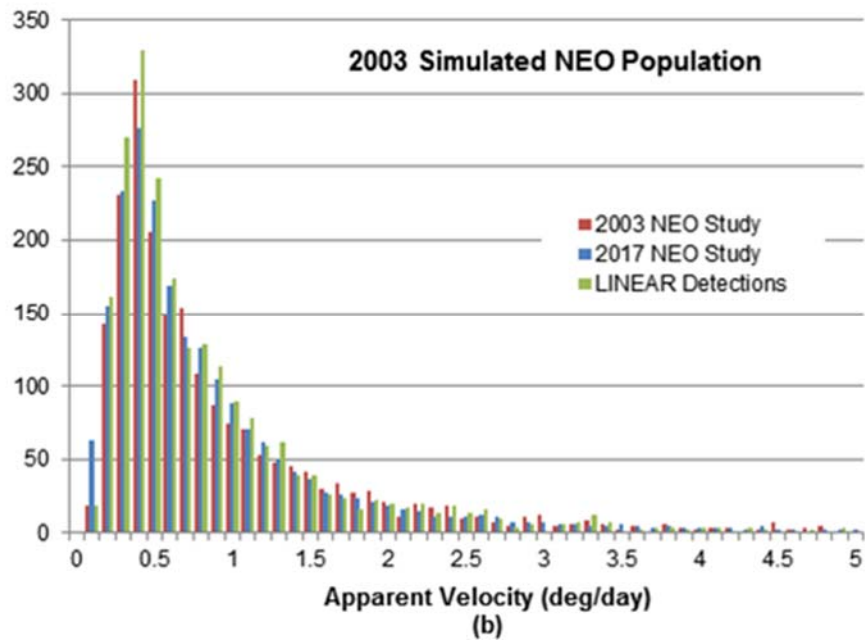
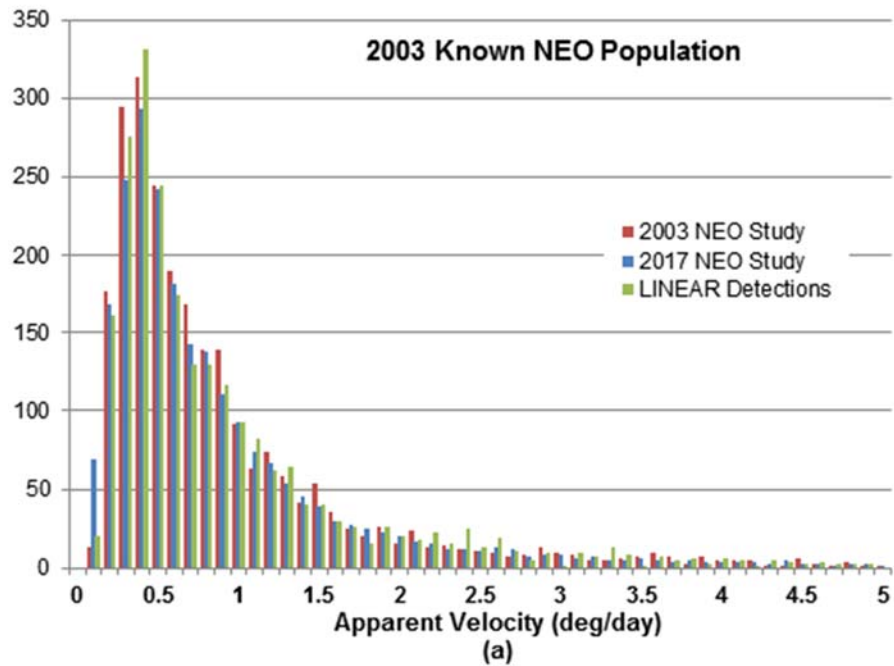


Figure 6-3. Distribution of the apparent velocity at time of detection for LINEAR: simulated and actual. A comparison of the 2003 SDT simulation and the modified 2017 SDT simulation. Two different input populations were used to validate the simulation tool: (a) actual known NEOs, as of 2003; (b) simulated population to $H \leq 22$.

Figure 6-4 shows the apparent magnitude distribution of NEOs detected by LINEAR and the apparent magnitude of the FROSST predicted detections for both of the input populations, for both versions of the simulation. The peaks align, and the modifications made for the current study resulted in slight improvements to the overall match. These improvements are due to the improved sensitivity curve better matching the peak and to the improved probability of detection algorithm more accurately representing the fall-off in detection beyond the peak.

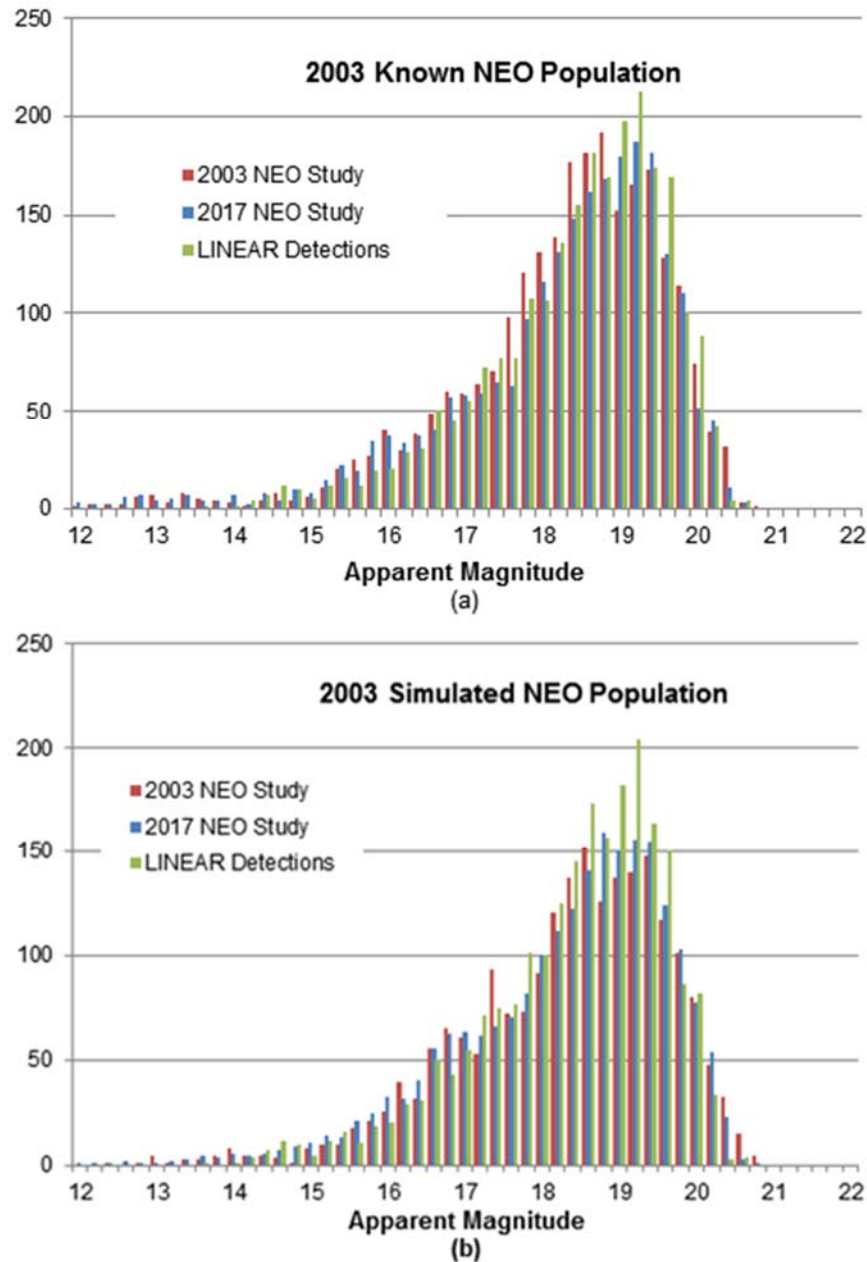


Figure 6-4. Distribution of the apparent magnitude of output detections for LINEAR: simulated and actual. A comparison of the 2003 SDT simulation and the modified 2017 simulation. Two different input populations were used to validate the simulation tool: (a) actual known NEOs as of 2003; (b) simulated population to $H \leq 22$.

Figure 6-5 shows the absolute magnitude distribution of NEOs detected by LINEAR and the absolute magnitudes of the FROSST predicted detections. The top plot corresponds to the input population of the known NEOs as of 2003. The lower plot corresponds to the simulated input population generated by Bottke. The match is very good for the known population. For the simulated population, the only significant divergence in these curves occurs at the $18 < H < 19.5$ range, where many NEO detections were new and near the limiting magnitude of the system. The LINEAR survey team was likely doing intentional tasked follow-up to confirm orbits, while the FROSST simulations only modeled search fields.

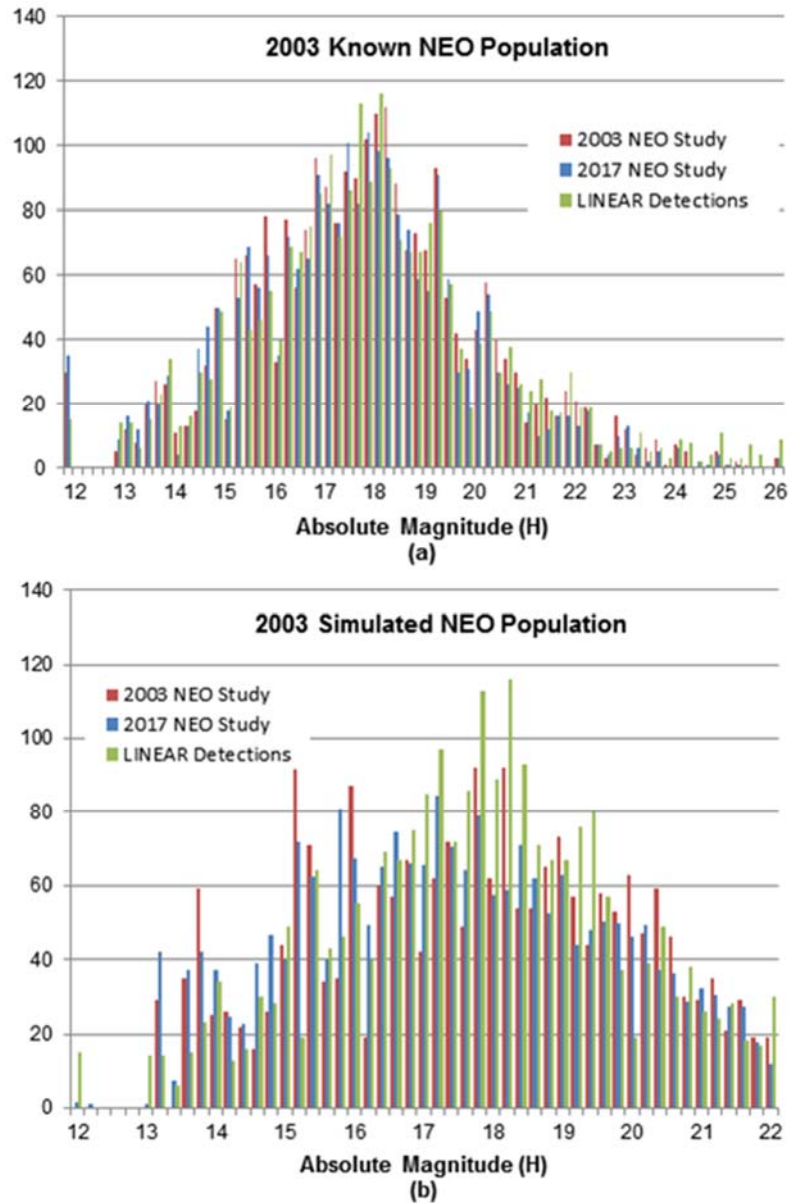


Figure 6-5. Distribution of the absolute magnitude of output detections for LINEAR: simulated and actual. A comparison of the 2003 SDT simulation and the modified 2017 simulation. Two different input populations were used to validate the simulation tool: (a) actual known NEOs as of 2003; (b) simulated population to $H \leq 22$.

6.3.2 Validation of SST

The SST tool suite was written to analyze data from WISE (Wright et al. 2010, Mainzer et al. 2011a). As described in Section 6.2.2, the SST consists of modules that generate a list of pointings for each exposure in the survey, predict the position of individual objects in each frame, compute thermal and visible fluxes, and tally detections. The SST uses the SWIFT symplectic integrator to predict the state vectors of individual objects at each time step. The SWIFT package is extensively used within the science community and has been validated as described in Levison and Duncan (1994) and Wisdom and Holman (1991).

The thermal modeling portion of the tool was validated by comparing asteroids detected by WISE to those detected by other observers. Comparisons were made to radar observations, stellar occultations of asteroids, spacecraft flyby missions, and other infrared telescopes such as IRAS and AKARI (Mainzer et al. 2011b,c; Usui et al. 2014; Ali-Lagoa et al. 2013; Greenberg et al. 2017). The results are in good agreement using standard thermal models, such as the Near-Earth Asteroid Thermal Model (NEATM, Harris 1998) and the Fast Rotating Model (Lebofsky and Spencer 1989).

The SST's model of the observatory sensitivity has been validated by comparison to the measured sensitivity of the WISE mission (Cardon et al. 2010). The IR observatory sensitivity is estimated by including the observatory-level image quality, as-measured detector performance characteristics, estimated in-band and out-of-band transmission curves, and noise performance. The results are in good agreement with measurements made of WISE sensitivity on orbit in all four IR channels (Cutri et al. 2012).

There have been multiple checks on the efficacy of the SST software suite when compared with other published results. The SST simulations of both Venus-trailing and L1-based IR surveys (published in Mainzer et al. 2015) agree to within 10% of similar simulations by Buie et al. (2016). Further, SST results for the Large Synoptic Survey Telescope (LSST) can be compared directly with LSST simulations published by Jones et al. (2016) and Chesley and Vereš (2016). These three studies agree to within <10% over decade timescales, indicating broad agreement in the methods and populations. An independent SST test of the Catalina Sky Survey, using fields from both the 1.5-meter and 0.7-meter telescopes, showed broad agreement (to within ~10%) with the results of Granvik et al. (2016). In short, the SST results compare favorably with those of other published simulation tools.

6.4 Establishing a Baseline

Using a uniform, statistical model as the input population is, in general, beneficial to the simulation; however, it makes establishing a baseline population more challenging. To assess the performance of each of the systems under consideration, it is necessary to assess the ability of each system to add to the current catalog of known PHOs. That task requires dividing the statistical set of PHOs into two subsets that represent the current known catalog and the set of undiscovered, or unknown, PHOs.

To establish a simulated catalog for 2016, the FROSST simulation tool was run for a number of years. The beginning date of June 2001 was chosen retroactively so that the end results would match the Harris population model in Table 2-1. The LINEAR-like system from the 2003 NEO SDT report was used. After six simulated years (June 2007), the aperture on the LINEAR-like system was increased from 1 meter to 1.5 meters to represent improvements in search technology. After another five simulated years (June 2012), the apertures were increased again to 2 meters, representing the

Panoramic Survey Telescope and Rapid Response System (Pan-STARRS), Catalina Sky Survey (CSS), Mt. Lemmon, and other capabilities. The simulation was run through January 2016 to match the Harris population estimate. The time periods for making the step up in aperture were chosen heuristically after looking at the actual PHO discovery rates published on the Minor Planet Center webpages, and noting years with jumps in discoveries. This method of running the simulator to establish the simulated catalog is important for two reasons: it assures the objects that are easiest to detect with a ground-based optical survey, and therefore, most representative of the objects detected by the current surveys, are deemed “known”; and it assures timeline continuity and appropriate refresh rates and accessibility for the current “unknown” objects.

Rather than doing a bin-by-bin match to the Harris population discussed in Section 2, the decision was made to establish the baseline as described above and to assure a reasonable match to the Harris population in the bins with the best knowledge, e.g., $H < 20$. See Figure 6-6. Assuming $H = 17.75$ corresponds to a diameter of 1 kilometer, this plot aligns reasonably with the Harris model at that point and estimates that we are at ~92% complete for PHOs with diameters larger than 1 kilometer.

If a decision were made in 2017 to acquire a next-generation asteroid search system, the acquisition process would take approximately six years. During the acquisition period, the existing search systems would continue to operate. Rather than use the 2016 simulated catalog as a baseline for system performance assessment, thereby giving the proposed systems credit for reducing impact risks that would have been handled by the existing systems, the baseline for the performance assessment was moved to 2023. The 2023 baseline was determined by extending the FROSST simulation of the larger aperture, LINEAR-like system for seven additional years. It is acknowledged that there are likely to be other search systems developed or enhanced over the next seven years that will be able to achieve more than the current systems are currently capable of; however, details of those systems aren’t known at this time. The most accurate assumption possible at this time is that the current systems will continue as they are. The resulting 2016 and 2023 baselines are shown in Figure 6-6. For comparison, the 2003 population model is included, with a completeness of just 51% at $H \leq 17.75$.

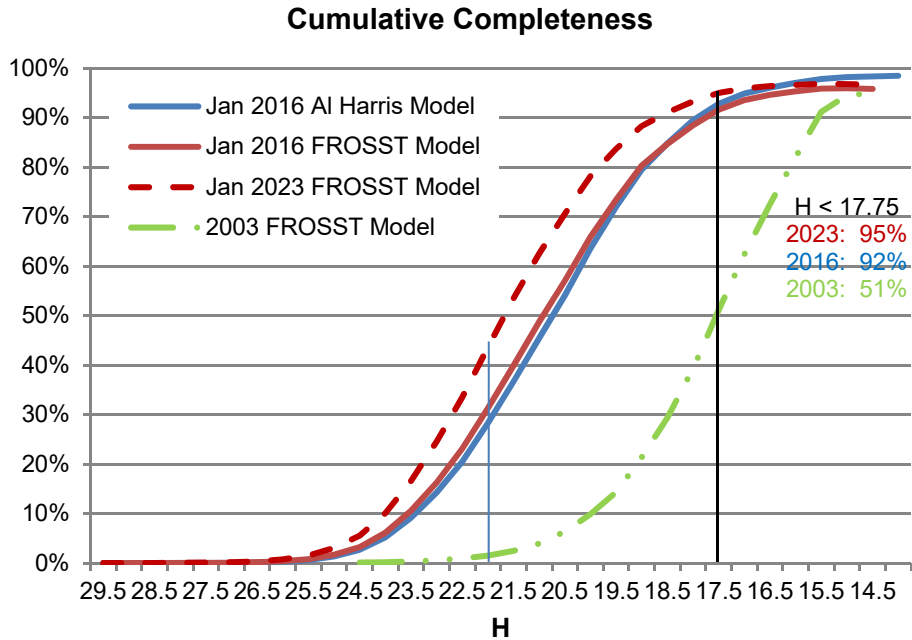


Figure 6-6. Establishing a baseline from the uniform statistical model of PHOs. The FROSST simulation estimate for known, cataloged objects is 92%, which is compared to the Harris cumulative completeness model, which is 93% (Section 2). The models are independent, and match well. The FROSST simulation is extrapolated to January 2023 to be used as the baseline in the remainder of this study. The completeness is estimated to be 95%. For reference, the 2003 FROSST PHO model is also included, where completeness was only 51% at $H < 17.75$.

The Harris PHO population is defined in H . This study is focused on the risk and damage of potential impactors and therefore is focused on the diameters of the objects. The input population for the simulation tools in this study is defined in H , diameter, and albedo, so it is easy to look at the completeness of the current surveys, and the extrapolated 2023 surveys, in terms of diameter. Figure 6-7 is the same survey completeness shown in Figure 6-6 but binned by diameter. In addition to the FROSST output for completeness, a ground-based optical simulator used by Mainzer et al. (2015) and Grav et al. (2016) (hereafter M15G16) was utilized to generate a completeness curve for the input population. These two simulator tools are completely independent, with the M15G16 tool sharing many similarities to the SST IR simulation tool. The comparable results serve as a sanity check on the methodology and on the parity of the simulation tools being used.

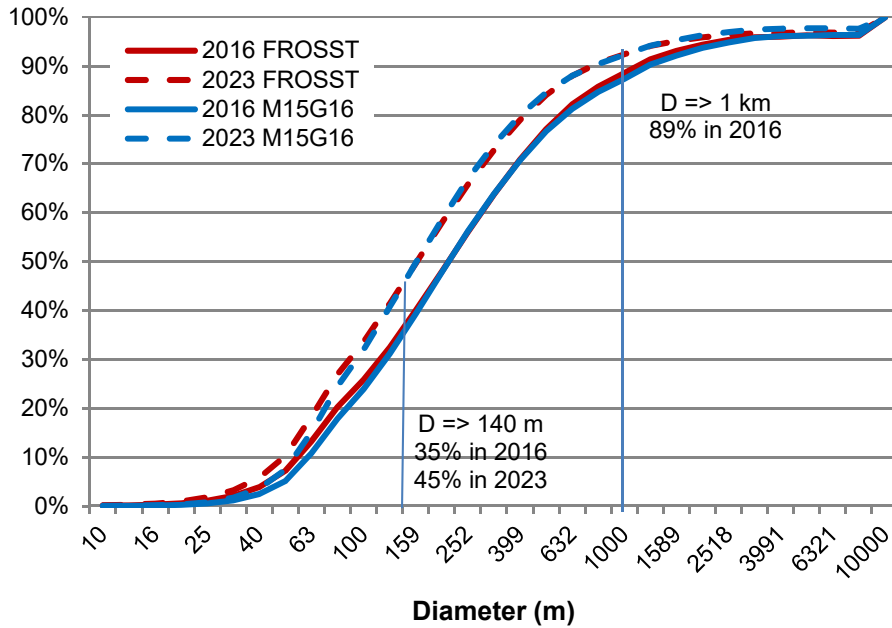


Figure 6-7. 2023 baseline for remainder of the study. Cumulative completeness in diameter bins. Determined independently with FROSST and with Mainzer et al. (2015) and Grav et al. (2016) (M15G16). M15G16 shares heritage with SST.

The end result of establishing a baseline is summarized in Figure 6-8. The input population from Figure 6-1 has been divided into “known” and “unknown” as of January 2023, and distributions in H , diameter, and albedo are shown. Figure 6-8c shows percent completion for each albedo bin. The completion ranges from ~40% at low albedos to ~65% at high albedos. The range in completion is because the significant majority of asteroid discoveries through 2016, and most likely through 2023, have been made by ground-based optical systems, which have a bias toward the brighter H objects within each diameter bin. For example, Figure 6-8d shows a single diameter bin, ranging from 126 to 159 meters, distributed by H . This bias toward higher albedos explains the difference in completeness of 92% at $H \Rightarrow 17.75$ (Figure 6-6) and the completeness of 89% at diameter $\Rightarrow 1$ kilometer (Figure 6-7).

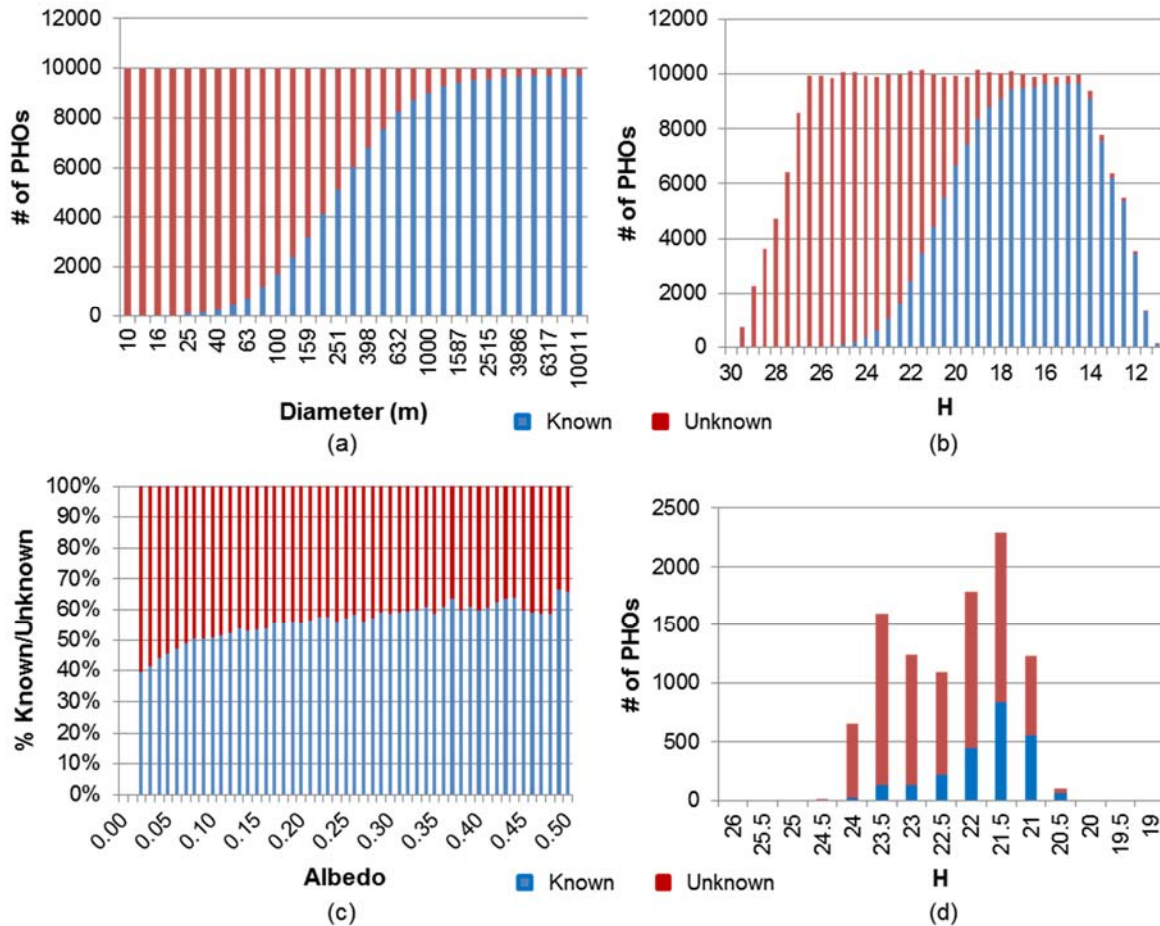


Figure 6-8. Distribution of the statistical input population for the simulations, divided into "known" and "unknown" as of January 2023: (a) diameter; (b) absolute magnitude H ; (c) albedo broken into percent by bin, ranging from 40% known at low albedo to 65% known at high albedo; (d) 126 m–159 m bin, distribution in H .

6.5 Results

The following sections present the results across a wide range of comparisons for single ground-based and space-based systems and for a number of networked systems. Two types of simulations were done for each case: assessment of cataloging capability and assessment of warning capability.

The output from the simulations is a list of detections including object number, time, location, velocity, absolute magnitude, apparent magnitude, sensor that made the detection, and sensor sensitivity at the time of detection. The detection list is then reduced to a list of cataloged objects, requiring three tracklets within 25 days, each tracklet occurring at least 24 hours apart for space-based systems or at least on separate observing nights for ground-based systems. The cataloged objects are binned according to diameter. A percent completion is computed for each bin on the basis of the number of objects in the bin and the number of objects cataloged.

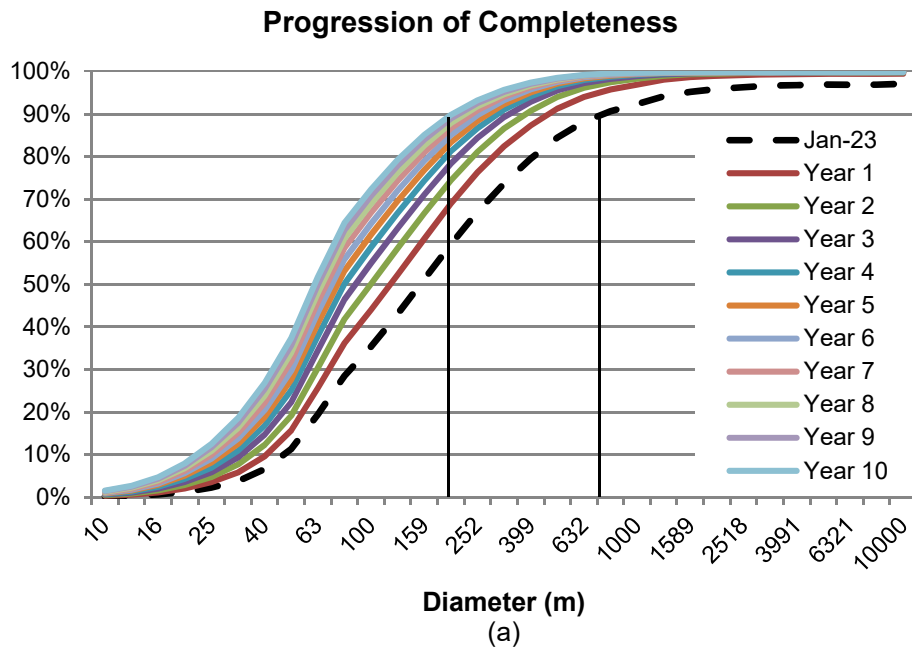
The Spaceguard report defined a goal of detecting 90% of all objects larger than 1 kilometer within 10 years. Given the precedence of defining a goal and assessing performance in terms of "all objects

larger than,” an effort has been made to convert the percent completeness numbers for each bin into integral completeness numbers. In future plots showing the cataloging capability of various systems, the curves show the percent complete for all objects larger than the value on the x-axis.

6.5.1 Cataloging

Cataloging requires detection of the same object three times within 25 days, as discussed in Section 5. This cataloging assumption has a significant effect on the overall performance of each system. This requirement makes repeat coverage a key parameter for success. To strive for full-sky coverage with a cadence that supports the cataloging requirement, the optimal operating points for the systems are generally found by trading some depth of coverage, i.e., sensitivity, for search area by shortening the integration time.

The cataloging performance measure is determined from the number of new objects added to the catalog each year for 10 years. While longer simulations were run and performance numbers are available for 20 years, it is unlikely any space-based systems would be designed for a lifespan beyond 10 years. Additionally, the biggest gains in cataloging occur in the early years, after which the growth slows as fewer objects with apparent magnitudes accessible by the system remain uncataloged. The baseline catalog was defined in the previous section. Figure 6-9 shows how a catalog grows over 10 years (Figure 6-9a), and for 20 years (Figure 6-9b) for a 1-meter space-based visible telescope. Each line in the plots corresponds to the integral completion of the catalog for sizes greater than H for a single year. The January 2023 baseline has the catalog 90% complete for all objects larger than 796 meters. After 10 years, this survey is 90% complete to 200 meters, and after 20 years, this survey is 90% complete to 126 meters.



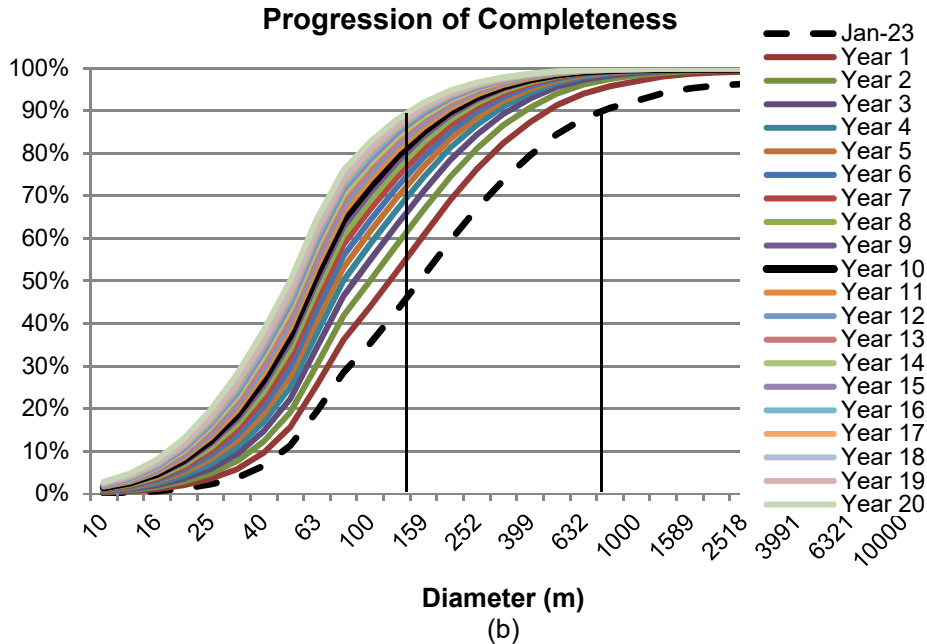


Figure 6-9. Growth of the catalog (a) over 10 years and (b) over 20 years. Note the limited additional growth over time.

6.5.2 Warning

Warning is the ability to detect an impactor prior to impact and during its last orbital period or during its last calendar year, whichever is shorter. For this study, a warning requires two tracklets, and both must occur at least six days prior to impact. Warning efficiency for a system is defined as the percentage of objects warned against for each bin of data. The population used to assess the warning capability of a system is 990 objects per diameter bin and was defined in Section 6.1.1.

The assumption in this study is that the benefits of warning only accrue for objects not yet cataloged. As the catalog grows, there are fewer objects to warn against. Given that the number of objects to warn against is continually changing, it is not possible to state the warning efficiency in terms of integral warning or warning against all objects greater than H . The warning efficiency is defined bin by bin.

6.5.3 Output Plots and Observations

6.5.3.1 Ground-Based Systems

All of the ground-based systems considered used the same 4×4 CCD configuration with the same 93% fill factor and comparable optics designs as described in Section 4. The CCDs have 10-micron pixels, which translate to a 0.26 arcsec instantaneous field of view (IFOV). Given that the seeing at sites under consideration is never better than 0.5 arcsec, and typically worse, and given that the apparent motion of PHOs is typically 0.5–1.0 degrees per day, the feasibility of binning the pixels in a 2×2 format was explored. Binning is beneficial when objects are fast and therefore can be kept in a single pixel longer, reducing trailing loss. It is also beneficial as the seeing degrades because

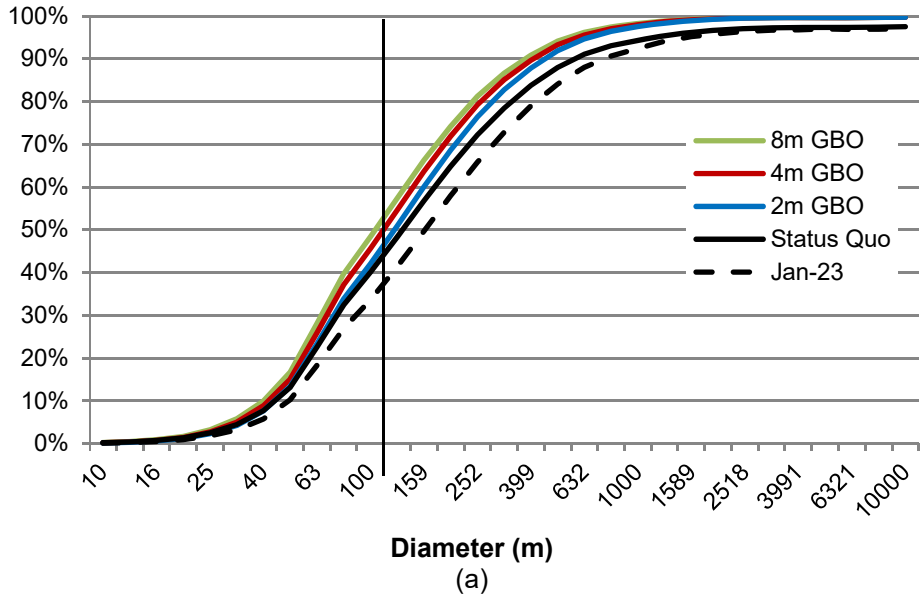
photons are scattered across more pixels. However, binning is a detriment as the sky background increases. The sky background increases by a factor of 4 with binning and can quickly outpace the gains of binning.

After analysis and simulation, the 2-meter system with the smaller aperture and, therefore less sky background, benefits from binning. At the other end is the 8-meter system. With a large aperture, the background signal grows, and the losses quickly surpass the gains; therefore, the 8-meter system is best operated in an unbinned, 0.26 arcsec mode. Finally, at the 4-meter midpoint of the systems under consideration, the gains and losses are comparable. The unbinned system performs slightly better than the binned system. From this point forward, when referring to the ground-based systems, only the 2-meter, 4-meter, and 8-meter systems will be cited, and the results will be for each system's best configuration—binned, unbinned, and unbinned, respectively.

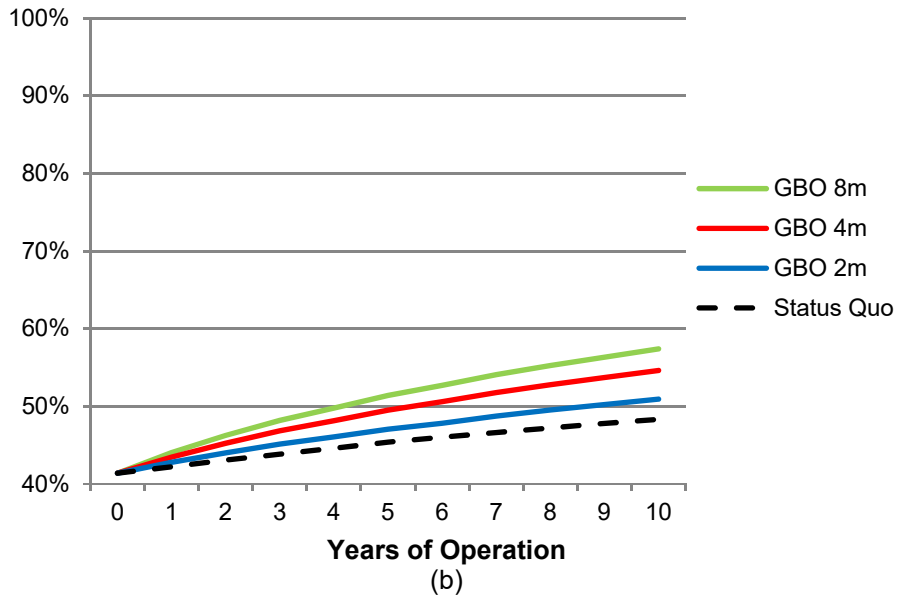
Figure 6-10 shows the cataloging capability and warning efficiency for the ground-based systems. The cataloging completeness is shown in Figure 6-10a as the completeness at 10 years across all diameter bins. Figure 6-10b is the completeness over 10 years for PHOs larger than 126 meters. This figure includes the January 2023 baseline and a status quo system—the current system that was used to generate the January 2023 estimate. By 2023, the current system will have been run for 12 years, and this plot is showing an additional 10 years beyond that. As seen previously in Figure 6-9, there is very little improvement in cataloging to be garnered by most systems after the first 10 years, let alone 22 years of operations. The difference in performance between the proposed 2-meter system and the status quo can be attributed to three things: a larger field of view for better sky coverage; a Southern Hemisphere location for access to objects not easily detected from the Northern Hemisphere; and better site conditions such as seeing and weather.

Note, whenever practical, the plot legends are sorted in order of system performance.

Completeness at 10 years: Ground-Based Systems



Completeness at 126 m: Ground-Based Systems



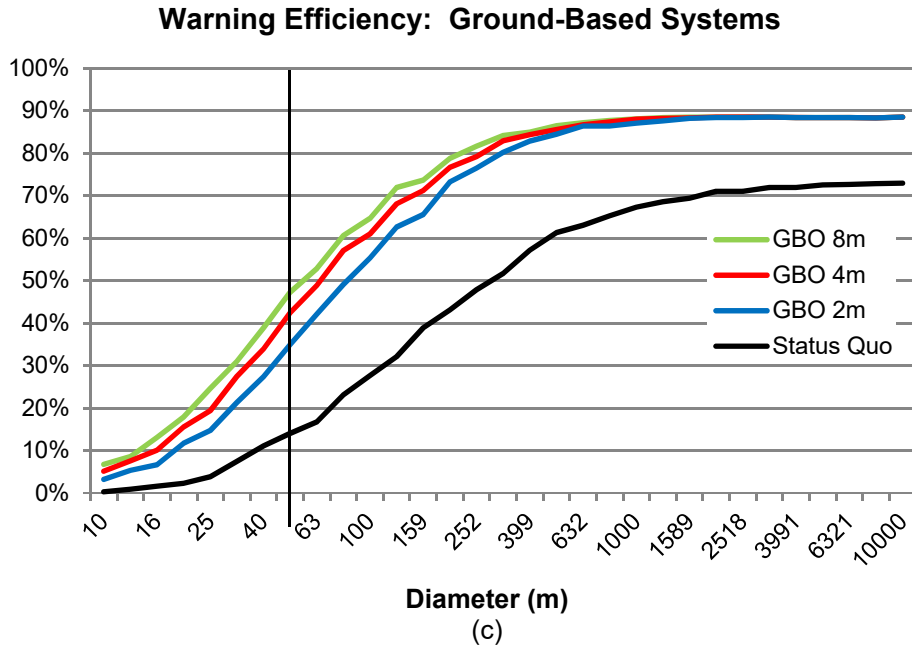


Figure 6-10. Ten-year completeness performance (a), completeness over time at 126 m (b), and warning efficiency (c) for the ground-based systems. Status Quo is the extrapolated performance of the existing systems.

6.5.3.2 Space-Based Systems

Two different technology types, five general orbits, and three different-sized telescopes were simulated and analyzed, for a total of 17 space-based systems. These systems are summarized in Table 6-2. The orbits are a 900-kilometer sunsynchronous low-Earth orbit (LEO), a geosynchronous orbit (GEO), an L1 orbit, and an L2 orbit, at the Earth’s first and second Lagrange points 1.5 million kilometers from Earth, and a Venus-trailing orbit modeled as a spacecraft at Venus’s L2 point. The 0.5-meter and 1-meter IR telescopes were analyzed at L1 and Venus-trailing, and a 20-centimeter IR system, co-hosted at GEO, was analyzed. The 0.5-meter and 1-meter visible band telescopes were analyzed at all five orbit locations, and a 2-meter visible band telescope was analyzed at LEO and GEO. All systems were assessed for cataloging and warning capability.

The space-based designs all offer a significant coverage capability over the ground-based designs because of the 24-hour-a-day availability. The same cataloging requirement of three tracklets in 25 days applies to the space-based and ground-based systems. The visible systems have a high search rate, primarily because of the shorter integration times, so there was no special effort made to tune the space-based visible search patterns to an optimal cadence. The IR systems have a lower search rate, so a relatively simple effort was made to match the cadence to the required cataloging requirement, but the search pattern implemented is most likely not optimal.

Table 6-2. Simulated space-based systems.

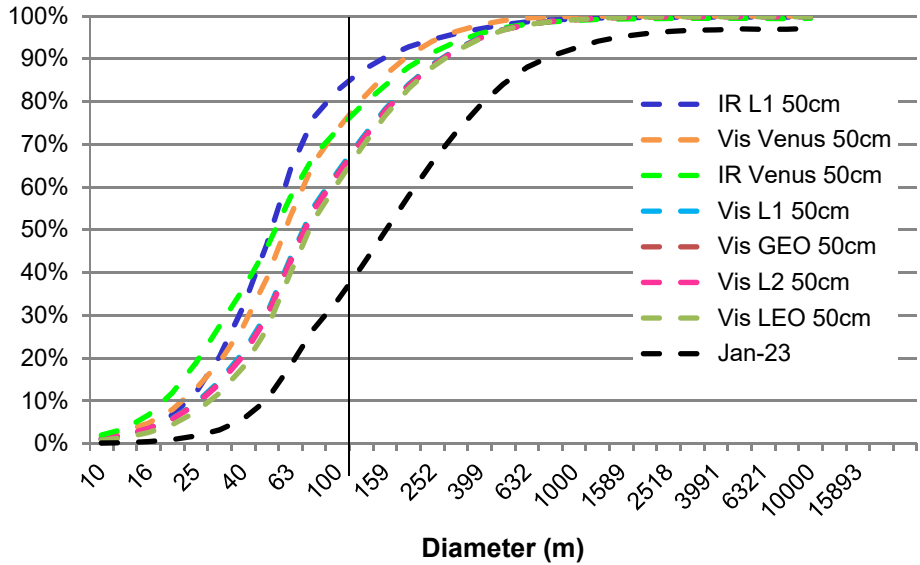
	0.2 m	0.5 m	1 m	2 m
Low Earth orbit (LEO)	–	Vis	Vis	Vis
Geosynchronous orbit (GEO)	IR	Vis	Vis	Vis
Lagrange 1 (L1)	–	IR, Vis	IR, Vis	–
Lagrange 2 (L2)	–	Vis	Vis	–
Venus-trailing	–	IR, Vis	IR, Vis	–

6.5.3.2.1 Comparing Systems of the Same Size

Figures 6-11 and 6-12 show the cataloging capabilities and warning efficiency of the different orbits and technologies for the 0.5-meter and 1-meter systems, respectively. Note that there is no significant difference in the cataloging capability of the visible systems at LEO, GEO, L1, and L2, while the Venus-trailing systems provide superior cataloging because their optimal solar phase angles and their position asynchronous to Earth provide better opportunities for detection of PHOs in resonance with the Earth. The top-performing 0.5-meter systems for cataloging are the IR system at L1, followed by the visible and IR systems at Venus. However, while the Venus-trailing systems are great for cataloging, they are in the worst location for warning. Their location is too far away and frequently too out of synch with Earth orbit to be a reliable warning system. Also of note, while there was very little difference in LEO, GEO, L1, and L2 for cataloging, the L1 system provides the best warning, followed closely by the GEO system. The L1 system benefits from solar phase angle, thereby outperforming L2, and the GEO system has access to more sky on a regular basis than the LEO system, which loses half the sky to the Earth keep-out zone for all fields and therefore has a more restricted search pattern.

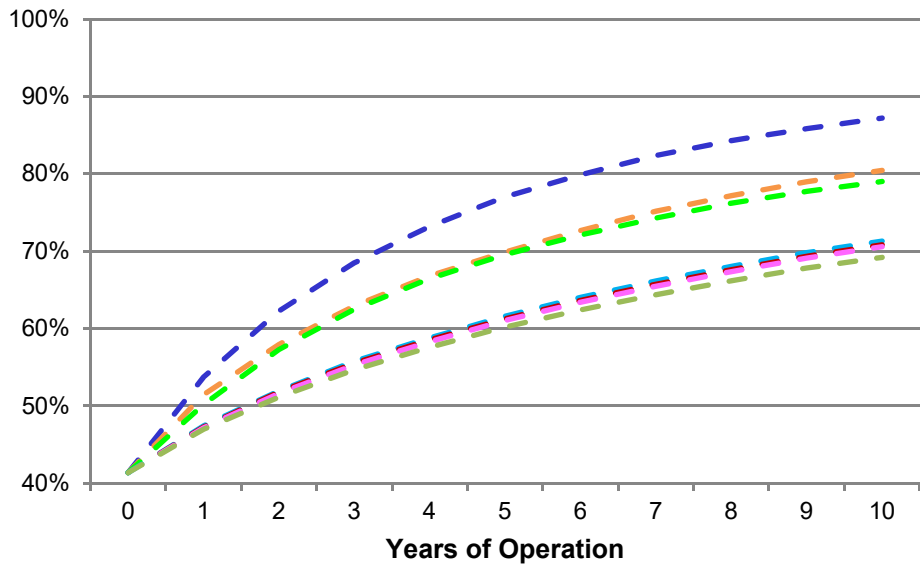
The 1-meter systems are relatively similar to the 0.5-meter systems with one notable exception. The 1-meter system at Venus is the worst system for cataloging because its smaller field of view results in loss of sky coverage and its warm location, which adversely affects sensitivity, counters any performance gains that might have come from location.

Completeness at 10 Years: 50 cm Systems



(a)

Completeness at 126 m: 50 cm Systems



(b)

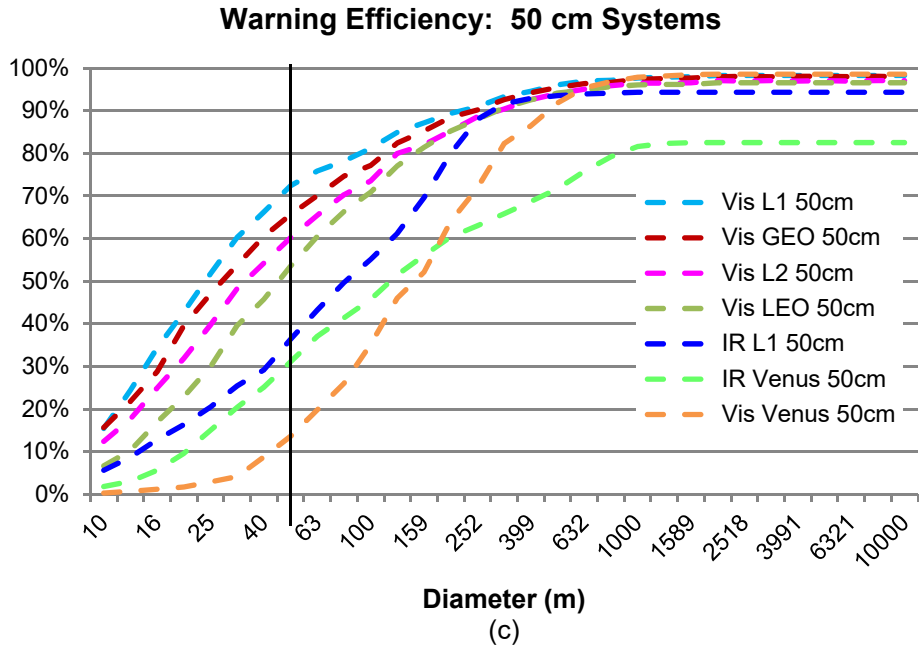
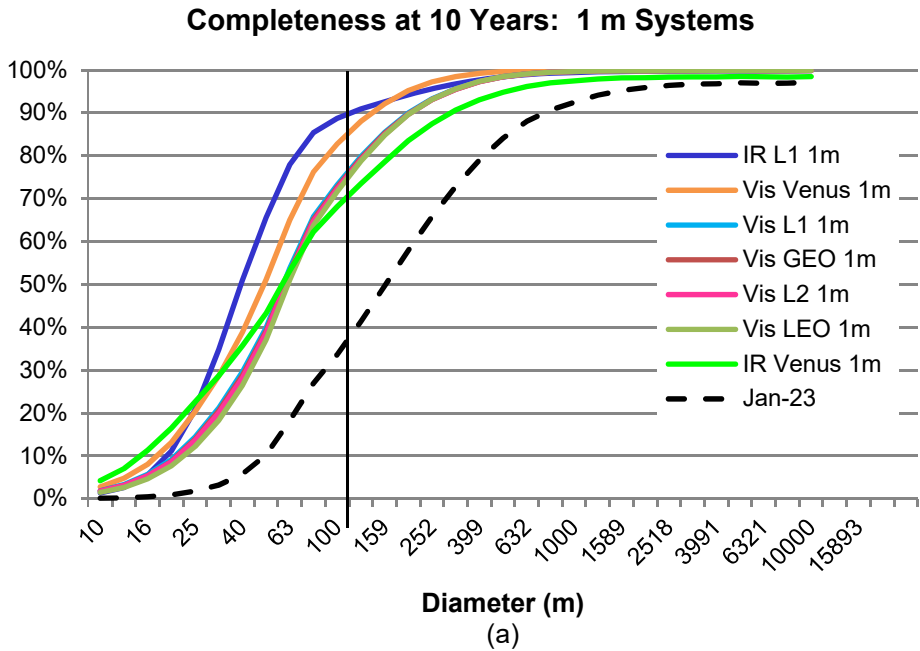


Figure 6-11. Ten-year completeness performance (a), completeness over time at 126 m (b), and warning efficiency (c) for 50 cm space-based systems, across orbit locations and technologies.



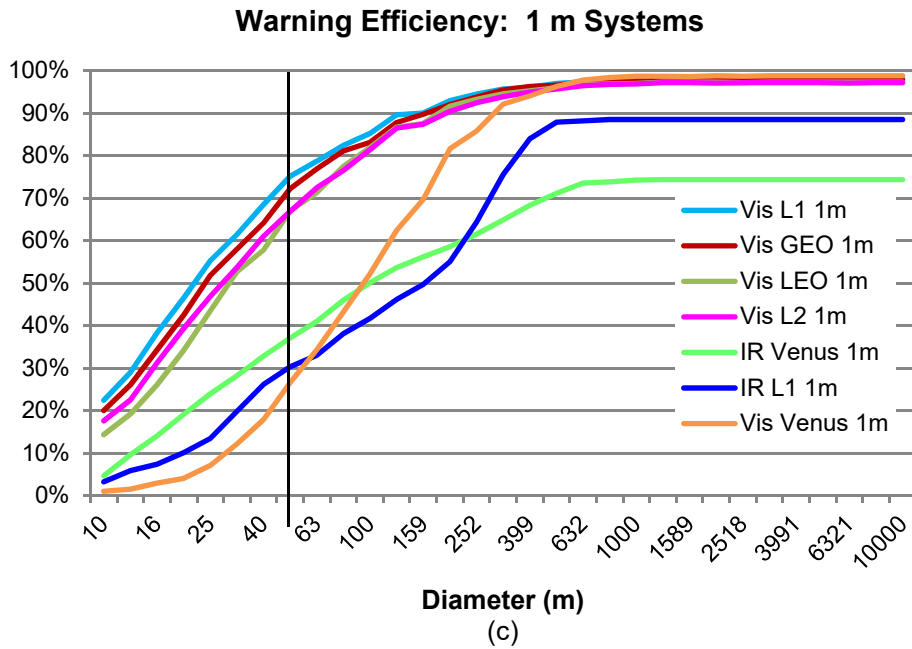
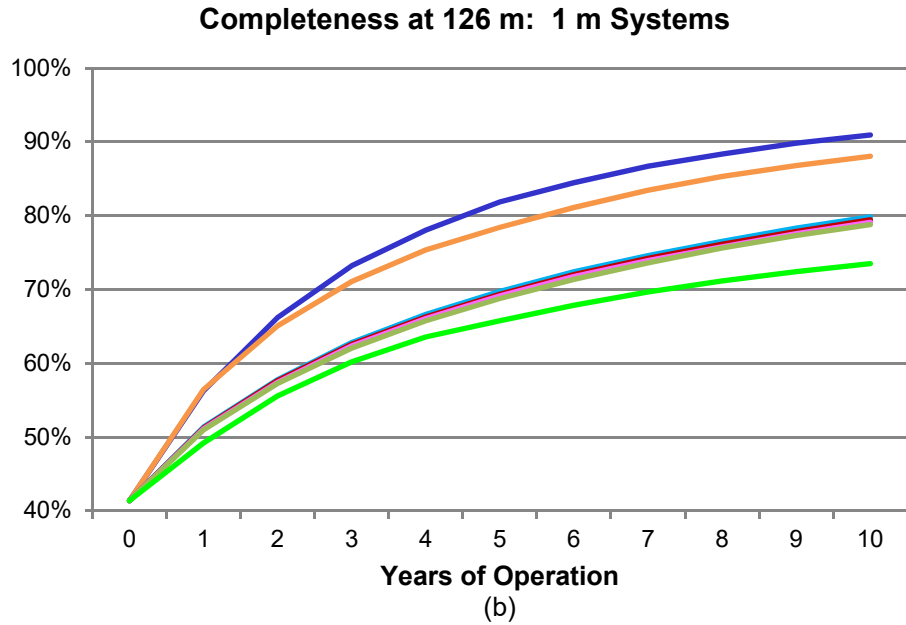


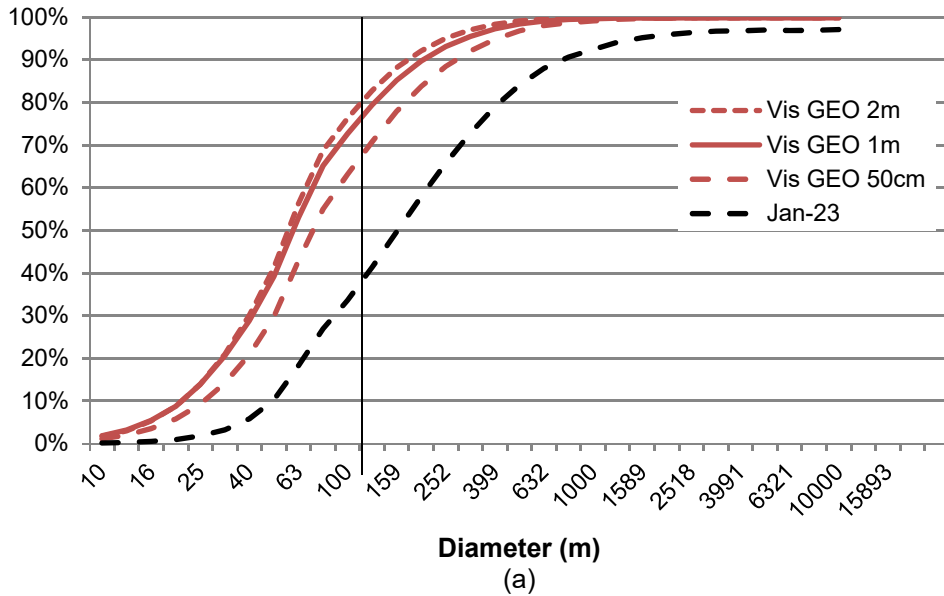
Figure 6-12. Ten-year completeness performance (a), completeness over time at 126 m (b), and warning efficiency (c) for 1 m space-based systems, across orbit locations and technologies.

6.5.3.2.2 Comparing Systems at the Same Location

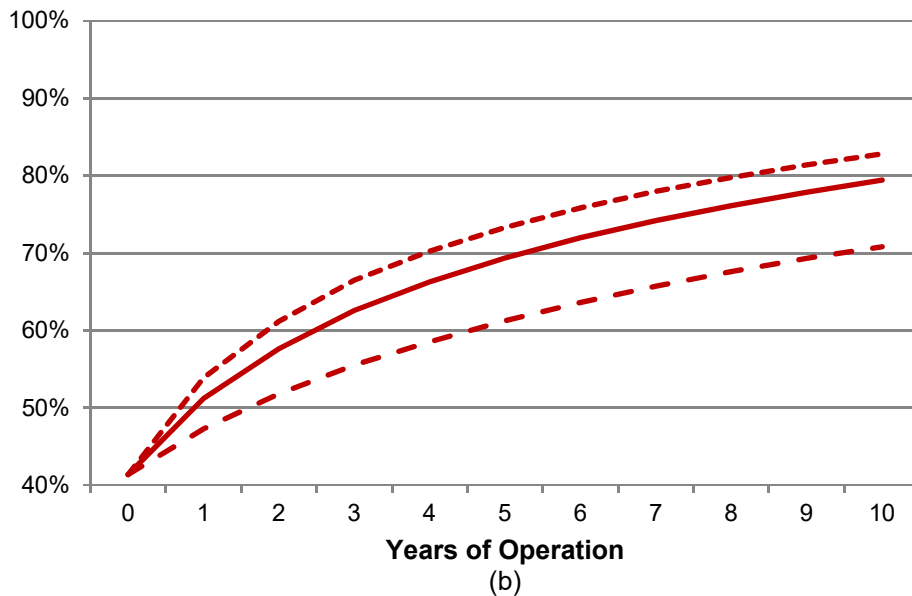
Figures 6-13 and 6-14 show the performance of the space-based systems at GEO and at L1 to help give insight into the variance resulting from the size of telescope and type of technology. Keep in mind from Section 4 that the search rate for the space-based systems decreases as the aperture increases for IR and

visible systems. The GEO and L1 systems, both visible and IR, show a marked jump in performance from 0.5 meters to 1 meter. However, the jump to 2 meters for the GEO system is smaller. The loss in search rate limits the benefits of the larger aperture. For the L1 systems, the benefits of IR for cataloging are apparent. Decades of search with ground-based optical systems have biased the remaining population toward lower albedo objects. However, for warning, the smaller field of view of the IR systems is a detriment. Sky coverage is a strong driver for warning.

Completeness at 10 Years: Geosynchronous Systems



Completeness at 126 m: Geosynchronous Systems



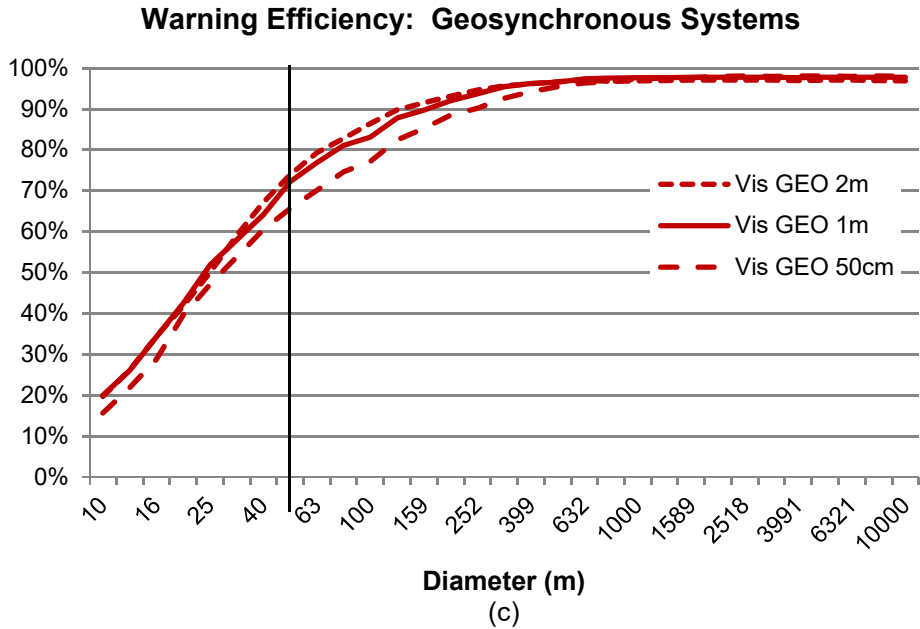
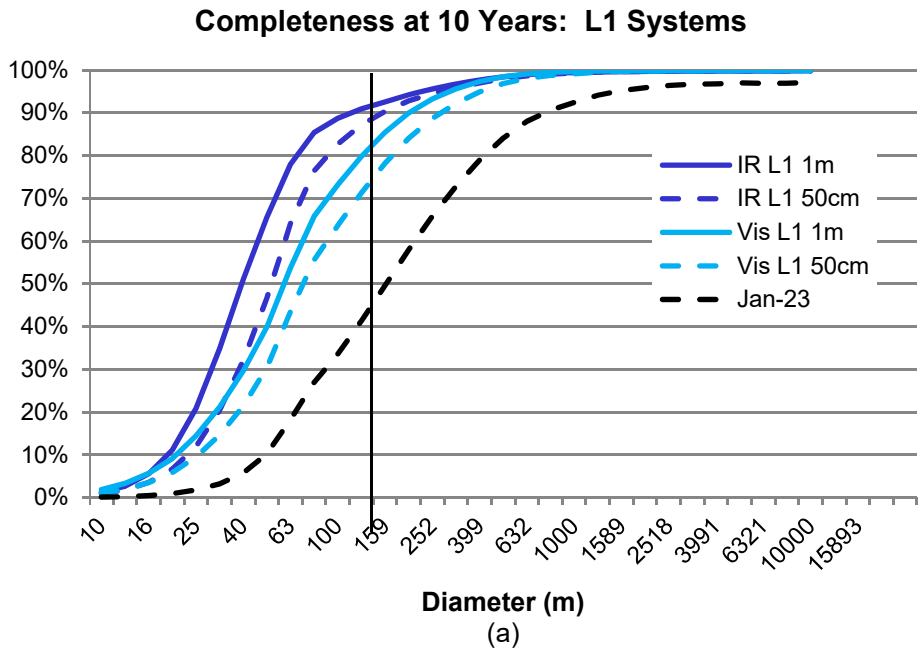


Figure 6-13. Ten-year completeness performance (a), completeness over time at 126 m (b), and warning efficiency (c) for systems located at GEO.



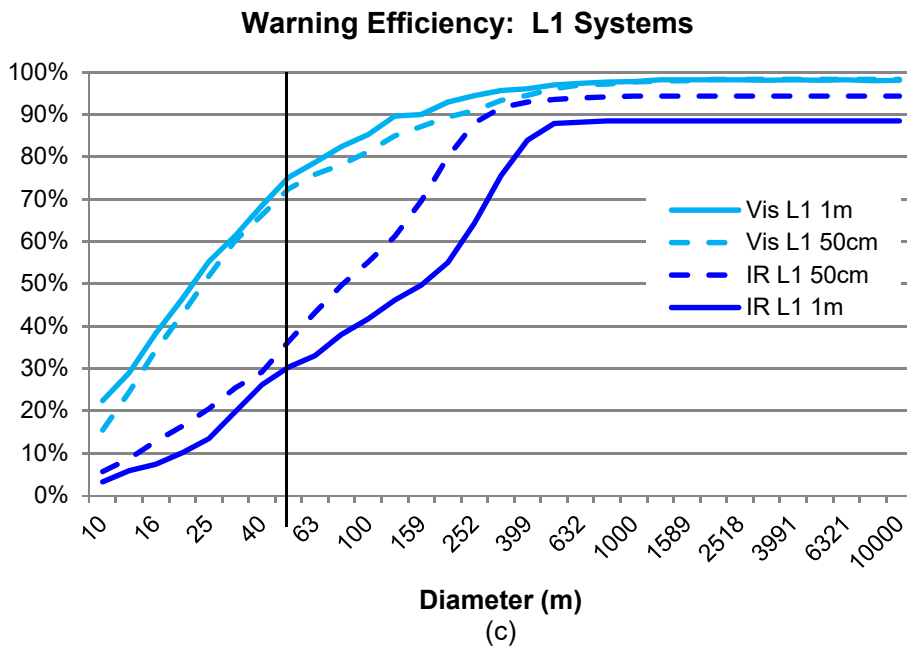
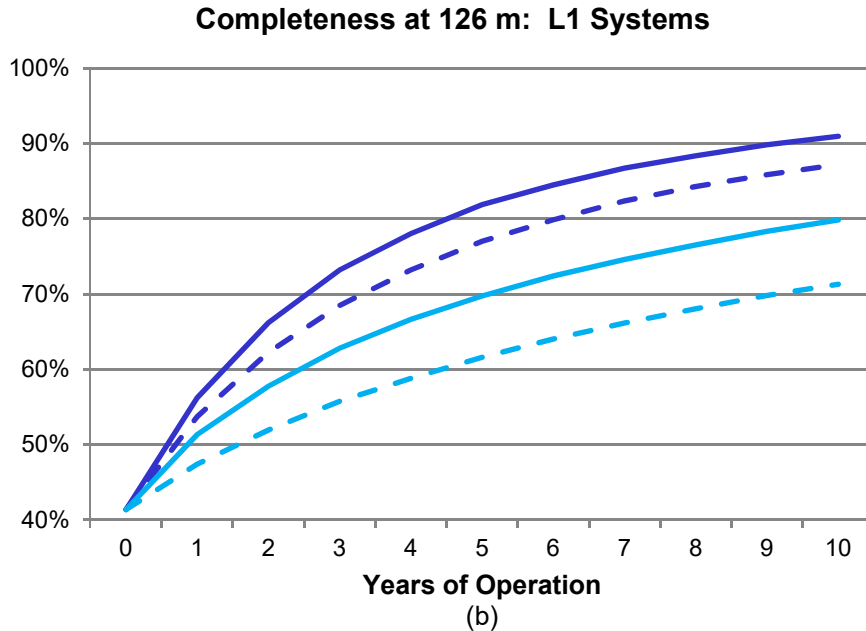


Figure 6-14. Ten-year completeness performance (a), completeness over time at 126 m (b), and warning efficiency (c) for systems located at L1.

6.5.3.2.3 Comparing Networks of Systems

A handful of networks were considered: a ground-based 4-meter telescope paired with a variety of visible and IR space-based systems, and a combination of a visible and IR space-based system at L1. Figure 6-15 shows the performance for the 4-meter ground system networked with the space-based visible systems. The addition to the GEO systems is negligible for cataloging and warning. The addition to the Venus systems is almost negligible for cataloging, but adds notable capability for

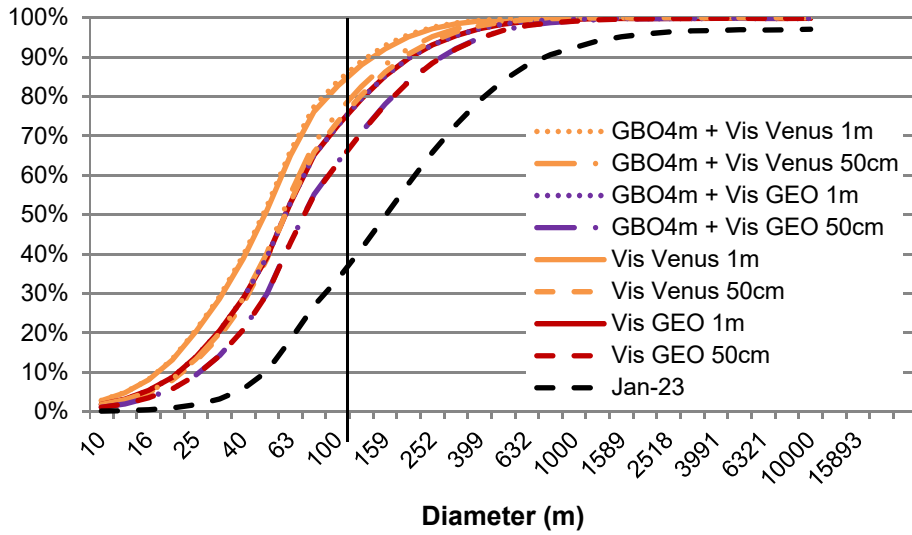
warning. For 50-meter PHOs, the warning efficiency goes from 14% to 48%, and from 25% to 55%, for the 0.5-meter and 1-meter systems, respectively.

Figure 6-16 shows the performance for the 4-meter ground system networked with the space-based IR systems. The addition of the ground system adds a few percent completeness to the cataloging performance of the systems at GEO, L1, and Venus. The significant improvement is for warning, with each case adding nearly 25% to the warning efficiency at 50 meters.

Figure 6-17 shows the performance of an IR and a visible system, both 0.5 meters at L1. These are modeled as two separate systems, both being utilized at 100%. An interesting excursion not explored in this study would be a dual-band system sharing a single bus. The combination of the dual technologies at L1 adds a few percent completeness for cataloging, and in the early years, the combination can add as much as 6% to the results for objects that are 126 meters or larger. For warning, the addition of the dual technology with a high search rate adds 50% efficiency at 50-meter PHOs. This network combines the best cataloging capability (IR 50 cm at L1) with one of the best warning capabilities (Vis 50 cm at L1).

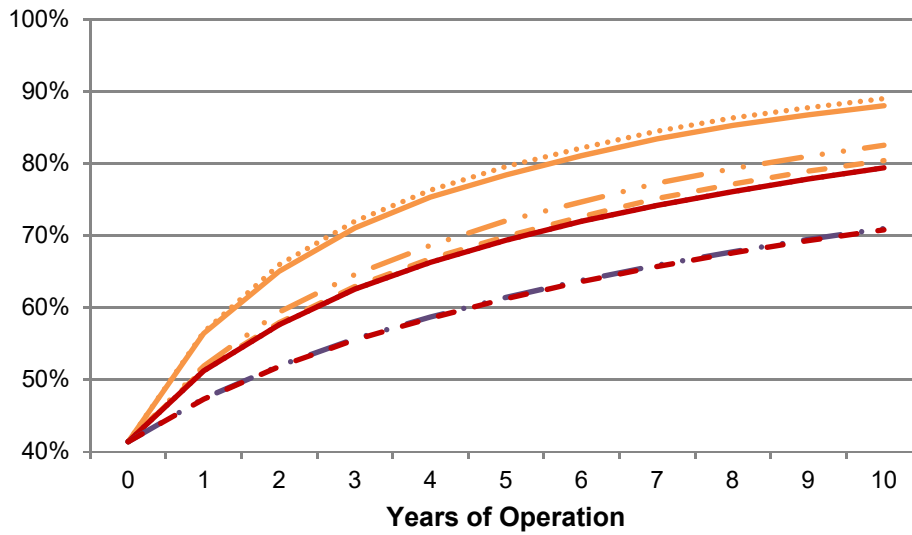
Figure 6-18 shows all the systems analyzed for this study. The order of the legend indicates the order of performance, based on completeness at the 126 m PHO bin.

Completeness at 10 Years: Visible Space Systems and Visible Ground System



(a)

Completeness at 126 m: Visible Space Systems and Visible Ground System



(b)

Warning Efficiency: Visible Space Systems and Visible Ground System

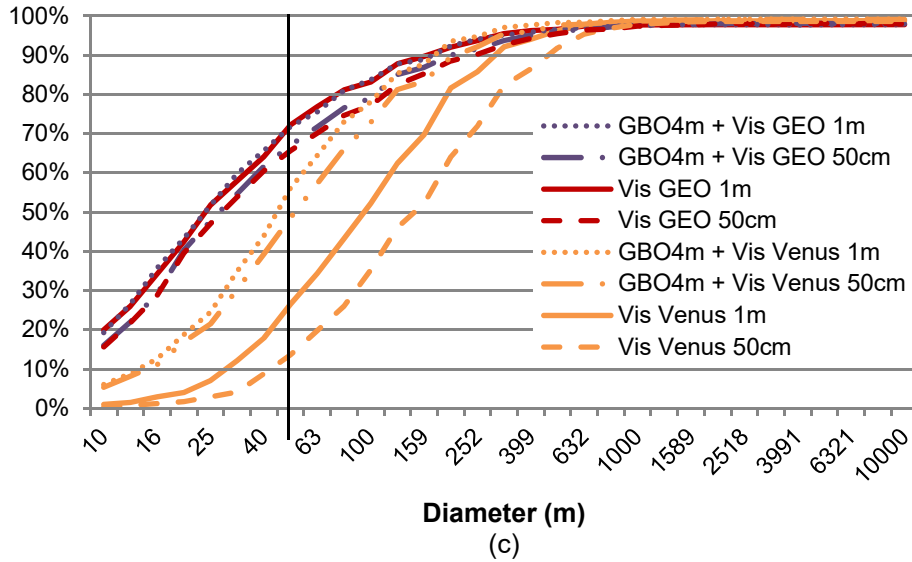
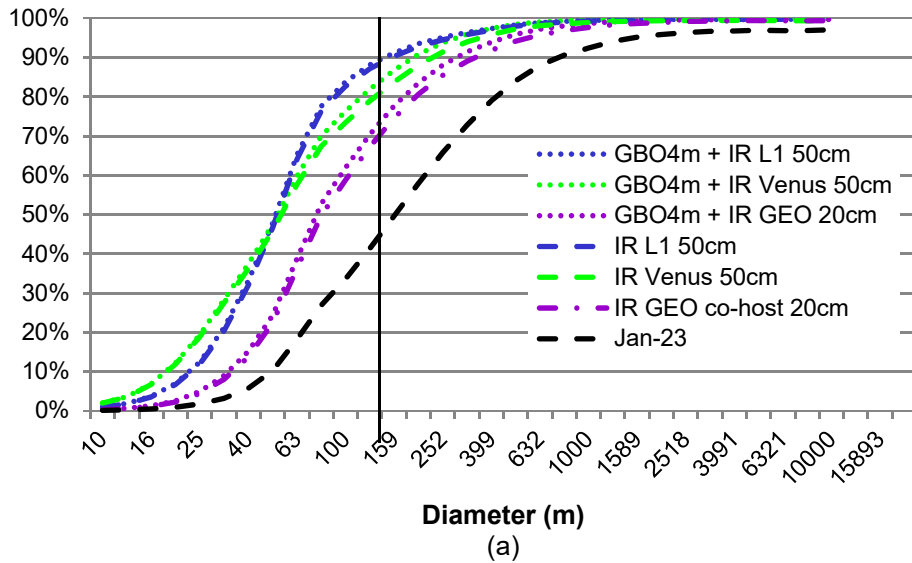
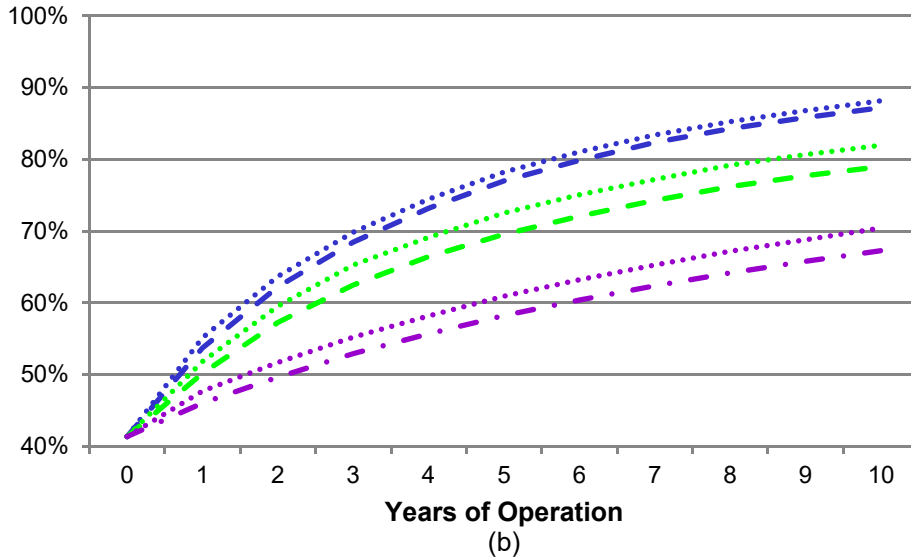


Figure 6-15. Ten-year completeness performance (a), completeness over time at 126 m (b), and warning efficiency (c) for 4-meter ground-based visible system networked with space-based visible systems.

Completeness at 10 Years: IR Space Systems and Visible Ground System



Completeness at 126 m: IR Space Systems and Visible Ground System



Warning Efficiency: IR Space Systems and Visible Ground System

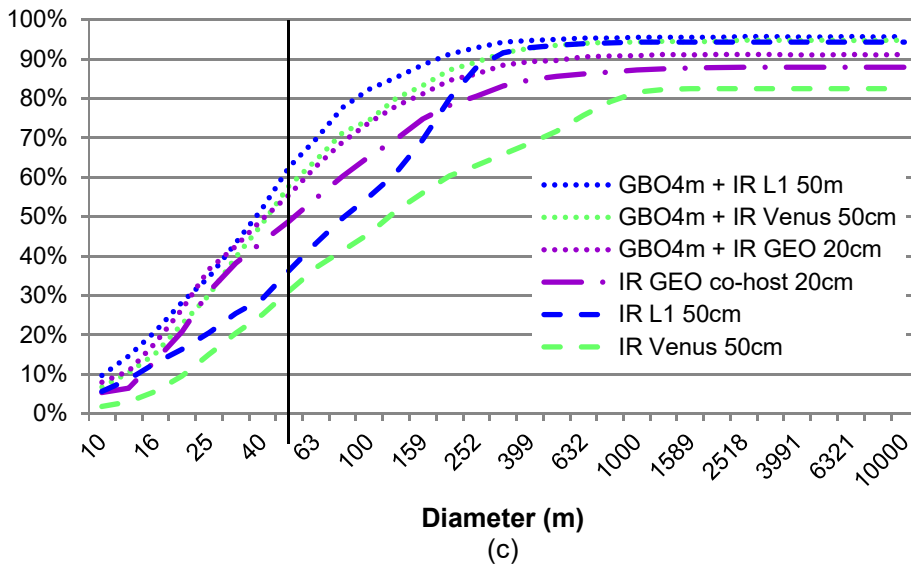
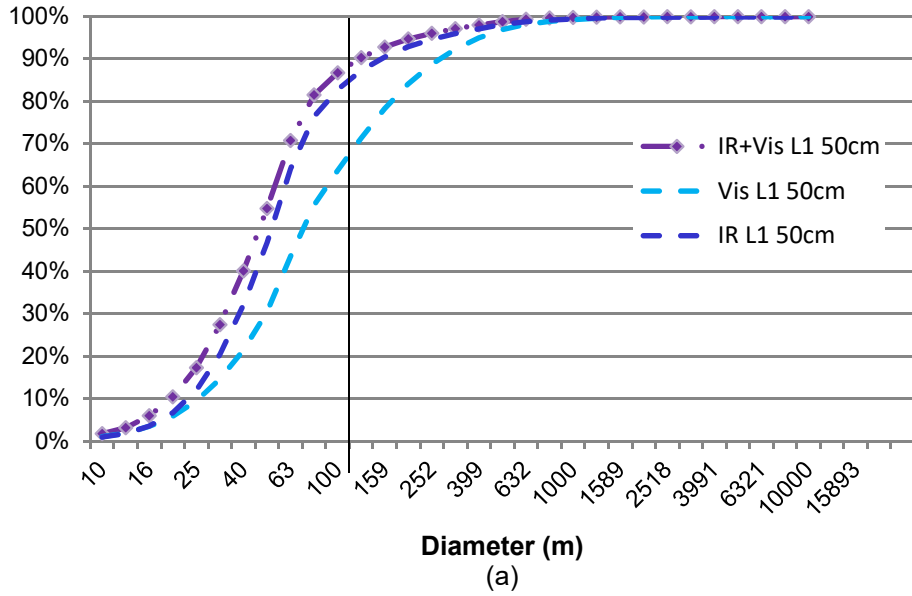
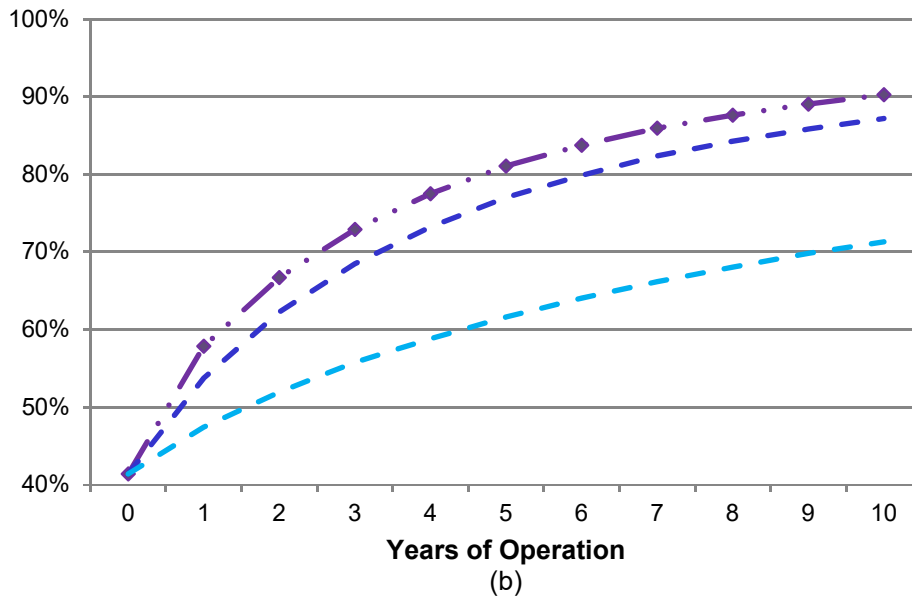


Figure 6-16. Ten-year completeness performance (a), completeness over time at 126 m (b), and warning efficiency (c) for 4-meter ground-based visible system networked with space-based IR systems.

Completeness at 10 Years: IR and Vis L1 50cm



Completeness at 126 m: IR and Vis L1 50 cm



Warning Efficiency: IR and Vis L1 50cm

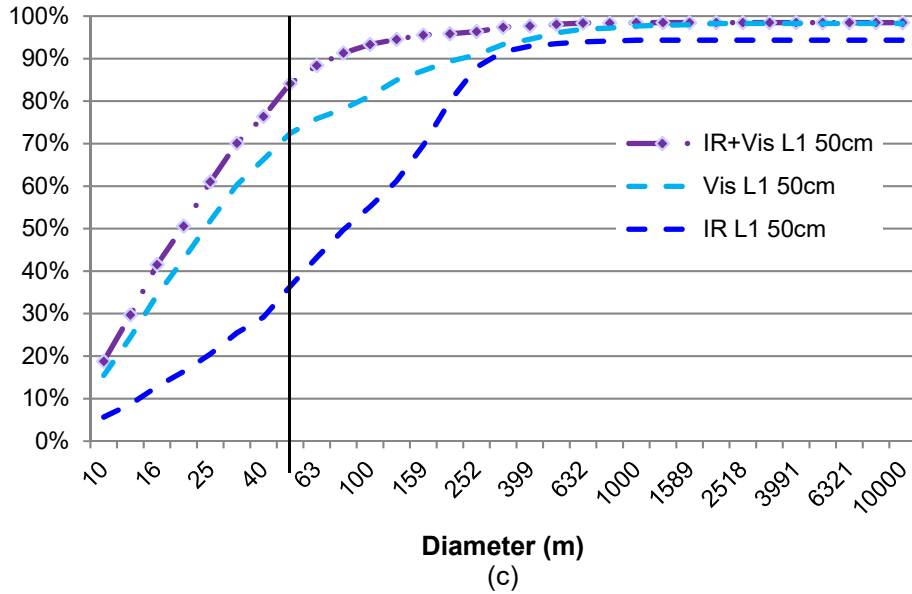
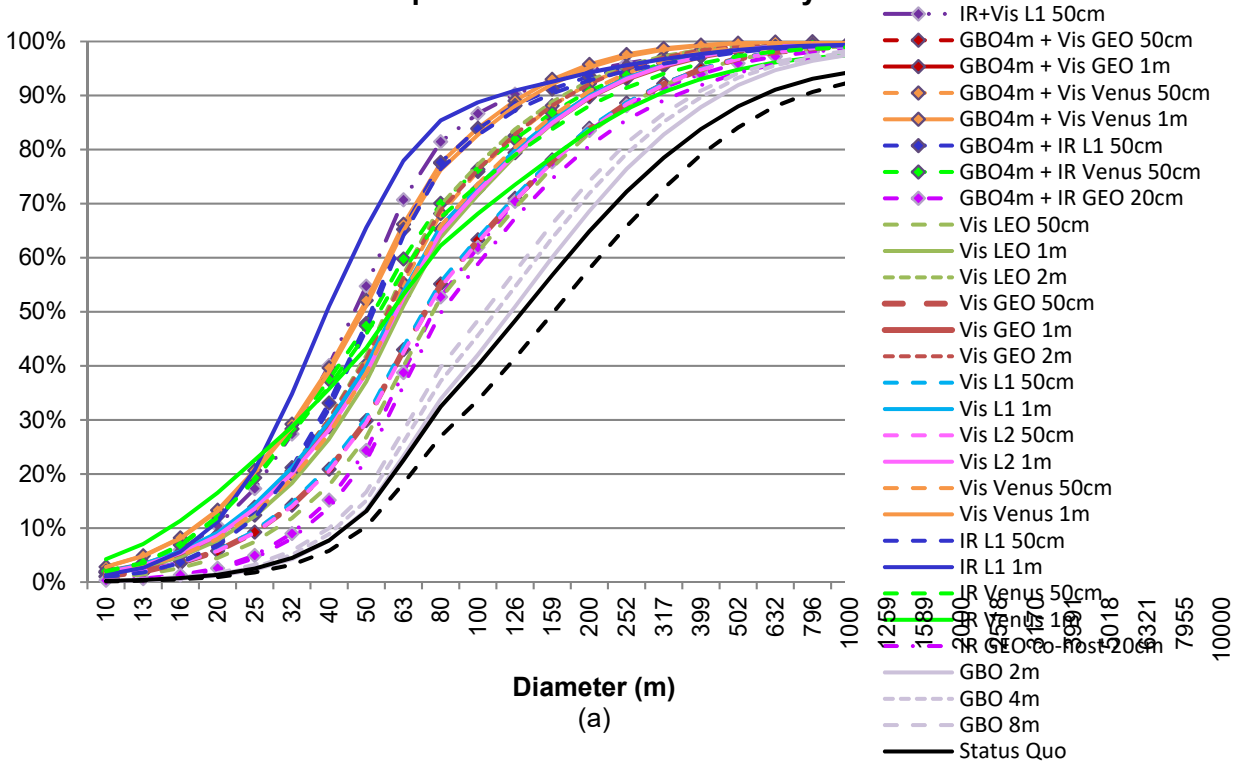
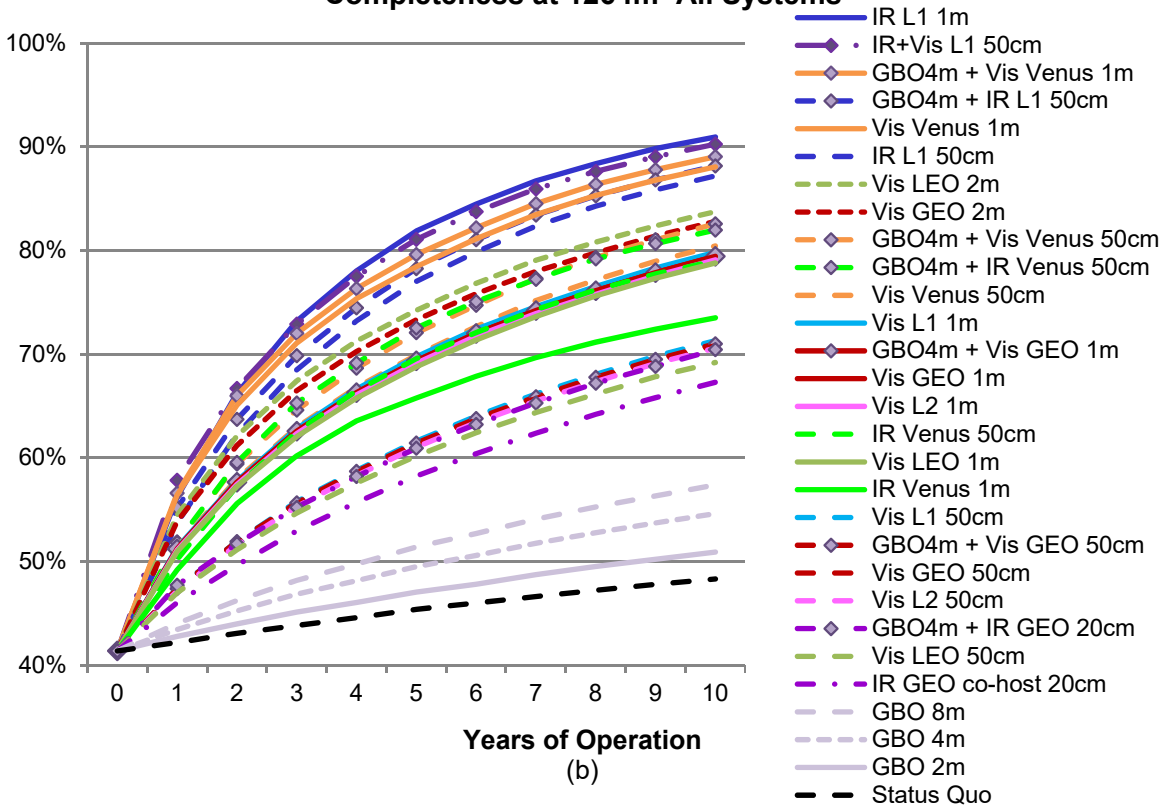


Figure 6-17. Ten-year completeness performance (a), completeness over time at 126 m (b), and warning efficiency (c) for a space-based IR system networked with a space-based visible system.

Completeness at 10 Years: All Systems



Completeness at 126 m: All Systems



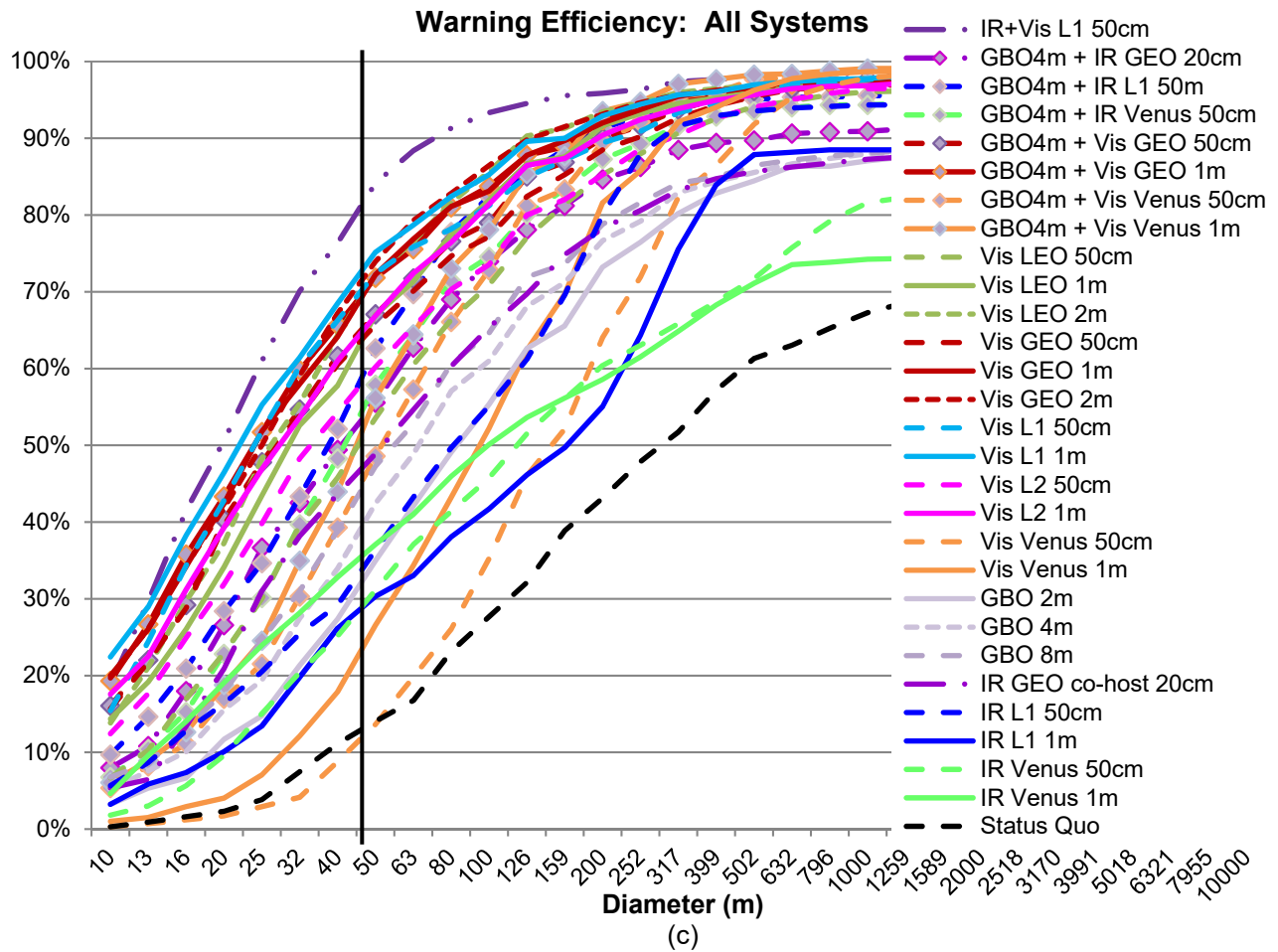


Figure 6-18. Ten-year completeness performance (a), completeness over time at 126 m (b), and warning efficiency (c) for all simulated systems. The systems in the legend are listed in order of performance at ~140 meter for cataloging and at 50 meter for warning.

7 SYSTEM COST ESTIMATION

A major consideration in determining the most appropriate means of detecting near-Earth objects (NEOs) is the cost of the observatories dedicated to the mission. To identify the most affordable options, this study compares the life-cycle costs of ground- and space-based observatory options against their associated benefits. Options with relatively favorable cost/benefit ratios are preferred.

The 2003 Science Definition Team report, “Study to Determine the Feasibility of Extending the Search for Near-Earth Objects to Smaller Limiting Diameters” (hereafter NEO SDT report), found that, while space-based observatories are generally more expensive to design, develop, and deploy than are ground-based observatories, they provide much better resolution, more access to sky, and continuous observations. By contrast, ground-based observatories generally cost less than space-based observatories to build, operate, maintain, and upgrade. The use of ground-based systems, however, is limited to nighttime operations, and their performance can be reduced further by weather and atmospheric distortion.

The goal of this section is to address for each observatory option the question posed in the Science Definition Team (SDT) charter: What would it cost to deploy and operate such a system for 10 years? Risk-adjusted cost estimates for the three ground-based and 15 space-based observatory options are described in Section 4. Note for costing purposes, the L1 and L2 options are treated as just one option.

The 2003 NEO SDT study relied on parametric cost-estimating relationships (CERs) and cost data from analogous systems for the estimates of the costs of both ground- and space-based observatory options. The current study continues the original study’s use of parametric CERs and supplements that data with results from the newer NASA Instrument Cost Model (NICM) Project Cost Estimating Capability and PRICE H™ models funded by NASA; these models take into account recent cost data on space-based instruments and spacecraft, respectively. The CERs for ground-based observatories used in the 2003 study are unchanged, but they have been checked where possible with cost data from the construction of the Space Surveillance Telescope (SST) completed in 2012 by MIT Lincoln Laboratory at White Sands, New Mexico.

Costs in this update are reported in FY2017 dollars. The original study reported costs and cost estimates in FY2003 dollars. Both historical cost data and CEEs from 2003 are adjusted to account for changes in prices since 2003. According to the 2016 NASA New Start Inflation Index, the cumulative inflation from FY2003 to FY2017 is 141 percent. This update uses the latest New Start Inflation Index values to adjust both initial study costs and historical costs to FY2017 dollars.

For this current study, observatory life-cycle cost covers all acquisition costs and 10 years of operations and maintenance. Observatory acquisition is assumed to require five years from authorization to proceed to observatory commissioning. No major maintenance is assumed for either ground- or space-based observatories during the operations phase. For the space-based observatories, which are assumed to be Class B, additional features, such as internally redundant avionics and resilient components, are included in the design of the space-based observatories to ensure a design life of 10 years.

7.1 Ground-Based Observatories

Three ground-based observatory options are assessed in the 2017 study:

1. 2-meter aperture diameter, visible spectrum detectors
2. 4-meter aperture diameter, visible spectrum detectors
3. 8-meter aperture diameter, visible spectrum detectors

While cost comparisons might be made to observatories with similar sized apertures, the NEO observatory costs would tend to be higher because their telescope and detector designs will have been optimized for the NEO mission.

In 2003, models did not exist to predict the costs associated with the design, construction, and operations of ground-based observatories. Instead, cost heuristics and parametric CERs based on previous completed projects and technology trends were used to generate reliable estimates of telescope construction costs.

The acquisition and commissioning costs of ground-based observatories cover telescope structure (e.g., telescope optics and facility), instruments (e.g., charge-coupled-device [CCD] imager, electronics, and cryostat and camera housing), and software development. For the 2003 study, analysts with Science Applications International Corporation and MIT Lincoln Laboratory developed parametric CERs from available observatory cost data that estimate instrument hardware costs as a function of focal plane array area and number of data channels. Software development costs were estimated with the open-source Constructive Cost Model (COCOMO). Operations and support costs for the 2003 study were modeled with cost data from and heuristics based on then-operational observatories.

Since 2003, little has changed in the state of the art for ground-based observatory cost estimating. Therefore, this updated study predicts life-cycle costs of ground-based observatory options on the basis of the 2003 methods; the validity of the hardware acquisition CERs was checked against the cost data from the SST observatory.

7.1.1 Ground-Based Telescope Development and Construction

Telescope development and construction include two major elements: facility construction and the design and development of telescope optics. The elements included in these activities are summarized as follows:

Facility construction

- Project management and engineering, including technical salaries
- Site development, e.g., leveling, generators, roads, etc.
- Transportation of mirrors and equipment to the site
- Dome construction, e.g., control room building, dome base, dome top, etc.
- Altitude-azimuth control systems
- Instrument mount

- Cranes and rigging for erecting the enclosure

Telescope optics

- Telescope structure, including telescope body and mount
- Optics support and control (and mirror moving container, if necessary)
- Optics: primary, secondary and tertiary mirrors
- Mirror coating/aluminizing

For estimating optics cost, the 2003 study and this update rely on a CER between aperture size and cost that has been described by many authors, including Schmidt-Kaler and Rucks (1997 and references therein) and Stepp et al. (2003). All of the authors observe that optics cost increases exponentially with increasing aperture diameter. The CER is as follows:

$$\text{Optics Cost} = \alpha D^{\gamma}$$

where α is a constant, γ is the exponential growth rate of the cost, and D is the aperture diameter in meters.

Based on data obtained from then-existing observatories, optics cost in thousands of FY2003 dollars was estimated using the values $\alpha = 2000$ and $\gamma = 1.3$. While the CER is valid for aperture diameters from 1 to 10 meters, it tends to overestimate the cost of larger-aperture telescopes and those cost-reduction techniques—light-weighting, segmenting of the mirror—have been employed. In the 2003 study, the aperture diameters under consideration were 1, 2, 4, and 8 meters, and their designs included no mirror segmentation or light-weighting. Therefore, the authors were confident in the validity of predicted costs. The same is true for this updated study.

After adjustment using the NASA New Start Inflation Index for 2016, the 2003 telescope CER was revised as follows:

$$\text{Facility Cost (FY17\$K)} = \alpha D^{\gamma}$$

where $\alpha = 2820$, D = aperture diameter in meters, and $\gamma = 1.3$.

Facility construction cost is predicted by a linear CER with aperture diameter D as the independent variable. Based on data analysis, the CER in thousands of FY2003 dollars is as follows:

$$\text{Facility Cost (FY03\$K)} = \beta D + \tau$$

where $\beta = 2500$ and $\tau = 2000$.

After an adjustment that uses the NASA New Start Inflation Index for 2016, the CER was revised for the current study:

$$\text{Facility Cost (FY17\$K)} = \beta D + \tau$$

where $\beta = 3525$ and $\tau = 2820$.

During the 2003 study, cost analysts found that the scatter in the cost data from the existing systems was primarily a result of differing reporting practices. Specifically, some “actuals” data were obtained from program websites and journals. Accordingly, the only cost data used in constructing the above CERs were those obtained from such reliable sources such as project offices and available in a predefined work breakdown structure.

Fifteen telescope optics and construction cost data points for ground-based observatories were available to construct the optics and facility CERs. Nevertheless, as was shown in the 2003 report, both CERs provide a close approximation to the cost of most pre-2003 telescope projects and the more recent SST observatory. Cost estimates for the three ground-based observatories proposed as 2017 options are summarized in Table 7-1.

Table 7-1. Estimated telescope construction cost (TCC) for ground-based observatories, by aperture diameter (meters).

Aperture Diameter (m)	Telescope Construction Cost		Percent Cost Increase
	FY2003\$	FY2017\$	
2	\$11.9M	\$16.8M	-
4	\$24.1M	\$34.0M	102%
8	\$51.9M	\$73.1M	115%

The slow and nearly linear increase in facility construction costs as a function of aperture diameter masks the larger difference in optics costs between, for example, the 4- and 8-meter options.

7.1.2 Ground-based Observatory: Instrument Design and Development

The costs of ground-based observatory instruments for the 2017 options account for the acquisition of four elements: (1) CCD imagers, (2) imager electronics, (3) the cryostat and camera housing, and (4) shutter. The first three elements were estimated in 2003 by using CERs developed at MIT Lincoln Laboratory. The last, C_{Shutter} (shutter cost), was estimated from cost data to be FY2017 \$214K. For 2017, the three CERs have been adjusted for inflation by using the 2016 NASA New Start Inflation Index rates. The instrument CERs by element are shown as follows:

CCD imagers. The estimated costs of unpackaged, scientific-grade, back-illuminated silicon (Si) CCD imagers are predicted with the following CER:

$$C_{\text{CCD}}(\text{FY17}\$K) = 18,330 A_{\text{Focal Plane}}$$

where $A_{\text{Focal Plane}}$ is the area of the focal plane in m^2 .

Imager electronics: The nonrecurring and recurring costs of analog front-end, signal conditioning, video chain, analog-to-digital conversion, multiplexing, data formatting, and mechanical packaging of the electronics boards are predicted as follows:

$$C_{\text{ElectronicS}}(\text{FY17}\$K) = 14.1 (\text{\#channels}).$$

Cryostat/Camera housing: The estimated costs of the focal plane assembly, CCD packaging, dewar window, cooling head, and internal cabling are based on the following CER:

$$C_{\text{Cryo}}(\text{FY17}\$K) = 3,525 A_{\text{Focal Plane}}$$

The total predicted instrument acquisition cost is the sum of the predicted CCD, electronics, and cryostat/camera housing costs. In other words,

$$C_{\text{Instr}}(\text{FY17}\$K) = C_{\text{CCD}} + C_{\text{Elec}} + C_{\text{Cryo}} + C_{\text{Shutter}}$$

The characteristics of the instruments for the ground-based observatory options are summarized in Section 4.1.4. In calculating the cost of the instruments, it was assumed that the focal plane area (240mm x 360mm) and number of channels (192) were identical in each of the three observatory options, regardless of telescope aperture size. The predicted acquisition costs for the three options are shown in Table 7-2. The total acquisition costs for the three ground-based observatory options are also given.

Table 7-2. Instrument acquisition costs for ground-based observatories.

Instrument	2/4/8 m Aperture
C_{CCD}	\$1,584K
C_{Elec}	\$2,707K
C_{Cryo}	\$305K
C_{Shutter}	\$212K
Total	\$4,808K

7.1.3 Ground-Based Observatory Operations and Support

Three activities make up the bulk of operations and support (O&S) costs of ground-based observatories:

- Observing-time labor
- Maintenance of the facility, optics, and instrument
- Periodic replacement of failed components

A CER derived from cost data for existing observatories is used to predict annual O&S costs other than software maintenance (see following section). This CER covers labor, hardware replacement, and the integration and commissioning of replacement components that may be more up to date than the original (failed) components. It does not account for upgrades in observatory performance. However, as specific components fail, it is likely that they will be replaced with newer, more capable components. The likely costs of these upgraded replacements are included in the cost generated by the CER.

The CER for the annual operations cost, C_{Ops} , of a single ground-based observatory is

$$C_{Ops} \text{ (FY17\$M)} = 0.634D + 0.064(TCC)$$

where D is the aperture diameter in meters and TCC is (estimated) total observatory construction cost.

In this equation, the first term estimates labor-hour costs on the basis of facility size and historical data. The second term describes the increase in operations costs with increase in aperture size. Calculating the total estimated O&S costs requires multiplying the annual O&S cost by the number of years of operation (10). Estimated O&S costs for all options are shown in Table 7-3. The table shows that O&S costs increase nonlinearly with aperture diameter.

Table 7-3. Operations and support (O&S) costs for ground-based observatories.

Aperture (m)	Annual O&S Cost		Total O&S Cost (10 years)
	FY2003\$	FY2017\$	FY2017\$
2	\$2.07M	\$2.92M	\$29.2M
4	\$4.16M	\$5.87M	\$58.7M
8	\$8.56M	\$12.07M	\$122.7M

7.1.4 Ground-Based Software Development

Costs of software development for the ground-based observatory options are estimated using the open-source Constructive Cost Model (COCOMO), which estimates software development labor as a function of the size of the development effort (expressed in source lines of code [SLOCs]), code application and complexity, and developer productivity.

For the 2003 study, size and other input parameters were derived from available cost data. Table 7-4 disaggregates by major function the number of SLOCs that are developed for the typical ground-based observatory. The total estimated SLOCs is 332,000 SLOCs. Based on historical data, the average annual cost of a software developer in FY2017 dollars is \$282K (FY2003 \$200K). The estimated level of effort and cost of software development for any ground-based observatory is described in Table 7-5.

Table 7-4. Software development sizes (reported in source lines of code [SLOCs]) by software module for ground-based observatory options, based on 2003 data.

Software Module	SLOCs
Total	332,000
Operations, e.g., telescope control, operator interface, scheduling	200,000
Data processing, e.g., data acquisition, image processing, detection algorithms	27,000
Data management, e.g., archiving, database management, data submission scripts	5,000
Orbit-fitting software	100,000

Table 7-5. Estimated software development costs and schedule durations for ground-based observatory options.

	Units	2 m	4 m	8 m
Cost	FY2017\$M	\$9.2M	\$9.2M	\$10.7M
Effort	Person-Months	390	390	455
Schedule	Months	22.1	22.1	23.5
Productivity	SLOC/FTE/ Month	851	851	730
Instructions	\$/SLOC	27.6	27.6	32.2
Staff	FTEs	17.7	17.7	19.3

The software development costs of the two smaller observatory options are each \$9.2M (17.7 FTEs); those of the 8-meter observatory are 16% higher at \$10.7M (19.3 FTEs).

After observatory commissioning, software maintenance will also require the annual equivalent of one FTE at \$282K per year. That estimated cost is added to the annual O&S cost.

7.1.5 Ground-Based Observatory Cost Roll-up

The total estimated costs of the ground-based system options are presented in Table 7-6. The second column shows the estimated acquisition cost based on the sum of the telescope construction cost (TCC), imager cost, and software development cost. The third column shows the annual O&S cost, including software maintenance. The baseline cost presented in the fourth column shows for each option the life-cycle cost, including ten years of O&S. The last column adjusts the baseline for risks with 30% unallocated cost reserves.

Table 7-6. Estimated life-cycle ground-based observatory options cost (in FY2017 \$M), with unallocated cost reserves.

Aperture Diameter (m)	Acquisition: TCC + Instrument + Software Development	Operations & Support (O&S) per Year (including software maintenance)	Baseline: Acquisition + 10 Years O&S	Total Including 30% Unallocated Cost Reserves
2	\$30.8M	\$3.20M	\$62.8M	\$81.6M
4	\$48.0M	\$5.90M	\$107.0M	\$139.1M
8	\$88.6M	\$12.30M	\$211.6M	\$275.1M

The estimated risk-adjusted life-cycle cost of the 8-meter option at \$268.8M is 3.5 times that of the 2-meter option and almost 2 times that of the 4-meter option.

7.2 Space-Based Observatories

For this 2017 study, life-cycle, risk-adjusted cost estimates are generated for the 15 space-based observatory options (10 visible, 5 infrared) described in detail in Section 4. The following list summarizes the details of the observatory options included in the analysis:

- *Option 1V*: 2-meter aperture diameter telescope, visible-band detectors, in low Earth, Sun-synchronous orbit (LEO S.S.)
- *Option 2V*: 2-meter aperture diameter telescope, visible-band detectors, in geosynchronous orbit (GEO)
- *Option 3V*: 1-meter aperture diameter telescope, visible-band detectors, in LEO S.S.
- *Option 4V*: 1-meter aperture diameter telescope, visible-band detectors, in GEO
- *Option 5V*: 1-meter aperture diameter telescope, visible-band detectors, in Sun-Earth Lagrange point orbit (L1/L2)
- *Option 6V*: 1-meter aperture diameter telescope, visible-band detectors, in 0.7 astronomical unit orbit (0.7AU)
- *Option 7V*: 0.5-meter aperture diameter telescope, visible-band detectors, in LEO S.S.
- *Option 8V*: 0.5-meter aperture diameter telescope, visible-band detectors, in GEO
- *Option 9V*: 0.5-meter aperture diameter telescope, visible-band detectors, in L1/L2
- *Option 10V*: 0.5-meter aperture diameter telescope, visible-band detectors, in 0.7AU
- *Option 11R*: 1-meter aperture diameter telescope, infrared (IR) detectors, in L1/L2 orbit
- *Option 21R*: 1-meter aperture diameter telescope, IR detectors, in 0.7 AU orbit
- *Option 31R*: 0.5-meter aperture diameter telescope, IR detectors, in L1/L2 orbit
- *Option 41R*: 0.5-meter aperture diameter telescope, IR detectors, in 0.7AU orbit
- *Option 51R*: 0.2-meter aperture diameter telescope, IR detectors, in (GEO) orbit hosted on a commercial satellite

All but the last option will require the acquisition of and integration with a dedicated spacecraft on a dedicated launch vehicle. The last option would likely be hosted on a communications satellite.

Lifecycle cost estimates for space-based observatory options in the 2017 study cover design and development of the mission (Phases A–D), including the following level-2 elements defined in the NASA Work Breakdown Structure (WBS):

- WBS 01/02/03: Project support functions that include program management (WBS 01), systems engineering (WBS 02), and safety and mission assurance (WBS 03)
- WBS 04: Science, including principal investigator, principal scientists, and instrument specialists
- WBS 05: Payload (i.e., the telescope assembly)
- WBS 06: Spacecraft (i.e., the spacecraft bus)
- WBS 07: Planning for and initial mission operations

- WBS 08: Launch vehicle and services
- WBS 09: Ground data systems
- WBS 10: Observatory (i.e., payload and spacecraft bus) integration and test
- WBS 12: Cost Reserves (WBS 12)

In addition, post-launch (Phase E) costs for mission operations and support (MO&S) for 10 years are estimated. Phase-E MO&S costs cover the management, engineering, and mission operations of the spacecraft and instrument, data communications, and the processing and storage of scientific data.

For the 2003 study, the NASA/Air Force Cost Model (NAFCOM) was used to estimate the acquisition costs of instrument payloads (WBS 05) and spacecraft buses (WBS 06). The NAFCOM-generated cost estimates covered hardware design and development, management and systems engineering, and integration and test. NAFCOM development has been discontinued, however, necessitating the use of different methodologies in this study. The bus hardware in the 2017 study was estimated by the Applied Physics Lab (APL), using a parametric estimating model developed by NASA called the Project Cost Estimating Capability (PCEC) and the commercial PRICE H™ model, and by comparing analogous buses. In addition to developing bus hardware costs, PCEC along with publicly available pricing information, was used to estimate the cost of the launch vehicles and services for each of the mission options.

Instrument payload (WBS 05) costs were estimated by the Space Dynamics Laboratory (SDL) of Utah State University by using a combination of the parametric NASA Instrument Cost Model (NICM) VII, cost histories of similar optical instruments, and engineering estimates. SDL also assisted in defining the technical and operational characteristics of the instrument options for purposes of cost estimation.

7.2.1 Spacecraft Bus

Estimating the costs of spacecraft buses (WBS 06) began with defining bus architectures that were capable of providing sustained operation of each instrument option. All buses were assumed to be Class B, with internally redundant avionics, large propulsion tanks when needed, and additional guidance, navigation, and control elements sufficient for a ten-year design life. All buses were powered by solar arrays, and all relied on monopropellant propulsion systems when needed. Minimal technology development is assumed for the spacecraft bus hardware.

The cost for the 15 different mission options considered in this study are strongly influenced by the four potential orbit choices presented. The unique aspects of each of these orbital environments impact the design parameters of the spacecraft subsystems in different ways. In costing the spacecraft buses in PCEC, the Wide-field Infrared Survey Explorer (WISE) mission was used as a starting point for the 0.5-meter-class options and Kepler was used as a starting point for the 1-meter-class options. Mass values by subsystem and technical inputs for each of the analogous missions were taken from NASA's Cost Analysis Data Requirement (CADRe) documentation at the time of each mission's launch. Starting with these technical inputs, other PCEC inputs were then varied on the basis of the orbital environmental characteristics to develop estimates for each of the 0.5-meter- and 1-meter-class options. A different estimating approach was used to develop the spacecraft bus estimate for the 2-meter-class options since PCEC does not yet have the capability to

estimate in the 2-meter telescope trade space. These larger options were estimated by using the PRICE H™ commercial parametric estimating suite, which builds the estimate up from component-level information, and by comparing to analogous buses. It should be noted that the flight-software development effort is included within the PCEC and PRICE H™ estimated hardware cost.

Historically derived hardware cost wrap factors were used to estimate mission support function costs as follows:

- WBS 01/02/03, Project Level Support Functions (PM/SE/MA): 19% of the estimated costs of WBS elements 05, 06, and 10. [Note: 19% is a typical factor for Discovery-class missions]
- WBS 05.x, Payload Support Functions (PM/SE/MA): 15% of the estimated hardware/software development costs
- WBS 10, Observatory Integration and Testing: 12% of estimated costs of WBS 05 and WBS 06

The inclusion of a WBS 05.01 adds conservatism to the bus cost estimate because that cost is typically included only when the bus is procured separately from the lead mission contractor. Likewise, the inclusion of a robust 12% for observatory integration and test is in addition to the extensive payload testing that is conducted prior to the payload's delivery for integration with the bus.

Costs of other level-2 WBS elements are estimated by using cost factors derived from the NASA Cost Analysis Data Report's mission cost data as follows:

- WBS 04, Science: 20% of estimated payload (WBS 05) cost
- WBS 07, Mission Operations (pre-Phase E): 8% of estimated WBS 05 and WBS 06 costs to account for mission planning, launch support, and initial operations and checkout
- WBS 09, Ground Data Systems: 9% of estimated WBS 05 and 06 costs to support development of systems for communication and data transfer and storage

In the short time between the previous NEO SDT study and now, the launch vehicle market has seen tremendous disruption with the introduction of additional commercial service providers and the retirement of the Delta II rocket line. The launch vehicle estimates (WBS 08) included in the life-cycle costs for the 15 options analyzed here roughly mirror current United Launch Alliance published pricing with an allowance for an additional kick motor for the 0.7AU cases. As the market forces continue to act, it is likely that the estimated launch vehicle costs presented here will continue to decline.

An additional cost of \$80 million was added to each of the four options (Option numbers 6V, 10V, 2IR, and 4IR from the list at the beginning of Section 7.2) positioned at 0.7 AU in order to cover the cost of an optical communications link for the download of large volumes of image data. The estimated cost is based on engineering judgement and includes some uncertainty as optical communication systems for deep space applications are still in the development stage although the technology has been proven for near Earth applications.

Option 5IR, a hosted payload in GEO, was designed and estimated on the basis of NASA experience with the use of communications satellites to host small payloads. NASA's Global-scale Observations of the Limb and Disk (GOLD) mission is scheduled to launch on a commercial satellite to GEO in 2017.

GOLD's reported accommodation cost was used as the basis for the \$15 million cost included in Option 5IR's WBS 6.0 cost. This accommodation cost is all inclusive as it provides the ride to GEO, necessary spacecraft resources (power, etc.) and a means to deliver instrument data back to the Earth.

Table 7-7 summarizes the estimated acquisition and launch (Phases A–D) costs of the 15 space-based options. Note that 30% unallocated cost reserves are added to the baseline cost estimate, a conservative strategy that, together with the absence of technology development for the spacecraft bus, should ensure a successful mission.

Table 7-7. Estimated costs of space-based observatory options (visible), with 30% unallocated cost reserves (FY2017 dollars).

Visible Detector (FY17\$M)	Option	1V	2V	3V	4V	5V	6V	7V	8V	9V	10V
	Aperture (m)	2.0	2.0	1.0	1.0	1.0	1.0	0.5	0.5	0.5	0.5
	Orbit	LEO (S.S.)	GEO	LEO (S.S.)	GEO	L1/L2	0.7AU	LEO (S.S.)	GEO	L1/L2	0.7AU
	Actively Cooled?	N	N	N	N	N	N	N	N	N	N
	Optical Communications?	N	N	N	N	N	Y	N	N	N	Y
NASA WBS	(% of 1m 0.7AU Ph.B-D)	92%	95%	55%	56%	69%	89%	38%	38%	48%	67%
Sum (1-12)	Total, Phases B-D	\$ 1,139	\$ 1,170	\$ 677	\$ 693	\$ 853	\$ 1,096	\$ 470	\$ 476	\$ 590	\$ 833
12	30% Cost Reserves (w/o LV)	\$ 229	\$ 236	\$ 122	\$ 126	\$ 163	\$ 211	\$ 75	\$ 76	\$ 102	\$ 150
Sum (1-10)	Baseline, Phases B-D, no reserves	\$ 910	\$ 934	\$ 554	\$ 567	\$ 690	\$ 886	\$ 395	\$ 400	\$ 488	\$ 683
1/2/3	PM, SE, S&MA	\$ 109	\$ 113	\$ 58	\$ 60	\$ 78	\$ 101	\$ 35	\$ 36	\$ 49	\$ 72
4	Science	\$ 43	\$ 43	\$ 23	\$ 23	\$ 26	\$ 31	\$ 16	\$ 16	\$ 19	\$ 24
5	Payload	\$ 215	\$ 214	\$ 115	\$ 114	\$ 132	\$ 155	\$ 79	\$ 78	\$ 96	\$ 119
6	Spacecraft	\$ 274	\$ 290	\$ 146	\$ 155	\$ 218	\$ 298	\$ 80	\$ 83	\$ 122	\$ 202
7	Mission Operations	\$ 25	\$ 26	\$ 13	\$ 14	\$ 20	\$ 27	\$ 7	\$ 7	\$ 11	\$ 18
8	Launch Vehicle & Services	\$ 147	\$ 147	\$ 147	\$ 147	\$ 147	\$ 184	\$ 147	\$ 147	\$ 147	\$ 184
9	Ground Systems	\$ 39	\$ 40	\$ 21	\$ 22	\$ 28	\$ 36	\$ 13	\$ 13	\$ 17	\$ 26
10	Observatory I&T	\$ 59	\$ 61	\$ 31	\$ 32	\$ 42	\$ 54	\$ 19	\$ 19	\$ 26	\$ 39

Table 7-8. Estimated costs of space-based observatory options (infrared), with 30% unallocated cost reserves (FY2017 dollars).

IR Detector (FY17\$M)	Option	1IR	2IR	3IR	4IR	5IR
	Aperture (m)	1.0	1.0	0.5	0.5	0.2
	Orbit	L1/L2	0.7AU	L1/L2	0.7AU	GEO
	Actively Cooled?	N	Y	N	Y	Y
	Optical Communications?	N	Y	N	Y	N
NASA WBS	(% of 1m 0.7AU Ph.B-D)	76%	100%	49%	73%	14%
Sum (1-12)	Total, Phases B-D	\$ 942	\$ 1,236	\$ 605	\$ 899	\$ 178
12	30% Cost Reserves (w/o LV)	\$ 183	\$ 243	\$ 106	\$ 165	\$ 41
Sum (1-10)	Baseline, Phases B-D. no reserves	\$ 758	\$ 994	\$ 499	\$ 734	\$ 137
1/2/3	PM, SE, S&MA	\$ 88	\$ 116	\$ 50	79	\$ 20
4	Science	\$ 35	\$ 44	\$ 21	\$ 30	\$ 15
5	Payload	\$ 174	\$ 221	\$ 103	\$ 150	\$ 75
6	Spacecraft	\$ 218	\$ 298	\$ 122	\$ 202	\$ 15
7	Mission Operations	\$ 20	\$ 27	\$ 11	\$ 18	\$ -
8	Launch Vehicle & Services	\$ 147	\$ 184	\$ 147	\$ 184	\$ -
9	Ground Data Systems	\$ 31	\$ 41	\$ 18	\$ 28	\$ -
10	Observatory I&T	\$ 47	\$ 62	\$ 27	\$ 42	\$ 11

Option 2IR is the most expensive option estimated since the 1-meter optical instrument requires a relatively expensive CMG-controlled bus operating in a deep space environment with the added expense of using an optical communications package. The hosted payload, with its relatively small 20-centimeter optics, is by far the least expensive because of the considerable savings offered in a commercial accommodation scenario. The other options are arrayed from 38%–95% of the estimated cost of Option 2IR.

7.2.2 Space-Based Instruments

The 15 instrument options under consideration in the 2017 NEO SDT study are optical instruments with either IR or visible imaging detectors. Technical and operational descriptive parameters for these 15 systems are summarized in Table 7-8.

Total Phase B/C/D development costs for each of these instruments were estimated by using the current version of the NASA Instrument Cost Model (NICM VIIc Rev2). With the exception of the 20-centimeter IR telescope, total costs for each instrument were calculated as the sum of two system costs within NICM: (1) the optical telescope assembly (OTA) and (2) the back-end instrument (detector, electronics, focal plane array thermal control, and other detector-related subsystems). The NICM includes OTA costs in the back-end instrument system for telescopes with aperture diameters less than 25 centimeters.

Standard NICM CERs were used to run Monte Carlo cost simulations (10,000 runs each) for the OTA and detector systems of each instrument option. Aperture diameter is the primary cost driver in the OTA CER, while instrument costs are driven by mass and peak power. Baseline mass and power values were established for each instrument through analysis and comparison of telescope and instrument analogies in the NICM database. Detailed NICM “resumes” were used to estimate

subsystem mass and power, with these values adjusted according to design and application similarity between each NEO instrument and the relevant analogy design(s). Finally, these resource estimates were reviewed and modified if necessary by SDL mechanical and electrical engineers with significant experience developing similar space-based telescopes and instruments.

Final NICM inputs used to generate total instrument cost estimates are shown in Table 7-8.

Table 7-9. System-specific cost model inputs.

System	Environ.	Instrument Mass* (kg)	Mass Basis of Estimate (from NICM analogy subsystems)	Max Power (W)	Power Basis of Estimate (from NICM analogy subsystems)
Options 1V/ 3V/ 7V: 0.5/1/2 m Visible LEO S.S.	Earth Orbiting	83 ± 30%	Det/Elect: Kepler (71 kg) Thermal: GALEX/HiRISE (7 kg) (+5 kg thermal for LEO)	139 ± 30%	Det/Elect: Kepler/HiRISE (119 W) Thermal: 20 W LEO, 10 W Helio
Options 2V/ 4V/ 8V: 0.5/1/2 m Visible GEO	Earth Orbiting		78 ± 30%		Det/Elect: Kepler (71 kg) Thermal: mean of GALEX / HiRISE (7 kg)
Options 5V/ 9V: 0.5/1 m Visible L1/L2	Planetary				
Options 6V/ 10V: 0.5/1 m Visible 0.7AU	Planetary				
Options 1IR/ 3IR: 0.5/1 m IR L1/L2	Planetary	55 ± 30%	Det / elect: WISE (22.8 kg) Thermal: AIRS (64 kg) x 0.5	189 ± 30%	Det/Elect: WISE (92 W) x 0.75 Thermal: AIRS (120 W)
Options 2IR/ 4IR: 0.5/1 m IR 0.7 AU	Planetary	30 ± 30%	Det / elect: WISE (22.8 kg) Thermal: GALEX/HiRISE (7 kg)	79 ± 30%	Det/Elect: WISE (92 W) x 0.75 Thermal: 10 W
Option 5IR: 0.2 m IR GEO	Earth Orbiting	40 ± 30%	Det/Elect: WISE (22.8 kg) x 0.75 OTA: LORRI (5.6 kg) x 1.25 Thermal: AIRS (64 kg) x 0.25	115 ± 30%	Det/Elect: WISE (92 W) x 0.6 Thermal: AIRS (120 W) x 0.5

*Per NICM VII CERs, mass is for back-end instrument only (excludes OTA and telescope-specific subsystems) for all instruments >25 cm. The 20 cm telescope mass includes OTA.

S.S. = Sun Synchronous, Det = Detector, Elect = Electronics, HiRISE = High Resolution Imaging Science Experiment is a camera on board the Mars Reconnaissance Orbiter, WISE = Wide-field Infrared Survey Explorer is a NASA infrared-wavelength astronomical space telescope, GALEX = Galaxy Evolution Explorer is a NASA ultraviolet space telescope, AIRS = Atmospheric Infrared Sounder is an instrument on board NASA's Aqua satellite, LORRI = Long-Range Reconnaissance Imager is a long-focal-length imager on NASA's New Horizons spacecraft, OTA = Optical Telescope Assembly on NASA's Hubble Space Telescope

The resulting NICM costs estimates for the 15 candidate instruments are summarized in Table 7-9. These cost estimates were initially generated in \$FY2004, then adjusted to \$FY2017 by using the 2015 NASA New Start Inflation Index factor of 1.366. Cost estimates in the table are reported at the 50% and 70% confidence levels.

Table 7-10. Space-based instrument cost summary.

NICM Instrument Cost at 50% and 70% Confidence Levels (\$M, FY2017)									
System	Option #	Telescope		Back End		Cryocooler /Technology		Total	
		50%	70%	50%	70%	50%	70%	50%	70%
2 m Visible (LEO SS)	1V	157	192	57	77	-	-	215	269
1 m Visible (LEO SS)	2V	57	70	57	77	-	-	115	147
50 cm Visible (LEO SS)	3V	21	26	57	77	-	-	79	103
2 m Visible (GEO)	4V	157	192	57	76	-	-	214	269
1 m Visible (GEO)	5V	57	70	57	76	-	-	114	147
50 cm Visible (GEO)	6V	21	26	57	76	-	-	78	103
1 m Visible (L1/L2)	7V	57	70	74	92	-	-	132	163
50 cm Visible (L1/L2)	8V	21	26	74	92	-	-	96	118
1 m Visible (0.7 AU)	9V	57	70	87	108	10	15	155	193
50 cm Visible (0.7 AU)	10V	21	26	87	108	10	15	119	149
1 m IR (L1/L2)	1IR	103	127	71	87	-	-	174	215
50 cm IR (L1/L2)	2IR	38	47	65	80	-	-	103	127
1 m IR (0.7 AU)	3IR	103	127	83	103	35	50	221	280
50 cm IR (0.7 AU)	4IR	38	47	77	95	35	50	150	192
20 cm IR (GEO)	5IR	0	0	50	67	25	35	75	102

All cost estimates assume a Technology Readiness Level for major components and subassemblies of six or greater. No significant technology development efforts are anticipated for any of the fifteen space-based options.

7.2.3 Mission Operations and Support Costs

For the 2017 NEO SDT study, MO&S costs for each space-based option are estimated by using the recently developed Mission Operations Cost Estimating Tool (MOCET). MOCET is based on the historical costs of robotic missions. It estimates MO&S costs by duration and type of activity—for example, checkout, normal cruise, maneuver, orbital insertion, and science operations.

For the current study, we assume a 10-year operational lifetime spent in transit, calibration, and then continuous performance of survey observations.

Because MOCET does not estimate the cost of telecommunications services, including telemetry and downloads of science data, those costs were calculated separately on the basis of the network used and were then added to the MOCET estimate. Specifically,

- **For the LEO/GEO Options 1V, 2V, 3V, 4V, 7V, 8V and 5IR**, the preferred network solution is the Near Earth Network (NEN). Data are transmitted through three 10-minute downlinks per day. It is assumed that the operations center is operated 24 hours a day (in three shifts) to monitor the transmissions for complete and uncorrupted data downlink. As NEN is a NASA owned, there is a relatively small fee for missions to utilize the service which equates to approximately \$0.2M over the expected ten year lifetime of the concepts analyzed here. The LEO operations cost is based on this three-shift assumption. However, as the operations team becomes more experienced and efficient, the operations may become more automated and the required operator hours may drop down to one shift per day, resulting in further savings.
- **The L1/L2 Options 5V, 9V, 1IR and 3IR** would likely exploit the Deep-Space Network (DSN) 34-meter antenna for tracking and data downlink. For those options, telemetry and science data are downlinked once every day over a period of 4.2 hours. Only one shift is required in the operations center. Calculated on the DSN pricing guidance and anticipated image transfer rates, the annual DSN service fee would be \$2.2M.
- **The heliocentric Options 6V, 10V, 2IR and 4IR**, which orbit at 0.7 AU, would use the DSN 3-meter antenna for tracking and telemetry downlink. Optical communications would be used to download the large volume of image data. The annual service fees for optical communications ground stations was assumed to be equal to those for the DSN in order to recover the setup costs of this new approach to satellite communications .
- **Option 5IR** would rely on its host spacecraft to provide communication services which is often bundled into the cost of accommodation. A \$5M per year cost is included in this case to account for the science data processing which would not be provided by the commercial host. This value was derived from costs of the GOLD and NEOWISE missions.

Table 7-12 summarizes the cost of operations and ground tracking for the fifteen space-based options over ten years of operation. Fifteen percent cost reserves are included.

Table 7-11. Estimated Phase E costs (FY2017 \$M), for space-based observatory options (visible).

Visible Detector (FY17\$M)	Option	1V	2V	3V	4V	5V	6V	7V	8V	9V	10V
	Aperture (m)	2.0	2.0	1.0	1.0	1.0	1.0	0.5	0.5	0.5	0.5
	Orbit	LEO (S.S.)	GEO	LEO (S.S.)	GEO	L1/L2	0.7AU	LEO (S.S.)	GEO	L1/L2	0.7AU
	Actively Cooled?	N	N	N	N	N	N	N	N	N	N
	Optical Communications?	N	N	N	N	N	Y	N	N	N	Y
Phase E	Total, Phase E	\$ 941	\$ 941	\$ 257	\$ 257	\$ 282	\$ 1,089	\$ 135	\$ 135	\$ 160	\$ 705
12	15% Cost Reserves	\$ 123	\$ 123	\$ 33	\$ 33	\$ 37	\$ 142	\$ 18	\$ 18	\$ 21	\$ 92
7	Mission Operations (Phase E), no reserves	\$ 818	\$ 818	\$ 223	\$ 223	\$ 245	\$ 947	\$ 117	\$ 117	\$ 139	\$ 613
7.0.1	Mission Operations	\$ 818	\$ 818	\$ 223	\$ 223	\$ 223	\$ 925	\$ 117	\$ 117	\$ 117	\$ 591
7.0.2	Communications (DSN, NEN)	\$ 0.2	\$ 0.2	\$ 0.2	\$ 0.2	\$ 22	\$ 22	\$ 0.2	\$ 0.2	\$ 22	\$ 22

Table 7-12. Estimated Phase E costs (FY2017 \$M), for space-based observatory options (IR).

IR Detector (FY17\$M)	Option	1IR	2IR	3IR	4IR	5IR
	Aperture (m)	1.0	1.0	0.5	0.5	0.2
	Orbit	L1/L2	0.7AU	L1/L2	0.7AU	GEO
	Actively Cooled?	N	Y	N	Y	Y
	Optical Communications?	N	Y	N	Y	N
Phase E	Total, Phase E	\$ 282	\$ 1,089	\$ 160	\$ 705	\$ 58
12	15% Cost Reserves	\$ 37	\$ 142	\$ 21	\$ 92	\$ 8
7	Mission Operations (Phase E), no reserves	\$ 245	\$ 947	\$ 139	\$ 613	\$ 50
7.0.1	Mission Operations	\$ 223	\$ 925	\$ 117	\$ 591	\$ 50
7.0.2	Communications (DSN, NEN)	\$ 22	\$ 22	\$ 22	\$ 22	\$ -

7.2.4 Space-Based Observatory Cost Roll-up

Table 7-13. Estimated life-cycle space-based observatory option costs (FY2017 \$M), with unallocated cost reserves (visible).

Visible Detector (FY17\$M)	Option	1V	2V	3V	4V	5V	6V	7V	8V	9V	10V
	Aperture (m)	2.0	2.0	1.0	1.0	1.0	1.0	0.5	0.5	0.5	0.5
	Orbit	LEO (S.S.)	GEO	LEO (S.S.)	GEO	L1/L2	0.7AU	LEO (S.S.)	GEO	L1/L2	0.7AU
	Actively Cooled?	N	N	N	N	N	N	N	N	N	N
	Optical Communications?	N	N	N	N	N	Y	N	N	N	Y
	Lifecycle Cost, with Cost Reserves	\$ 2,084	\$ 2,115	\$ 935	\$ 951	\$ 1,137	\$ 2,187	\$ 606	\$ 611	\$ 751	\$ 1,539
	Unallocated Cost Reserves	\$ 352	\$ 359	\$ 156	\$ 159	\$ 200	\$ 353	\$ 92	\$ 93	\$ 123	\$ 242
	Phases A-D Baseline	\$ 914	\$ 938	\$ 556	\$ 569	\$ 692	\$ 888	\$ 396	\$ 401	\$ 489	\$ 684
	Phase E Baseline	\$ 818	\$ 818	\$ 223	\$ 223	\$ 245	\$ 947	\$ 117	\$ 117	\$ 139	\$ 613

Table 7-14. Estimated life-cycle space-based observatory option costs (FY2017 \$M), with unallocated cost reserves (IR).

IR Detector (FY17\$M)	<i>Option</i>	<i>1IR</i>	<i>2IR</i>	<i>3IR</i>	<i>4IR</i>	<i>5IR</i>
	Aperture (m)	1.0	1.0	0.5	0.5	0.2
	Orbit	L1/L2	0.7AU	L1/L2	0.7AU	GEO
	Actively Cooled?	N	Y	N	Y	Y
	Optical Communications?	N	Y	N	Y	N
	Lifecycle Cost, with Cost Reserves	\$ 1,226	\$ 2,327	\$ 766	\$ 1,605	\$ 236
	Unallocated Cost Reserves	\$ 220	\$ 385	\$ 127	\$ 257	\$ 48
	Phases A-D Baseline	\$ 760	\$ 996	\$ 500	\$ 735	\$ 138
	Phase E Baseline	\$ 245	\$ 947	\$ 139	\$ 613	\$ 50

7.3 Summary

The cost estimates presented in Section 7 of this report demonstrate that space-based observatories can vary widely in life-cycle costs but tend to be more expensive than their ground-based counterparts. They also carry with them more technical challenges and risks than comparable ground-based systems. Space-based systems do, however, offer significant advantages, particularly in the cataloging of NEOs. The question arises, “What is ‘comparable’ when comparing the cost of these two types of observatories?” To answer this, it is necessary to assess the cost of a given system (or combination of systems) as a function of the benefit that can be derived. This is the focus of Section 8.

This page is intentionally blank.

8 COST / BENEFIT CONCLUSIONS

8.1 Approach

This current study by the Near-Earth Object Science Definition Team (NEO SDT) examines the seven questions posed by NASA to the NEO SDT, as specified in the team’s charter (see Section 1.2). The key question is, “What are the smallest objects for which the search should be optimized?” The other questions in the charter help define the NEO search system options to be evaluated in this study.

Providing useful responses to those questions requires an understanding of the relationships between the costs of implementing NEO search efforts, particularly for small asteroids, and the benefits accrued by those efforts. The current study process for understanding those relationships is constructed along similar lines to the cost/benefit analysis described in the NEO SDT’s 2003 report, “Study to Determine the Feasibility of Extending the Search for Near-Earth Objects to Smaller Limiting Diameters” (Stokes et al. 2003).

In order to understand the cost/benefit potential of each NEO search technology examined in this study, a series of hypothetical, but technically realizable, search systems was defined, as described in Section 4. These systems include both ground-based visible observatories and several space-based systems that use infrared or visible detectors. The various systems were selected for their potential NEO detection and tracking capabilities, as well as for their technical feasibility. While the 2003 report only considered NEO search systems operating at visible wavelengths, progress over the decade since that report was written has made infrared detection systems practical, and so they are included in this study.

In this section, we define and quantify the benefits from cataloging potentially hazardous objects (PHOs) (Sections 8.1 and 8.3) and assign monetary values to life and property (Section 8.2). Next, we present the computed benefits from cataloging and warning (Sections 8.4 and 8.5, respectively), and finally, the cost/benefit ratio derived for each system (Section 8.6).

8.1.1 Definition of Benefit

For the purposes of this study, we define benefit as “reducing the uncertainties of hazards to life, injuries, and property/infrastructure damage resulting from PHO impacts on Earth over a 100-year time horizon.”

We begin with the current situation, in which

- Some PHOs have been discovered and cataloged, and found to not have any possibility of impacting the Earth for the next century; and
- The PHO population model predicts that some number of PHOs remain undiscovered, and some of those currently undiscovered PHOs may impact Earth sometime within the next century, potentially causing fatalities, injuries, and/or property/infrastructure damage.

The undiscovered PHOs represent uncertainty because, in principle, any of them might be a future Earth impactor. As NEO survey systems discover and catalog these PHOs, the PHOs are either

identified as Earth impactors or found not to be Earth impactors. As PHOs that will not impact Earth are cataloged, the uncertainty regarding the remaining potential PHO impact hazard is reduced. Therefore, NEO survey systems provide benefit by either (a) reducing the PHO impact hazard uncertainty through cataloging PHOs that will not impact Earth or (b) discovering and cataloging PHOs that are on a course to impact Earth and thereby providing warning necessary for mitigation activities (PHO mitigation processes are beyond the scope of this study, but current research and design efforts for PHO mitigation—ranging from civil defense and disaster response/management to in-space missions to deflect or disrupt a PHO—are well documented in the extant literature).

Thus, the benefit of an NEO survey system grows with time as survey systems become operational and catalog more and more PHOs. In so doing, the surveys remove more and more of the uncertainty regarding the PHO impact hazard. However, the benefit of an NEO survey system will asymptotically approach a limit over time as it discovers all of the PHOs that it is capable of seeing within its operational lifetime (each survey system naturally has a faint limit, i.e., it cannot see PHOs that do not become brighter in the sky than the faintest apparent magnitude to which the survey system is sensitive).

8.1.2 Improvements on the Previous Study

The cost/benefit analysis presented herein improves on that performed in the previous study (Stokes et al. 2003) via the following five process improvements:

1. Improved evaluation of the worldwide value of a statistical life (VSL).
2. Improved relationship between the value of statistical property/infrastructure damage and the predicted number of fatalities, based on actual historical data of natural disasters.
3. Calibration of the spectrum of injuries and damage to a common scale for which there is defined government guidance for its application.
4. Scaling of all injuries and damage by the amount of overpressure that would be experienced at a range of distances from the impact site for impacting PHOs of various sizes.
5. Unification of these principles by defining contour intervals of overpressure via physics-based models of impact effects that relate to the common injury and damage scales; and use of the statistical values of life and property damage to generate a quantitative monetary value for the benefits of each PHO that the modeled search system would discover and catalog.

The quantitative assessment of benefit for each NEO survey system examined in this study is performed by comparing each system's estimated cost to an estimate of the benefit that the system would provide in terms of reducing the uncertainty of future PHO impacts on Earth. The cost estimation process and resulting cost estimates for each NEO survey system are described in Section 7. In this section, we provide a detailed description of the benefit estimation process and present results for the estimated benefit offered by each NEO survey system.

8.2 Assigning Statistical Values

Estimating benefit as a monetary value requires converting fatalities, injuries, and property/infrastructure damage to dollar values. That conversion requires definitions for the value of a statistical life (VSL) and the value of a statistical injury (VSI). We believe that, in principle, each individual life is infinitely valuable. However, when we evaluate the public benefit of a potential lifesaving system, a statistical monetary value must be assigned to each life in the model for the purpose of making comparisons to the costs of the potential lifesaving systems. This approach is taken in a variety of areas, e.g., public transportation safety systems, and so VSL is the subject of a great deal of literature in economics.

8.2.1 Value of a Statistical Life

An extensive body of economics literature on VSL exists, especially for the United States. Because asteroid impacts may occur anywhere in the world, it is important to arrive at a worldwide average value for VSL when evaluating the benefits of any asteroid detection and cataloging system. The 2003 report of the NEO SDT used a value of VSL based on an Environmental Protection Agency value for U.S. VSL and the ratios of income per person in the United States and the world; this calculation yielded a value of \$1.6 million \pm \$1.1 million in 2003 dollars.

To arrive at an improved worldwide VSL, we have used data from Viscusi and Aldy (2003). They compiled data from many studies of VSL that covered a variety of nations and that included about 30 studies of the United States and more than 20 studies of other countries. They normalized all study values to a common year (2000). There is significant scatter in the VSL values derived in the different studies, in part because of the different concepts and methods the studies used to derive their VSLs. However, both the average and median values of these collections of studies show some consistent patterns across countries. The median VSL across several developed nations (United Kingdom, Austria, Canada, Japan, Australia) is close to the U.S. value (78% of the U.S. value). The median value for a number of developing countries (South Korea, India, Taiwan, Hong Kong) is 17% of the U.S. value. From these ratios of previous study values, an estimate of a worldwide VSL number can be generated. Because the combined population of developing countries greatly exceeds the combined population of developed nations, a worldwide VSL should be a little higher than the value for developing countries and much less than the value for developed countries. Rounding the ratio of developing to developed country VSLs yields a worldwide VSL set as 20% of the U.S. value.

A recent U.S. value of VSL from the Department of Transportation is \$9.4 million in FY2015 dollars. Inflating this figure to FY2017 dollars yields a value of \$10.4 million; thus, the worldwide VSL used in this report is \$2.08 million. This figure is somewhat smaller than the VSL used in the 2003 report, which inflated to FY2017 dollars would be \$2.28 million, corresponding to 22% of the U.S. value.

8.2.2 Property Damage

In the 2003 NEO SDT report (Stokes et al. 2003), property damage estimates were scaled to the number of fatalities, and a value was selected based on an observation by Canavan (1995), who defined the losses from impacts with global effects as a 20-year interruption in Earth's gross product resulting from damages and evacuation of large regions. The value of statistical property damage (VSPD) was taken as

$$\text{VSPD2003} = (20 \text{ years}) * (\text{GDP}/\text{Population})$$

With the global gross domestic product (GDP) in FY2014 of \$77.9 trillion and global population of about 7.4 billion people, this number would be about \$210,000 of property damage for each fatality.

A more accurate estimate of property damage can be determined by using the EM-DAT, the International Emergency Disasters Database. Developed by the World Health Organization and the Belgian government, EM-DAT is a worldwide database of the effects of natural disasters. It is maintained by the Centre for Research on the Epidemiology of Disasters (CRED) in Brussels. To get a realistic relationship between fatalities and property damage, we have used the worldwide data from the nearly 5000 natural disasters occurring over the decade from 2004 through 2013. This decade was chosen to be recent, but not so new as to miss some relevant data that might not yet have been incorporated into the database. This decade also includes data on the entry of the Chelyabinsk meteor into Earth's atmosphere in 2013, the first extraterrestrial disaster in the database. The EM-DAT data we used include all natural disaster types—classified as biological, climatological, extraterrestrial, geophysical, hydrological, meteorological—and those disasters that involve multiple causes and are thus classified as complex. In the 2004 to 2013 decade, nearly 5000 disasters affecting more than 2 billion people were reported. Dividing the greater than \$1.6 trillion in total reported worldwide property damage throughout the decade by the more than one million deaths from natural disasters yields a property damage relationship of \$1.51 million per fatality in real-year dollars over the 2004 to 2013 decade. This value can be adjusted to FY2017 dollars by applying the NASA New Start Inflation Index to the FY2009 midpoint year of the decade. This calculation yields an FY2017 estimate of property damage per fatality of VSPD = \$1.77 million.

A brief sensitivity analysis was performed to estimate the error range on this VSPD. Using other decadal intervals with starting years spaced five years apart and adjusting the calculations for these intervals for inflation showed residual fluctuation of about 20%.

8.2.3 Abbreviated Injury Scale

While there is an extensive body of literature on VSL, somewhat less has been written about the value of a statistical injury (VSI). Most blast effects are not fatal and represent portions of a spectrum of injuries and property damage. The VSI is also appropriate when one is considering the effects of small impacts, such as the recent Chelyabinsk event, or the effects on people located farther away from a large event. An economics concept covering these less extreme effects is the Abbreviated Injury Scale (AIS), a six-level scoring scale that was developed by the Association for the Advancement of Automotive Medicine and that characterizes effects as ranging from minor and moderate to serious, critical, and unsurvivable (fatal). U.S. government publications have given guidance on how to assign quantitative dollar values to AIS levels as fractions of a VSL (U.S. Department of Transportation 2015). The mapping of AIS values to VSI, as a fraction of VSL, is presented in Table 8-1. The values in Table 8-1 should apply to both U.S. and international values.

Table 8-1. AIS values mapped to VSI values as fractions of VSL.

AIS Level	Severity	Fraction of VSL
AIS 1	Minor	0.003
AIS 2	Moderate	0.047
AIS 3	Serious	0.105
AIS 4	Severe	0.266
AIS 5	Critical	0.593
AIS 6	Unsurvivable	1.000

These severity descriptions can also be used to describe the spectrum of property damage. In that case, the AIS levels would refer to fractional values of VSPD from minor damage through AIS 6, which would represent total destruction.

8.2.4 Overpressure Drives Injury and Property Damage

When a PHO impacts on Earth, it may break apart as it penetrates the atmosphere, and it may explode at some altitude above the Earth’s surface. Some or all of the PHO, broken apart or largely intact, may strike the Earth’s surface, forming a crater. In either case—explosion at altitude or energy release upon striking the surface—zones of substantial overpressure are created in the region surrounding the center of the event. The Asteroid Threat Assessment Program (ATAP) results presented in Section 3 use physics-based models to estimate overpressure contours around a PHO impact site. Personal injury levels, property damage, and fatalities from impact events are all driven by the local overpressure experienced. Several authors and government publications describe the effects of overpressure on people and property (Glasstone and Dolan 1977; Sartori 1983; NOAA Office of Response and Restoration 2017). From these descriptions of the effects of overpressure, four overpressure ranges have been selected that correspond to the top four levels of injury and damage in the AIS. These overpressure intervals and their effects are listed in Table 8-2.

Table 8-2. Overpressure intervals and their effects.

Overpressure (psi)	Injury Range (from—to)	Damage Range (from—to)	AIS Level	Fraction of VSL & VSPD
1 < psi ≤ 2	Flying glass—broken bones from buckled walls and roofs	Partial collapse of roofs and walls— destruction of most wood frame houses	Serious	0.105
2 < psi ≤ 4	Flying debris—near universal serious injuries and widespread fatalities	Doors and windows blown out of most houses— residential structures collapse	Severe	0.266
4 < psi ≤ 10	Universal serious injuries—most people die	Severe building damage— probable total collapse	Critical	0.593
psi >10	Almost all to all people die	All but the very strongest buildings collapse	Unsurvivable	1.000

8.3 Quantifying Benefit

The benefits of building and operating a particular NEO search and cataloging system are defined as the reduction in the hazard uncertainty in terms of deaths, injuries, and property compared to uncertainties regarding those hazards without the new search system. The reduction in hazard uncertainty is then expressed in monetary terms using the values of VSL, VSPD, and the guidance on scaling of these values based on the severity of injury in the AIS.

Let $f_i(t)$ be the fraction of PHOs of size i remaining in the hazard pool at time t , where the hazard pool is the collection of undiscovered PHOs in the population model. For purposes of this study, t_0 has been set to be the beginning of the year 2023. The year 2023 was chosen for t_0 assuming that any discovery system could be built in five years and would become operational in 2023. The final time, at our time horizon of 100 years after t_0 , is denoted as t_f .

Let T_i be the hazard from PHOs of size i , which is the number of statistically expected impacts R_i of size i , multiplied by V_i , which is the value associated with damage caused by an impact of size i . Thus,

$$T_i = R_i V_i$$

R_i is the expected fractional number of impacts by objects of size i from time t_0 until time t . So, $R_i(t)$ will be equal to the expected number of impacts in the time span $t - t_0$.

The values of V_i are equal to worldwide averages of fatalities and injuries computed from the 1, 2, 4, and 10 psi overpressure contours, plus property loss values assessed from the same overpressure contours.

The quantified hazard $H(t)$ is, therefore, given by

$$H(t) = \sum_i f_i(t) R_i(t) V_i(t)$$

When a new discovery and cataloging system comes online, it will find more objects and reduce the remaining undiscovered fraction $f_i(t)$. The benefit of adding a new system k is

$$B_k(t) = H_k(t) - H_{init}(t)$$

where $H_{init}(t)$ and $H_k(t)$ are the hazards before and after adding the new discovery system.

8.4 Benefit Results

Each system accrues annual benefits (AB) based on the total hazard uncertainty retired. The benefits come from discovery and tracking of objects capable of causing both global and sub-global effects, as well as from providing warning for imminent impactors (Section 8.5). Table 8-3 gives the total accrued benefits for cataloging global and sub-global impactors. All systems accumulate significant benefits in excess of their costs after only a few years in most cases, because even a single large impact can cause extreme damage. The status quo, which represents continuation of the currently operating ground-based systems with no new systems as well as the network-paired space and ground-based systems, are included for comparison. The total benefit values in Table 8-3 are compared to the total

system lifecycle costs described in Section 7 to produce benefit/cost ratios, which are tabulated in Table 8-5 in descending order of benefit/cost ratio (Section 8.6).

Table 8-3. Accumulated total benefit value, including global effects, for each modeled system.

System	Year 1 (2024) \$M	Year 2 (2025) \$M	Year 3 (2026) \$M	Year 4 (2027) \$M	Year 5 (2028) \$M
GBO 4 m + Vis Venus 1 m	512	1111	1769	2460	3169
Vis Venus 1 m	511	1106	1760	2449	3155
Vis LEO 2 m	476	1063	1696	2357	3032
Vis + IR L1 50 cm	469	1028	1644	2296	2968
Vis GEO 2 m	463	1043	1670	2325	2997
GBO 4 m + Vis Venus 50 cm	439	989	1605	2260	2941
Vis Venus 50 cm	431	969	1574	2220	2893
Vis L1 1 m	422	956	1547	2171	2818
Vis L2 1 m	417	948	1538	2160	2805
Vis LEO 1 m	417	951	1543	2168	2815
Vis GEO 1 m	416	948	1538	2162	2809
GBO 4 m + Vis GEO 1 m	416	948	1538	2162	2809
GBO 4 m + IR L1 50 cm	402	908	1482	2098	2739
GBO 4 m + IR Venus 50 cm	352	839	1397	2003	2639
GBO 4 m + Vis GEO 50 cm	344	800	1314	1866	2443
Vis GEO 50 cm	340	792	1303	1852	2427
Vis L1 50 cm	339	789	1298	1846	2422
Vis L2 50 cm	334	780	1288	1833	2406
Vis LEO 50 cm	334	780	1283	1824	2392
IR L1 50 cm	320	775	1314	1902	2522
IR L1 1 m	318	776	1315	1906	2528
GBO 4 m + IR GEO 20 cm	286	668	1113	1597	2109
IR Venus 50 cm	241	613	1059	1565	2110
GBO 8 m	204	521	900	1319	1772
GBO 4 m	188	483	837	1230	1655
IR Venus 1 m	175	448	773	1147	1549
GBO 2 m	162	417	729	1076	1455
IR GEO 20 cm	158	412	733	1099	1498
Status quo	25	75	143	228	332

Table 8-4 breaks out sub-global impactors only and gives the accrued benefit fractions as both percentages of the total sub-global PHO impact hazard and the associated accumulated benefit in dollars.

Table 8-4. Accumulated benefits for all modeled NEO survey systems as percentage of sub-global hazard uncertainty eliminated and millions of dollars per year.

System	Year 5 (2028) %	Year 5 (2028) \$M	Year 10 (2033) %	Year 10 (2033) \$M	Year 20 (2043) %	Year 20 (2043) \$M
IR L1 1 m	84%	255	90%	652	94%	1561
Vis + IR L1 50 cm	84%	259	90%	648	94%	1539
GBO 4 m + Vis Venus 1 m	83%	258	90%	645	94%	1533
Vis Venus 1 m	83%	252	89%	631	93%	1506
GBO 4 m + IR L1 50 cm	81%	233	88%	600	93%	1457
IR L1 50 cm	81%	220	87%	578	92%	1423
Vis LEO 2 m	80%	223	86%	564	91%	1372
Vis GEO 2 m	79%	216	85%	550	90%	1349
GBO 4 m + IR Venus 50 cm	79%	202	85%	532	90%	1325
GBO 4 m + Vis Venus 50 cm	78%	201	85%	531	91%	1332
Vis Venus 50 cm	77%	189	84%	503	89%	1274
Vis L1 1 m	77%	188	83%	497	89%	1262
GBO 4 m + Vis GEO 1 m	77%	186	83%	492	89%	1250
Vis GEO 1 m	77%	186	83%	492	89%	1250
Vis L2 1 m	76%	184	83%	488	89%	1242
IR Venus 50 cm	76%	178	83%	481	88%	1223
Vis LEO 1 m	76%	182	83%	482	89%	1229
IR Venus 1 m	74%	155	79%	416	84%	1052
Vis L1 50 cm	71%	131	78%	370	85%	1007
GBO 4 m + Vis GEO 50 cm	71%	131	78%	368	84%	1001
Vis GEO 50 cm	71%	130	77%	365	84%	995
Vis L2 50 cm	71%	128	77%	361	84%	986
GBO 4 m + IR GEO 20 cm	70%	125	77%	351	83%	954
Vis LEO 50 cm	70%	123	76%	347	83%	947
IR GEO 20 cm	68%	102	74%	300	81%	845
GBO 8 m	64%	68	68%	201	73%	581
GBO 4 m	63%	57	66%	170	71%	497
GBO 2 m	61%	42	64%	127	68%	380
Status quo	59%	23	61%	76	64%	251

Figure 8-1 shows each system’s accrued annual benefits for sub-global effects only relative to the overall hazard. The vertical axis is the percentage of the sub-global PHO impact hazard uncertainty that has been removed. Figure 8-2 shows the same data as Figure 8-1, but expressed in dollars per year of eliminated sub-global hazard uncertainty accrued over the years of operation of each modeled

search system. Both figures start with the assumed initial operation year of 2023 and show the benefits over 10 years of operation. The initial values in Figure 8-1 assume that current detection systems continue to operate until the new systems come online on January 1, 2023. Figure 8-2 displays benefit value earned starting from January 1, 2023.

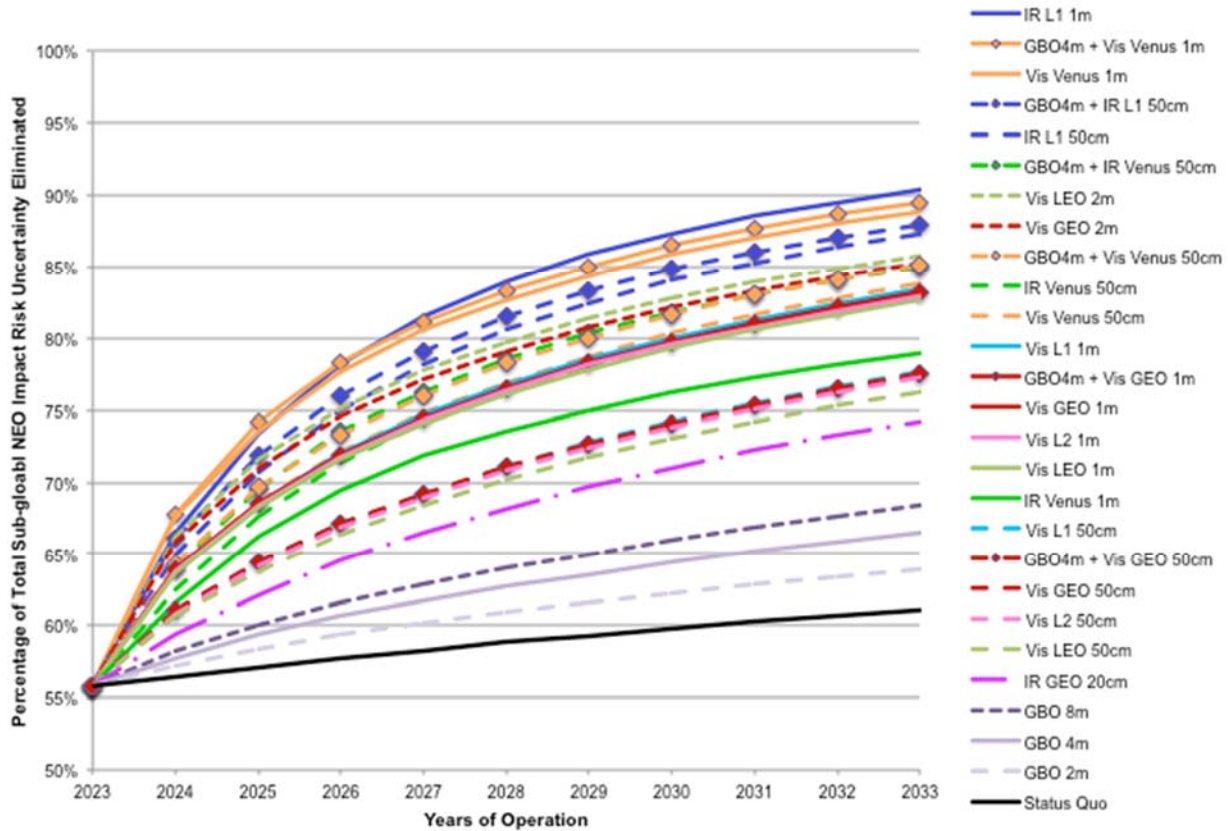


Figure 8-1. Accrued annual benefits of all modeled NEO search systems, expressed as a percentage of the total sub-global PHO impact risk uncertainty eliminated.

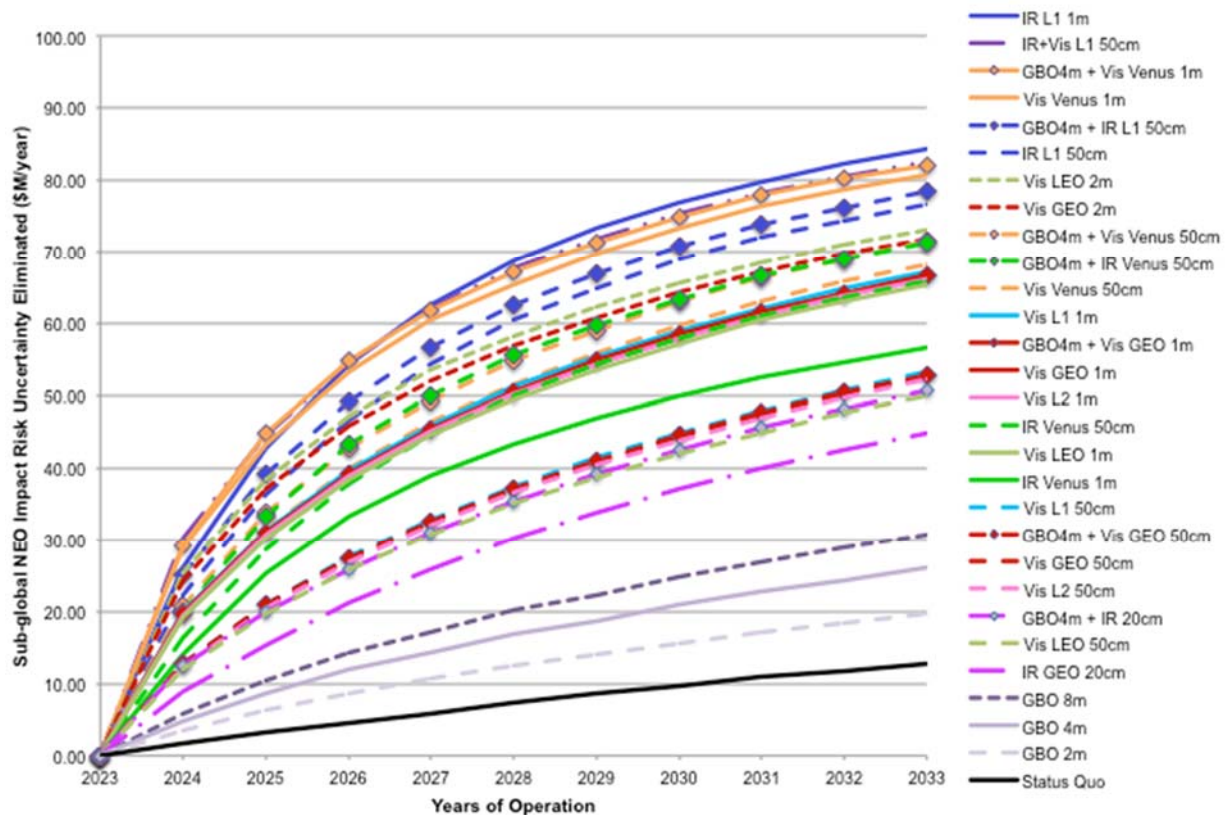


Figure 8-2. Accrued annual benefits of all modeled NEO search systems, expressed as sub-global PHO impact risk uncertainty elimination benefit value in millions of FY2017 U.S. dollars per year.

These benefit curves incorporate the potential life, injury, and property damage effects of PHO impacts causing sub-global effects only and are quite different from the straight fraction of cataloging completeness of the PHO population. The benefits from the elimination of sub-global hazard uncertainty by these systems are calculated by using the effects of overpressure during potential impacts, as well as the average population and property affected, to derive the reduction in potential deaths, injuries, and property damage. The dollar values are computed on the basis of the statistical values of life and property damage scaled by the abbreviated injury scale. Therefore, the percentage reduction in the overall hazard and the dollar values assigned to it are very nonlinear with respect to object size and reflect the much higher potential damage from larger objects.

A cursory view of the benefit curves shows that they all have a similar characteristic of a higher initial slope in the accrued benefit that rolls over after a few years to an asymptotic lower slope as they continue to accumulate additional benefits more slowly in later years. This behavior shows that when new systems come online, they discover objects within the first few years that are sufficiently bright to be detected in the volume of space defined by the systems' limit of detection. After that, the systems have to wait for the smaller and darker objects to drift into their observable region of space, at which time those smaller and darker objects become detectable.

The initial benefit accrual slopes of the space-based systems are significantly higher than those of the ground-based systems, in part because of their ability to operate more frequently (without concerns for daytime, clouds, bad weather, and other effects). Therefore, the space-based systems discover the readily detectable objects more quickly and reach a given benefit level much earlier than the ground-based telescopes. The space systems, therefore, also roll over to their asymptotic slopes years earlier than the ground-based systems.

The overall accrued benefit of the space-based systems after 10 years of operation is significantly higher than that of the ground-based systems for all except the smallest of the space-based systems. The outlier is the 20-centimeter infrared (IR) telescope in geosynchronous orbit.

The ABs of several of the systems are very close, and it is difficult to distinguish among them in Figures 8-1 and 8-2 as several of the plot traces overlay each other. However, the system with the highest accrued benefit is the IR 1-meter system at L1. It is closely followed by the IR 1-meter system in Venus-trailing orbit at ~ 0.7 AU and the IR 50-centimeter system at L1. Both figures also contain combined networks of a ground-based system and a space-based system working jointly. These networks generate some of the highest benefits of all over time because they enjoy the very high performance of the space-based system augmented by some additional capability from the ground.

Among the space-based systems, IR telescopes are significantly more effective than the visible systems of the same size at the same location. For example, a 50-centimeter IR system at L1 has about 5% higher AB after 10 years than a 1-meter visible system at L1 after 10 years of operation. Figure 8-3 shows all of the space-based systems on an expanded scale to help clarify the differences among them.

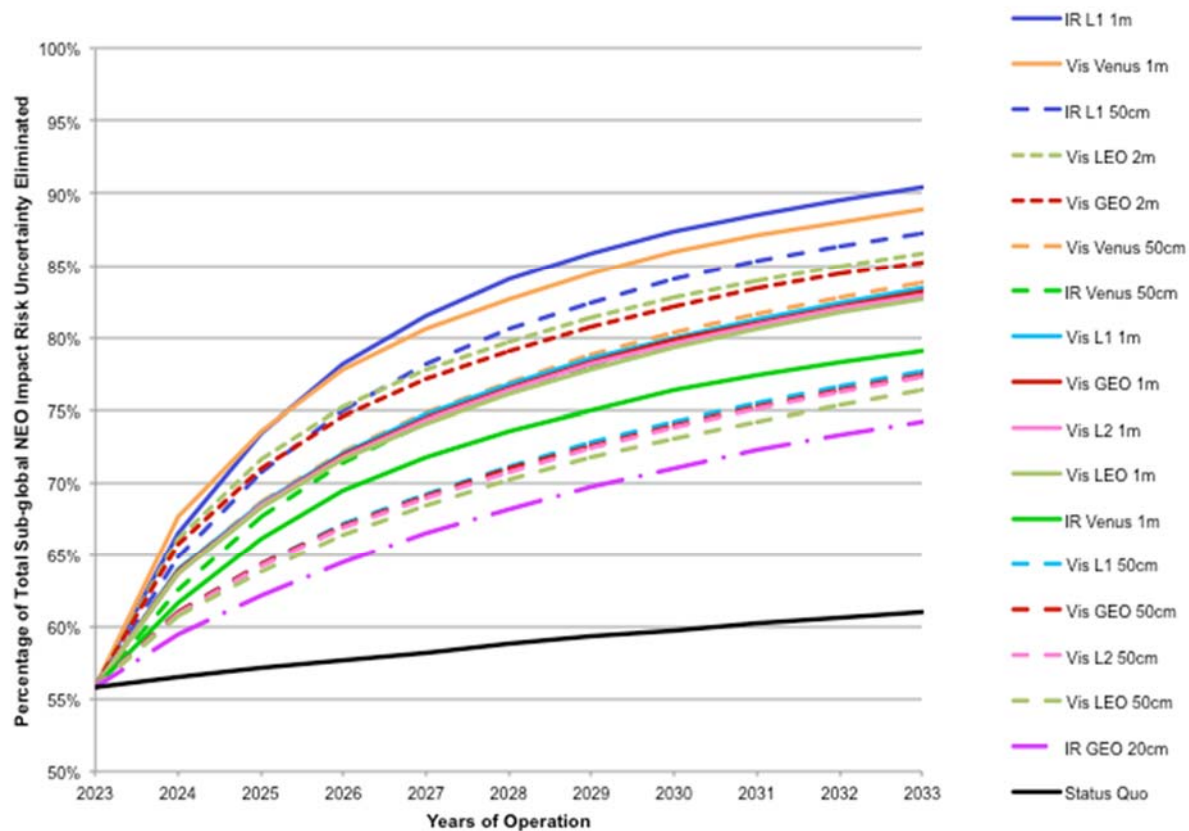


Figure 8-3. Accrued annual benefits of modeled space-based NEO search systems, expressed as a percentage of the total sub-global PHO impact risk uncertainty eliminated.

Figure 8-4 shows all of the ground-based systems. The accrued benefit for sub-global impactor discovery for the ground-based systems differs by about 10% after 20 years. The largest difference among the systems is in the first few years of operation. When a new system comes online, its enhanced capability discovers and catalogs most of the objects available at its detection limit within a few years. Then, the accrual of benefits by all systems approaches nearly the same asymptotic slope, as the systems have to wait for the smaller and darker objects to drift into their range. The highest AB of the ground-based systems is an 8-meter telescope. It achieves about a 5% greater AB than a 2-meter telescope after 10 years of operation. Given the relatively small differences in AB among some of the space-based systems and the corresponding clustering of AB among the ground-based systems, policy decisions to construct any one of these systems may be dominated by their relative costs.

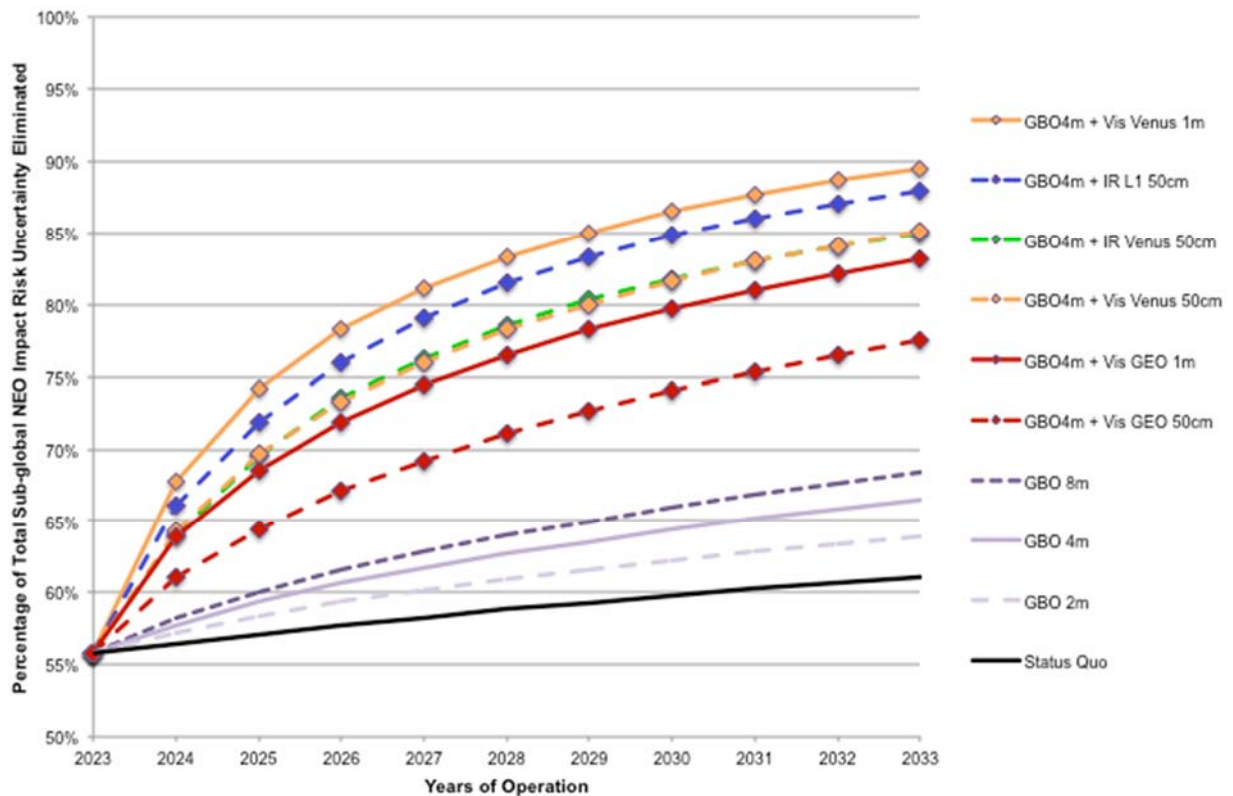


Figure 8-4. Accrued annual benefits of modeled ground-based NEO search systems, expressed as a percentage of the total sub-global PHO impact risk uncertainty eliminated.

Figure 8-5 shows the accrued benefits in terms of the percentage of sub-global PHO impact hazard uncertainty elimination value earned relative to the value available to be earned at the start of operations in January 2023. These plots, therefore, start with an ordinate of zero and show the fraction of the hazard uncertainty not yet eliminated at the initial time that would be removed by the modeled NEO survey systems during their operations.

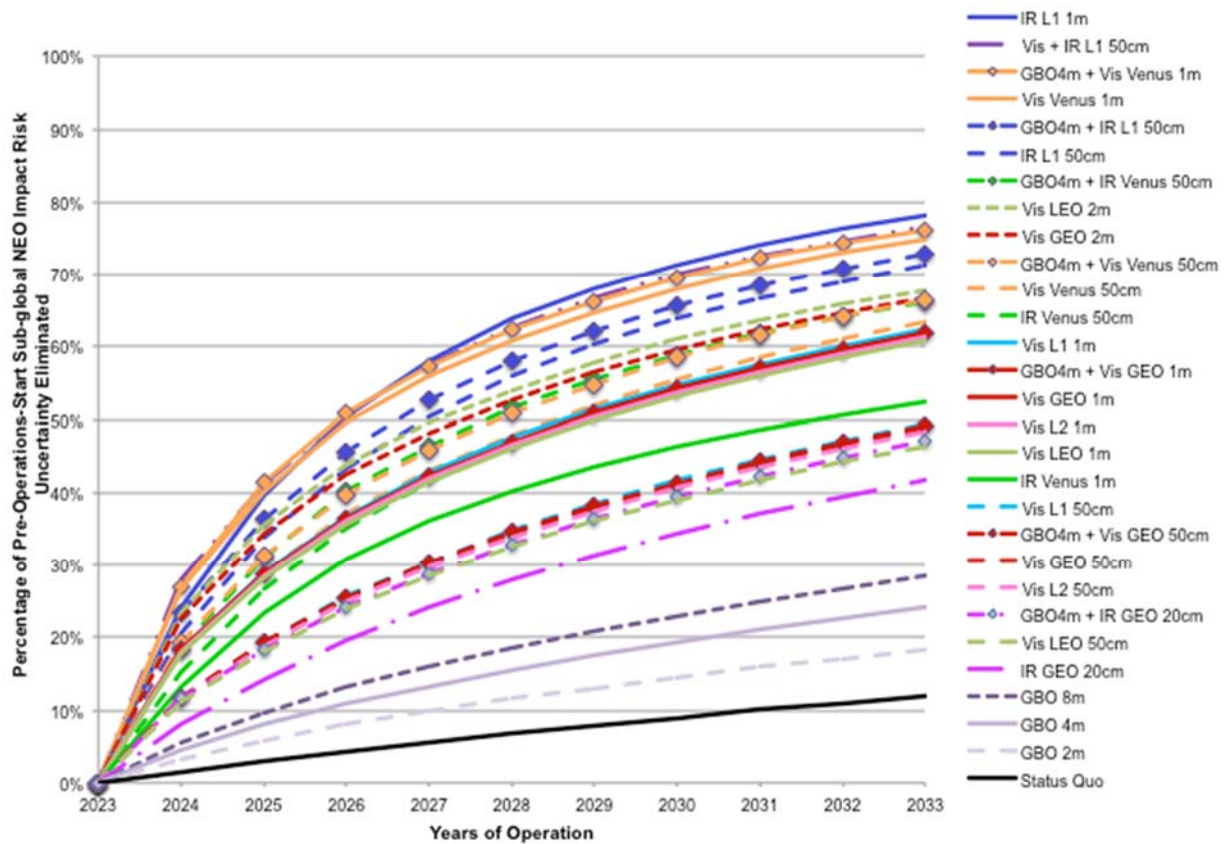


Figure 8-5. Accrued benefits in terms of the percentage of sub-global PHO impact hazard uncertainty elimination value earned relative to the value available to be earned at the start of operations in January 2023.

8.5 Warning

Search systems can also provide warning of impending impacts (in addition to their primary task of discovering and cataloging NEOs). The warning role refers to discoveries of relatively near-term impending impacts for which there is insufficient time to develop an in-space mitigation mission. A system's performance in detecting near-term Earth impactors is distinct from the performance presented in previous sections for discovering and cataloging potentially hazardous NEOs. If an impending impact is detected with sufficient advance notice, the people in the vicinity of the impact site could be evacuated. Therefore, all loss of life and injuries from the impact event could be eliminated, while the property damage would still be incurred. Thus, we compute the benefit value associated with warning performance in the same manner as described previously, except that only the benefit value associated with preventing loss of life and injury can be earned. Furthermore, only sub-global effects are included because evacuating the impact site of a global-effects class impactor is insufficient to prevent substantial loss of life around the world.

For a warning to be useful, it must provide sufficient time for the evacuation. The Mass Evacuation Incident Annex of the Federal Emergency Management Agency (FEMA) states that evacuation

planning may require 72 hours of planning time prior to the start of an evacuation, followed by the duration of the actual evacuation event. To ensure that there will be sufficient time for a warning to be useful, warning has been defined as effective if a potential impactor has been detected by a search system at least six days and up to a year before impact.

Figure 8-6 shows the warning efficiency of all the modeled search systems as a function of NEO diameter. Warning efficiency is computed as the percentage of simulated impactors for which the aforementioned warning detection criteria are satisfied. The combined visible and IR space-based survey system performs particularly well for warning, followed by space-based systems located near Earth or at L1.

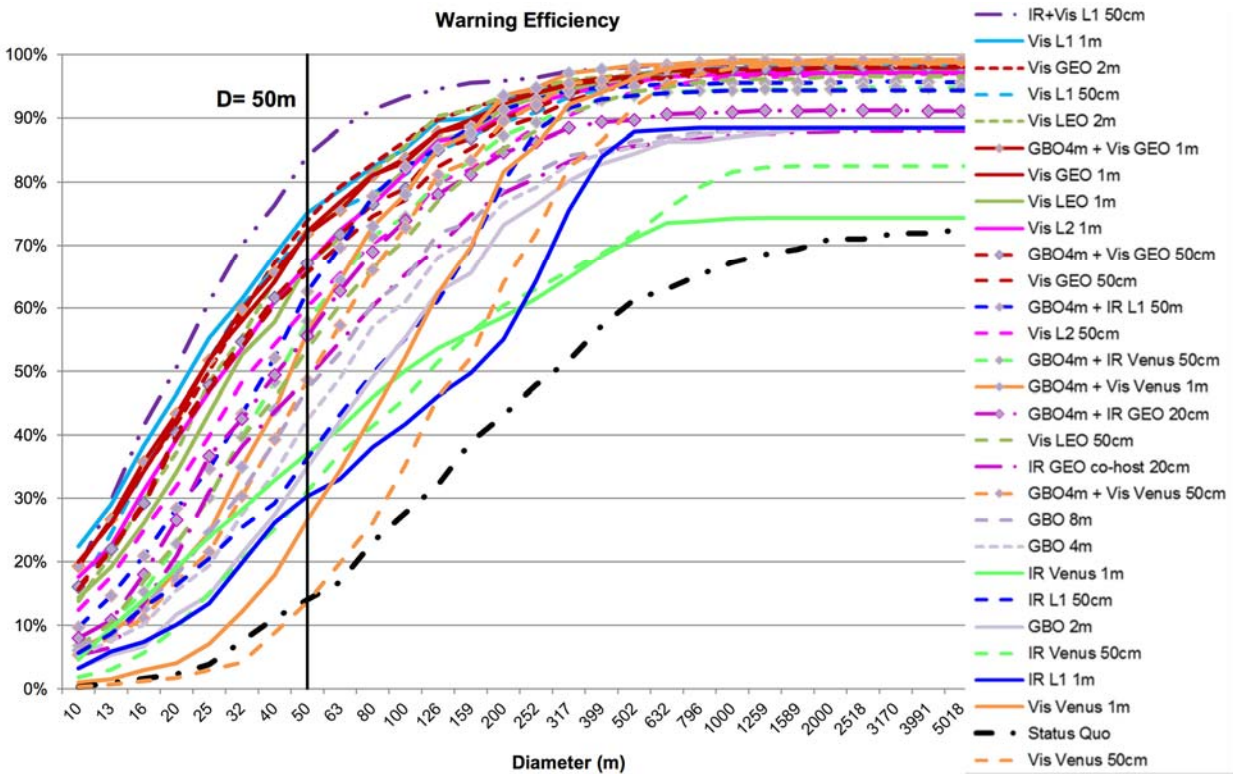


Figure 8-6. Warning efficiency of modeled systems as a function of PHO diameter.

Figure 8-7 presents the warning benefit value earned by the modeled systems in terms of millions of dollars per year. The evolution of the warning benefit value earned over time is computed by convolving the warning efficiency (per NEO diameter bin) with the system cataloging rates. This approach accounts for the fact that fewer potential impactors are present in the undiscovered population as more and more non-impacting NEOs are discovered and cataloged.

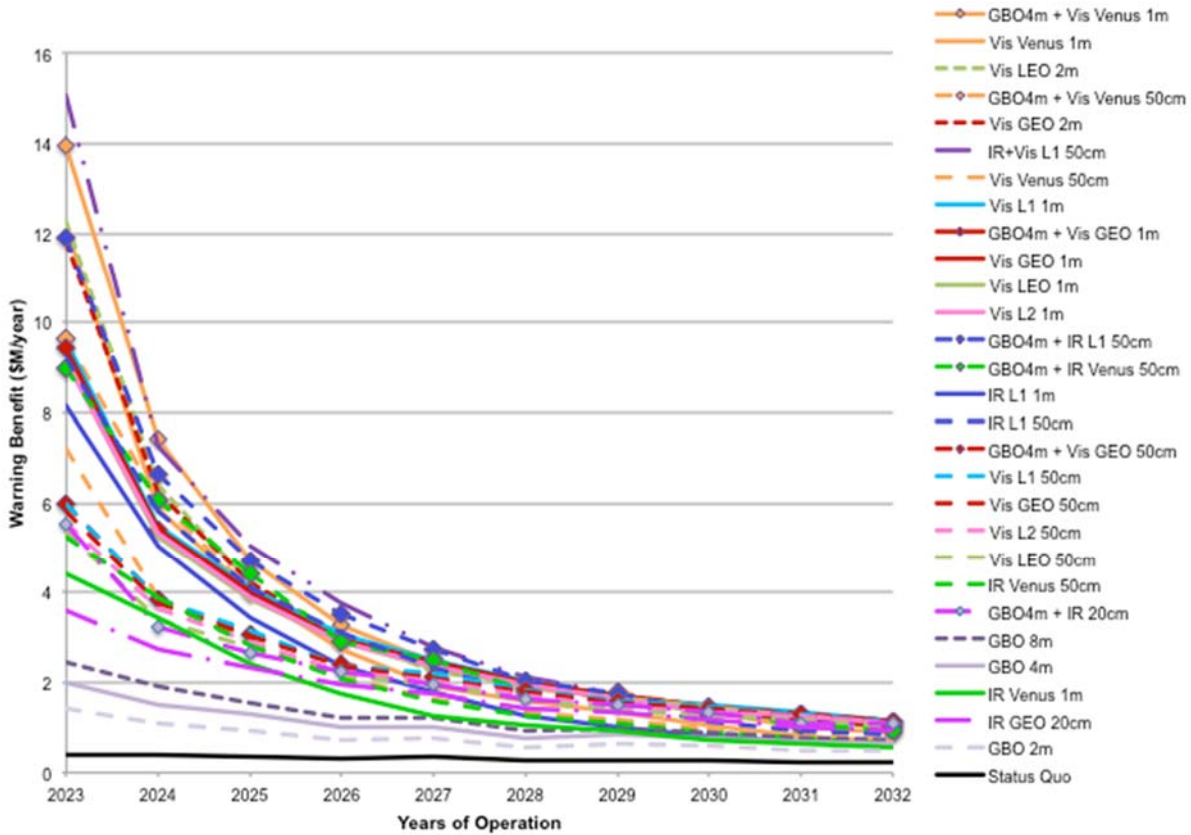


Figure 8-7. Warning benefit value earned by the modeled systems over time.

8.6 Cost/Benefit Comparison

The total risk from an unwarned PHO impact stems from both global and sub-global impactors. For purposes of comparing a system’s benefit to its cost, we compute its total benefit, including global and sub-global effects. Table 8-5 presents the cumulative benefit value, including global effects, earned by each modeled NEO survey system during the first five years of operation, in millions of FY2017 U.S. dollars.

Table 8-5. Benefit/cost ratios for the modeled NEO survey systems.

System	Year 1 (2024)	Year 2 (2025)	Year 3 (2026)	Year 4 (2027)	Year 5 (2028)
GBO 2 m	2.0	5.1	8.9	13.1	17.7
GBO 4 m	1.4	3.5	6.0	8.8	11.9
GBO 4 m + IR GEO 20 cm	0.8	1.8	3.0	4.3	5.6
GBO 8 m	0.7	1.9	3.3	4.8	6.4
IR GEO 20 cm	0.7	1.7	3.1	4.7	6.3
Vis GEO 50 cm	0.6	1.3	2.1	3.0	4.0
Vis LEO 50 cm	0.6	1.3	2.1	3.0	3.9
GBO 4 m + Vis GEO 50 cm	0.5	1.1	1.8	2.5	3.3
Vis L1 50 cm	0.5	1.1	1.7	2.5	3.2
Vis LEO 1 m	0.4	1.0	1.7	2.3	3.0
Vis L2 50 cm	0.4	1.0	1.7	2.4	3.2
GBO 4 m + IR L1 50 cm	0.4	1.0	1.6	2.3	3.0
Vis GEO 1 m	0.4	1.0	1.6	2.3	3.0
IR L1 50 cm	0.4	1.0	1.7	2.5	3.3
GBO 4 m + Vis GEO 1 m	0.4	0.9	1.4	2.0	2.6
Vis L1 1 m	0.4	0.8	1.4	1.9	2.5
Vis L2 1 m	0.4	0.8	1.4	1.9	2.5
Vis Venus 50 cm	0.3	0.6	1.0	1.4	1.9
GBO 4 m + Vis Venus 50 cm	0.3	0.6	1.0	1.3	1.8
IR L1 1 m	0.3	0.6	1.1	1.6	2.1
Vis Venus 1 m	0.2	0.5	0.8	1.1	1.4
Vis LEO 2 m	0.2	0.5	0.8	1.1	1.5
GBO 4 m + Vis Venus 1 m	0.2	0.5	0.8	1.1	1.4
Vis GEO 2 m	0.2	0.5	0.8	1.1	1.4
GBO 4 m + IR Venus 50 cm	0.2	0.5	0.8	1.1	1.5
IR Venus 50 cm	0.2	0.4	0.7	1.0	1.3
IR Venus 1 m	0.1	0.2	0.3	0.5	0.7

The benefit/cost ratio is highlighted in green for each system in the column corresponding to the break-even year (benefit/cost ratio ≥ 1). The ground-based systems have the highest benefit/cost ratios despite the fact that their overall cataloging and warning performances are much lower than the performances of the space-based systems. This is simply because the ground-based systems have much lower costs than the space-based systems. However, the majority of the space-based systems

break even during their second or third year of operations. By year 10, the systems have earned between \$3.4 billion and \$6.8 billion, with a mean of \$5.4 billion. By year 20, the minimum, maximum, and mean benefit values are \$8.4 billion, \$14.2 billion, and \$12.1 billion, respectively. Figure 8-8 provides a plot showing the total benefit earned by each modeled system over 10 years of operations, in millions of dollars.

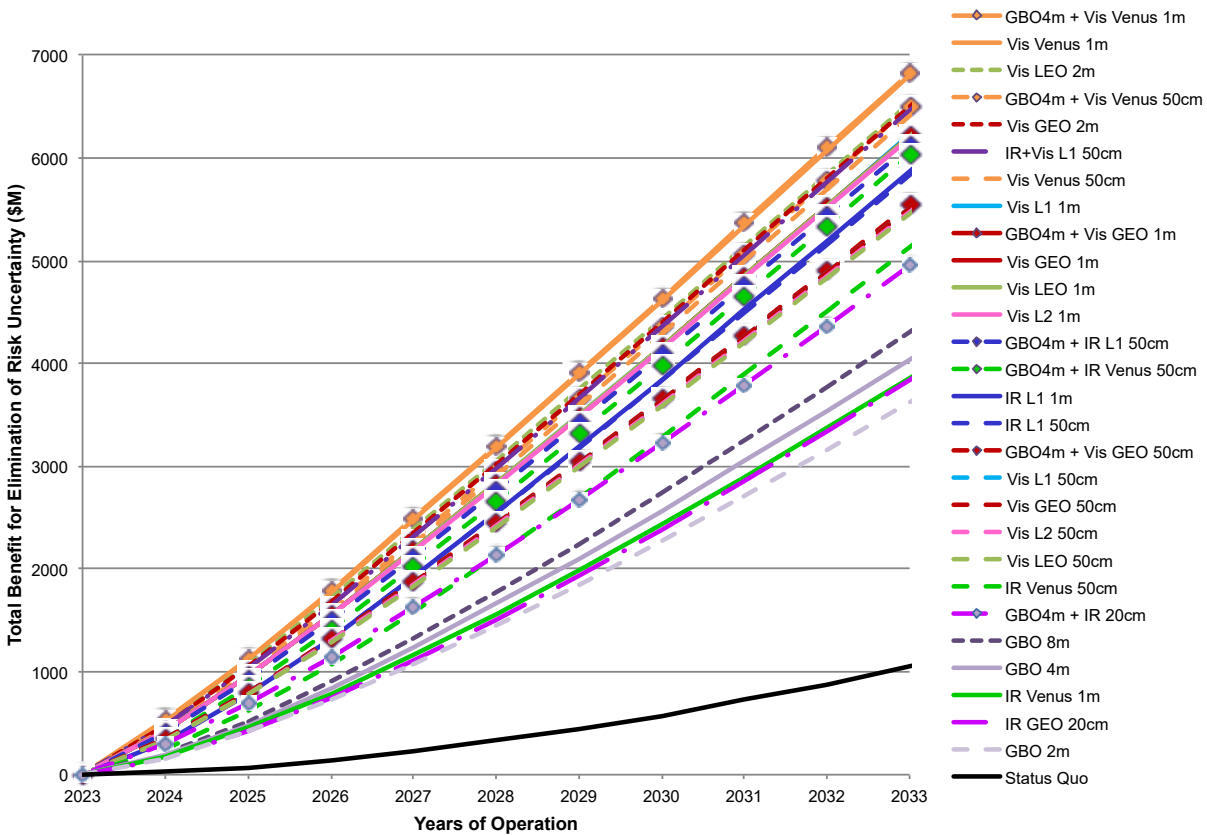


Figure 8-8. Total benefit value earned by each modeled system, in millions of dollars, over 10 years of operations.

9 SYSTEM COMPARISONS AND SUMMARY OF STUDY RESULTS

9.1 Establishing a Realistic Goal

In 2011, the current NEO survey systems achieved the Spaceguard goal of finding more than 90% of 1-kilometer and larger near-Earth asteroids (Mainzer et al. 2011e; Tricarico 2017), which are large enough to cause global effects (though we note that global effects can begin at sizes down to 500 meters for fast-moving metal-dominated objects, which make up ~10% of the population [Tholen 1984]). Current surveys use the number of discovered near-Earth asteroids as a success metric. However, since these objects have perihelion distances out to 1.3 AU, many of them do not pose a real threat to Earth until their orbits evolve over thousands of years into the region of the Earth's neighborhood at 1 AU. Hence, the Near-Earth Object (NEO) Science Definition Team (SDT) considered only potentially hazardous objects (PHOs), or asteroids and short-period comets that can currently approach the Earth's orbit to within 0.05 AU (i.e., 7.5 million kilometers, Ostro and Giorgini 2004).

Surveys have discovered ~25% of PHOs larger than 140 meters (Mainzer et al. 2011e, 2012; Grav et al. 2016; Granvik et al. 2016) and are expected to reach 43% by 2023. The NEO SDT concluded that a realistic goal for the next generation of search surveys is to construct a search system that is capable of retiring 90% of the risk uncertainty posed by impacts of asteroids capable of causing sub-global effects. At the same time, such a system would subsequently halve the remaining global risk uncertainty attributed to the PHOs that will remain undiscovered by the current search efforts (i.e., those PHOs larger than 1 kilometer). Figure 9-1 shows the cumulative expected casualties per year as a function of object size, with the global risk uncertainty on the right side of the figure and the sub-global risk uncertainty on the left. Moreover, the uncertainty of the number of PHOs left to be discovered must be of an acceptably low level to result in meaningful measurements of retired risk uncertainty.

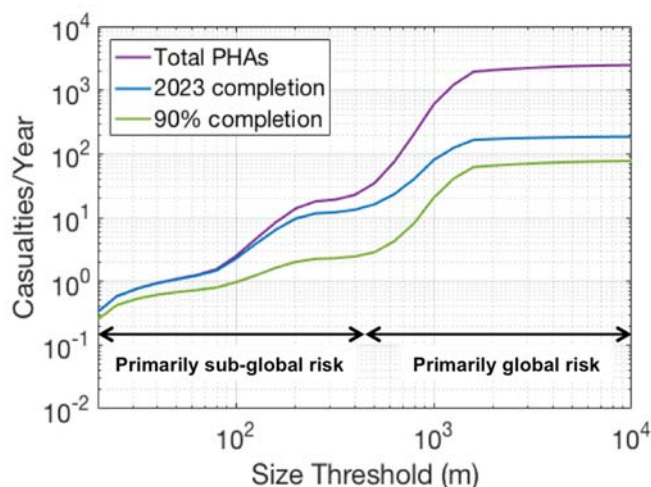


Figure 9-1. Cumulative expected casualties per year as a function of undiscovered object size. The three curves represent the total potentially hazardous asteroid (PHA) population, the projection of current survey progress to 2023, and the point where the sub-global risk uncertainty has been reduced by 90%.

Using realistic estimates of the NEO population and a risk analysis that considered both land and water impacts, the SDT determined that to retire 90% of the remaining risk caused by sub-global effect impacts requires that the next generation of searches find and catalog 90% of those PHOs larger than 140 meters in diameter (Figure 9-2). Such a search would eliminate 90% of the hazard uncertainty that is due to sub-global impact consequences. Such systems would also discover and catalog about 31% of the PHOs in the 50–60-meter size range, and would have a substantial probability of providing short-term warning from a previously undiscovered impactor of that size by detecting it somewhat before impact. Tunguska-sized PHOs (about 50 meters in diameter) are just at the limit where a rocky body would be expected to cause a significant air blast in the Earth’s atmosphere, whereas rocky PHOs about 140 meters and larger would be expected to punch completely through the Earth’s atmosphere, causing a cratering event on the Earth’s surface (Hills and Goda 1993).

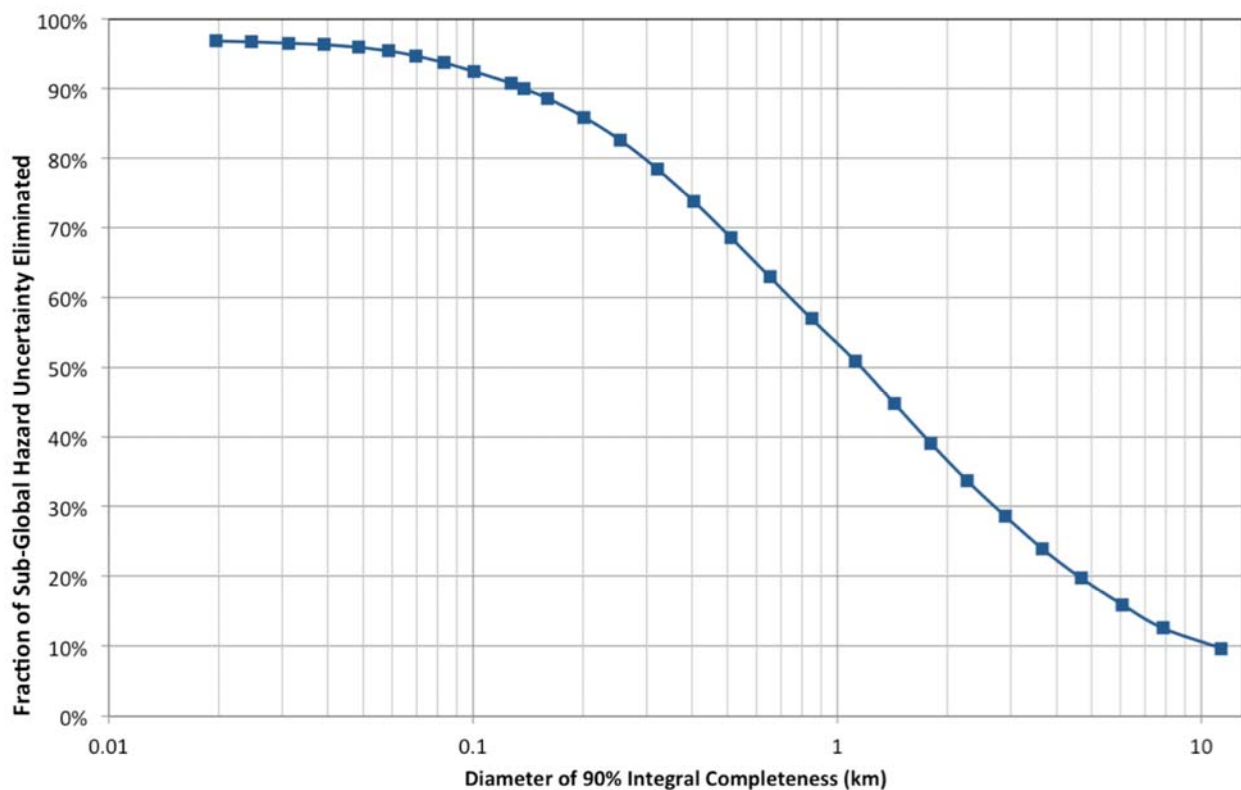


Figure 9-2. Fraction of impact hazard uncertainty eliminated as a function of size of PHO for which population is discovered to 90% completeness.

The above goal remains reasonable when one considers the uncertainty estimates for the sub-global hazard that were established by the SDT’s analysis.

9.2 Performance Overview for Systems Designed to Meet the Goal

9.2.1 Cataloging and Warning Efficiency

The systems considered in the analyses conducted by the SDT included search telescopes located at ground-based sites, space-based platforms, and combination networks of both ground-based and space-based systems. Both visible and thermal infrared (IR) space telescopes were considered. From the team's analyses, the SDT determined that, for a particular diameter limit, the search system that covers the sky with the greatest combination of sensitivity and area covered per day is the most efficient system for discovering and cataloging new PHOs. Not surprisingly, the rate at which a particular telescope can discover PHOs is highest in the first year and decreases in subsequent years (see Figure 6-9). Once a PHO is discovered and cataloged, its motion can be extrapolated into the future to assess the likelihood that it could make an Earth-threatening encounter. At that point, a PHO is not considered a threat (and requires no warning) because subsequent observations will either rule out an Earth impact or, if not, a mitigation campaign could presumably prevent the impact. Warning is the ability to at least detect an impactor during its final orbital period, and it was assumed that the benefits from warning (e.g., timely evacuation) are only relevant for those objects that are not yet cataloged.

As the survey progresses, it is necessary to determine the uncertainty in the cumulative survey completeness estimate for NEOs larger than 140 meters. The uncertainty in the survey completeness is driven by the uncertainty in the diameter measurement and the degree to which the survey efficiency can be characterized.

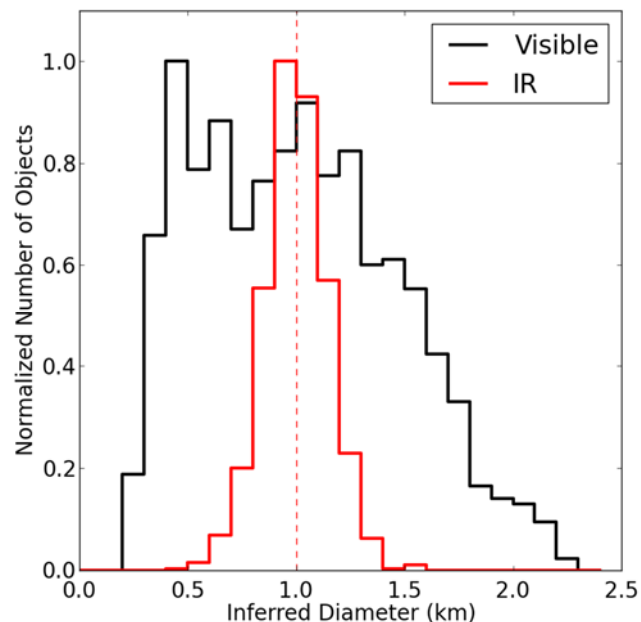


Figure 9-3. Simulation of 1000 NEOs, each 1 km in diameter (red dashed line), with albedos given by the distribution of Mainzer et al. (2011e) and Wright et al. (2016). The histograms show the diameters computed for these simulated objects using IR data with $\pm 15\%$ measurement error (red solid line), and the diameters computed using data from a visible telescope using H magnitudes with a ± 0.2 magnitude measurement error and an assumed albedo of 0.14 (black line).

To assess the effects of diameter uncertainty, the SDT performed a Monte Carlo simulation of 1000 objects, each with a diameter of 1 kilometer and the albedo distribution measured by the Wide-field Infrared Survey Explorer (WISE) (Mainzer et al. 2011e; Wright et al. 2016), shown in Figure 9-3. To estimate the uncertainty in the cumulative survey completeness measured by a visible survey, an absolute magnitude (H) for each object was first computed. Since visible light surveys do not measure albedo, it must be assumed. Usually this assumption is a mean value of 0.14. Taking the observed H magnitude and computing the diameter spreads the objects into many bins on either side of 1 kilometer (the black line in Figure 9-3). This computation affects the uncertainty in the survey completeness estimate because it affects whether or not a given NEO is determined to be above or below the targeted size, be it 1 kilometer or 140 meters. Diameters measured for the same objects by an IR telescope with an assumed Gaussian error of $\pm 15\%$ are given by the red line in Figure 9-3. Thus, completeness estimates made from visible light observations alone have greater associated uncertainty than those made using IR measurements.

9.2.2 Ground-Based Visible Light Systems

For ground-based systems, telescopes with apertures of 4 and 8 meters using a $9k \times 9k$ E2V tiled mosaic of charge-coupled-device (CCD) detectors had roughly comparable performance, and the 4-meter telescope did nearly as well (see Figure 6-10). While simulations were run based on a Maunakea site, the benefits associated with a Southern Hemisphere site accrued faster, so all ground-based observatories were subsequently assumed to be at the Large Synoptic Survey Telescope site in Chile. The rapid accrual is because the systems through 2023 are all still Northern Hemisphere systems, and there is a statistical group of high-eccentricity objects that spend little or no time north of the ecliptic and exterior to the Earth; these objects are more readily detected with a Southern Hemisphere system. All ground-based systems are assumed to require the same observational cadence as the space-based systems in order to successfully link tracklets of the same object to one another.

9.2.3 Space-Based Systems and Combined Ground- and Space-Based Systems

Telescopes in space have several advantages over their ground-based counterparts. Telescopes orbiting at the Sun-Earth L1 or L2 Lagrange points or in Venus-like orbits near 0.7 AU can cover more sky than can their ground-based counterparts. They can observe for a much larger fraction of the day, and there are no losses resulting from weather or seeing. Telescopes operating at thermal IR wavelengths detect NEOs at wavelengths where the objects emit more photons, and they measure object diameters with greater accuracy than visible-light telescopes can, leading to more accurate assessments of survey completeness and improved physical characterization knowledge as the objects are discovered. Much higher data transmission rates to Earth are achievable for telescopes operating in Earth orbit or at L1 or L2 than for those in Venus-like orbits, allowing full-frame images to be downlinked. With full-frame images, legacy science data processing algorithms can be used to extract moving objects at low signal-to-noise (SNR) levels with high reliability. Preservation of whole images also allows for future “precovery” detections to be extracted for objects discovered after the images were initially processed.

Infrared systems, which are very efficient in terms of cataloging PHOs, are more effective than visible space telescopes of equivalent size (Figure 6-14a). Search telescopes of equal aperture sizes located at L1 or L2 each had a better warning efficiency than comparable systems in Venus-like orbits

because of their closer proximity to Earth (Figures 6-11b and 6-12b). Telescopes at either L1 or L2 have similar cataloging efficiency. The overall cataloging efficiency, and particularly the warning efficiency, could be improved by a network of space and ground-based systems (see Figures 6-15 and 6-16). A combination of the very capable cataloging system—i.e., the infrared L1 system—with the very capable warning system—i.e., the visible light L1 system—results in a high-performance system across the board (see Figure 6-17) with strong cost/benefit returns (Figures 8-5 and 8-8).

9.2.4 Cost/Benefit Ratios

Table 8-5 in Section 8.6 summarizes the total cost/benefit ratios for each of the systems; for all the search systems under consideration, the benefits derived match or exceed their costs within a year or two. Efficiency and cost vary between the systems, but all of them have extremely high returns on investment. It should be noted, however, that, as shown in Figure 9-5 below, some systems can reach the stated goal within 25 years, while others do not.

The first systems to break even are the 2-meter and 4-meter ground-based systems, which break even after the first year, followed by the IR GEO 20-centimeter co-hosted system, which breaks even after two years of operation. These findings are not unexpected because, while these systems offer modest NEO search performance compared to some of the other systems, they are the least costly. However, Figures 8-1 and 9-5 show that the IR GEO 20-centimeter system and all of the ground-based systems considered (2-meter, 4-meter, or 8-meter) still leave ~30–40% risk uncertainty remaining after 10 years. None of these systems achieve risk uncertainty elimination of 90% in under 25 years. By comparison, a number of other systems break even in only two to four years and achieve 90% risk uncertainty elimination in less than 25 years. Figure 9-5 below shows these systems, with the years to 90% risk reduction on the bottom axis, and the cost to achieve that reduction on the vertical axis.

9.3 Space-Based IR Systems versus Ground-Based Visible System Performance

A number of ground-based visible, space-based IR, and networked systems are capable of meeting the goal of retiring 90% of the risk from sub-kilometer-sized PHOs. Space-based IR systems and mixed IR/visible systems will generally accomplish the goal more quickly than will single or multiple ground-based visible systems (Figure 6-15a). None of the ground-based systems studied in the report were able to reach 90% survey completeness for PHOs >140 meters in under 25 years, effectively deferring the objective to another generation. The increased efficiency, and hence shorter completion time, associated with IR systems would come at a higher cost. In general, the mixed space-based IR and ground-based visible systems do not have as attractive a cost/benefit ratio as either the space-based IR system or ground-based visible system alone. In a mixed system with a ground-based visible system, the more capable space-based IR system will dominate the cataloging results, and the addition of the ground-based visible system brings mainly only warning capability for the extra cost. In a mixed system with a space-based visible system, the more capable space-based IR system will still dominate the cataloging results, but the addition of the space-based visible system brings strong warning and notable additional cataloging capability, albeit at notable cost. If a decision is made to meet the 90% goal with an advanced PHO search within 10 years, and if one accepts the experience-based assumptions that went into the simulations, then the preferred option is to use space-based IR systems, possibly in conjunction with a visible system. The mixed system adds cost but has the advantage of providing improved warning, somewhat higher levels of survey completeness, improved orbital knowledge, and ancillary data, such as albedo, for a large number of targets.

9.4 Time and Expense Required to Complete the Survey Goal

Depending upon the time or expense constraints assumed, a number of options are available for meeting the stated goal to retire 90% of the sub-global hazard uncertainty. For a 10-year survey period constraint, Figure 9-4 plots the cost of the systems versus the fraction of the sub global risk uncertainty remaining at the end of a 10-year operations period. Figure 9-5 plots the costs for various systems versus the number of survey years required to meet the 90% goal. In both plots, the most attractive systems (i.e., lowest cost, highest efficiency) would be nearest the lower-left plot origin. Each plotted point is labeled with the system characteristics. There are large uncertainties inherent with the data for both the horizontal and vertical placement of these points, so systems that appear close to one another on these plots should be considered comparable.

It is evident from these two plots that if one insists upon meeting the stated goal within 10 years, then either the 1-meter aperture IR system in L1 orbit or a mixed 0.5-meter IR and visible L1 system will provide the cataloging efficiency to accomplish this goal with the lower estimated costs. However, a 0.5-meter aperture IR system in L1 orbit, with or without a 4-meter ground-based system, also accomplishes the 90% goal more cost-effectively in slightly more than 10 years. Figures 9-4 and 9-5 show that there are some less costly space-based and ground-based options available if several decades are allowed to meet the goal.

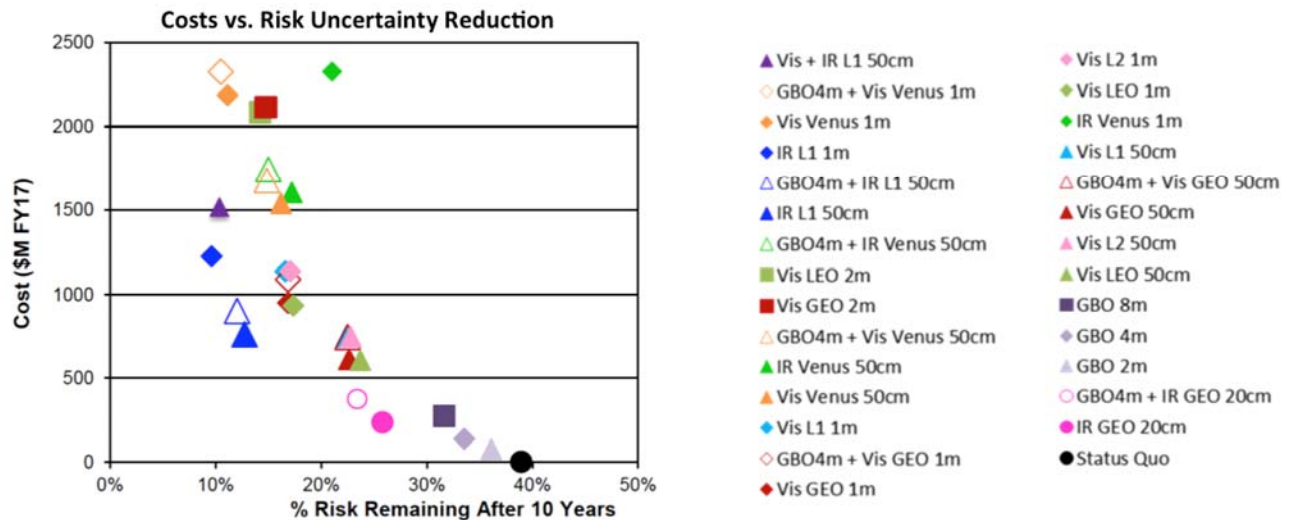


Figure 9-4. For various ground-based, space-based, and combined search systems, the system cost is plotted versus the percentage of the sub-global risk uncertainty remaining after a 10-year survey.

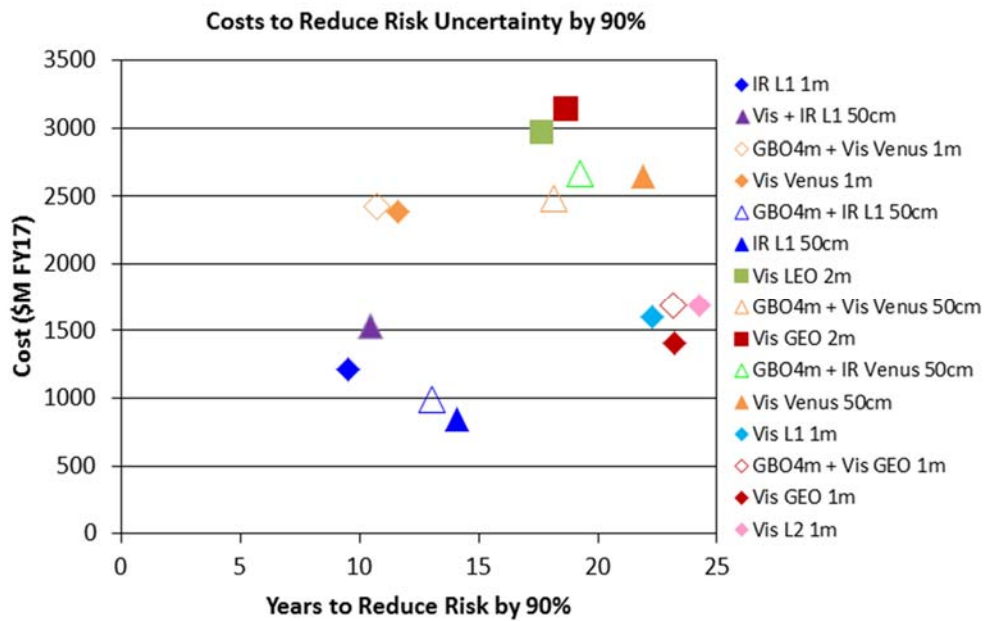


Figure 9-5. The cost of various space-based and ground-based search systems is plotted against the number of search years required to reduce by 90% the sub-global risk uncertainty from impacts by sub-kilometer sized objects. Only systems that can reach 90% in under 25 years are plotted.

This page is intentionally blank.

10 RESPONSES TO THE CHARTER QUESTIONS

The charter for the Near-Earth Object Study Definition Team (SDT) stated seven specific questions to be answered by the effort. The questions and answers are as follows:

1. *What are the smallest objects for which the search should be optimized?* The SDT finds that the search system could be constructed to produce a catalog that is 90% complete for potentially hazardous objects (PHOs) larger than 140 meters, which corresponds to characterizing 90% of the impact risk from sub-global effects.

2. *Should comets be included in any way in the survey?* The SDT's analysis indicates that the frequency with which long-period comets (of any size) closely approach the Earth is roughly one-hundredth the frequency with which asteroids closely approach the Earth and that the fraction of the total risk represented by comets is approximately 1%. The relatively small risk fraction, combined with the difficulty of generating a catalog of comets, leads the SDT to the conclusion that, at least for the next generation of NEO surveys, the limited resources available for NEO searches would be better spent on finding and cataloging Earth-threatening near-Earth asteroids and short-period comets. An effective NEO search system would naturally provide an advance warning of at least months for most threatening long-period comets.

3. *What is technically possible?* Current technology offers asteroid detection and cataloging capabilities an order of magnitude better than the capabilities available in the operating systems now used for detection and cataloging. NEO search performance is generally not now limited by technology, but rather by resources. This report outlines a variety of search system examples, all of which are possible using current technology. Some of these systems, when operated over a period of 9 to 25 years, would generate a catalog that is 90% complete for NEOs larger than 140 meters (see Figure 9-5).

4. *How would the expanded search be done?* From a cost/benefit point of view, there are a number of attractive options for executing an expanded search that would vastly reduce the risk posed by unwarned PHO impacts. The SDT identified a series of specific space-based and mixed ground- and space-based systems that could accomplish the next-generation search.

5. *What would it cost?* For a search period from 9 to 25 years, the SDT identified several systems that would characterize, at varying rates, 90% of the sub-global risk for NEO impacts, with costs ranging between \$750 million and \$2 billion in FY2017 dollars. All of these systems have risk-characterization benefits that well exceed the costs of system acquisition and operation.

6. *How long would the search take?* A period of 9 to 25 years is sufficient to generate a catalog 90% complete to 140-meter diameter. The specific period depends on the choice of search technology and the investment allocated.

7. *Is there a transition size above which one catalogs all the objects and below which the design is simply to provide warning?* The SDT concluded that, given sufficient time and resources, a search

system could be constructed to completely catalog hazardous objects with sizes down to the limit at which air blasts would be expected for non-metallic objects (about 50 meters in diameter). Below this limit, there is relatively little direct damage caused by the object (excepting the ~5% metal-rich objects that can penetrate the atmosphere at smaller sizes). Over the 9- to 25-year interval (starting in 2023) during which the next-generation search would be undertaken, the SDT finds that cataloging is the preferred and affordable approach down to approximately the 140-meter-diameter level and that these search systems would inherently provide an impact warning for 60–90% of objects as small as 50 meters.

10.1 SDT Specific Findings

The SDT has developed three specific findings for NASA as a result of the analysis effort:

Finding 1. Future goals related to searching for potential Earth-impacting objects are best stated explicitly in terms of the statistical risk characterized and should be firmly based on cost/benefit analyses. This finding recognizes that searching for potential Earth-impacting objects is of interest primarily to eliminate the statistical risk associated with the hazard of impacts. The “average” rate of destruction from impacts is large enough to be of great concern; however, although a significant impact could occur at any time, the estimated average event rate is quite low. Thus, a search to determine if there are PHOs likely to impact the Earth within the next few hundred years is prudent. Such a search would best be executed in a way that eliminates the maximum amount of statistical risk uncertainty per dollar of investment.

Finding 2. It would be most productive to develop and operate a NEO search program with the goal of discovering and cataloging the potentially hazardous population sufficiently well to eliminate 90% of the uncharacterized risk from sub-kilometer objects (i.e., sub-global impact effects). The above goal is sufficient to reduce the average casualty rate uncertainty from about 180 casualties per year to fewer than 80 per year. Any such search would find the majority of the larger objects remaining undiscovered, thus greatly decreasing the global risk from these larger objects. Over a period of 9 to 25 years, a number of system approaches are capable of meeting this search metric with quite good cost/benefit ratios.

Finding 3. The satisfaction of the 140-meter cataloging objective will require space-based search system(s). Infrared (IR) and visible sensors in the 0.5- to 1.0-meter aperture range are credible and cost/benefit-favorable options that use available technology. The best cost/benefit and lowest-risk systems, of those assessed, are located at L1. The fastest completion of the objective, using the assessed systems, is provided by a large-aperture IR system or a combined visible and IR system located at L1. Search systems located near the Earth (at L1/geosynchronous orbit/low Earth orbit) have the additional advantage of providing a substantial warning benefit while the catalog is being completed.

Appendix 1: 2016 Study Charter

Study Charter

NEO Observations Science Definition Team Update to Determine the Feasibility of Enhancing the Search and Characterization of NEOs

Introduction

The Planetary Defense Coordination Office (PDCO) within the Science Mission Directorate of the National Aeronautics and Space Administration (NASA) is currently working to discover all the Near Earth Objects (NEOs) that pose a significant impact hazard to the Earth and to obtain good orbital information for them. For the original study in 2003, the metric for this program was to discover 90% of the NEOs with sizes larger than 1 km and to obtain good orbital information for them by December 31, 2008. That goal was reached in 2010. In the NASA Authorization Act of 2005, based on the 2003 study findings Congress directed extending the search down to 90% of NEOs 140 meters and larger, to be accomplished by 2020. There continues to be increasing interest by the public and by the Congress, highlighted by the Chelyabinsk Event in February 2013, as to the wisdom of extending the current effort to objects even smaller than 140 meters. This update to the study is being undertaken to determine:

1. What are the smallest objects for which the search should be optimized?
2. Should comets be included in any way in the survey?
3. What is technically possible?
4. How would the expanded search be done?
5. What would it cost?
6. How long would the search take?
7. Is there a transition size above which one catalogs and tracks all the objects, and below which the design is simply to provide sufficient warning?

It should be emphasized that NASA's current goal for NEO detection has not officially changed. However, we believe that this study represents a prudent step in preparing for the future of NEO detection and tracking. Finally, we must stress that NASA is a space agency. Analysis of the capabilities and appropriateness of space-based solutions are to be included.

Need for the Study

It might, at first, be thought that a simple extrapolation of the performance of present archetype ground based facilities would be all that is required. However, both the difficulty of detecting an object and the number to be detected increase dramatically with decreasing size. Current ground-based search efforts with 1 to 2 meter class telescopes do well to survey an appreciable portion of the night sky in one lunation to 21.5 magnitude. A simple extrapolation of the current ground-based effort to 100 meter or smaller sized objects would require searching the night sky each lunation to 25.5 magnitude. At some point as one goes for detection of objects down to smaller sizes (100 meters or less), it will become impossible to perform such a search from the ground.

In addition, present models of the increase in the number of objects with decreasing object size suggest that there may be more than 100,000 objects with sizes greater or equal to 100 meters. Thus, astrometric follow-up needed to obtain predictive orbits of small objects may prove prohibitive. Therefore it may be that a dual approach—cataloging larger NEOs and obtaining good orbits for them while also establishing an early warning system for recently discovered small objects to allow for a timely response on the ground—will be required.

Current ground-based searches have used the visible portion of the spectrum, not only because of the need to work through the atmosphere of the Earth, but also because large-format infrared detector arrays lagged the developments in the visible. If space-based detection systems are considered, the IR region of the spectrum may be superior if the technology has sufficiently matured. The issue must be examined.

Approach

The PDCO will select a Science and Definition Team (SDT) composed of 10 to 12 Scientists and Engineers including those currently leading NEO search teams, those who model the NEO population, and those with technical expertise in the design and operation of ground-based and space-based survey telescopes, including the areas of visible and IR large detector arrays, to address the questions above and to provide a non-advocate technical report to the PDCO. Under an existing task plan with PDCO, APL will provide logistical and technical support. The duration of the study is expected to be 9 months. The NEO Observations Program Scientist will be an *ex officio* member of the SDT.

The team will be encouraged to document any joint uses of these facilities or the data that would be useful for other scientific studies.

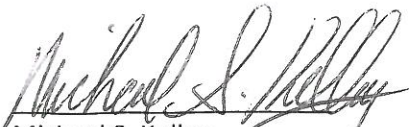
Liaison with Other Executive Branch Departments

The Department of Defense (DoD) and other US Government agencies may have expertise relevant to the subject. An example of this would be the Defense Advanced Research Projects Agency developed Space Surveillance Telescope. In addition, other elements of the Government may have some ancillary interest in the results of such a search effort (which might detect other classes of moving objects not germane to NASA's focused objectives). Because of these factors, a US Government interagency working group being established by the Office of Science and Technology Policy to review and establish policies germane to Planetary Defense will be informed of progress and findings from the study, and may assign an individual or two to participate in some manner.

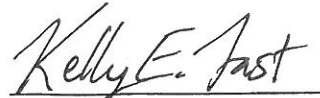
Expected Product

The agency looks forward to an annotated briefing and technical report that include findings that may answer the questions above for a presentation to the Science Mission Directorate Associate Administrator and other interested parties as required.

Concurrence:


Michael S. Kelley
Near Earth Object Observations Program Scientist

5/19/2016
Date


Kelly E. Fast
Near Earth Object Observations Program Manager

5/19/2016
Date


Lindley M. Johnson
Planetary Defense Officer

5/19/16
Date


David C. Schurr
Program Director

5/31/16
Date

Approval:


James L. Green
Director, Planetary Science Division

5/31/16
Date

Appendix 2: Key to Plots (Sections 6, 8, and 9)

A unique color is used for each system, based on location and type of technology.

A unique line type and/or marker is used for each primary mirror size.

Tech+Location	Curves	Size	Scatter Plots
IR+Vis L1	-----	0.5 m	▲
Vis LEO	—————	1 m	◆
Vis GEO	-----	2 m	■
Vis L1	- · - · - · -	0.2 m	●
Vis L2	- · - · - · -	0.5 m Network	▲
Vis Venus	- · - · ◆ - · -	1 m Network	◆
IR L1	- · - · ◆ - · -	IR+Vis Network	
IR Venus			
IR GEO			
GBO 2m			
GBO 4m			
GBO 8m			
Status Quo			

This page is intentionally blank.

REFERENCES

- Aftosmis, M.J., M.J., Berger, and J.E., Melton. 1998. "Robust and Efficient Cartesian Mesh Generation for Component-Based Geometry." *AIAA Journal* 36(6): 952–960.
- Aftosmis, M.J., M. Nemec, D. Mathias, and M. Berger. 2016a. "Numerical Simulation of Bolide Entry with Ground Footprint Prediction." Paper presented at the 54th AIAA Aerospace Sciences Meeting, San Diego, Calif., 4–8 January.
- Aftosmis, M., M.J. Berger, M.J. Nemec, and D.L. Mathias. 2016b. "Three-Dimensional Parametric Modeling of Airburst Events for Asteroid Risk Assessment." Paper presented at the Second International Workshop on Asteroid Threat Assessment: Asteroid-generated Tsunami (AGT) and Associated Risk Assessment, Seattle, Wash., 23–24 August.
- A'Hearn, M. 2016. Private communication to D.K. Yeomans, October 13.
- Alí-Lagoa, V., J. de León, J. Licandro, M. Delbó, H. Campins, N. Pinilla-Alonso, and M.S. Kelley. 2013. "Physical Properties of B-Type Asteroids from WISE Data." *Astronomy and Astrophysics* 554: article id. A71.
- Amante, C. and B.W. Eakins. 2009. ETOPO1 1 Arc-Minute Global Relief Model: Procedures, Data Sources and Analysis. NOAA Technical Memorandum NESDIS NGDC-24. National Centers for Environmental Information, NOAA. doi:10.7289/V5C8276M [accessed August 2016].
- Andraschko, M., J. Antol, S. Horan, and D. Neil. 2011. "Commercially Hosted Government Payloads: Lessons from Recent Programs," Paper in *Proceedings of the 2011 IEEE Aerospace Conference* 1–15. Big Sky, Mont., 5–12 March.
- Bacon, C.M., C.W. McMurtry, J.L. Pipher, W.J. Forrest, and J.D. Garnett. 2005. "Burst Noise in the HAWAII-1RG multiplexer." Paper in *Proceedings of SPIE* 5902: 116–127.
- Bacon, C.M., C.W. McMurtry, J.L. Pipher, A. Mainzer, and W. Forrest. 2010. "Effect of Dislocations on Dark Current in LWIR HgCdTe Photodiodes." Paper in *Proceedings of SPIE* 7742: 77421U-1–77421U-9.
- Baggett, S.M., R.J. Hill, R.A. Kimble, J.W. MacKenty, A. Waczynski, H.A. Bushouse, N. Boehm, et al. 2008. "The Wide-Field Camera 3 Detectors." Paper in *Proceedings of SPIE* 7021: 70211Q-1–70211Q-11.
- Bailey, R.B., J.M. Arias, W.V. McLevige, J.G. Pasko, A.C. Chen, C. Cabelli, L.J. Kozlowski, et al. 1998. "Prospects for Large-Format IR Astronomy FPAs Using MBE-Grown HgCdTe Detectors with Cutoff Wavelength $> 4 \mu\text{m}$." Paper in *Proceedings of SPIE* 3354: 77–86.
- Bauer, J.M. 2017. Private communication to D.K. Yeomans, January 17.
- Bauer, J.M., T. Grav, Y.R. Fernández, A.K. Mainzer, E.A. Kramer, J.R. Masiero, T. Spahr, et al. 2017. "D"ebiasing the NEOWISE Cryogenic Mission Comet Populations." *The Astronomical Journal* 154(2): 53–61.

REFERENCES (continued)

- Berger, M.J., 2016. "Simulations and Analysis of Asteroid-Generated Tsunamis Using the Shallow Water Equations." Paper presented at the Second International Workshop on Asteroid Threat Assessment: Asteroid-generated Tsunami (AGT) and Associated Risk Assessment, Seattle, Wash. 23–24 August.
- Boslough, M.B.E. and D.A. Crawford. 2008. "Low-Altitude Airbursts and the Impact Threat." *International Journal of Impact Engineering* 35(12):1441–1448. Paper presented at the Hypervelocity Impact 2007 Symposium.
- Boslough, M. 2016. "Computational Modeling of Airbursts for Asteroid-Generated Tsunami." Paper presented at the Second International Workshop on Asteroid Threat Assessment: Asteroid-generated Tsunami (AGT) and Associated Risk Assessment, Seattle, Wash., 23–24 August.
- Bottke, W.F., M. Broz, D.P. O'Brien, A. Campo Bagatin, A. Morbidelli, and S. Marchi. 2015. "The Collisional Evolution of the Asteroid Belt." Chapter in *Asteroids IV*, edited by P. Michel, F. DeMeo, and W.F. Bottke, 701–724. Tucson: University of Arizona Press.
- Bottke, W.F., A. Morbidelli, R. Jedicke, J.-M. Petit, H. Levison, P. Michel, and T.S. Metcalfe. 2002. "Debiased Orbital and Size Distributions of the Near-Earth Objects." *Icarus* 156: 399–433.
- Bottke, W.F., D. Vokrouhlický, and D. Nesvorný. 2007. "An Asteroid Breakup 160 Myr Ago as the Probable Source of the K-T Impactor." *Nature* 449: 48–53. doi:10.1038/nature06070.
- Brown, P.G., J.D. Assink, L. Astiz, R. Blaauw, M.B. Boslough, J. Borovička, N. Brachet, et al. 2013. "A 500-kiloton Airburst over Chelyabinsk and an Enhanced Hazard from Small Impactors." *Nature* 503: 238–241.
- Buie, M.W., H.J. Reitsema, and R.P. Linfield. 2016. "Surveying the Inner Solar System with an Infrared Space Telescope." *The Astronomical Journal* 152(5): article id. 122, 1–23.
- Bus, S. and R. Binzel. 2002. "Phase II of the Small Main-Belt Asteroid Spectroscopic Survey: A Feature-Based Taxonomy." *Icarus* 158(1): 146–177.
- Canavan, G.H. 1995. "Cost and Benefit of Near-Earth Object Defenses." Paper in *Proceedings of the Planetary Defense Workshop* 273–298. Lawrence Livermore National Laboratory, Livermore, Calif., 22–26 May.
- Cardon, J. H. Latvakoski, M. Larsen, J. Elwell, A. Mainzer, and I. Heinrichsen. 2010. "WISE Ground Characterization Challenges and Accomplishments." Paper in *Proceedings of SPIE* 7796: article id. 77960D.
- Cellino, A., M. Di Martino, E. Dotto, P. Tanga, V. Zappala, S.D. Price, M.P. Egan, et al. 2000. "Spaceguard-1: A Space-Based Observatory for NEO Physical Characterization and Discovery." Paper in *Proceedings of SPIE* 4013: 433–443.

REFERENCES (continued)

- Cellino, A., K. Muinonen, and E.F. Tedesco. 2004. "Rationale and Orbital Options for a Dedicated Space-Based Observatory for NEOs." *Advances in Space Research* 33(9): 1576–1583.
- Cellino, A, R. Somma, L. Tommasi, R. Paolinetti, K. Muinonen, J. Virtanen, E.F. Tedesco, and M. Delbò. 2006. "NERO: General Concept of a Near-Earth Object Radiometric Observatory." *Advances in Space Research* 37(1): 153–160.
- Center for International Earth Science Information Network (CIESIN), United Nations Food and Agriculture Programme, and Centro Internacional de Agricultura Tropical. 2005. "Gridded Population of the World (GPW), v3." Palisades, N.Y.: NASA Socioeconomic Data and Applications Center. Online at <http://dx.doi.org/10.7927/H4639MPP> [accessed August 2016].
- Chesley, S.R. and P. Vereš. 2016. "The Large Synoptic Survey Telescope: Projected Near-Earth Object Discovery Performance." Paper in *the Proceedings of the 2016 IEEE Aerospace Conference*, Big Sky, Mont., 5–12 March.
- Chesley, S. and S. Ward. 2006 "A Quantitative Assessment of the Human and Economic Hazard from Impact-generated Tsunami." *Natural Hazards* 38: 355-374. DOI 10.1007/s11069-005-1921-y.
- Chodas, P.W. 1996. "Estimating Earth Impact Probabilities for Long Period Comets." *Bulletin of the American Astronomical Society* 28: 1086.
- Cibin, L., M. Chiarini, A. Milani Comparetti, F. Bernardi, R. Ragazzoni, G.M., Pinna, I. Zayer, et al. 2012. "Wide Eye Debris Telescope Allows to Catalogue Objects in Any Orbital Zone." *Memorie della Societa Astronomica Italiana Supplementi* 20: 50–57.
- Collins, G.S., H.J. Melosh, and R.A. Marcus. 2005. "Earth Impact Effects Program: A Web-based Computer Program for Calculating the Regional Environmental Consequences of a Meteoroid Impact on Earth." *Meteoritics and Planetary Science* 40(6): 817–840.
- Cutri, R. M., E.L. Wright, T. Conrow, J. Bauer, D. Benford, H. Brandenburg, J. Dailey, et al. 2012 Explanatory Supplement to the WISE All-Sky Data Release Products. Online at http://wise2.ipac.caltech.edu/docs/release/allsky/expsup/sec4_4b.html.
- D’Abramo, G., A.W. Harris, A. Boattini, S.C. Werner, A.W. Harris, and G.B. Valsecchi. 2001. "A Simple Probabilistic Model to Estimate the Population of Near-Earth Asteroids." *Icarus* 153(1): 214–217.
- DeGroot, M.H. 1975. *Probability and Statistics*. Reading, Mass.: Addison-Wesley Publishing Company.
- DeMeo, F.E., R.P. Binzel, S.M. Slivan, and S.J. Bus. 2009. "An Extension of the Bus Asteroid Taxonomy into the Near-Infrared." *Icarus* 202(1): 160–180.
- Denneau, L., R. Jedicke, T. Grav, M. Granvik, J. Kubica, A. Milani, P. Veres, et al. 2013. "The Pan-STARRS Moving Object Processing System." *Publications of the Astronomical Society of the Pacific* 125: 357–395.

REFERENCES (continued)

Dorn, M., J.L. Pipher, C. McMurtry, S. Hartman, A. Mainzer, M. McKelvey, R. McMurray, D. Chevara, and J. Rosser. 2016. "Proton Irradiation Results for Long-Wave HgCdTe Infrared Detector Arrays for NEOCam." *Journal of Astronomical Telescopes, Instruments, and Systems* 2(3): id. 036002.

Dressel, L. 2016. *Wide Field Camera 3 Instrument Handbook, Version 8.0*. Baltimore: Space Telescope Science Institute.

European Southern Observatory (ESO) website. 2012. "Paranal Astroclimatology." Online at <http://www.eso.org/sci/facilities/paranal/astroclimate.html>.

Ewart, R. and R. Lowell. 2011. "Dynamic Radiation Modeling for Space Mission Operability Determination." Paper presented at the AIAA SPACE 2011 Conference & Exposition, AIAA SPACE Forum, Long Beach, Calif., 27–29 Sept. Online at <http://dx.doi.org/10.2514/6.2011-7148>.

Farnocchia, D., S.R. Chesley, P.W. Chodas, P. Tricario, M.S.P. Kelly, and T.L. Farnham. 2014. "Trajectory Analysis for the Nucleus and Dust of Comet C/2013 A1 (Siding Spring)." *Astrophysical Journal* 790: 114–120.

Fazio, G.G., J.L. Hora, L.E. Allen, M.L.N. Ashby, P. Barmby, L.K. Deutsch, J.-S. Huang, et al. 2004. "The Infrared Array Camera (IRAC) for the Spitzer Space Telescope." *The Astrophysical Journal Supplement Series* 154(1): 10–17.

Fernández, Y.R., M.S. Kelly, P.L. Lamy, I. Toth, O. Groussin, C.M. Lisse, M.F. A'Hearn, et al. 2013. "Thermal Properties, Sizes, and Size Distribution of Jupiter-Family Cometary Nuclei." *Icarus* 226(1): 1138–1170.

Finley, P.T., R.B. Schweickart, and R.A. Hopkins. 2004. "The Space Infrared Telescope Facility (SIRTF) Cryogenic Telescope Assembly (CTA) Cryogenic and Thermal System." *Cryogenics* 44(6–8): 367–373.

Francis, P.J. 2005. "The Demographics of Long-Period Comets." *The Astrophysical Journal* 635: 1348–1361.

Gehrz, R.D. and E.A. Romana. 2003. "Charter and Activities of the SIRTF Focus In-Orbit Checkout (IOC) Integrated Products Team (IPT) and Optical Performance of the CTA." Paper in *Proceedings of SPIE* 4850: 62–71.

Gemini Observatory website. 2012. "Science Operations Statistics." Online at www.gemini.edu/sciops/statistics/#weatherloss.

Girard, J.J. W.J. Forrest, C.W. McMurtry, J.L. Pipher, M.Dorn, and A. Mainzer. 2014. "Cosmic Ray Response of Megapixel LWIR Arrays from TIS." Paper in *Proceedings of SPIE* 9154: 91542A–91542A-10.

Glasstone, S. and P.J. Dolan. 1977. *The Effects of Nuclear Weapons*. U.S. Department of Defense and Energy Research and Development Administration. Washington D.C.: U.S. Government Printing Office.

REFERENCES (continued)

- Granvik, M., A. Morbidelli, R. Jedicke, B. Bolin, W.F. Bottke, E. Beshore, D. Vokrouhlický, M. Delbò, and P. Michel. 2016. “Super-catastrophic Disruption of Asteroids at Small Perihelion Distances.” *Nature* 530: 303–306.
- Grav, T., A. Mainzer, J. Bauer, J. Masiero, T. Spahr, R.S. McMillan, R. Walker, et al. 2011. “WISE/NEOWISE Observations of the Jovian Trojans: Preliminary Results.” *The Astrophysical Journal* 742(1): article id. 40, 1–10.
- Grav, T., A. Mainzer, and T. Spahr. 2016. “Modeling the Performance of the LSST in Surveying the Near-Earth Object Population.” *The Astronomical Journal* 151(6): article id. 172, 1–8.
- Grav, T., A. Mainzer, J. Bauer, J. Masiero, T. Spahr, R.S. McMillan, R. Walker, et al. 2012. “WISE/NEOWISE Observations of the Hilda Population: Preliminary Results.” *The Astrophysical Journal* 744(2): article id. 197, 1–15.
- Greenberg, A.H., J.-L. Margot, A.K. Verma, P.A. Taylor, S.P. Naidu, M. Brozovic, and L.A.M. Benner. 2017. “Asteroid 1566 Icarus’s Size, Shape, Orbit, and Yarkovsky Drift from Radar Observations.” *The Astronomical Journal* 153(3): article id. 108, 1–16.
- Greene, T., C. Beichman, M. Gully-Santiago, D. Jaffe, D. Kelly, J. Krist, M. Rieke, and E.H. Smith. 2010. “NIRCam: Development and Testing of the JWST Near-Infrared Camera.” Paper in *Proceedings of SPIE* 7731: 77310C-1–77310C-9.
- Greenstreet, S., H. Ngo, and B. Gladman. 2012. “The Orbital Distribution of Near-Earth Objects inside Earth’s Orbit.” *Icarus* 217(1): 355–366.
- Gural, P.S., J.A. Larsen, and A.E., Gleason. 2005. “Matched Filter Processing for Asteroid Detection.” *The Astronomical Journal* 130(4): 1951–1960.
- Harris, A.W., 1998. “A Thermal Model for Near-Earth Asteroids.” *Icarus* 131(2): 291–301.
- Harris, A.W. and G. D’Abramo. 2015. “The Population of Near-Earth Asteroids.” *Icarus* 257: 302–312.
- Hartig, G. F., J.E. Krist, A.R. Martel, H.C. Ford, and G.D. Illingworth. 2003. “On-Orbit Alignment and Imaging Performance of the HST Advanced Camera for Surveys.” Paper in *Proceedings of SPIE* 4854: 532–543.
- Hawarden, T.G., H.A. Thronson, A.J. Penny and J. Bally. 1995. “EDISON Program: Designing the Next-Generation Infrared Space Observatory.” Paper in *Proceedings of SPIE* 2478: 11–19.
- Heinze, A.N., S. Metchev, and J. Trollo. 2015. “Digital Tracking Observations Can Discover Asteroids 10 Times Fainter Than Conventional Searches.” *The Astronomical Journal* 150(4): 1–25.

REFERENCES (continued)

Hills, J.G. and M.P. Goda. 1998. "Damage from the Impacts of Small Asteroids." *Planetary and Space Science* 46(2-3): 219-229.

Hills, J.G. and M.P. Goda. 1993. "The Fragmentation of Small Asteroids in the Atmosphere." *Astronomical Journal* 105(3): 1114-1144.

Hoffmann, W.F., J.L. Hora, J.E. Mentzell, C. Marx, and P. Eisenhardt. 2003. "Simfit and Focus Diversity: Methods for Determining the Focus of the SIRTf Telescope in Space without a Focus Slew." Paper in *Proceedings of SPIE* 4850: 428-440.

Holman, M.J., J.J. Kavelaars, T. Grav, B.J. Gladman, W.C. Fraser, D. Milisavljevic, P.D. Nicholson et al. 2004. "Discovery of Five Irregular Moons of Neptune." *Nature* 430: 865-867.

Hosted Payload Guidebook. 2010. Futron Corporation.

[https://science.larc.nasa.gov/hostedpayload/HostedPayloadGuidebook final with acknowledgment.pdf](https://science.larc.nasa.gov/hostedpayload/HostedPayloadGuidebook%20final%20with%20acknowledgment.pdf).

International Astronomical Union. Minor Planet Center website, <http://www.minorplanetcenter.net/>.

Ivezić, Z., T. Axelrod, W.N. Brandt, D.L. Burke, C.F. Claver, A. Connolly, K.H. Cook, et al. 2008. "Large Synoptic Survey Telescope: From Science Drivers to Reference Design." *Serbian Astronomical Journal* 176: 1-13.

Jedicke R., M. Granvik, M. Micheli M., E. Ryan T. Spahr T., and D.K. Yeomans. 2015. "Surveys, Astrometric Follow-up and Population Statistics." Chapter in *Asteroids IV*, edited by P. Michel, F. DeMeo, and W. Bottke, 795-814. Tucson: University of Arizona Press.

Jenkins, J.M., D.A. Caldwell, H. Chandrasekaran, J.D. Twicken, S.T. Bryson, E.V. Quintana, B.D. Clarke, et al. 2010. "Overview of the Kepler Science Processing Pipeline." *The Astrophysical Journal Letters* 713(2): 87-91.

Jones, L., M. Jurić, and Z. Ivezić. 2016. "Asteroid Discovery and Characterization with the Large Synoptic Survey Telescope." Paper in *Proceedings of the International Astronomical Union Symposium on Asteroids: New Observations, New Models* 318: 282-292.

Kaiser, N., H. Aussel, B.E. Burke, H. Boesgaard, K. Chambers, M.R. Chun, J.N. Heasley, et al. 2002. "Pan-STARRS: A Large Synoptic Survey Telescope Array." Paper in *Proceedings of SPIE* 4836: 154-164.

Kavelaars, J.J., M.J. Holman, T. Grav, D. Milisavljevic, W. Fraser, B.J. Gladman, J.-M. Petit, et al. 2004. "The Discovery of Faint Irregular Satellites of Uranus." *Icarus* 169(2): 474-481.

Kessler, M.F., J.A. Steinz, M.E. Anderegg, J. Clavel, G. Drechsel, P. Estaria, J. Faelker, et al. 1996. "The Infrared Space Observatory (ISO) Mission." *Astronomy and Astrophysics* 315: L27-L31.

REFERENCES (continued)

Keys, S. 2006. Personal communication.

Koshimura, S., S. Hayashi, and H. Gokon. 2013. "Lessons from the 2011 Tohoku Earthquake Tsunami Disaster," *Journal of Disaster Research* 8(4):549–560.

Larson, S., J. Brownlee, C. Hergenrother, and T. Spahr. 1998. "The Catalina Sky Survey for NEOs." *Bulletin of the American Astronomical Society* 30: 1037.

Lawrence, J.S., M.C.B., Ashley, A. Tokovinin, and T. Travouillon. 2004. "Exceptional Astronomical Seeing Conditions above Dome C in Antarctica." *Nature* 431: 278–281.

Lebofsky, L.A., and J.R. Spencer. 1989. "Radiometry and Thermal Modeling of Asteroids." Chapter in *Asteroids II* edited by R.P. Binzel, T. Gehrels, and M.S. Matthews, 128–147. Tucson: University of Arizona Press.

Lee, T.J., T.G. Hawarden, H.A. Thronson, C.M. Mountain, J.K. Davies, J. and M.S. Longair. 1990. "Radiatively-Cooled Telescopes for Infrared Space Astronomy." In *Proceedings of the 29th Liège International Astrophysical Colloquium, From Ground-Based to Space-Borne Sub-mm Astronomy*: 375–379. European Space Agency, Liège, Belgium, 3–5 July.

Levison, H.F. and M.J. Duncan. 1994. "The Long-Term Dynamical Behavior of Short-Period Comets." *Icarus* 108(1): 18–36.

Leinert, Ch., S. Bowyer, L.K. Haikala, M.S. Hanner, M.G. Hauser, A.-Ch. Levasseur-Regourd, I. Mann, et al. 1998. "The 1997 Reference of Diffuse Night Sky Brightness." *Astronomy and Astrophysics Supplement* 127: 1–99.

Levi, A., J. Simonds, and C. Gruber. 2011. "CHIRP Technology Demonstration Project." Paper presented at the AIAA SPACE 2011 Conference and Exposition, Long Beach, Calif., 27–29 Sept.

Lindgren, L., U. Lammers, U. Bastian, J. Hernández, S. Klioner, D. Hobbs, A. Bombrun, et al. 2016. "Gaia Data Release 1. Astrometry: One Billion Positions, Two Million Proper Motions and Parallaxes." *Astronomy & Astrophysics* 595 (A4): 1–32.

Magnier, E.A., E. Schlafly, D. Finkbeiner, M. Juric, J.L. Tonry, W.S. Burgett, K.C. Chambers, et al. 2013. "The Pan-STARRS 1 Photometric Reference Ladder, Release 12.01." *The Astrophysical Journal Supplement Series* 205(2): 1–13.

Mainzer, A.K., J.M. Bauer, R.M. Cutri, T. Grav, E.A. Kramer, J.R. Masiero, C.R. Nugent, et al. 2016. "NEOWISE Diameters and Albedos V1.0." *NASA Planetary Data System* 247.

Mainzer, A., J. Bauer, R.M. Cutri, T. Grav, J. Masiero, R. Beck, P. Clarkson et al. 2014. "Initial Performance of the NEOWISE Reactivation Mission." *The Astrophysical Journal* 792(1): article 30.

REFERENCES (continued)

- Mainzer, A., J. Bauer, T. Grav, J. Masiero, R.M. Cutri, J. Dailey, P. Eisenhardt et al. 2011a. "Preliminary Results from NEOWISE: An Enhancement to the Wide-Field Infrared Survey Explorer for Solar System Science." *The Astrophysical Journal* 731(1): article 53.
- Mainzer, A., T. Grav, J. Masiero, J. Bauer, E. Wright, R.M. Cutri, R.S. McMillan et al. 2011b. "Thermal Model Calibration for Minor Planets Observed with Wide-field Infrared Survey Explorer/NEOWISE." *The Astrophysical Journal* 736(2): 100.
- Mainzer, A., T. Grav, J. Masiero, J. Bauer, E. Wright, R.M. Cutri, R. Walker, and R.S. McMillan. 2011c. "Thermal Model Calibration for Minor Planets Observed with WISE/NEOWISE: Comparison with Infrared Astronomical Satellite." *The Astrophysical Journal Letters* 737(1): L9.
- Mainzer, A., T. Grav, J. Masiero, E. Hand, J. Bauer, D. Tholen, R.S. McMillan, et al. 2011d. "NEOWISE Studies of Spectrophotometrically Classified Asteroids: Preliminary Results." *The Astrophysical Journal* 741(2): 90.
- Mainzer, A., T. Grav, J. Bauer, J. Masiero, R.S. McMillan, R.M. Cutri, R. Walker, et al. 2011e. "NEOWISE Observations of Near-Earth Objects: Preliminary Results." *The Astrophysical Journal* 743(2): 156–173.
- Mainzer, A., T. Grav, J. Masiero, J. Bauer, R.S. McMillan, J. Giorgini, T. Spahr, et al. 2012. "Characterizing Subpopulations within the Near-Earth Objects with NEOWISE: Preliminary Results." *The Astrophysical Journal* 752(2): 110–126.
- Mainzer, A., M. Larsen, M.G. Stapelbroek, H. Hogue, J. Garnett, M. Zandian, R. Mattson, et al. 2008. "Characterization of Flight Detector Arrays for the Wide-field Infrared Survey Explorer." Paper in *Proceedings of SPIE* 7021: 70210X–70210X-12.
- Mainzer, A., F. Usui, and D.E. Trilling. 2015. "Space-Based Thermal Infrared Studies of Asteroids." Chapter in *Asteroids IV* edited by P. Michel, F.E. DeMeo, and W.F. Bottke, 89–106. Tucson: University of Arizona Press.
- Mathias, D.L., L.F. Wheeler, and J.L. Dotson. 2017. "A Probabilistic Asteroid Impact Risk Model: Assessment of Sub-300 m Impacts." *Icarus* 289: 106–119. doi: 10.1016/j.icarus.2017.02.009.
- Mathias, D., L. Wheeler, M. Aftosmis, D. Robertson, P. Register, M. Berger, and R. LeVeque. 2016. "Ensemble Asteroid Threat Characterization: Water versus Land Impacts." Paper presented at the Second International Workshop on Asteroid Threat Assessment: Asteroid-generated Tsunami (AGT) and Associated Risk Assessment, Seattle, Wash., 23–24 August.
- Mazrouei, S., R.R. Ghent, W.F. Bottke, A.H. Parker. 2017. "New Evidence for a Phanerozoic Increase in the Impact Flux on the Moon and Earth." Submitted to *Nature Astronomy*.

REFERENCES (continued)

McMurtry, C.W., M. Dorn, M.S. Cabrera, J.L. Pipher, W.J. Forrest, A. Mainzer, and A. Wong. 2016. "Candidate 10 micron HgCdTe Arrays for the NEOCam Space Mission." Paper in *Proceedings of SPIE* 9915: 99150D–99150D-8.

McMurtry, C., D. Lee, J. Beletic, C-Y.A. Chen, R.T. Demers, M. Dorn, D. Edwall, et al. 2013. "Development of Sensitive Long-Wave Infrared Detector Arrays for Passively Cooled Space Missions." *Optical Engineering* 52(9): 091804-1–091804-9.

McNaught, R. 1999. Personal communication.

Meyzonnette, J.-L. 2007. "Probability of Detection and Minimal Value of SNR" in "The Design of Electro-optical Sensors" in *Semiconductor Sensors and Applications* course offered by the Institut d'Optique Graduate School. Online at http://optique-ingenieur.org/en/courses/OPI_ang_M05_C05/co/Contenu_16.html.

Mill, J.D., R.R. O'Neil, S. Price, G.J. Romick, O.M. Uyp, E.M. Gaposchkin, G.C. Light, et al. 1994. "Midcourse Space Experiment: Introduction to the Spacecraft, Instruments, and Scientific Objectives." *Journal of Spacecraft and Rockets* 31(5): 900–907.

Miyashita, A., N. Takato, T. Usuda, F. Uraguchi, and R. Ogasawara. 2004. "Statistics of the weather data, environment data, and the seeing of the Subaru Telescope." *Proceedings of SPIE*, 5489: 207–217.

Monet, D.G., T. Axelrod, T. Blake, C.F. Claver, R. Lupton, E. Pearce, R. Shah, and D. Woods. 2013. "Rapid Cadence Collections with the Space Surveillance Telescope." *American Astronomical Society Meeting Abstracts* 221: 352.17.

Moretto, G., J.R., Kuhn, and P.R. Goode. 2012. "Reviewing Off-Axis Telescope Concepts: A Quest for Highest Possible Dynamic Range for Photometry and Angular Resolution." Paper in *Proceedings of SPIE* 8444: 84440Y-1–84440Y-15.

Morgan, J., W. Siegmund, and C. Hude. 2006. "The Design of the Pan-STARRS Telescope #1." Paper presented at the Advanced Maui Optical and Space Surveillance Technologies Conference, Maui, Hawaii, 14–17 September.

Morrison D. and E. Venkatapathy. 2017. "Asteroid Generated Tsunami: Summary of NASA/NOAA Workshop." NASA Technical Memorandum, NASA/TM-219463.

Müller, T.G., C. Kiss, P. Scheirich, P. Pravec, L. O'Rourke, E. Vilnius, and B. Altieri. 2014a. "Thermal Infrared Observations of Asteroid (99942) Apophis with Herschel." *Astronomy and Astrophysics* 566: 1–21.

Müller, T., Z. Balog, M. Nielbock, T. Lim, D. Teyssier, M. Olberg, U. Klaas, et al. 2014b. "Herschel Celestial Calibration Sources: Four Large Main-Belt Asteroids as Prime Flux Calibrators for the Far-IR/sub-mm Range." *Experimental Astronomy* 37(2): 253–330.

REFERENCES (continued)

- Murakami, H., H. Baba, P. Barthel, D.L. Clements, M. Cohen, Y. Doi, K. Enya, et al. 2007. "The Infrared Astronomical Mission AKARI." *Publications of the Astronomical Society of Japan* 59(s2): s369.
- Nesvorný, D., D. Vokrouhlický, A. Morbidelli, W.F. Bottke. 2009. "Asteroidal Source of L Chondrite Meteorites." *Icarus* 200(2): 698–701.
- Neugebauer, G., H.J. Habing, R. van Duinen, H.H. Aumann, B. Baud, C.A. Beichman, D.A. Beintema, et al. 1984. "The Infrared Astronomical Satellite (IRAS) Mission." *The Astrophysical Journal, Part 2* 278: L1–L6.
- NOAA Office of Response and Restoration. 2017. "Overpressure Levels of Concern." Online at <http://response.restoration.noaa.gov/oil-and-chemical-spills/chemical-spills/resources/overpressure-levels-concern.html>.
- Nugent, C.R., A. Mainzer, J. Bauer, R.M. Cutri, E.A. Kramer, T. Grav, J. Masiero, et al. 2016. "NEOWISE Reactivation Mission Year Two: Asteroid Diameters and Albedos." *The Astronomical Journal* 152(3): 63.
- Nugent, C.R., A. Mainzer, J. Masiero, J. Bauer, R.M. Cutri, T. Grav, E. Kramer, et al. 2015. "NEOWISE Reactivation Mission Year One: Preliminary Asteroid Diameters and Albedos." *The Astrophysical Journal* 814(2): 117.
- Onaka, P., C. Rae, S. Isani, J.L., Tonry, A. Lee, R., Uyeshiro, L. Robertson, and G. Ching. 2012. "GPC1 and GPC2: The Pan-STARRS 1.4 Gigapixel Mosaic Focal Plane CCD Cameras with an on-Sky on-CCD Tip-Tilt Image Compensation." Paper in *Proceedings of SPIE* 8453: 84530K-1–84530K-12.
- Ostro, S.J. and J.D. Giorgini. 2004. "The Role of Radar in Predicting and Preventing Asteroid and Comet Collisions with Earth." *Mitigation of Hazardous Comets and Asteroids*. M. Belton, T.H. Morgan, N. Samarasinha, and D.K. Yeomans, eds. Cambridge, U.K.: Cambridge University Press.
- Pollock, R., R.E. Haring, J.R. Holden, D.L. Johnson, A. Kapitanoff, D. Mohlman, C. Phillips, et al. 2010. "The Orbiting Carbon Observatory Instrument: Performance of the OCO Instrument and Plans for the OCO-2 Instrument." Paper in *Proceedings of SPIE* 7826: 78260W-1–78260W-13.
- Popova, O.P., J. Borovička, W.K. Hartmann, P. Spurny, E. Gnos, I. Nemtchinov, and J.M. Trigo-Rodriguez. 2011. "Very Low Strengths of Interplanetary Meteoroids and Small Asteroids." *Meteoritics and Planetary Science* 46(10): 1525–1550.
- Price, S.D., M.P. Egan, S.J. Carey, D.R. Mizuno, and T.A. Kuchar. 2001. "Midcourse Space Experiment Survey of the Galactic Plane." *The Astronomical Journal* 121(5): 2819–2842.
- Price, S.D. and M.P. Egan. 2001. "Spaced Based Infrared Detection and Characterization of Near Earth Objects." *Advances in Space Research* 28(8): 1117–1127.

REFERENCES (continued)

- Rabinowitz, D. L. 1991. "Detection of Earth-Approaching Asteroids in Near Real Time." *The Astronomical Journal* 101(4): 1518–1529.
- Rauscher, B.J., D.J. Lindler, D.B. Mott, Y. Wen, P. Ferruit, and M. Sirianni. 2011. "The Dark Current and Hot Pixel Percentage of James Webb Space Telescope 5 μm Cutoff HgCdTe Detector Arrays as Functions of Temperature." *Publications of the Astronomical Society of the Pacific* 123(906): 953–957.
- Register, P.J., D.L. Mathias, and L.F. Wheeler. 2017. "Asteroid Fragmentation Approaches for Modeling Atmospheric Energy Deposition." *Icarus* 284: 157–166.
- Ressler, M.E., K.G. Sukhatme, B.R. Franklin, J.C. Mahoney, M.P. Thelen, P. Bouchet, J.W. Colbert, et al. 2015. "The Mid-Infrared Instrument for the James Webb Space Telescope, VIII: The MIRI Focal Plane System." *Publications of the Astronomical Society of the Pacific* 127(953): 675–685.
- Rieke, G.H., E.T. Young, C.W. Engelbracht, D.M. Kelly, F.J. Low, E.E. Haller, J.W. Beeman, et al. 2004. "The Multiband Imaging Photometer for Spitzer (MIPS)." *The Astrophysical Journal Supplement Series* 154(1): 25–29.
- Roach, F.E. and J.L. Gordon. 1973. "The Light of the Night Sky." *Geophysics and Astrophysics Monographs*. Boston: D. Reidel Publishing Company.
- Robertson, D.K. 2016. "Tsunami Generation from Asteroid Airburst and Ocean Impact, and Van Dorn Effect." Paper presented at the Second International Workshop on Asteroid Threat Assessment: Asteroid-generated Tsunami (AGT) and Associated Risk Assessment, Seattle, Wash., 23–24 August.
- Samarasinha, N.H. 2007. "Rotation and Activity of Comets." *Advances in Space Research* 39(3): 421–427.
- Sampath, D., A. Akerstrom, M. Barry, J. Guregian, M. Schwalm, and V. Ugolini. 2010. "The WISE Telescope and Scanner: Design Choices and Hardware Results." Paper in *Proceedings of SPIE* 7796: id. 779609.
- Sartori, L. 1983. "The Effects of Nuclear Weapons." *Physics Today* 36(3): 32–41.
- Schmidt-Kaler, T. and P. Rucks. 1997. "Telescope Costs and Cost Reduction." Paper in *Proceedings of SPIE* 2871: 635–640.
- Schueler, C. 2012. "FD-CHIRP: Hosted Payload System Engineering Lessons." Paper in *Proceedings of SPIE* 8516: 851607-1–851607-10.
- Schwalm, M., M. Barry, G. Perron, D. Sampath, F. LaMalva, J. Guregian, and B. Crowther. 2005. "Cryogenic Telescope, Scanner, and Imaging Optics for the Wide-field Infrared Survey Explorer (WISE)." Paper in *Proceedings of SPIE* 5904: 59040K-1–59040K-7.

REFERENCES (continued)

- Sekanina, Z. and D.K. Yeomans. 1984. "Close Encounters and Collisions of Comets with the Earth." *The Astronomical Journal* 89(1): 154–161.
- Shao, M., B. Nemati, C. Zhai, S.G. Turyshev, J. Sandhu, G.W. Hallinan, and L.K. Harding. 2014. "Finding Very Small Near-Earth Asteroids using Synthetic Tracking." *The Astrophysical Journal* 782(1): 1–10.
- Shao, M., C. Zhai, T. Werne, B. Nemati, L.K. Harding, and G. Hallinan. 2014. "Detection of a Small Fast Moving Near Earth Asteroid with Synthetic Tracking." American Astronomical Society Meeting Abstracts #223.
- Simonds, J., J.Z. Jacquot, C.Kersten, P. Lew, and G. Sullivan. 2010. "Lessons Learned from Hosting an Infrared Payload on a Communications Satellite." Paper in the *Proceedings of the 2010 IEEE Aerospace Conference*.
- Soares-Santos, M., R. Kessler, E. Berger, J. Annis, D. Brout, E. Buckley-Geer, H. Chen, et al. 2016. "A Dark Energy Camera Search for an Optical Counterpart to the First Advanced LIGO Gravitational Wave Event GW150914." *The Astrophysical Journal Letters* 823(L33): 1–6.
- Stepp, L.M., L.G. Daggert, and P.E. Gillett. 2003. "Estimating the Cost of Extremely Large Telescopes." Paper in *Proceedings of SPIE* 4840: 309–321.
- Stokes, G.H., J.B. Evans, H.E.M. Vigg, F.C. Shelly, and E.C. Pearce. 2000. "Lincoln Near-Earth Asteroid Program (LINEAR)." *Icarus* 148(1): 21–28.
- Stokes, G.H., D.K. Yeomans, W.F. Bottke, S.R. Chesley, J.B. Evans, R.E. Gold, A.W. Harris, et al. 2003. "Study to Determine the Feasibility of Extending the Search for Near-Earth Objects to Smaller Limiting Diameters." Report of the Near-Earth Object Science Definition Team, Lexington, Mass.: National Aeronautics and Space Administration.
- Storrie-Lombardi, L.J., and S.R. Dodd. 2012. "Spitzer Warm Mission: Maximizing the Science Return in the Extended Mission Phase." Paper in *Proceedings of SPIE* 8448: 84481E-1–84481E-9.
- Stuart, J., and R. Binzel. 2004. "Bias-Corrected Population, Size Distribution, and Impact Hazard for the Near-Earth Objects." *Icarus* 170(2): 295–311.
- Tedesco, E.F., P.V. Noah, M. Noah, and S.D. Price. 2002a. "The Supplemental IRAS Minor Planet Survey." *The Astronomical Journal* 123(2): 1056–1085.
- Tedesco, E.F.; M.P. Egan, and S.D. Price. 2002b. "The Midcourse Space Experiment Infrared Minor Planet Survey." *The Astronomical Journal* 124(1): 583–591.
- Tedesco, E.F., K. Muinonen, and S.D. Price. 2000. "Space-Based Infrared Near-Earth Asteroid Survey Simulation." *Planetary and Space Science* 48(9): 801–816.

REFERENCES (continued)

Tholen, D.J. 1984. Asteroid Taxonomy from Cluster Analysis of Photometry. PhD thesis, University of Arizona, Tucson.

Thomas, C.A., D.E. Trilling, J.P. Emery, M. Mueller, J.L. Hora, L.A.M. Benner, B. Bhattacharya, et al. 2011. "ExploreNEOs. V. Average Albedo by Taxonomic Complex in the Near-Earth Asteroid Population." *The Astronomical Journal* 142(3): article id. 85.

Thronson, H.A., Jr., J.K. Davies, J. Hackwell, T.G. Hawarden, R.F. Knacke, D. Lester, D.; and C.M. Mountain. 1992. "EDISON—The Next Generation Infrared Space Observatory." *Space Science Reviews* 61(1–2): 145–169.

Tonry, J.L. 2011. "An Early Warning System for Asteroid Impact." *Publications of the Astronomical Society of the Pacific* 123(899): 58–73.

Toon, O.B., K. Zahnle, D. Morrison, R.P. Turco, and C. Covey. 1997. "Environmental Perturbations Caused by the Impacts of Asteroids and Comets." *Reviews of Geophysics* 35(1): 41–78.

Tricarico, P. 2017. "The Near-Earth Asteroid Population from Two Decades of Observations." *Icarus* 284: 416–423.

Trilling, D.E., M. Mueller, J.L. Hora, A.W. Harris, B. Bhattacharya, W.F. Bottke, S. Chesley, et al. 2010. "ExploreNEOs. I. Description and First Results from the Warm Spitzer Near-Earth Object Survey." *The Astronomical Journal* 140(3): 770–784.

U.S. Department of Transportation. "Guidance on Treatment of the Economic Value of a Statistical Life (VSL) in U.S. Department of Transportation Analyses–2015 Adjustment." 17 June 2015. <https://www.transportation.gov/regulations/guidance-treatment-economic-value-statistical-life-us-department-transportation-analyses>.

Usui, F., S. Hasegawa, M. Ishiguro, T.G. Müller, and T. Ootsubo. 2014. "A Comparative Study of Infrared Asteroid Surveys: IRAS, AKARI, and WISE." *Publications of the Astronomical Society of Japan* 66(3): article id. 5611.

Usui, F., T. Kasuga, S. Hasegawa, M. Ishiguro, D. Kuroda, T.G. Müller, T. Ootsubo, and H. Matsuhara. 2013. "Albedo Properties of Main Belt Asteroids Based on the All-Sky Survey of the Infrared Astronomical Satellite AKARI." *The Astrophysical Journal* 762(1): 56–70.

Usui, F., D. Kuroda, T.G. Müller, S. Hasegawa, M. Ishiguro, T. Ootsubo, D. Ishihara, et al. 2011. "Asteroid Catalog Using Akari: AKARI/IRC Mid-Infrared Asteroid Survey." *Publications of the Astronomical Society of Japan* 63(5): 1117–1138.

Van Dorn, W.G., B. LeMehaute, and L.-S. Hwang. 1968. "Handbook of Explosion-Generated Water Waves: Volume I. State of the Art." Rep. TC-130. Pasadena, Calif.: Tetra Tech Inc.

REFERENCES (continued)

- Vereš, P. and S.R. Chesley. 2017. "High-Fidelity Simulations of the Near-Earth Object Search Performance of the Large Synoptic Survey Telescope." *The Astronomical Journal* 154(1): 44 pages.
- Vereš, P., D. Farnocchia, R. Jedicke, and F. Spoto. 2014. "The Effect of Parallax and Cadence on Asteroid Impact Probabilities and Warning Times." *Publications of the Astronomical Society of the Pacific* 126(939): 433–444.
- Viscusi, W.K. and J.E. Aldy. 2003. "The Value of a Statistical Life: A Critical Review of Market Estimates Throughout the World." *Journal of Risk and Uncertainty* 27(1): 5–76.
- Vokrouhlický, D., W.F. Bottke, S.R. Chesley, D.J. Scheeres, and T.S. Statler. 2015. "The Yarkovsky and YORP Effects." Chapter in *Asteroids IV*, edited by P. Michel, F. DeMeo, and W.F. Bottke, 509–532. Tucson: University of Arizona Press.
- Ward, S. and E. Asphaug. 2000. "Asteroid Impact Tsunami: A Probabilistic Hazard Assessment," *Icarus*. 145(1): 64–78.
- Waszczak, A., T.A. Prince, R. Laher, F. Masci, B. Bue, U. Rebbapragada, T. Barlow et al. 2017. "Small Near-Earth Asteroids in the Palomar Transient Factory Survey: A Real-Time Streak-Detection System." *Publications of the Astronomical Society of the Pacific* 129(973): 034402.
- Weibull, W.A. 1951. "A Statistical Distribution Function of Wide Applicability." *Journal of Applied Mechanics* 293–297.
- Werner, M.W., T.L. Roellig, F.J. Low, G.H. Rieke, M. Rieke, W.F. Hoffmann, E. Young, et al. 2004. "The Spitzer Space Telescope Mission." *The Astrophysical Journal Supplement Series* 54(1): 1–9.
- Wheeler, L.F., D.L. Mathias, and P.J. Register. 2017. "Fragment-Cloud Model for Asteroid Breakup and Atmospheric Energy Deposition." In press, *Icarus*. doi:10.1016/j.icarus.2017.02.011.
- Wheeler, L., D. Mathias, and P. Register. 2016. "Analytic Tsunami Models for Physics-Based Impact Risk Assessment." Paper presented at the Second International Workshop on Asteroid Threat Assessment: Asteroid-generated Tsunami (AGT) and Associated Risk Assessment, Seattle, Wash., 23–24 August.
- Wisdom, J., and M. Holman. 1991. "Symplectic Maps for the n-body Problem." *The Astronomical Journal* 102: 1528–1538.
- Wright, E.L., P.R.M. Eisenhardt, A.K. Mainzer, M.E. Ressler, R.M. Cutri, T. Jarrett, J.D. Kirkpatrick, et al. 2010. "The Wide-field Infrared Survey Explorer (WISE): Mission Description and Initial On-orbit Performance." *The Astronomical Journal* 140(6): 1868–1881.
- Wright, E.L., A. Mainzer, J. Masiero, T. Grav and J. Bauer. 2016. "The Albedo Distribution of Near Earth Asteroids." *The Astronomical Journal* 152 (4): 79–83.

REFERENCES (continued)

Wright, E.L. 1998. "Angular Power Spectra of the COBE DIRBE Maps." *The Astrophysical Journal* 496(1): 1–8.

Wright, E.L. 1985. "On Using a Space Telescope to Detect Faint Galaxies." *Publications of the Astronomical Society of the Pacific* 97: 451–453.

Zahnle, K., P. Schenk, H. Levison, and L. Dones. 2003. "Cratering Rates in the Outer Solar System." *Icarus* 163(2): 263–289.

This page is intentionally blank.

ACRONYMS AND ABBREVIATIONS

μm	micrometer	FCM	fragment-cloud model
AB	annual benefits	FOR	field of regard
AO	adaptive optics	FOV	field of view
AIS	Abbreviated Injury Scale	FROSST	Fast Resident Object Surveillance System
APL	Applied Physics Laboratory (Johns Hopkins University)	FWHM	full width at half-maximum
arcsec	arcsecond	g/cc	gram per cubic centimeter
ATLAS	Asteroid Terrestrial Last Alert System	GDP	gross domestic product
AU	astronomical unit	GEO	geostationary, geosynchronous
CCD	charge-coupled device	GOLD	Global-scale Observations of the Limb and Disk
CER	cost-estimating relationship	HgCdTe	mercury cadmium telluride
CHIRP	Commercially Hosted Infrared Payload	IBC	impurity band conduction
cm	centimeter	IFOV	instantaneous field of view
CMG	control moment gyroscope	InSb	indium antimonide
CMOS	complementary metal-oxide semiconductor	IR	infrared
COCOMO	Constructive Cost Model	IRAS	Infrared Astronomical Satellite
CPU	central processing unit	ISO	Infrared Space Observatory
CRED	Centre for Research on the Epidemiology of Disasters	J-PAS	Javalambre Physics of the Accelerating Universe Astrophysical Survey
CSS	Catalina Sky Survey	JPL	Jet Propulsion Laboratory
CTIA	capacitive transimpedance amplifier	JWST	James Webb Space Telescope
DARPA	Defense Advanced Research Projects Agency	K	thousand, Kelvin
DSN	Deep Space Network	KBO	Kuiper Belt object
EMCCD	electron multiplying CCD	km	kilometer
ECA	Earth-crossing asteroid	kt	kiloton
ESA	European Space Agency	LD	lunar distance
ESO	European Southern Observatory	LINEAR	Lincoln Near-Earth Asteroid Research
FEMA	Federal Emergency Management Agency	LPC	long-period comet
		LSST	Large Synoptic Survey Telescope

ACRONYMS AND ABBREVIATIONS (continued)

LSSTC	LSST Collaboration	Pan-STARRS	Panoramic Survey Telescope and Rapid Response System
LWIR	long-wavelength infrared	PHA	potentially hazardous asteroid
m	meter	PHO	Potentially hazardous object
M	million	PCEC	Project Cost Estimating Capability
MBA	main-belt asteroid	PSF	point-spread function
Mbit	megabit	psi	pounds per square inch
Mbps	megabits per second	QE	quantum efficiency
MOCET	Mission Operations Cost-Estimating Tool	RAM	random-access memory
MOID	minimum orbit intersection distance	s	second
MO&S	mission operations and support	SAIC	Science Applications International Corporation
MPa	megapascal	SDL	Space Dynamics Laboratory
MPC	Minor Planet Center	SDT	Study Definition Team
MSX	Midcourse Space Experiment	Si:As	silicon-arsenic
Mt	megaton	SLOC	source line of code
MWIR	mid-wavelength infrared	SNR	signal-to-noise ratio
Myr	million years	SOHO	Solar and Heliospheric Observatory
NAFCOM	NASA/Air Force Cost Model	SPC	short-period comet
NASA	National Aeronautics and Space Administration	SST	Space Surveillance Telescope
NEA	near-Earth asteroid	SST	Survey Simulation Tool
NEATM	Near-Earth Asteroid Thermal Model	SWIR	short-wavelength infrared
NEO	near-Earth object	Tbit	terabit
NEOWISE	NEO Wide-field Infrared Survey Explorer	TDI	time-delay integration
NESI	noise equivalent spectral irradiance	TIS	Teledyne Imaging Systems
NICM	NASA Instrument Cost Model	TMA	three-mirror anastigmat
O&S	operations and support	TRL	technology readiness level
OTA	orthogonal transfer array, optical telescope assembly	UR	University of Rochester
		WBS	work breakdown structure
		WISE	Wide-field Infrared Survey Explorer